University of Nottingham
UK | CHINA | MALAYSIA

Theranostic apoferritin nanocages for brain tumours: dual delivery of temozolomide and lead sulfide quantum dots

Thesis submitted to the University of Nottingham for the degree of Doctor of Philosophy
September 2025

Reyhan Dilsu Colpan

Supervisors:
Dr. Tracey D. Bradshaw
Dr. Lyudmila Turyanska
Prof. Neil R.Thomas

School of Pharmacy, Faculty of Science
University of Nottingham

Abstract

Glioblastoma (GBM) is the most common and aggressive (grade 4) primary brain tumour, arising from malignant transformation of glial cells, a consequence of genetic and epigenetic alterations. Its global incidence is 3-5 cases per 100, 000 person-years. GBM remains a clinical challenge, a consequence of treatment resistance, poor delivery because of restrictive barriers such as the blood brain barrier (BBB), ATP-binding cassette proteins, and tumour localisation. Median survival, with standard of care treatment which includes temozolomide (TMZ), is ~16 months. However, TMZ chemotherapy is limited by toxicity, drug resistance, chemical properties of TMZ, and poor drug accumulation at the tumour site. Resistance mechanisms include overexpression of *O*6-methylguanine-DNA methyltransferase (MGMT), drug efflux transporters (P-glycoprotein (P-gp)), base excision repair (BER), and mismatch repair (MMR) deficiency.

GBM imaging is essential for tumour characterisation, localisation, and surgery, particularly in addressing GBM-specific challenges such as anatomical barriers and deeply located tumours. Therefore, deep tissue imaging with near infrared region II (NIR-II, 1000-1700 nm) rather than near infrared region I (NIR-I, 650-900 nm) has gained attention. In this context, quantum dots (QDs), particularly lead sulfide quantum dots (PbS QDs), can be used in NIR-II/ short wave infrared (SWIR) probes for cancer imaging applications due to their advantageous properties, including stable optical emission when compared to traditional fluorescent agents. However, their potential toxicity is the major limitation for their use in cancer imaging.

This PhD project investigated a novel theranostic formulation for the treatment and monitoring of GBM, addressing the need for new targeted drug delivery systems (DDS) using nanoparticles (NPs) to overcome both diagnostic and therapeutic limitations. Therefore, the combination of diagnostic and therapeutic approach in one construct, called as theranostics, has gained attention. Among various DDS, apoferritin (AFt) is a promising candidate for

improving delivery to the brain by exploiting overexpression of transferrin receptor 1 (TfR1) on GBM and BBB endothelial cells. Herein, we developed a dual function theranostic platform based on horse spleen AFt nanocages co-encapsulated with TMZ and PbS QDs, AFt-PbS-TMZ, for simultaneous TfR1 targeted delivery of therapeutic and imaging agents. AFt-PbS-TMZ (12.1 ± 0.6 nm in diameter from high resolution transmission microscopy) demonstrated high encapsulation efficiencies (74.4 ± 11.25% for TMZ, one QD for each cage) and pH-dependent TMZ release (70% at pH 5.5, 33% at pH 7.4; after 24 h at 37°C).

In two-dimensional (2D) *in vitro* cultures, PrestoBlue (PB) assay results with AFt-PbS-TMZ demonstrated enhanced inhibitory effects with lower IC_{50} values (3.5 ± 0.1 μM for U373M, 8.5 ± 0.7 μM for U373V, 10.9 ± 2.7 μM for U87MG) for GBM cells, whereas non-cancerous MRC-5 fibroblasts and human astrocytes exhibited IC_{50} > 30 μM ($p < 0.001$) post-treatment with 6 days, demonstrating GBM selectivity related to higher TfR1 expression in GBM cells, confirmed by western blot and flow cytometry methods. In addition, AFt delivery overcame TMZ resistance-mediated by MGMT; AFt-TMZ and AFt-PbS-TMZ overwhelmed the MGMT suicide repair protein, rapidly depleting its expression in MGMT-positive U373M cells.

To enable more predictive translation of 2D culture results into *in vivo* models, three-dimensional (3D) *in vitro* GBM models were utilised. In 3D spheroid cultures, AFt-PbS-TMZ leveraged AFt's co-delivery advantages to achieve enhanced inhibition, IC_{50} was 5.0 ± 0.5 μM, and it significantly ($p < 0.0001$) reduced spheroid volume over 6 days. This was likely due to enhanced TfR1 expression in spheroid cultures compared to 2D monolayers. In addition, deep tissue photoluminescence (PL) studies confirmed that PbS QDs signalling in U87MG spheroid cultures post-treatment with AFt-PbS-TMZ for 6 days and can be imaged *in vivo*.

In conclusion, these findings highlight the potential of AFt-PbS-TMZ as an inherent TfR1 targeted theranostic agent, combining GBM therapy and imaging abilities in a single nano-sized (12 nm) platform. The pH-responsive TMZ release and NIR-II emission from PbS QDs have a potential to address both diagnostic and therapeutic needs of GBM.

Publications and conference proceedings

Poster presentations

- Colpan R.D., Thomas, N.R., Turyanska L., Bradshaw T.D. *Development of Theranostic Apoferritin Nanocages for Diagnosis and Treatment of Glioblastoma*. 14th Academy of Pharmaceutical Sciences (APS), University of Reading, UK, 5-7th September 2023.
- Colpan R.D., Thomas, N.R., Turyanska L., Bradshaw T.D. *Theranostic Apoferritin Nanocages for Diagnosis and Treatment of Glioblastoma.* Allied Health Professionals PGR conference (AHPGR), University of Nottingham, UK, 18th April 2024.
- Colpan R.D., Thomas, N.R., Turyanska L., Bradshaw T.D. *Transferrin Receptor-1 Targeted Apoferritin Nanocages for Theranostic Applications in Glioblastoma.* Cancer Research Nottingham, University of Nottingham, UK, 24th January 2025.
- Colpan, R. D., Ward, E. B., Zhang, D., Ling, B., Iqbal, U., Moreno, M., Thomas, N. R., Turyanska, L., Bradshaw, T. D. *Dual-function Apoferritin Nanocages: Transferrin Receptor-1 Targeted Theranostics for Glioblastoma Treatment & Imaging,* Biodiscovery Institute (BDI) Research Day, University of Nottingham, UK, 15th September 2025.

Oral presentations

- Colpan, R. D., Ward, E. B., Zhang, D., Ling, B., Iqbal, U., Moreno, M., Thomas, N. R., Turyanska, L., Bradshaw, T. D. *Dual-function Apoferritin Nanocages: Transferrin Receptor-1 Targeted Theranostics for Glioblastoma Treatment & Imaging.* Oral presentation at the 19th Nanoscience and Nanotechnology Conference (NanoTR-19), Middle East Technical University, Turkey, 27–29th August 2025.
- Colpan, R. D., Ward, E. B., Zhang, D., Ling, B., Iqbal, U., Moreno, M., Thomas, N. R., Turyanska, L., Bradshaw, T. D. *Protein-based Targeted Delivery & Imaging for Glioblastoma Management.* Flash presentation at online mini symposium between China Pharmaceutical University and University of Nottingham, 5th September 2025.
- Colpan, R. D., Ward, E. B., Zhang, D., Ling, B., Iqbal, U., Moreno, M., Thomas, N. R., Turyanska, L., Bradshaw, T. D. *A cross-disciplinary solution: How a natural protein may help us treat and track deadly brain cancer* Oral presentation at the East Midlands Doctoral Network Conference (EMDoc), UK,19th September 2025.

Publications

- Colpan, R.D., Ward, E. B., Zhang, D., Ling, B., Iqbal, U., Moreno, M., Thomas, N. R., Turyanska, L., Bradshaw, T. D. *Co-encapsulation of temozolomide and PbS quantum dots in apoferritin for transferrin receptor 1 targeting, imaging and treatment of glioblastoma.* DOI: 10.1039/D5NA00557D, *Nanoscale Adv.,* 2025.

Acknowledgements

I am deeply grateful to my primary supervisor, Dr. Tracey D. Bradshaw, for her invaluable guidance, unwavering support, and constant encouragement throughout my PhD journey, and for always being supportive, understanding, and inspiring during the most challenging times. My sincere thanks go to my second supervisor, Dr. Lyudmila Turyanska, for her supportive feedback, patient guidance in preparing figures and publishing papers, and for always offering encouragement and invaluable teaching. Their unwavering support has opened many opportunities for me and has been played a key role in my personal and professional development. In addition, I would like to thank my third supervisor, Prof. Neil R. Thomas, for his support, valuable advice, and thought-provoking questions that inspired me to think more deeply and allowed me to better comprehend the project.

Next, I would like to acknowledge my sponsors, the Turkish Ministry of Education, for supporting me as an externally funded PhD student at the University of Nottingham, and the National Research Council Canada (NRC) for their contribution to my PhD. I am especially grateful to University of Nottingham and NRC collaboration for giving me the opportunity to visit Canada during my PhD, which greatly enriched my research experience. I would like to thank all project collaborators at the NRC, including Maria Moreno, Dongling Zhang, Binbing Ling, Umar Iqbal for their valuable collaboration, teaching new microscopy techniques, and warm hospitality in Ottawa.

I would also like to thank previous PhD students at the University of Nottingham who generously helped me to teach several techniques, including Dr. Kaouthar Bouzinab, Dr. Maria Cassioli, Dr. Amelia Hatfield, as well as the broader apoferritin research group for our valuable monthly discussion sessions. I am also grateful to my colleague Ellie B. Ward for her contribution to my quantum dot studies during my PhD. In addition, I would want to thank Michael Fay at Nanoscale and Microscale Research Centre, University of Nottingham for help in microscopy facilities, Dr. Michael Pan and Dr. David Onion for their help and training in flow

cytometry, and Dr. Robert Markus and Seema Bagia for their assistance and training with microscopy facilities. My thanks also go to the C62/C64 lab members, our lab manager, Ann Williams, as well as other members from the Boots Science Building labs and Biodiscovery Institute. Furthermore, I would also like to thank Prof. Ruman Rahman from School of Medicine, University of Nottingham, for his support throughout my PhD journey as my internal assessor, providing valuable feedback during yearly viva sessions, and for kindly supplying the astrocyte cell line, which enabled me to expand my studies.

Notably, I would like to expand my deepest gratitude and appreciation to my parents. My special thanks go to my mother, Mine Colpan, my sister, Dr. Dicle Colpan Gungordu, and my brother-in-law, Burak Gungordu, for their encouragement and generous support in helping me pursue my career goals, even during the most challenging times. I would want to expand my appreciation to my father-in-law Ozcan Kilic and my mother-in-law Fusun Kilic for their kindness, understanding, and constant support during my PhD. I am also grateful to our dog, Maya, and our cat, Avatar, for their emotional support especially in stressful moments.

My gratitude also extends to my dear friends who support me during my PhD and to my Master of Science supervisor Dr. Aysegul Erdemir, for inspiring me to pursue an academic career and for her guidance during the early stages of my journey.

Most importantly, my heartfelt thanks go to my husband, Tolga Kaan Kilic, for standing by me through every difficult moment, providing his endless patience, understanding, and belief in me, and for being a constant source of energy, positivity, and motivation.

Thank you all for being part of this chapter of my life.

List of Abbreviations

1° Ab	Primary antibody
2-HG	2-hydroxyglutarate
2° Ab	Secondary antibody
2D	Two-dimensional
3D	Three-dimensional
5-ALA	5-aminolevulinic acid
ABC	ATP-binding cassette
acetyl-CoA	Acetyl coenzyme A
AFt	Apoferritin
AI	Artificial intelligence
AIC	5-Aminoimidazole-4-carboxamide
AMT	Adsorption-mediated transcytosis
APS	Ammonium persulfate
ATCC	American type culture collection
ATP	Adenosine triphosphate
ATRX	Alpha 2 thalassemia/mental retardation syndrome X-linked
Au	Gold
BBB	Blood brain barrier
BBTB	Blood-brain tumour barrier
BCRP	Breast cancer resistant protein
BECs	Brain endothelial cells
BEGM	Bronchial Epithelial Cell Growth Medium
BER	Base excision repair
BSA	Bovine serum albumin
BTZ	Bortezomib
CdS	Cadmium sulfide
CdSe	Cadmium selenide
CdTe	Cadmium telluride
CI	Combination index
clogP	Logarithm of the partition coefficient
CNS	Central nervous system
CT	Computed tomography
CXCR4	Chemokine (C-X-C motif) receptor 4
DDS	Drug delivery systems
DHLA	Dihydrolipoic acid
DHLA–PEG	Dihydrolipoic acid–polyethylene glycol
DIPG	Diffuse intrinsic pontine glioma
DL	Drug loading
DLS	Dynamic light scattering
DMG	Diffuse midline glioma
DMSO	Dimethyl sulfoxide
DNA	Deoxyribonucleic acid
DOX	Doxorubicin
DR%	Percentage of drug release
DSBs	DNA double strand breaks
DTG	Dithioglycerol
ECM	Extracellular matrix
EE	Encapsulation efficiency
EGFR	Epidermal growth factor receptor
EPR	Enhanced permeability and retention

ErbB1	Erythroblastic leukemia viral oncogene homolog 1
EVs	Extracellular vesicles
FADH	Flavin adenine dinucleotide (reduced)
FAO	Fatty acid oxidation
FBS	Foetal bovine serum
FDA	Food and Drug Administration
Fe	Iron
FGS	Fluorescence-guided surgery
FI	Fluorescein isothiocyanate
Ft	Ferritin
FWHM	Full width at half maxima
GBM	Glioblastoma
Gd	Gadolinium
GI_{50}	50% growth inhibition
GLUT	Glucose transporter
gp60	Glycoprotein 60
GSCs	GBM stem cells
GSH	Glutathione
H	Heavy
h	hour
HAS	Human serum albumin
HBV	Hepatitis B virus
HDL	High-density lipoprotein
HER1	Human epidermal growth factor receptor 1 (also EGFR)
HER2	Human epidermal growth factor receptor 2
HOMO	Highest occupied molecular orbital
HPLC	High-performance liquid chromatography
HPV	Human papillomavirus
HR-TEM	High resolution transmission electron microscopy
i.v.	Intravenous
IC_{50}	Half maximal inhibitory concentration
ICG	Indocyanine green
IDH	Isocitrate dehydrogenase
IDH-WT	Isocitrate dehydrogenase-wild type
IR	Insulin receptor
JAK/STAT	Jasus kinase/ signal transducer and activator of transcription
JCPyV	JC polyomavirus
L	Light
LC-MS	Liquid chromatography-mass spectrometry
LDL	Low-density lipoprotein
LDLR	Low density lipoprotein receptor
LOH	Loss of heterozygosity
LP	Long-pass
LUMO	Lowest unoccupied molecular orbital
MCT-1	Monocarboxylate transporter-1
MEK/ERK	Mitogen-activated protein kinase/extracellular signal regulated kinase
MEM	Minimum essential medium
MFI	Mean fluorescence intensity
MGMT	*O*6-methylguanine DNA methyltransferase
miRNAs	Micro ribonucleic acids
MMR	Mismatch repair
MnO_2	Manganese dioxide
MRI	Magnetic resonance imaging
MS2	Emesvirus zinderi
MTIC	Monomethyl triazene 5-(3-methyltriazen-1-yl)-imidazole-4-carboxamide

MTT	3-(4,5-Dimethylthiazol-2-yl)-2,5-diphenyltetrazolium bromide
MW	Molecular weight
MWCO	Molecular weight cut-off
*N*3-MeA	*N*3-methyladenine
*N*7-MeG	*N*7-methylguanine
Na_2S	Sodium sulfide
NaCl	Sodium chloride
NADH	Nicotinamide adenine dinucleotide
NaOAc	Sodium acetate
native-PAGE	Non-denaturing polyacrylamide gel electrophoresis
ncRNAs	Non-coding RNAs
NEAA	Non-essential amino acids
NIR	Near infrared region
NIR-I	First near infrared region
NIR-II	Second near infrared region
NLCs	Nanostructured lipid carriers
NP-40	Nonidet P-40
NPs	Nanoparticles
NRF2	Nuclear factor erythroid 2-related factor 2
NSCs	Neuronal stem cells
*O*6-MeG	O6-methylguanine
OPCs	Oligodendrocyte precursor cells
Orbi-SIMS	Orbitrap secondary ion mass spectrometry
OVA	Ovalbumin
P-gp	P-glycoprotein
PARP1	Poly (ADP-ribose) polymerase 1
PB	PrestoBlue
$Pb(Ac)_2.3H_2O$	Lead acetate.trihydrate
PbS	Lead sulfide
PBS	Phosphate buffer saline
PbS QDs	Lead sulfide quantum dots
PbSe	Lead selenide
PD	Pharmacodynamic
PDGFR	Platelet-derived growth factor receptor
PDI	Polydispersity index
PDT	Photodynamic therapy
PEG	Polyethylene glycol
PET	Positron emission tomography
PGA	Poly (glycolic acid)
PI3K	Phosphatidylinositol-3-kinase
PI3K/AKT	Phosphoinositide 3-kinase/protein kinase B
PK	Pharmacokinetic
PL	Photoluminescence
PLA	Poly (lactic acid)
PLGA	Poly (lactic-co-glycolide)
PS	Photostability
PTEN	Phosphatase and tensin homolog
PTT	Photothermal therapy
PTX	Paclitaxel
PY	Protein yield
QDs	Quantum dots
QY	Quantum yield
Qβ	Oubevirus durum
RGD	Arginylglycylaspartic acid
RMT	Receptor-mediated transcytosis

ROI	Regions of interest
RONS	Reactive nitrogen species
ROS	Reactive oxygen species
RPMI-1640	Roswell Park Memorial Institute 1640 medium
RT	Radiotherapy
RT	Room temperature
RTKs	Receptor tyrosine kinases
SCARA5	Scavenger receptor class A member 5
SD	Standard deviation
SDS	Sodium dodecyl sulfate
SDS-PAGE	Sodium dodecyl sulfate polyacrylamide gel electrophoresis
siRNA	Small interfering RNA
SLNs	Solid lipid nanoparticles
SPARC	Secreted protein acidic and rich in cysteine
SWIR	Short-wave infrared
T/E	Trypsin/EDTA
T_0	Time-zero
$t_1/_2$	Half-life
TBST	Tris-buffered saline and tween 20
TCA	Tricarboxylic acid cycle
TEM	Transmission electron microscopy
TEMED	*N,N,N′,N′*-Tetramethyl ethylenediamine
TERT	Telomerase reverse transcriptase
Tf	Transferrin
TfR	Transferrin receptor
TfR1	Transferrin receptor 1
TGA	Thioglycolic acid
TGL	1-Thioglycerol
TME	Tumour microenvironment
TMV	Tobacco mosaic virus
TMZ	Temozolomide
TNS	Trypsin/EDTA neutralization neutralisation solution
TP53	Tumour protein 53
Trx	Thioredoxin
TTFields	Tumour treating fields
ULA	Ultra-low attachment
UPLC-MS/MS	Ultra-performance liquid chromatography-tandem mass spectrometry
UV-vis	Ultraviolet - visible
v/v	Volume/volume
VCR	Vincristine
VEGFR	Vascular endothelial growth factor receptor
VLDL	Very low-density lipoprotein
VLPs	Virus-like particles
WHO	World Health Organisation
WNT/β	Wingless-related integration site/ β-catenin
α-KG	Alpha-ketoglutarate
τ	Time constant

Table of Contents

List of Figures

List of Tables

Chapter 1 Introduction

1.1 Brain tumours

1.1.1 Overview of brain tumours

Brain tumours are characterised by the uncontrolled proliferation of cells within and/or around the brain, displaying numerous hallmarks of cancer.[1, 2] These tumours are classified into two main types: (1) primary tumours, developing directly within the brain, and (2) secondary (metastatic) tumours, resulting from the spread of malignant cells to the brain from lung cancer, breast cancer, and melanoma.[3] In addition to this classification, brain tumours can be categorised as either malignant or non-malignant (benign). Although benign tumours do not invade or metastasise, they can still pose a potential threat due to their size and location causing pressure on brain tissue.[4] Considering brain tumours represent a subset of central nervous system (CNS) cancers, with 90% occurring in the brain and cause significant mortality and morbidity across all age groups[5], it is crucial to consider the broader classification of CNS tumours.

1.1.2 Central nervous system and its tumours classification

CNS tumours arise from abnormal growths in the brain or spinal cord. According to the 2021 World Health Organisation (WHO) reclassification, CNS tumours are categorised 13 different types based on the molecular and histological characteristics.[6] Among these CNS tumours, brain tumours constitute the major subgroup and represent a significant global challenge due to high mortality rates compared to other malignancies. The common brain tumours include gliomas, meningiomas, and choroid plexus tumours.[7] The most common malignant histology in adult brain tumours is glioma.[5] Gliomas encompass various subtypes such as astrocytoma, oligodendroglioma, and glioblastoma (previously glioblastoma multiforme; GBM) (Figure 1.1).[6]

These tumours present poor survival outcomes, thus necessitate novel research for effective therapies.

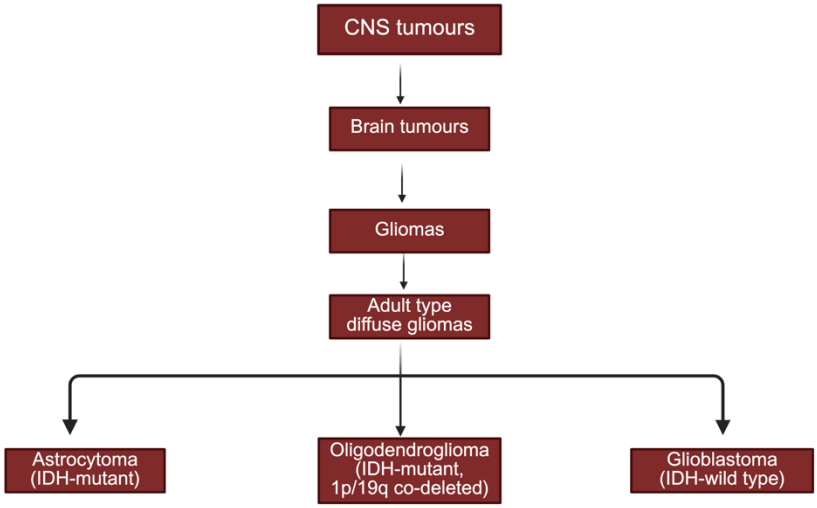

Figure 1.1 Schematic classification of central nervous system (CNS) tumours and brain tumours subtypes focused on glioblastoma (GBM) according to World Health Organisation (WHO) 2021.[6] Created with BioRender.

1.1.3 Epidemiology of brain tumours

Brain tumours are characterised by high mortality rates and reduced quality of life. The incidence varies depending on the age, gender, and socioeconomic status.[8] For example, the incidence of brain tumours in the adults is ten-times higher than that observed in paediatric populations.[9]

In 2021, more than 258,000 deaths were attributed to brain cancer globally, demonstrating its lethal nature. In addition, the number of individuals diagnosed with brain tumours exceeded 975,000 cases in the same year.[8] The number of diagnoses of brain tumours has increased over recent years and is expected to rise further in the next decades.[9]

1.1.4 Tumour grading

Tumour grading is critical in the evaluation of brain tumours. According to WHO, brain tumours, e.g. gliomas, are categorised into four grades from 1 to 4 depending on their malignancy and

aggressiveness.[10] Grade 1 tumours are slow growing, characterised limited spread and higher survival rates, whereas grade 4 tumours have a worse prognosis and have metastasised.[11] In particular, gliomas are classified into low-grade gliomas (grades 1 and 2) and high-grade gliomas (grades 3 and 4) based on their malignancy.[6] Table 1.1 demonstrates some examples of gliomas depending on their tumour grade.

Table 1.1 Classification of brain tumours by World Health Organisation (WHO) grade with representative examples.[6] Diffuse midline glioma (DMG, previously referred to as diffuse intrinsic pontine glioma (DIPG).

Tumour Grade (WHO 2021)	Examples of Brain Tumours
Grade 1	Pilocytic astrocytoma, meningioma
Grade 2	Diffuse astrocytoma, oligodendroglioma
Grade 3	Anaplastic astrocytoma, anaplastic oligodendroglioma
Grade 4	GBM, diffuse midline glioma (DMG), diffuse hemispheric glioma, embryonal tumours

1.1.5 Glioblastoma

1.1.5.1 Overview of glioblastoma

GBM, previously referred to as glioblastoma multiforme prior to the 2021 WHO classification, is one of the most lethal brain tumours in adults.[12] It is classified as WHO grade 4, the highest grade, due to its rapid growth, invasive nature, genetic heterogeneity, resistance to treatment, high recurrence, and high mortality rate.[13]

GBM is a difficult-to-treat tumour due to its diffuse and heterogenous nature (multiforme) and also its anatomical localisation in the brain, with 95% of cases found in the frontal, temporal, parietal, and occipital lobes[14] (Figure 1.2). Although the tumour can originate from any region of the brain, it is most observed in the frontal and temporal lobes[15], where it can invade surrounding areas due to its microvascular growth. The microvascular growth of the tumour contributes to the damage of nearby healthy brain tissues.[16] GBM symptoms include persistent headaches, seizures, motor impairments, and cognitive decline, demonstrating the tumour's impact on several brain regions.[10, 15]

The development of GBM can be affected by the combination of several factors, including genetic mutations, environmental factors (e.g. radiation exposure), and genetic syndromes (e.g. Li-Fraumeni syndrome).[10] This multifactorial biology makes GBM a complex and aggressive brain tumour. Therefore, understanding the epidemiology and pathophysiology of GBM is essential.

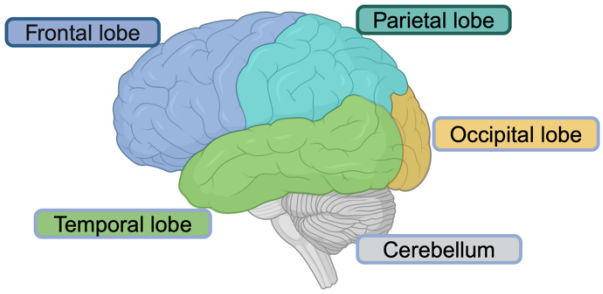

Figure 1.2 The brain regions where glioblastomas (GBMs) may originate. Created with BioRender.

1.1.5.2 Epidemiology of glioblastoma

GBM is the most prevalent CNS tumour, representing 15% of all CNS tumours and 45% of primary malignant brain tumours.[17] The incidence of GBM varies from 3 to 5 cases per 100, 000 person-years globally.[10] In addition, its incidence can vary according to age and gender, being more common (1.5-times higher) in men than women.[10] In particular, the peak age is reported to be > 65 years old, particularly between 75 and 84 years old.[18, 19] Although GBM can occur in any ethnic group, Caucasians (European, Middle Eastern, North African) have an increased incidence compared to other groups.[10] GBM also shows slightly higher incidence in developed countries.[10]

1.1.5.3 Pathophysiology of glioblastoma

GBM may occur in the brain, cerebellum (< 3%), brainstem (< 5%), and spinal cord (< 5%), arising from glial cells, especially astrocytes.[15, 19] Primary GBM originates from neuronal stem cells (NSCs), while secondary GBM tumours arising from astrocytes.[19] Figure 1.3 illustrates

the potential origins of GBM from these cells. The study with genetic remodelling of GBM in mice demonstrated that GBM originated from three different cell types: NSCs, NSCs-derived astrocytes, and oligodendrocyte precursor cells (OPCs).[13]

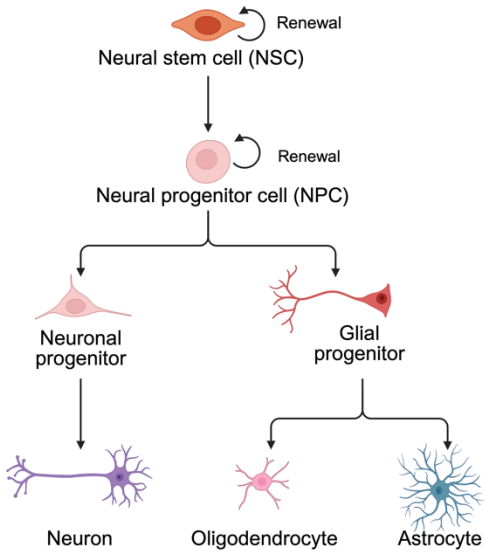

Figure 1.3 Schematic illustration of differentiation of neuronal stem cells (NSCs), and potential origins of glioblastoma (GBM) from these cells. Created with BioRender.

Several mutations and triggering mutations cause altered gene expression in GBM, differing from healthy brain cells, resulting in abnormal proliferation, angiogenesis, and genotypic diversity.[19] Primary tumours involve epidermal growth factor receptor (EGFR) amplification, phosphatase and tensin homolog (PTEN) deletion, telomerase reverse transcriptase (TERT) promoter mutation, *O*6-methylguanine DNA methyltransferase (MGMT) promoter methylation, and loss of heterozygosity (LOH) at positions 10q and 10p, whereas secondary tumours include isocitrate dehydrogenase 1/2 (IDH 1/2) mutations, tumour protein 53 (TP53) mutation, alpha 2 thalassemia/mental retardation syndrome X-linked (ATRX) chromatin remodelling mutation, LOH at 10q and 19q.[20]

In the 2021 WHO classification of CNS tumours, GBM classified as isocitrate dehydrogenase-wild type (IDH-WT, referring primary GBM), is associated with a worse prognosis. In addition to IDH status, the WHO classification has incorporated the following molecular biomarkers:

TERT promoter methylation, EGFR amplification, combined chromosome 7 gain and chromosome 10 loss to define GBM and distinguish it from other high-grade gliomas. On the other hand, IDH-mutant GBM is categorised as a lower-grade glioma with a better prognosis.[12] This revised WHO classification focuses on the genetic and prognostic differences between the subtypes of GBM to better understand the tumour behaviour and resistance profiles, guiding novel treatment strategies.

1.1.5.4 Genetic and molecular biomarkers of glioblastoma: overexpressed receptors

GBM is characterised by numerous genetic alterations and dysregulated molecular signalling pathways. Among these, several cell surface receptors are notably overexpressed, playing critical roles in the key cellular processes including proliferation, invasion, metastasis, angiogenesis, and therapeutic resistance.[16, 21] Overexpressed receptors include CD44, integrins, insulin receptors (IR), platelet-derived growth factor receptor (PDGFR), vascular endothelial growth factor receptor (VEGFR), low density lipoprotein receptor (LDLR), glucose transporter (GLUT), EGFR, and transferrin receptor 1 (TfR1).[21] Figure 1.4 illustrates the some of the well-studied overexpressed receptors in GBM. These receptors provide promising candidates for targeted drug delivery strategies to enhance GBM treatment. Therefore, it is essential to comprehend their functions and expression patterns.

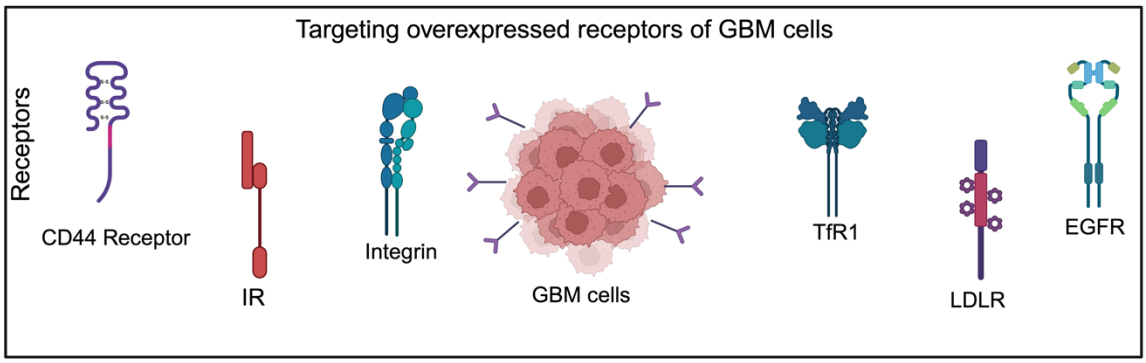

Figure 1.4 Key cell surface receptors overexpressed in glioblastoma (GBM) cells for targeted delivery.

One of the hallmarks of GBM is `invasion and metastasis`[2], which is largely driven by enhanced cell migration. During migration, GBM cells overexpress several transmembrane receptors such as integrins and CD44 receptors. These overexpressed receptors facilitate interaction with the extracellular matrix (ECM) and promote mobility. Integrins, heterodimeric transmembrane receptors, composed of α and β subunits, play a critical role in cell adhesion, migration, and signalling. In GBM, overexpression of integrins enhances the tumour cells' ability to migrate through the brain tissue. On the other hand, CD44 is a cell surface glycoprotein, involved in cell-cell and cell-matrix interactions. CD44 receptors mediate cell migration, invasion and stemness.[22]

IRs are often upregulated in GBM cells compared to normal brain tissue, promoting proliferation, survival, and metabolic adaptation. Additionally, IRs have been reported to undergo transcytosis through the BBB.[21] In addition, both PDGFR and VEGFR are commonly overexpressed transmembrane tyrosine kinase receptors located on the cell surface.[23]

LDLR and GLUT proteins regulate the transport of cholesterol and lipids and glucose into the cells, respectively. Therefore, both are upregulated on the GBM cell surface to meet the increased demands for energy production, making them potential therapeutic targets.[21]

EGFR, a transmembrane receptor of tyrosine kinase, is one of the most well-studied overexpressed receptors in GBM. EGFR triggers several critical signalling pathways, such as phosphatidylinositol-3-kinase (PI3K), AKT, mTOR, RAS/MAPK, and JAK/STAT, which regulate cell proliferation, migration, and survival[24] (Figure 1.5). It is often amplified and overexpressed in 50% of GBM cases. The overexpressed receptor drives signalling pathways contributing to aggressive tumour growth, invasion, and resistance mechanisms. EGFR influences glutamine metabolism and proto-oncogene MYC family regulation in glioma cells. Therefore, it serves a critical molecular biomarker for GBM.[24, 25]

In addition to EGFR (known as human epidermal growth factor receptor 1 (HER1) or erythroblastic leukemia viral oncogene homolog 1 (ErbB1)), human epidermal growth factor

receptor 2 (HER2) is another member of the EGFR tyrosine kinase family. It is overexpressed in variety of cancers. Although HER2 overexpression is well-established in breast cancer, HER2 levels are also upregulated in up to 80% of GBM tumours.[26]

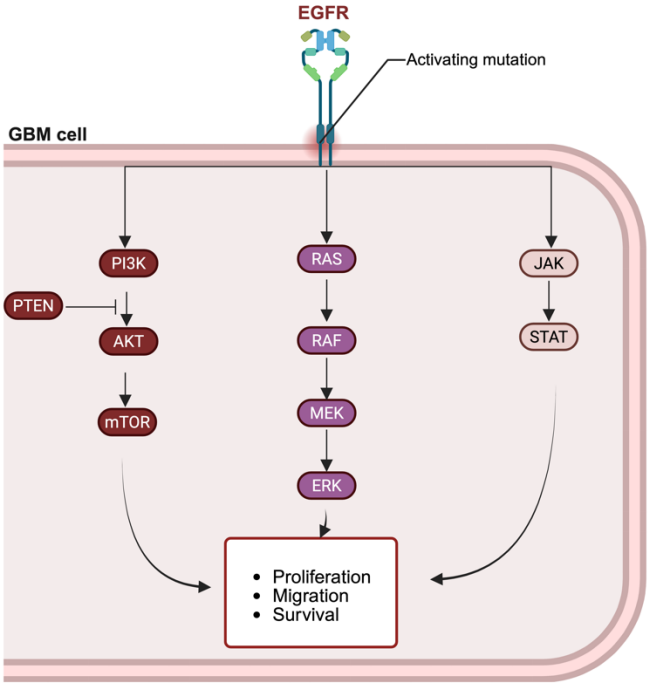

Figure 1.5 Epidermal growth factor receptor (EGFR) signalling networks involved in glioblastoma (GBM).[25] Created with BioRender.

TfR1 (also known as CD71), a type II transmembrane glycoprotein, is critical for cellular iron uptake and plays a significant role in transporting iron across the BBB via capillary endothelial cells.[21] In healthy brain tissue, TfR1 expression is tightly regulated to maintain iron homeostasis.[27] High levels of this receptor are present in the brain endothelial cells to facilitate iron transport.[21] TfR1 is negligibly expressed in glial cells.[28] However, in GBM, TfR1 is overexpressed up to 100-fold higher than non-cancerous brain cells such as astrocytes[29] (Figure 1.6). Similarly, Shen *et al.* demonstrated significant differences in TfR1 expression between healthy brain and tumour tissues.[30] This increased overexpression demonstrates and accommodates the elevated iron demands of highly proliferative GBM cells. Consequently, it facilitates enhanced iron uptake through TfR1-mediated endocytosis, which is essential for cellular processes such as deoxyribonucleic acid (DNA) synthesis and proliferation.[27]

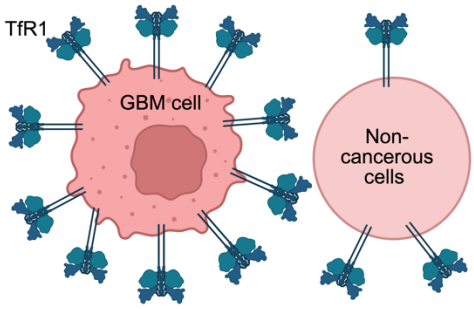

Figure 1.6 Illustration of transferrin receptor 1 (TfR1) expression difference between glioblastoma (GBM) cells and non-cancerous cells. Created with BioRender.

Although TfR1 overexpression contributes to GBM growth via activation of cellular signalling pathways involved in proliferation and survival, it also presents a promising biomarker for targeted drug delivery approaches in brain tumours. While TfR1 overexpression in brain capillary endothelial cells facilitates the transport of drugs and molecules across the BBB, its higher expression in GBM cells enhances the accumulation of drugs/molecules at tumour tissues, thus reducing off-target toxicity.[21] As a result, TfR1-targeted treatments for GBM have gained attention due to their potential to improve therapeutic outcomes.[31]

1.1.5.5 Glioblastoma subtype classification

The classification of GBM into molecular subtypes is crucial for understanding the biological heterogeneity of this complex disease.[32] In 2006, Phillips *et al.* categorised high grade gliomas to three subtypes including proneural, mesenchymal, and proliferative depending on the gene expression profiles.[33] According to this classification, patients with proneural phenotype exhibited longer overall survival compared to those with mesenchymal and proliferative subtypes.[33] In 2010, Verhaak *et al.* classified GBM into four subtypes including classical, mesenchymal, proneural, and neural based on the analysis of gene expression profiles from 200 patient derived GBM samples.[34] Each subtype is characterised by distinct genetic alterations; for example, proneural subtype is enriched in oligodendrocyte markers whereas mesenchymal subtype exhibits altered expression of astrocyte and microglial markers.[35] In 2017, Wang *et al.* reclassified GBM using RNA-sequencing into three subtypes including

proneural, classical, and mesenchymal, suggesting that neural subtype might not be tumour specific; it may represent contamination with normal neuronal tissue rather than tumour intrinsic subtype.[32] Additionally, during and after chemotherapy, GBM phenotypes exhibit increased plasticity associated with epithelial-mesenchymal transformation (EMT) in tumours with epithelial origin. Therefore, this phenotypic shift has been associated with therapeutic resistance and malignant profiles. Consequently, the presence of mesenchymal subtype at diagnosis and at recurrence has been correlated with poorer patient outcomes.[35] In line with the most recent 2021 WHO classification[12], the three subtypes proposed by Wang *et al.* are widely accepted as clinically relevant model of GBM heterogeneity. Figure 1.7 shows the molecular biomarkers of three subtypes of GBM.

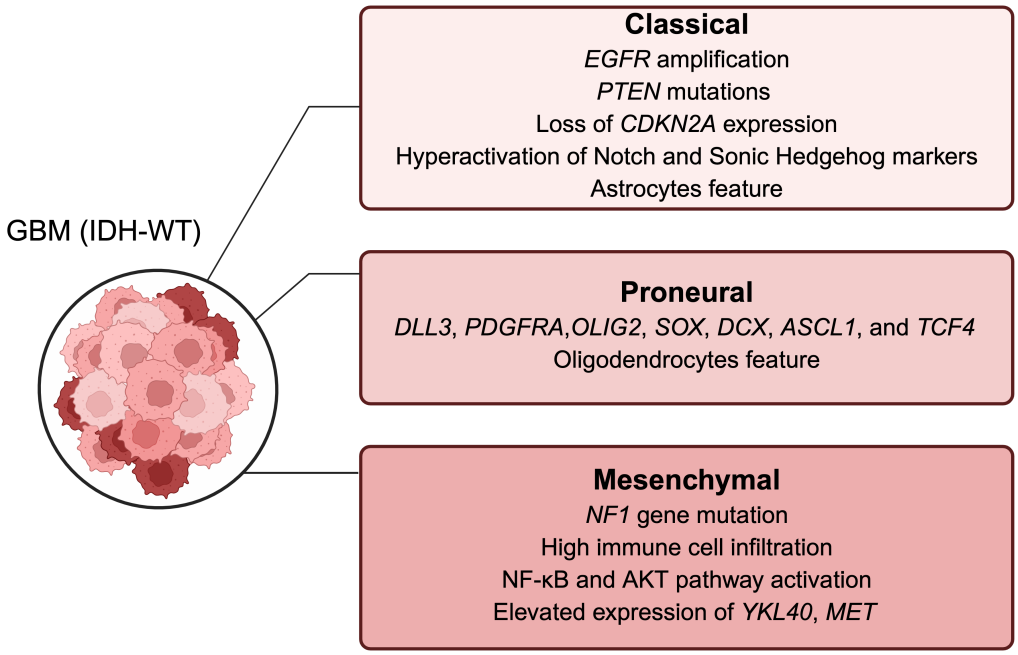

Figure 1.7 Glioblastoma (GBM) subtype classification and their characteristic gene expression profiles.[35] Created with BioRender.

1.2 Challenges and treatment strategies for glioblastoma

1.2.1 Challenges in treating glioblastoma

There are several obstacles in GBM treatment. These include blood brain barrier (BBB), blood-brain tumour barrier (BBTB), tumour microenvironment (TME), and heterogenic nature of GBM. Brain tumours are protected by the BBB, a selectively permeable diffusion barrier. BBB maintains brain homeostasis by preventing the entry of toxins, pathogens, and therapeutic agents (small or large molecules) into the brain; thus, posing a significant challenge in GBM treatment.[36, 37] It has been reported that 20% of small molecules (molecular weight < 500 Da and size < 100 nm diameter) and no large therapeutic agents can cross the BBB to reach the tumour cells. Therefore, the BBB represents a barrier to effective drug delivery, contributing to limited therapeutic efficacy and tumour recurrence in GBM.[38, 39]

The BBB is both a biophysical and biochemical barrier, consisting of brain endothelial cells (BECs), astrocytes, pericytes, microglial cells, and neurons.[40] BECs utilise transmembrane proteins such as ocludins, claudins, junctional adhesion molecules to form the neurovascular unit with neurons by tight junctions.[11] BECs are found to be rich in specific transmembrane proteins to sequester nutrients or remove waste.[40] Pericytes regulate BECs` gene expression and trigger astrocytes to release growth factors in response to injury.[36] Astrocytes play a critical role in the formation and maintenance of the BBB. These glial cells are located near to both neurons and BECs. Notably, astrocytes regulate the flow of essential metabolites (such as glucose) to neurons. Additionally, they are involved in regulating ion homeostasis and controlling iron transport into the brain.[40]

As a biochemical barrier, the passage of drugs/molecules through BBB depends on several factors such as size, liposolubility, electric charge, interactions with blood proteins, and interactions with BBB proteins. Additionally, blood pressure also plays a role in the drug's passage through the BBB.[38]

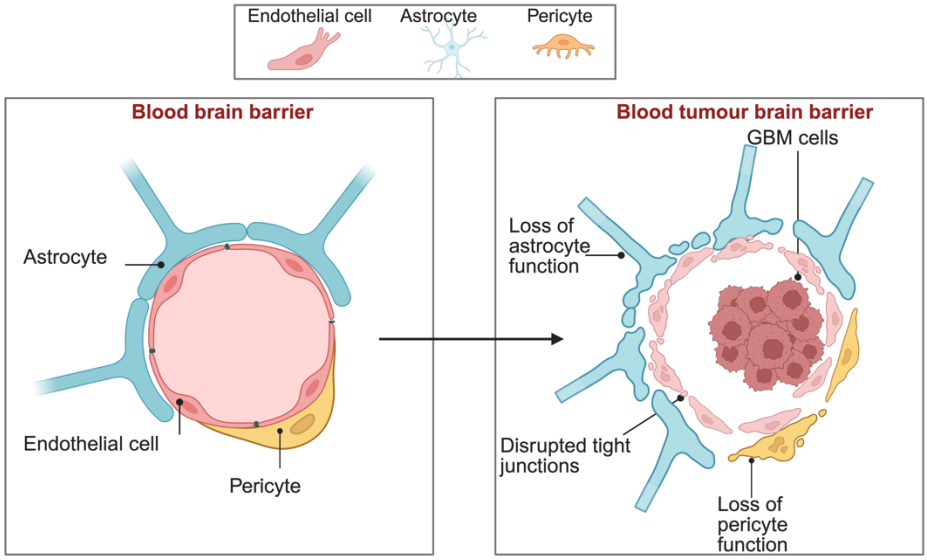

Figure 1.8 Illustration of healthy blood brain barrier (BBB) versus blood tumour brain barrier (BBTB). Created with BioRender.

In GBM, the BBB becomes dysfunctional in the presence of brain tumours, forming what is called as the BBTB (Figure 1.8). The BBTB is characterised by leaky and abnormal blood vessels, differing from healthy BBB. In the BBTB, the loss of astrocyte and pericyte function, along with disrupted tight junctions can occur due to the tumour-induced vascular leakage and increased permeability, making it difficult for treatments to reach and treat the tumour.[11]

GBM, as a solid tumour, is characterised by a large mass, creating a nutrient gradient throughout the tumour. For instance, the core regions of tumour tend to be hypoxic and necrotic, whereas the infiltrating front of tumour is typically oxygen-rich. This intratumoural heterogeneity leads to treatment challenges such as chemoresistance by changing TME.[39]

The main challenges in GBM treatment, particularly related to BBB drug delivery, involve several barriers such as physical, transportation, metabolic, and immune barriers.[41] Therefore, BBB-targeted drug delivery approaches are needed for more effective treatment of GBM.

1.2.2 Treatment strategies for glioblastoma

The standard of care of treatment for GBM consists of a multimodal approach combining different treatment strategies including surgery, radiotherapy (RT), chemotherapy, and tumour

treating fields (TTFields).[42, 43] However, surgery can only be performed in 50%-70% of GBM cases, depending on the tumour location.[16] Additionally, due to the diffuse infiltration of GBM cells, surgery alone cannot completely remove all malignant tissue.[42] Consequently, GBM management requires a multimodal approach combining multiple treatment strategies.

RT can be administered as monotherapy (RT alone) or a combination therapy (with surgery or chemotherapy) to generate reactive oxygen species (ROS) and DNA double strand breaks (DSBs).[13] RT alone achieves a median survival of 12.1 months but also exposes patients to the risks of ionising radiation.[16] The chemotherapeutic agents for GBM include alkylating agents such as temozolomide (TMZ), biodegradable carmustine wafers (Gliadel®), lomustine, and fotemustine which exert their effects through alkylating DNA base pairs. In addition, 5-aminolevulinic acid (5-ALA), an orally administered amino acid derivative, selectively accumulates in GBM cells as a result of altered heme metabolism and transporter expression, hence 5-ALA uptake in the tumour cells produces a fluorescence metabolite which facilitates improved resection of tumour tissue.[44] Furthermore, targeted therapy agents such as anti-VEGF monoclonal antibody bevacizumab, BRAF inhibitor dabrafenib and MERK1/2 inhibitor trametinib combination are also employed in treatment strategies.[13, 16] Figure 1.9 presents a timeline summarising the Food and Drug Administration (FDA)-approved treatments for GBM. However, molecular targeted therapy has not been broadly approved for GBM due to the lack of objective responses shown in phase III trials. In addition, BRAF inhibitor dabrafenib has only been approved for BRAF V600E mutated GBMs, which are very rare (1-2%).[45] Among them, TMZ is widely used chemotherapeutic drug, and the combination therapy of TMZ and RT increased the patient survival to 14.6 months.[16] As part of multimodal GBM therapy, bevacizumab can be used in combination with chemotherapy and/or RT treatments as an anti-angiogenic monoclonal antibody. Although bevacizumab improves progression-free survival, it does not improve overall survival of GBM patients. Therefore, it is mostly used for recurrent GBM.[13]

FDA-approved TTFields therapy delivers alternating electric fields via transducer arrays worn on a shaved scalp to disrupt mitosis and induce apoptosis in rapidly dividing GBM cells, offering a limited toxicity and mild side effects (such as skin irritation).[13] Kirson *et al.* were the first to demonstrate that low-intensity alternating electric fields at 100–300 kHz inhibit the growth of various cancer cell lines, such as glioma, melanoma, breast, lung, and prostate, and suppress tumour growth *in vivo*.[46] Currently, it is used in the clinic and combining TTFields with TMZ has been shown to improve progression-free survival (~5 months) and overall survival[47] from 16 months to 20.9 months.[13, 36] TTFields has been approved for clinical use in several countries including United States, Sweden, Israel, and Japan.[48] However, it has not been approved for clinical adoption by the National Health Service (NHS) in the United Kingdom, as it was rejected based upon health economic grounds.[49]

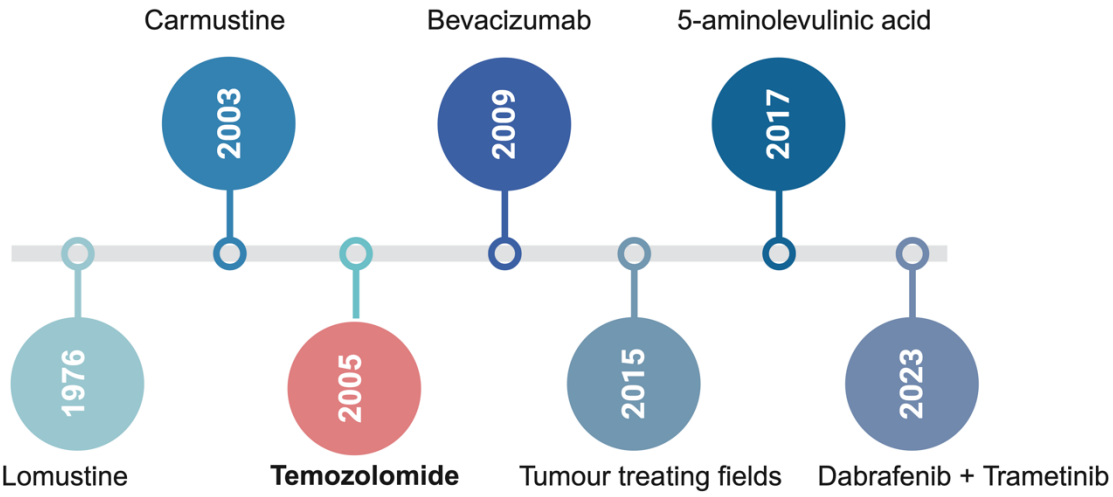

Figure 1.9 The summary of Food and Drug Administration (FDA)-approved glioblastoma (GBM) treatments.[16, 47] Created with BioRender.

1.2.3 Temozolomide in the treatment of glioblastoma

1.2.3.1 Mechanism of action of temozolomide

TMZ, an imidazotetrazine derivative, is a key orally administered chemotherapeutic drug in GBM treatment. Figure 1.10 demonstrates the structure of TMZ ($C_6H_6N_6O_2$). The exceptional

ability of TMZ to pass through the BBB, supported by its small size and lipophilic nature, (the logarithm of the partition coefficient (clogP) for TMZ is -0.81)[50], is linked to its effectiveness for treating brain cancers.[39, 51] Although TMZ can transcytose and cross the BBB (it is estimated that < 1% of administered TMZ crosses BBB), p-glycoprotein (P-gp) does pump a certain amount back across the BBB, out of the brain[52] (see Section 1.2.3.4).

TMZ is a DNA alkylating drug that has been used in the clinic since 2005 to kill GBM cells by methylating *O*6-guanine, arresting the GBM cell cycle at the G2/M phase, producing DNA double-strand breaks, and leading to apoptosis or autophagic death of GBM cells.[47] Currently, in the clinic, the Stupp protocol administers TMZ concomitantly with RT for 6 weeks, followed by 28-day cycles of TMZ on five consecutive days within the interval of four weeks.[53, 54]

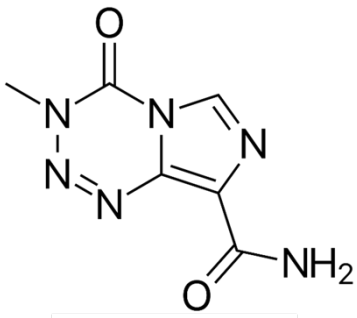

Figure 1.10 The chemical structure of temozolomide (TMZ). Created with Chem Draw.

TMZ is a prodrug (194.1 g/mol) that is stable at pH 5.5 (half-life ($t_{1/2}$) >100 h), however at pH 7.4, it has a short plasma half-life, $t_{1/2}$ ~ 1.8 h. At physiological pH, TMZ degrades rapidly into its metabolites including monomethyl triazene 5-(3-methyltriazen-1-yl)-imidazole-4-carboxamide (MTIC, $t_{1/2}$ ~2 min) and 5-aminoimidazole-4-carboxamide (AIC) and reactive methyldiazonium ions ($t_{1/2}$ ~0.4 s) alkylate DNA.[55-57] Degradation rates of both TMZ and MTIC are highly pH-dependent.[56] Although TMZ remains stable at acidic pHs, its active metabolite MTIC is stable at alkaline pHs. When TMZ is converted to MTIC in the plasma, MTIC is rapidly degraded ($t_{1/2}$ ~2 min), limiting its ability to cross the BBB due to its polarity and instability.[42] Therefore, considering the pH-dependent stability of TMZ, nanotechnological advancements

offer promising strategies to improve TMZ stability under physiological conditions while leveraging its stability in acidic pH for targeted drug delivery.

The methyldiazonium cation methylates DNA bases (mostly purine bases) generating *N*7-methylguanine (*N*7-MeG), *N*3-methyladenine (*N*3-MeA) and *O*6-methylguanine (*O*6-MeG). *N*7-MeG and *N*3-MeA comprise ~70% and ~9% of DNA adducts respectively; these adducts can be repaired easily by base excision repair (BER) via poly (ADP-ribose) polymerase 1 (PARP1).[55] However, these adducts become highly cytotoxic when BER is disrupted. Although *O*6-MeG adducts comprise only ~ 6% of DNA adducts, this pathway is considered the major route of TMZ cytotoxic action, inducing single and double stranded DNA breaks.[55] Figure 1.11 illustrates the stepwise mechanism of action of TMZ and shows the chemical structures of TMZ ($C_6H_6N_6O_2$), MTIC ($C_5H_8N_6O$), and AIC ($C_4H_6N_4O$).

The cellular response to *O*6-MeG adducts can be broadly classified into three categories based on cell repair status: (1) MGMT-positive, (2) MGMT-negative/mismatch repair (MMR)-proficient, and (3) MGMT-negative/MMR-deficient. In the first condition, MGMT-positive cells can repair *O*6-MeG adducts via MGMT, a suicide repair enzyme, thus the cells can survive after TMZ treatment, representing the least effective TMZ mechanism[58] (see Section 1.2.3.3). In the second condition, MGMT-negative/MMR-proficient cells pair thymine and *O*6-MeG instead of cytosine; this mispairing is recognised by the intact MMR system. However, functional MMR only recognises and removes thymine bases, while *O*6-MeG persists. This futile process of repair and re-insertion leads to replication fork collapse, DNA double strand breaks, and autophagic and/or apoptotic cell death, representing the most effective cytotoxic mechanism of TMZ.[55] In the third condition, MGMT-negative/ MMR-deficient cells neither recognise nor repair *O*6-MeG adducts. As a result, *O*6-MeG adducts are tolerated, persisting in daughter cells which leads to hypermutative phenotype, genomic instability, and therapeutic resistance[59] (Figure 1.11). Among them, the activity of TMZ can be ranked as follows: MGMT-negative/MMR-proficient cells > MGMT-negative/MMR-deficient > MGMT-positive. Therefore, it is essential to develop effective strategies for enhancing TMZ cytotoxic action.

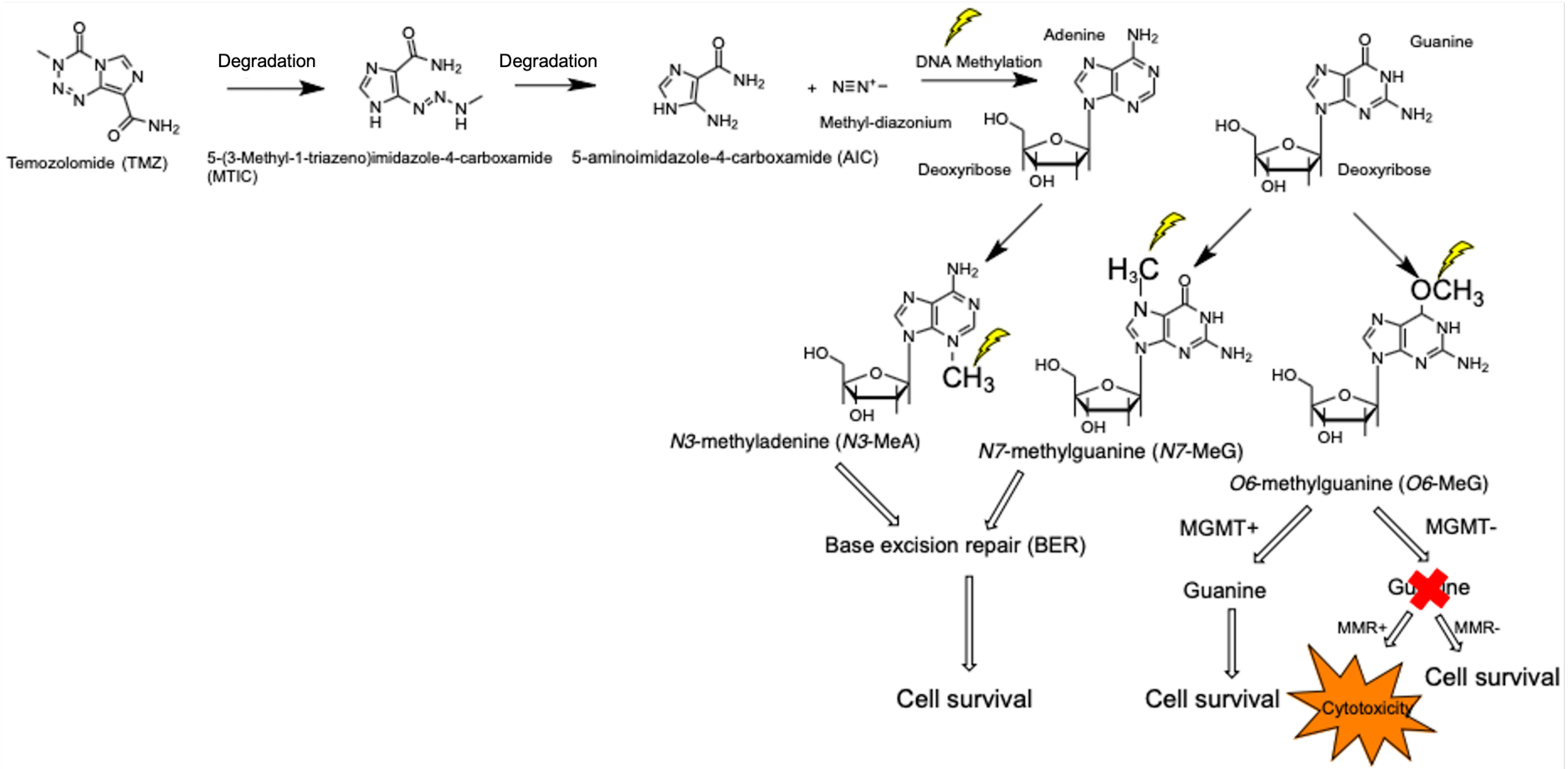

Figure 1.11 The scheme of the mechanism of action of temozolomide (TMZ). Created with Chem Draw.

1.2.3.2 Temozolomide resistance in glioblastoma

TMZ resistance represents a major obstacle that must be overcome for developing more effective GBM treatment. The tumours develop resistance to TMZ after exposure, referred to as acquired resistance, due to the heterogeneous and mutation-prone nature of GBM. In addition, approximately 50% of GBM patients show a lack of response to TMZ therapy, known as inherent resistance.[17] Both acquired and inherent resistance mechanisms in GBM limit treatment strategies, contributing to poor prognosis and high recurrence rates.[60]

Several mechanisms contribute to the development of TMZ resistance. These mechanisms include DNA repair pathways, chemoresistance, signalling pathways, autophagy and apoptosis regulation, metabolic reprogramming, and alternative resistance pathways (involving GBM stem cells, epigenetic modifications, micro ribonucleic acids (microRNAs), etc.).[61] Understanding these mechanisms is crucial for development of more effective treatment strategies for GBM.

1.2.3.3 DNA repair and temozolomide resistance

The MGMT gene, located on chromosome 10, encodes a DNA repair protein.[23] MGMT protein is found in both the cytoplasm and nucleus; its main function is to protect normal cells from tumourigenesis by repairing DNA damage.[62]

In GBM cells, MGMT removes alkyl groups of *O*6 position of guanine, caused by TMZ. The repair mechanism includes the transfer of methyl group to an active site of MGMT protein, specifically to a cysteine residue. However, the cysteine residue in MGMT becomes irreversibly modified by the methyl group, causing inactivation of the protein. As a result, MGMT protein cannot be reused for further DNA repairs, which is why it is called a suicide repair protein. For instance, in T98G GBM cells (MGMT-positive), the half-life of MGMT protein has been reported to be ~60 h under untreated conditions but decreases to < 12 h following TMZ treatment.[63] This indicates that MGMT is degraded by proteolysis after its DNA repair

function. To continue its function, MGMT must be resynthesised. However, in some GBM cells, overexpressed MGMT enhances the repair of DNA damage induced by TMZ. Therefore, the cells become more resistant to TMZ (Figure 1.12). This overexpression of MGMT is one of the major challenges in GBM treatment. [60, 61, 64]

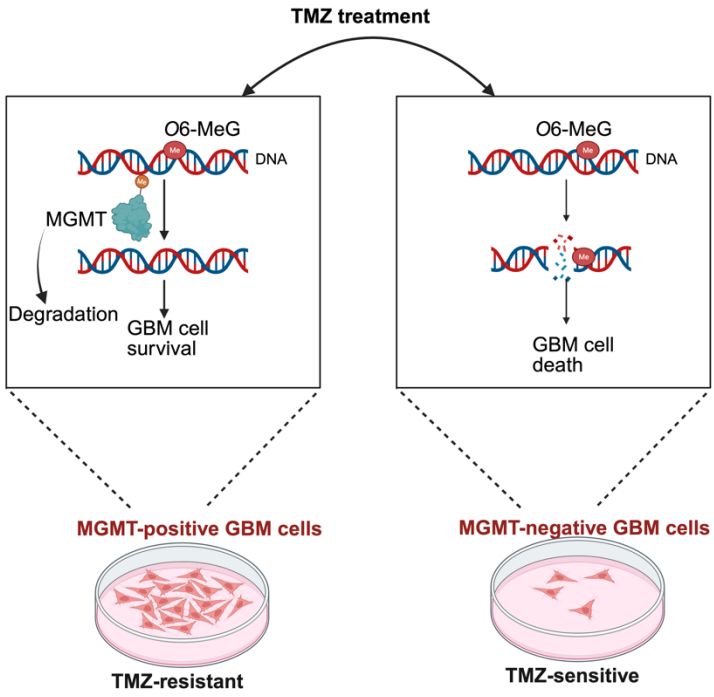

Figure 1.12 Correlation between DNA repair protein *O*6-methylguanine DNA methyltransferase (MGMT) and temozolomide (TMZ) resistance in MGMT-positive and MGMT-negative glioblastoma (GBM) cells. Created with BioRender.

The amount of MGMT expression, which is determined by cytosine-phosphate-guanine (CpG) methylation status of the *MGMT* gene promoter region, in GBM cells determines the susceptibility or intrinsic resistance of the cells to TMZ.[17] A low abundance of MGMT results in improved survival of patients treated with TMZ while a high abundance of MGMT confers poor prognosis for GBM patients.[17] For instance, Spiegl-Kreinecker *et al.* reported a 20-month difference in the survival of patients treated with TMZ, depending on their MGMT status.[65] Therefore, MGMT silencing or inhibition strategies have been investigated to overcome TMZ resistance for improved treatment outcomes.[61]

TMZ resistance and regulation of MGMT activity in GBM is also related to other DNA repair mechanisms, including BER and MMR pathways.[61] The BER mechanism functions in the

repair of single nucleotides.[17] The relationship between TMZ and BER lies in the recognition and removal of *N*7-MeG and *N*3-MeA adducts induced by TMZ through the BER pathway.[17] In this pathway, several proteins are involved including PARP-1, DNA polymerase β**,** and DNA ligase III to restore the DNA integrity. Among them, PARP-1 identifies the single-stranded DNA breaks. When BER is disrupted, these *N*7-MeG and *N*3-MeA adducts become highly cytotoxic.[66] Therefore, to enhance TMZ cytotoxic activity; the combination therapies of PARP-1 inhibitors (e.g. olaparib, niraparib) and TMZ have been studied.[58, 67] In addition, recent studies showed the PARP and MGMT interaction following TMZ treatment to enhance MGMT's DNA repair function through post-translational modification, poly (ADP-ribosyl)ation (PARylation), improving MGMT's ability to bind DNA and repair TMZ-induced DNA damage hence promoting resistance.[61]

The MMR system recognises and corrects DNA mismatched bases.[17] A protein complex including MSH2, MSH6, MLH1, and PMS2 proteins works in this system.[55] During DNA replication, in the absence of MGMT, *O*6-MeG pairs with thymine instead of cytosine; this is recognised by the MSH2-MSH6 complex of the DNA MMR system.[60] However, MMR only recognises thymine bases and removes thymine, while *O*6-MeG remains intact. MMR status is one of the key factors to determine TMZ response.[55] When MMR functions, it can recognise the *O*6-MeG-thymine mismatch and remove the newly synthesised strand containing thymine, leading to cell death, as described (Section 1.2.3.1), thus limiting TMZ effectiveness.[17] However, in MMR-deficient cells, the *O*6-MeG lesion is tolerated and persists in daughter cells, causing a hypermutative phenotype.[59] Therefore, MMR deficiency leads to increased resistance, and poor treatment outcomes, and is mostly seen in recurrent GBM.[61]

1.2.3.4 Chemoresistance mechanisms

Drug efflux transporters, membrane proteins, transport the chemotherapeutic drugs, such as TMZ, out of the cells.[52] These transporters reduce the intracellular drug levels, make GBM

cells less sensitive to TMZ, contributing to chemoresistance. These are part of the ATP-binding cassette (ABC) transporter superfamily members including ABCB1 (also known as p-glycoprotein (P-gp)), ABCC1 (MRP1), and ABCG2 (also known as breast cancer resistant protein (BCRP)).[52]

P-gp (~170 kDa) is located on the cell membrane and exports drugs from the cells, which requires adenosine triphosphate (ATP) hydrolysis. Encoded by the *ABCB1* gene, P-gp is well-studied membrane protein among ABC transporter family members.[68] Chemotherapeutic drugs, e.g. TMZ, act as substrates for P-gp.[69] In particular, P-gp transports MTIC, and limits TMZ efficacy.[61] Therefore, TMZ's major limitation is its rapid degradation to MTIC, which is subsequently effluxed by P-gp, reducing its therapeutic effect. In addition, overexpression of P-gp has been observed in various cancerous cells and endothelial cells of BBB, resulting in increased drug efflux and the ability of cancer cells to evade apoptosis.[52] Therefore, recent studies have focused on P-gp-mediated resistance, such as the development of P-gp inhibitors.[68] Another transporter, ABCC1 (MRP1) eliminates TMZ-induced DNA damage products, reducing oxidative stress signals and supressing DNA damage response pathways.[70]

BCRP is another transporter protein that supports the survival of stem cells under hypoxic conditions, which further induce its expression. Although BCRP is not the primary transporter for TMZ, it indirectly contributes to TMZ resistance by removing DNA repair and stress related responses.[61]

1.2.3.5 Survival signalling pathways in temozolomide resistance

Dysregulation in various signalling pathways plays a critical role in promoting TMZ resistance in GBM. The key pathways involved in TMZ resistance include phosphoinositide 3-kinase/protein kinase B (PI3K/AKT), mitogen-activated protein kinase/extracellular signal

regulated kinase (MEK/ERK), wingless-related integration site/ β-catenin (WNT/ β-catenin), janus kinase/ signal transducer and activator of transcription (JAK/STAT), Notch, Hedgehog, p53.[37, 52, 61] Figure 1.13 demonstrates these signalling pathways involved in TMZ resistance. Each pathway plays a unique role in the maintaining the survival, stemness, and genomic stability of GBM cells; thus offering new targets for development of novel GBM therapies for to overcome TMZ resistance.[37]

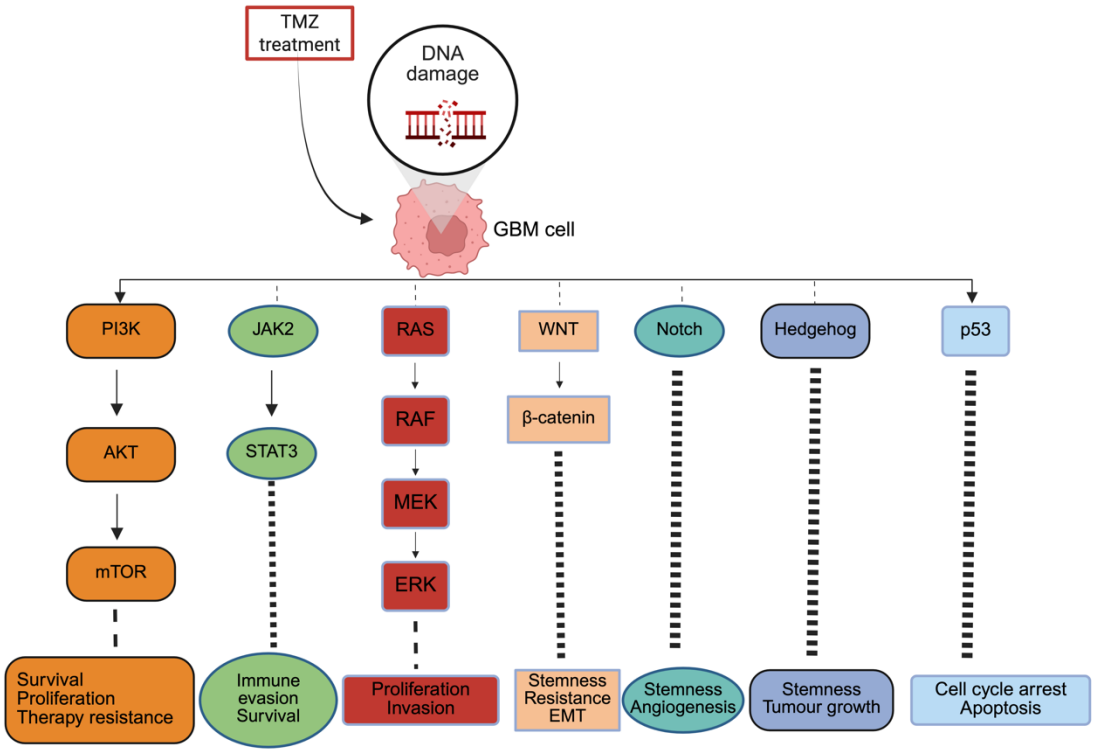

Figure 1.13 A Schematic representation of major signalling pathways involved in temozolomide (TMZ) resistance in glioblastoma (GBM). Created with BioRender.

PI3K/AKT has been widely studied in GBM due to mutations and amplification of receptor tyrosine kinases (RTKs). Among RTKs, EGFR plays a crucial role in cell signalling pathways driving proliferation and survival. In GBM, EGFR amplification has been observed ~60% of patients, leading to activation of the downstream of PI3K/AKT pathway. Additionally, EGFRvIII, a mutant variant, is found ~50% of GBM.[17] Both EGFR amplification and EGFRvIII enhance the ability of GBM cells to survive TMZ-induced DNA damage and contribute tumour regrowth. In addition, activation of the EGFR pathway can trigger several downstream signalling

pathways, including PI3K/AKT, RAS/RAF/MEK/ERK, and STAT[37] (see Figure 1.5). Additionally, within PI3K/AKT pathway, tumour suppressor PTEN is frequently inactivated in GBM, occurring ~90% of primary GBM because of mutations or deletions.[71] PTEN functions as a negative regulator of PI3K/AKT pathway, its loss leads to PI3K/AKT signalling pathway activation and therefore promotes tumour progression.[71]

In GBM, reprogramming of stem cells, ROS activation and non-coding RNAs (ncRNAs) can also activate survival RAS/RAF/MEK/ERK and PI3K/AKT pathways.[61] Additionally, WNT/β-catenin signal transduction plays a critical role in TMZ resistance.[17] Following TMZ treatment, GBM cells exhibit β-catenin upregulation, leading to TMZ resistance.[37] Hypoxic conditions also increase resistance via activation of WNT/β-catenin pathway.[61] In GBM, activation of the WNT/β-catenin pathway promotes the stem-like properties of the tumour cells, make tumours more resistant to TMZ.[17]

JAK/STAT signalling supports GBM resistance and is primarily associated with stemness. In particular, STAT3 overactivation is implicated in GBM, and has been linked to MGMT upregulation, which contributes to TMZ resistance in GBM.[17] In addition to JAK/STAT signals, the upregulation of Hedgehog- and Notch-mediated signalling pathways regulate stem cell maintenance and self-renewal, leading to poor treatment outcomes.[37] The p53 pathway is crucial for regulating DNA damage response hence it is activated following TMZ treatment. In GBM, mutations or inactivation in *TP53* gene are observed in 27-34% of GBM patients and contribute to TMZ resistance by conferring loss of function as a tumour suppressor protein.[72] For instance, Li-Fraumeni syndrome is inherited (autosomal dominant) predisposition to many cancers including brain a consequence of inherited *TP53* mutations (loss of tumour suppressor activity).[73]

As mentioned above, TMZ resistance in GBM can originate from complex cellular signalling and mechanisms by promoting survival and reducing drug accumulation. Therefore,

multitargeted strategies that target these signalling pathways are necessary to overcome TMZ resistance.

1.2.3.6 Autophagy in temozolomide resistance pathway

GBM cells develop resistance to TMZ through the regulation of autophagy and apoptosis (programmed cell death). These distinct mechanisms present different roles in the cell response to TMZ treatment, determining whether the cell will undergo death or survive. Autophagy is a cellular process that involves the degradation and recycling of damaged organelles, including endoplasmic reticulum and mitochondria, and proteins to maintain metabolic homeostasis under certain conditions such as hypoxia, chronic nutrient deprivation, DNA damage, and radiation.[17, 37] While autophagy includes the formation of autophagosomes and enhanced lysosomal degradation activity[61], apoptosis is characterised by apoptotic body formation and membrane blebbing (Figure 1.14). GBM characteristically displays the cancer hallmark 'apoptosis evasion'[2] and TMZ is known to cause autophagic cell death in TMZ-sensitive, apoptosis-resistance GBM cells.[17]

TMZ triggers autophagy by activating various signalling pathways, which can be controversial as it may either promote cell survival or lead to cell death in cancer cells under stress conditions (e.g. DNA damage).[17] If the GBM cell can repair the DNA damage through autophagy (cell-eating) via recycling cellular components and escape from apoptosis, it promotes GBM cell survival. In contrast, if DNA damage cannot be repaired through the activated autophagy mechanism, autophagic cell death is triggered.[17] In addition, when autophagic cell death is inhibited, then TMZ can cause apoptotic cell death in GBM cells.[74, 75] Therefore, although TMZ induces cell death via apoptosis in a few cells, GBM cells can evade apoptosis activating autophagy, this makes them more resistant to treatment. Therefore, inhibiting autophagy can enhance TMZ sensitivity.[37] For instance, Lin *et al.* reported that resveratrol inhibits autophagy by suppressing the ROS/ERK pathway, which increases TMZ sensitivity, showing a synergistic effect with tumour volume reduction and prolonged survival time *in vivo* (mouse xenograft).[76]

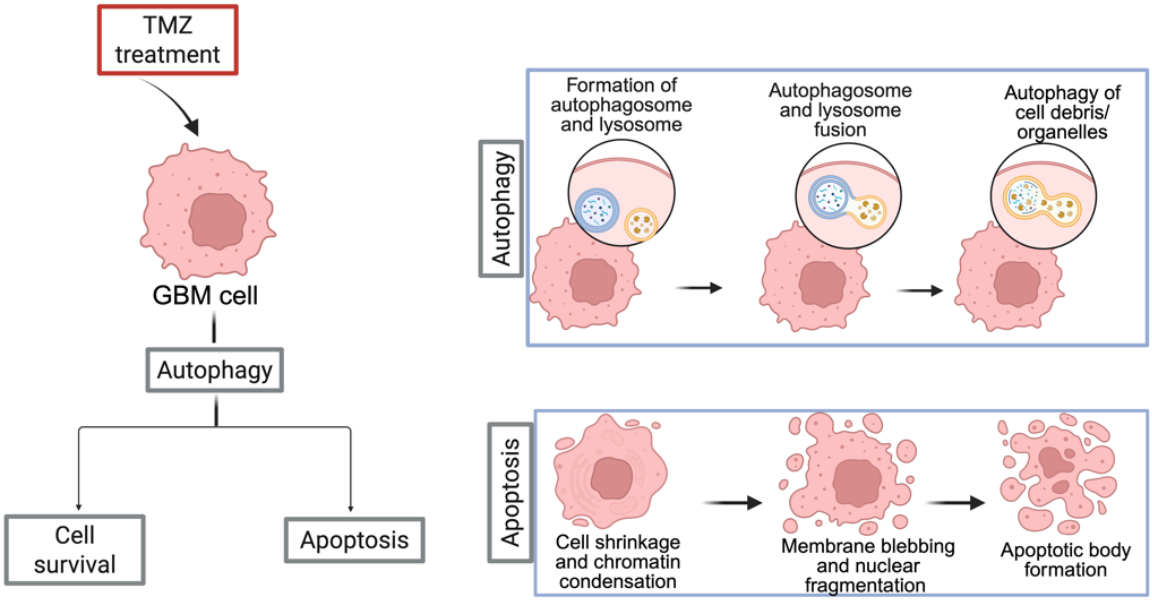

Figure 1.14 Overview of temozolomide (TMZ)-induced autophagy and apoptosis mechanisms in glioblastoma (GBM) cells. Created with BioRender.

1.2.3.7 Metabolic reprogramming in temozolomide resistance

Abnormal energy metabolism (a further cancer hallmark)[77] is observed in GBM cells, distinct from healthy cells, to enable rapid energy production and support aggressive tumour growth.[61] The altered metabolic processes include aerobic glycolysis, known as the Warburg effect, tricarboxylic acid cycle (TCA), fatty acid oxidation (FAO), and reactive oxygen and nitrogen species (RONS).[37, 61] Tumour cells use aerobic glycolysis for ATP production, even in the presence of oxygen, a process associated with rapid proliferation and prioritised nutrient consumption.[37] Increased glycolysis leads to an acidic TME with lactate accumulation.[37] Moreover, GBM cells enhance FAO, lipid, purine, and tryptophan metabolism to produce ATP.[61]

The TCA cycle, also known as the Krebs cycle, plays an important role in cellular energy metabolism in the mitochondria.[78] Normally, the cycle involves the oxidation of acetyl coenzyme A (acetyl-CoA) to produce nicotinamide adenine dinucleotide (NADH), flavin adenine dinucleotide (reduced) (FADH), and ATP.[78] However, in GBM, metabolic

reprogramming of the TCA cycle alters its function to contribute to tumour progression and TMZ resistance. One of the key drivers of this altered energy metabolism in GBM is the mutation of IDH genes (*IDH1* and *IDH2*).[79] Mutant IDH enzymes produce an oncometabolite, 2-hydroxyglutarate (2-HG), rather than normal product, alpha-ketoglutarate (α-KG), in the TCA cycle. In particular, the accumulation of oncometabolite 2-HG in high concentrations (5-30 mM) disrupts cellular metabolism, promotes glycolysis, and increases metabolic turnover.[80] These changes support GBM cell growth and survival under stress conditions, such as TMZ treatment, contribute to TMZ resistance mechanisms.[37]

GBM cells adapt their ROS and RONS metabolism to low-oxygen environments, resulting in increased levels of ROS and RONS.[37] When cells have been treated with TMZ, the DNA damage caused by TMZ also leads to oxidative stress, leading to higher levels of oxidative stress.[81] To survive, the GBM cells activate antioxidant defence mechanisms (e.g. redox-regulated glutathione (GSH) and thioredoxin (Trx) systems) and related signalling pathways (e.g. nuclear factor erythroid 2-related factor 2 (NRF2) pathway) to prevent cellular damage[37, 81]; this also enables GBM cells to survive the toxic effects of TMZ-induced DNA damage. This mechanism adapts the cells to maintain ROS balance and contribute to TMZ resistance. In addition, ROS can also affect other resistance mechanisms, such as autophagy.[17]

1.2.3.8 Alternative mechanisms in temozolomide resistance

There are several alternative mechanisms which contribute to TMZ resistance. These mechanisms include epigenetic modifications, GBM stem cells (GSCs), micro ribonucleic acids (miRNAs), and extracellular vesicles (EVs).[17, 82] For example, histone acetylation, an epigenetic modification, can promote the activation of DNA repair pathways, contributing to TMZ resistance.[61] Additionally, GSCs are key drivers of TMZ resistance in GBM. The markers commonly used to identify GSCs include CD133, CD44, CD15, CD70, Nanog, SOX-2, and Nestin. Although GSCs comprise 1% of the cells in GBM tumours, they are a major contributor to regrowth of tumours following TMZ treatment.[17]

For example, several miRNAs have been reported to be involved in the regulation of MGMT (inhibition of MGMT suppression or promotion of its expression), thus driving resistance in GBM cells.[61] In addition, EVs can transport resistance-related proteins (e.g. P-gp, ABCB1, MGMT) from resistant cells to sensitive tumour cells, hence contributing to TMZ resistance.[82]

1.2.4 Limitations of temozolomide in glioblastoma treatment

Although TMZ has been used for GBM treatment, several limitations reduce its clinical use.[47] The key constraints of TMZ chemotherapy include non-specific toxicity, drug resistance, chemical properties of TMZ, and poor drug accumulation (Figure 1.15).[13]

Although TMZ can cross the BBB moderately easily, there are concerns related to poor drug accumulation in the brain (only 1%) and within GBM regions.[83] Contributing to poor intratumoural drug accumulation are drug efflux transporters (P-gp), instability of TMZ at pH ≥ 7.0[84] hence, extending TMZ's stability at physiological pH is required to achieve greater drug accumulation.[42] In addition, TMZ has poor solubility and rapid plasma clearance, which hinder its pharmacokinetic profile.[57]

TMZ's clinical efficacy is limited due to its role as a substrate for P-gp, expressed in BBB. Resistance to TMZ, arises due to overexpression of MGMT or deficiency in MMR. MGMT repair enzymes can reduce TMZ's cytotoxic effect.[85] Therefore, the amount of MGMT expression in tumour cells determines the susceptibility or resistance of the cells to TMZ.[17] In this context, Hegi *et al.* developed a clinical investigation of methylation status in MGMT gene promoter, revealing that silencing the promoter with methylation improved responsiveness to TMZ compared to those without MGMT promoter methylation.[86] This test identifies patients who are more likely to respond, and similarly, spares those whose tumours express high levels of MGMT from unnecessary exposure to a cytotoxic drug.

Both inherent and acquired resistance mechanisms, as mentioned above, further hinder its cytotoxic activity.[83] Additionally, TMZ's non-specific toxicity affects healthy tissues and

produces several side effects.[16] These limitations highlight the need for novel, nanotechnology-based approaches to stabilise TMZ at physiological pH, enhance tumour targeting, minimise systemic toxicity, and overcome biological barriers and efflux mechanisms.

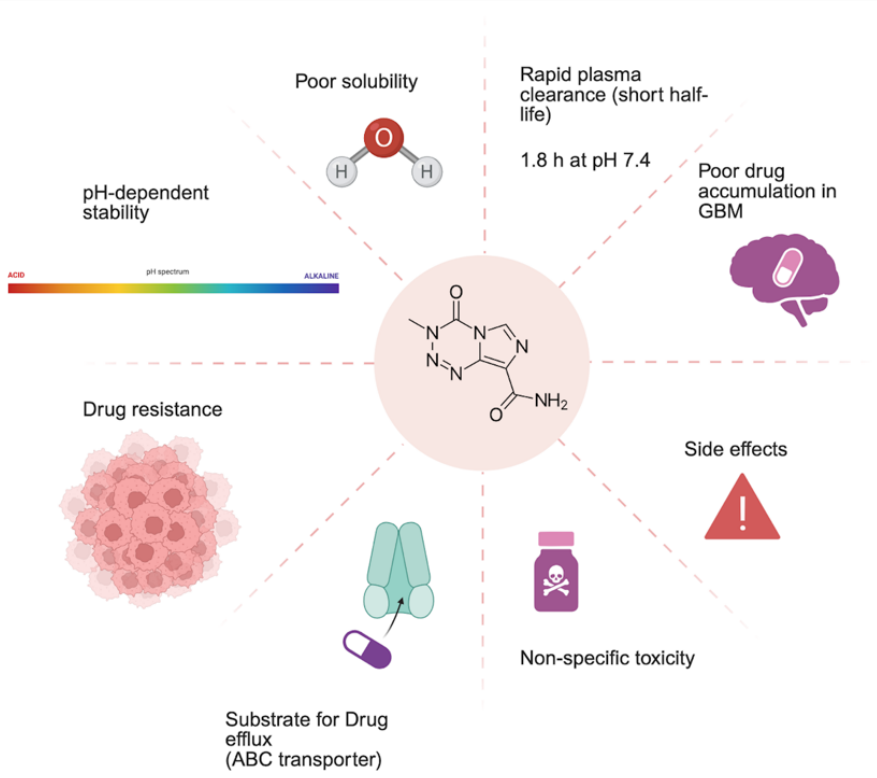

Figure 1.15 Limitations of temozolomide (TMZ) treatment in current GBM treatment. Created with BioRender.

1.3 Imaging and diagnostic approaches in glioblastoma

1.3.1 The role of imaging in the glioblastoma management

Imaging is a key component for GBM management, from initial diagnosis to treatment planning to guide further clinical decisions, monitoring therapeutic response, and detection of recurrence.[87] In addition, it is important for tumour characterisation, localisation, and GBM surgery, particularly considering the challenges of GBM such as barriers and tumours deep localisation. These challenges not only impact treatment strategies but also influence diagnosis.[11]

Imaging techniques (conventional or modern) used in the clinic each have distinct advantages and limitations. However, imaging possesses a dramatic effect on GBM patient outcomes, predicting treatment resistance and guide personalised medicine, consequently contributing to improved survival rate and quality of life of GBM patients.[88] Therefore, there is a growing need for the development and integration of conventional and advanced imaging techniques for enhanced GBM diagnosis.

1.3.2 Diagnostic methods for glioblastoma

There are both conventional and advanced imaging techniques used for GBM diagnosis, including computed tomography (CT), magnetic resonance imaging (MRI), positron emission tomography (PET), and fluorescence imaging.[89] Each technique has advantages and limitations. For example, CT is often used in the earliest investigations with fast image acquisition and availability.[90] MRI is a gold standard for diagnosis and post-treatment management of GBM together with radiographic characterisation.[91] However, it is difficult to distinguish tumour grades and treatment related response by conventional MRI alone.[92] Therefore, more advanced techniques have been investigated. For example, gadolinium (Gd)-based contrast agents have been used in contrast-enhanced MRI for the diagnosis of GBM.[93] However, Gd-based agents (group I, such as gadodiamide, gadopentetate, dimeglumine, and gadoversetamide) have been withdrawn or restricted from clinical use because of safety concerns such as the risk of nephrogenic systemic fibrosis in patients with advanced chronic kidney disease.[94] PET enhances the relevance of GBM diagnosis and monitoring beyond MRI using radiotracers, such as glucose metabolism tracers (e.g. ^{18}F- fluorodeoxyglucose) and amino acid transport tracers, for imaging purposes.[95]

Fluorescence imaging is a non-invasive technique that can provide real-time feedback, high sensitivity, minimal radiation, making it effective for visualising organs; however, it can not penetrate bone (e.g. the skull).[96] This technique is utilised to visualise the tumour with fluorescence contrast agents, organic dyes, and inorganic quantum dots (QDs). Fluorescence

imaging for GBM often uses FDA-approved dyes, such as 5-ALA and indocyanine green (ICG), particularly in fluorescence-guided surgery (FGS) to visualise tumour vessels and distinguish malignant tissue from healthy tissue during surgical resection of tumour tissue .[97] However, these organic dyes suffer from several limitations, including depth penetration, photobleaching, poor stability, short circulation time, and low brightness.[98]

The electromagnetic spectrum in the near infrared region (NIR) is ideal for fluorescence imaging due to reduced scattering, absorption, and autofluorescence from tissues.[99] Fluorescence imaging in the first near infrared region (NIR-I, 650-900 nm) has gained attention owing to its sensitivity, harmless radiation, and low cost.[100] However, NIR-I has many limitations such as low resolution and specificity limiting depth penetration in tumour imaging. In biological tissues, the exciting or emitting light can be absorbed by water, haemoglobin, oxygenated haemoglobin, skin, fat, proteins, and cell structures, which can negatively impact the image quality.[99] (Figure 1.16). There are no organic dyes suitable for *in vivo* imaging in the NIR region, QDs offer a suitable and promising alternative.

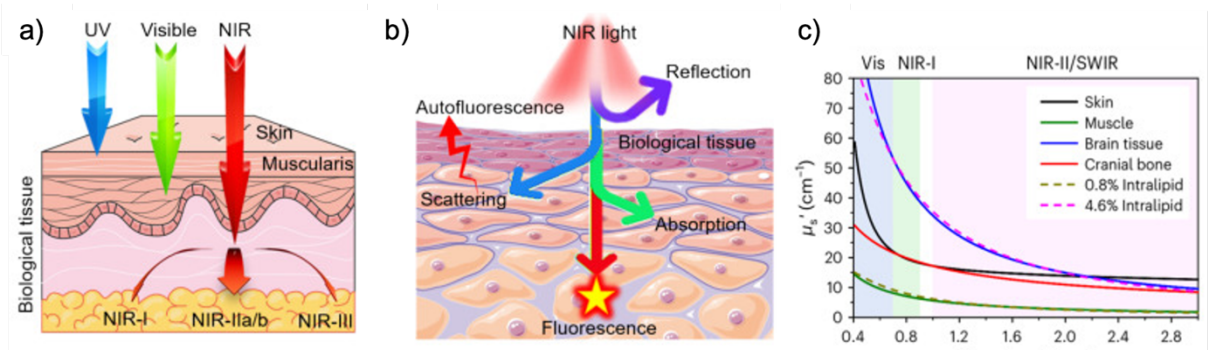

Figure 1.16 Illustration of **(a)** *in vivo* penetration of light in biological tissues in different wavelengths. **(b)** illustration of the problems of near infrared (NIR)-light reaching the biological tissue. **(c)** Optical transparency windows in the near infrared region-I (NIR-I) and near infrared region II (NIR-II)/ short wave infrared (SWIR) window in some biological tissues.[101]

Recent studies demonstrated that NIR-I limitations for imaging are significantly reduced in the second near infrared region (NIR-II, 1000-1700 nm) imaging, also known as short-wave infrared (SWIR) radiation; NIR-II enables high quality fluorescence imaging with reduced background and deep tissue penetration potential.[102] SWIR imaging relies on the ability of light

at longer wavelengths to penetrate biological tissues more deeply than in the visible region due to lower absorption of biological tissues and reduced light scattering.[101] As a result, the absence of background allows detection of tumours and healthy tissues, which is critical for GBM. Although SWIR-based techniques have been investigated, they have not achieved clinical adoption, mostly due to lack of suitable materials and delivery options. However, their potential to enhance GBM imaging makes them a promising field of the study. Particularly, inorganic QDs can be used as imaging probes in the SWIR region.

1.3.3 Quantum dots as imaging agents

Quantum dots, QDs, are semiconductor nanocrystals, exhibiting unique optical and electronic properties which can be tuneable by altering their composition, size, and crystal structure.[103] QDs typically have diameters in the range 2-10 nm. Depending on the size, their optical absorption and emission changes due to quantum confinement effects. QDs have broad absorption, narrow optical emission with quantum yields up to ~35%.[104] QDs (smaller than 10 nm in diameter) tend to show quantum confinement effects, leading to the formation of discrete electronic energy levels and a size-dependent bandgap.[105] With decreasing QD size, the strength of quantum confinement increases, resulting in an increase of energy gap and a blue shift in their optical properties[103] (Figure 1.17). Upon absorption of photons (energy above the energy gap), electrons from valance band (lowest unoccupied molecular orbital (LUMO)) states are excited to into conduction band (highest occupied molecular orbital (HOMO)) states.[105]

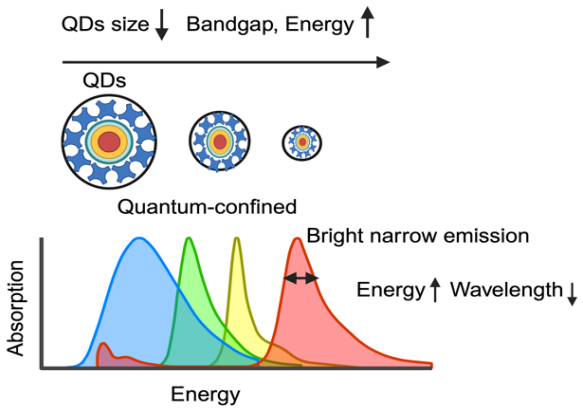

Figure 1.17 Schematic illustration of size dependent properties of semiconductor quantum dots (QDs) resulting from quantum-confinement effects.

Due to the quantum size effect, QDs exhibit different properties from conventional fluorescent probes.[106] They offer several advantages compared to traditional organic fluorescent dyes, making them attractive in bioimaging applications: (1) higher fluorescence efficiency, (2) higher photostability, (3) a narrow emission spectrum, (4) a broad excitation wavelength range, (5) tuneable size, shape, and composition, (6) resistance to degradation (7) large Stokes shift.[99] Figure 1.18 summarises optical properties of QDs. These properties make QDs promising candidates for long-term imaging *in vitro* and *in vivo*.[105, 107]

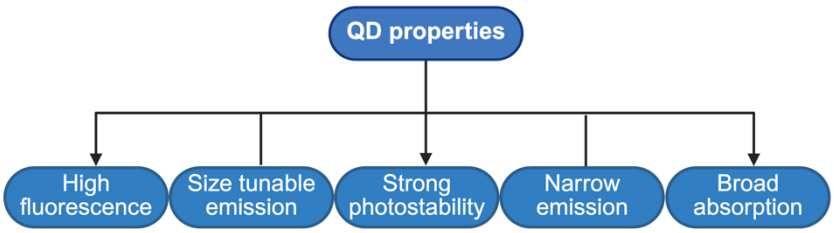

Figure 1.18 Optical properties of quantum dots (QDs).[108] Created with BioRender.

For synthesis of aqueous QDs, three main components are required: a metal precursor containing capping agent (stabiliser) and a chalcogenide (group 16 element e.g. S and Se) precursor. To ensure colloidal stability and stable morphological and optical properties in aqueous solution, QDs are capped with ligands,[109] typically small molecules such as thioglycolic acid (TGA) and 1-thioglycerol (TGL) , in which thiol-groups bind directly onto the QD surface, and polyethylene glycol (PEG), a polymeric coating stabiliser that provides

stabilisation and allows functionalisation.[109, 110] Figure 1.19 illustrates the molecular structures of commonly used thiol-based QD capping agents.

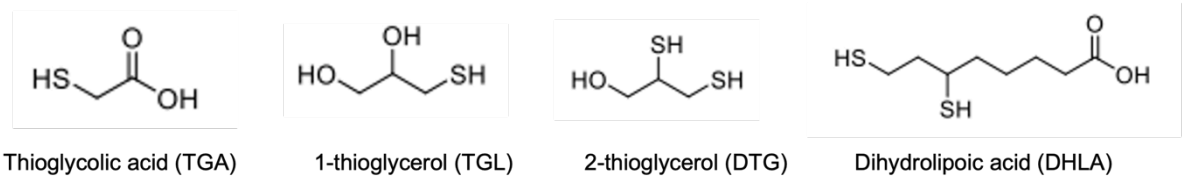

Thioglycolic acid (TGA) 1-thioglycerol (TGL) 2-thioglycerol (DTG) Dihydrolipoic acid (DHLA)

Figure 1.19 Thiol-based quantum dot (QD)-capping ligands. Created with Chem Draw.

QDs can be categorised based on several factors, including chemical composition, size, emission wavelength, core-shell structure and biocompatibility.[107] According to QD chemical composition, group II-IV QDs, such as cadmium telluride (CdTe), cadmium selenide (CdSe), cadmium sulfide (CdS) have emission in the visible range. However, their potential as imaging agents is limited due to light absorption by biological tissues. On the other hand, the IV-VI semiconductor QDs, such as lead sulfide (PbS) and lead selenide (PbSe) have optical emission tuneable in the NIR-II wavelength range (1000-1700 nm) of low absorption of biological tissues, hence are promising candidates for bioimaging.[104, 107]

QDs can be used in molecular imaging and cell tracking applications.[105] Several studies have investigated the potential of semiconductor QDs for cancer imaging, particularly for *in vivo* imaging in the NIR-I region. However, NIR-I imaging may not provide sufficiently high resolution and depth penetration for intractable tumours such as GBM.[99] Therefore, there is a need to take advantage of NIR-II region for *in vitro*, *in vivo* and *ex vivo* imaging applications. Recently, Wang *et al.* reported that biocompatible core-shell Pb/CdS QDs, emitting in the NIR-II region, achieved the superior imaging depth of up to 1100 μm of the vessel through the intact skull of the mouse.[111]

Among several QDs, lead sulfide QDs (PbS QDs) have gained attention due to their strong and tuneable fluorescence emission in the NIR-II region. This optical window is critical for deep tissue imaging; hence it allows higher resolution and deeper tissue penetration compared to NIR-I.[112] Despite the advantageous properties and recent advances in NIR-II brain imaging, NIR-II probes are limited by the availability and sensitivity of bioimaging systems with detection

in this wavelength range (1000-1700 nm). In addition, the metal-based toxicity concerns of these QDs restrict their clinical use. To overcome these limitations, PbS QDs can be capped with different ligands, peptides, antibodies, and/or encapsulated within different nanocarriers to reduce their cytotoxic effects.[108] For example, Zamberlan *et al.* capped PbS QDs with dihydrolipoic acid–polyethylene glycol (DHLA–PEG) for *in vivo* imaging applications.[113] In addition, element doping of QDs has been investigated, Shi *et al.* demonstrated that Zn-doping of PEGylated PbS QDs enhanced the stability, and their PL *in vivo* imaging, allowing blood capillaries to be distinguished.[114]

In another study, Qu *et al.* investigated the fluorescence imaging performance of PbS QDs emitting at multiple wavelengths across the NIR-I and NIR-II/SWIR windows in mouse scalp, skull, and brain.[115] They found that tissue attenuation (absorption and scattering) decreased at longer wavelengths, demonstrating SWIR's suitability for imaging brain tissue and tumours, and the possibility to develop PbS QD-based deep tissue probes. In this thesis, the development of PbS QD-based deep tissue probes for diagnostic, therapeutic, and theranostic applications has been investigated by encapsulating PbS QDs into nanocarriers to further improve their activity in the imaging.

1.4 Nano formulations for drug delivery and theranostic approaches in glioblastoma

1.4.1 Advantages of nanoparticles in glioblastoma treatment

With the advancement of nanotechnology, drug delivery systems (DDS) have been employed in diagnostic, therapeutic, and theranostic approaches to overcome challenges associated with GBM.[116] Nanoparticles (NPs, 1-500 nm) can improve GBM treatment by enhancing therapeutic activity through increased drug accumulation at tumour tissues, sustained and controlled release, improved ability to cross the BBB via the enhanced permeability and retention (EPR) effect or targeted delivery, and protection of the drug from degradation.[117]

NPs can be used as passive or active tumour-targeting mechanisms.[118] Passive targeting, an energy-independent mechanism, relies on the EPR effect, a phenomenon observed in tumours due to increased vascular permeability and impaired lymphatic drainage. Figure 1.20 illustrates the difference between NPs` accumulation in healthy and tumour tissues, demonstrating the role of EPR. This effect allows NPs to accumulate in tumour tissues, which contribute to drug delivery with NPs. However, the passive targeting strategy is often limited, offering less than two-fold increase in drug accumulation, and dependent on the tumour type, size, grade and vascularisation.[118, 119] In particular, only a small fraction (≤ 1%) of administered NPs accumulate in the GBM via the EPR effect.[119]

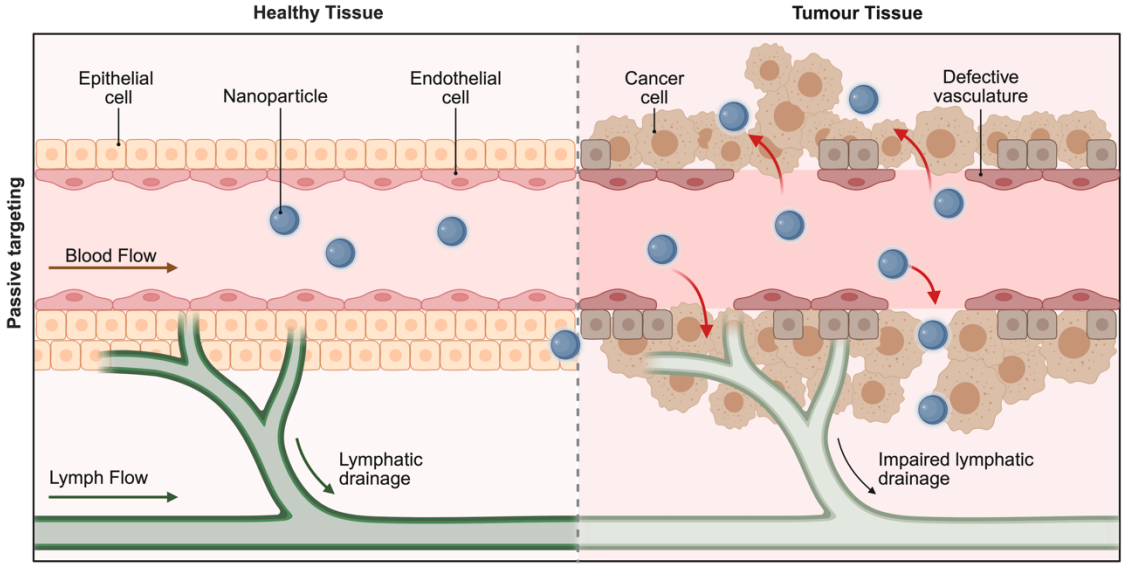

Figure 1.20 Schematic illustration of passive targeting: enhanced permeability and retention (EPR) effect. Created with BioRender.

To overcome the limitations of passive targeting in GBM, energy-dependent active targeting strategies have been developed. These includes adsorption-mediated transcytosis (AMT), which involves electrostatic interactions between positively charged NPs and the negatively charged cell membranes, and receptor-mediated transcytosis (RMT), where NPs are surface-modified with ligands, antibodies, peptides, and receptor-binding molecules (Figure 1.21) that bind to overexpressed receptors on tumour cells.[120]

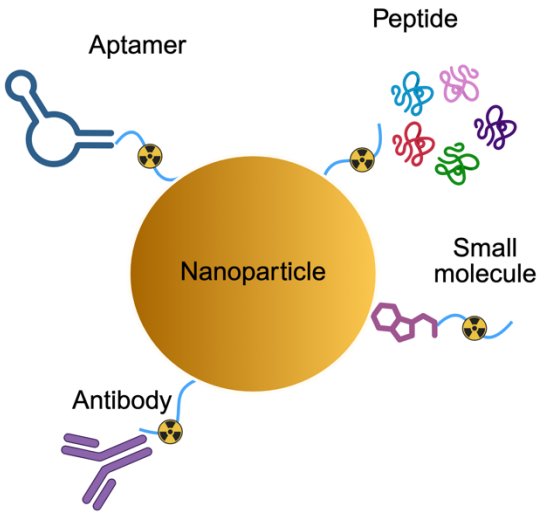

Figure 1.21 Active targeting mechanisms with nanoparticles (NPs). Created with BioRender.

These active targeting mechanisms enhance drug accumulation and therapeutic activity of drugs in brain tumours such as GBM.[119] In particular, RMT is one of the most promising active targeting strategies for brain tumours.[121] It facilitates the transport of NPs across the BBB by targeting overexpressed receptors such as transferrin receptor (TfR), which are commonly upregulated in BBB endothelial cells and GBM.[122] RMT allows NPs to be delivered with high specificity, selectivity, affinity for brain tumours.[119]

1.4.2 Nanoparticle types used in drug delivery

Different types of NPs have been used as DDS in the GBM treatment. Liposomes, dendrimers, mesoporous silica NPs, micelles, polymeric NPs, QDs and several organic/inorganic nanocarriers have been developed from various materials to improve transportation of drugs to target sites exploiting controlled release capabilities and prolonged blood circulation (Figure 1.22). Each NPs offers unique advantages and disadvantages for GBM therapy.[16]

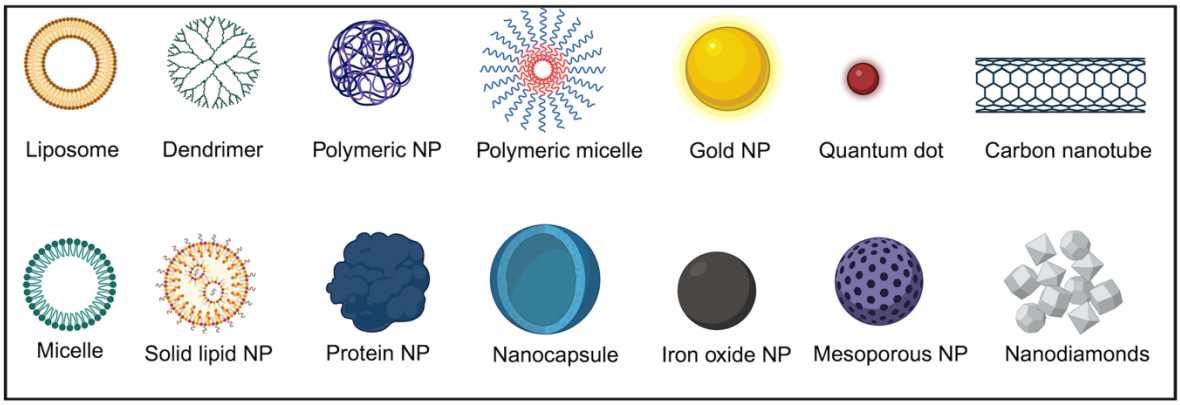

Figure 1.22 Schematic representation of the various types of drug delivery systems (DDS). Created with BioRender.

1.4.2.1 Polymeric nanoparticles in glioblastoma treatment

Polymeric NPs, constructed with a core polymer matrix, are commonly employed as DDS to encapsulate therapeutic agents, or conjugate them to the surface.[123] Polymeric NPs offer several advantages for GBM treatment including controlled and sustained drug release, enhanced drug stability, biodegradability, biocompatibility, high drug loading capacity, and the ability to functionalise with ligands targeting overexpressed receptors (such as EGFR and TfR).[124] Commonly used biodegradable synthetic polymers such as poly (lactic acid) (PLA), poly (glycolic acid) (PGA), and poly (lactic-co-glycolide) (PLGA) have been approved by the FDA.[125] However, they also present certain limitations such as low physicochemical stability, the initial burst drug release, and limited ability to cross the BBB without surface modification or targeting strategies.[124, 125]

Polymeric NPs have been widely studied in the treatment of GBM, particularly for improving stability and therapeutic activity of TMZ.[126-129] For instance, Jain *et al.* described TMZ loaded PLGA NPs` effect in C6 glioma cells; demonstrating prolonged activity of TMZ and retention of anti-metastatic activity.[126] Some studies utilised the active targeting strategies to increase the activity of polymeric NPs. For example, to improve the brain delivery of TMZ, Ramalho *et al.* developed PLGA NPs functionalised with monoclonal antibody for TfR to encapsulate TMZ

in *in vitro* U215 and U87 GBM cell lines, demonstrating improved anti-proliferative activity of TMZ.[127] Similarly, Banstola *et al.* developed PLGA NPs loaded with TMZ and conjugated with the anti-EGFR antibody panitumumab, and evaluated them in U87MG (EGFR-overexpressing) and LN229 (EGFR-low expression) GBM cell models.[129] Their results demonstrated that functionalised PLGA NPs enhanced cytotoxicity compared to the non-functionalised counterparts in the U87MG cell line, suggesting the advantage of receptor-mediated endocytosis in GBM therapy.[129] More recently, a study conducted by Ramalho *et al*. showed that the suitability of PLGA NPs for co-encapsulation by loading both TMZ and bortezomib (BTZ; Velcade 26S proteasome inhibitor), conjugated with TfR ligands to enhance GBM targeting ability.[128] The results demonstrated rapid cellular uptake in both U251 (TMZ-sensitive) and T98T (TMZ-resistant) human GBM cell lines.[128]

Polymeric micelles represent a promising DDS for GBM treatment. In a study by Sun *et al.,* TfR-targeted polymeric micelles *(*TfR-T12 peptide-modified PEG-PLA polymer) were developed to deliver paclitaxel (PTX) to GBM*;* both *in vitro* and *in vivo* studies concluded that TfR-T12 peptide significantly ($p < 0.05$) increased apoptosis in U87MG cells, and enhanced brain accumulation ($p < 0.05$) compared to naked PTX a consequence of active targeting to GBM cells.[130] In another instance, Yu *et al.* demonstrated that TfR-targeted TMZ nano-micelles, using the biodegradable polymer PEG-PLA, significantly ($p < 0.001$) enhanced the growth inhibition of U251 human glioma cells compared to control after 48 h treatment. This effect was associated with significantly ($p < 0.001$) enhanced ROS production and 84% induced apoptosis.[131]

Despite significant progress with polymeric NPs, several challenges with polymeric DDS remain unresolved, including potential toxicity, stability, and reproducibility.[132] Additionally, polymeric NPs possess multivariable parameters such as size, shape, surface charge, and the presence of targeting moieties, which can alter the interactions with biological systems.[133] Furthermore, they require additional designs to achieve active targeting mechanisms to reach to brain, controlled release, and stability in physiological pH, these factors that directly affect

delivery, biodistribution, circulation stability, and clearance. These multivariable parameters also complicate large-scale production while ensuring consistency and safety for human health.[132, 133]

1.4.2.2 Lipid nanoparticles in glioblastoma treatment

Lipid NPs, including liposomes, solid lipid nanoparticles (SLNs), and nanostructured lipid carriers (NLCs), have emerged as promising DDS for improving GBM treatment.[134] These systems offer several advantages such as the ability to deliver both hydrophilic and hydrophobic drugs, improved drug solubility, low toxicity, controlled drug release, the ability of surface modification to evade immune recognition.[134]

Liposomes are spherical NPs consisting of a phospholipid bilayer surrounding a hollow core, and they have been extensively studied for GBM treatment.[123] For example, Gao *et al.* formulated liposome encapsulated TMZ (NP size: 156.7 ± 11.4 nm) to prolong the half-life of the drug (~1.8 h at pH 7.4), enhance brain targeting by pinocytosis of endothelial cells in the BBB, and reduce the systemic effects of TMZ for glioma tumour treatment.[135] *In vivo* pharmacokinetic studies demonstrated that the liposome formulation extended the *in vivo* circulation time (~7.0-fold), and biodistribution studies in mice revealed that the liposome-TMZ formulation reduced toxicity by decreasing accumulation in the heart (~0.7-fold) and lungs (~0.8-fold) while increasing TMZ concentration in the brain (~1.2-fold).[135]

Functionalised and/or co-encapsulated lipid NPs were reported to enhance the targeted delivery of drugs/molecules.[136-138] For instance, Lam *et al.* developed TfR-targeted liposomes co-encapsulating the bromodomain inhibitor JQ1 and TMZ for GBM treatment.[136] *In vivo* studies with tumour bearing mice demonstrated enhanced drug accumulation in brain endothelial walls, leading to DNA damage, apoptosis, and a 1.5–2-fold reduction in tumour burden, with improved survival.[136] In another study, Ak *et al.* developed monocarboxylate transporter-1 (MCT-1)-targeted SLNs co-encapsulating carmustine and TMZ, which induced

higher levels (~1.2-fold) of apoptosis compared to non-targeted formulations.[138] Zhang *et al.* investigated NLC utilising two ligands: lactoferrin (for passage across the BBB and receptor-mediated endocytosis into GBM cells) and arginylglycylaspartic acid (RGD) tripeptide (which binds to αvβ3, overexpressed on neurovascular endothelial cells).[137] The co-encapsulation of TMZ and vincristine in co-modified NLC demonstrated synergistic activity and greater cellular uptake ($p < 0.05$) compared to non-targeted NLC with greatest ($p < 0.05$) tumour inhibition *in vivo.*[137]

Based on these studies using various DDS, surface receptor functionalisation on NPs has emerged as a promising strategy for delivering cargos to brain tumours. Although most NPs have been externally functionalised to target GBM cells, alternative approaches, such as protein-based NPs, can eliminate the need for additional modifications.

1.4.2.3 Protein-based nanoparticles in glioblastoma treatment

Proteins are biodegradable, and generally recognised as safe materials for drug delivery nanocarriers.[139] Compared to other NPs, protein-based NPs offer unique advantages: (1) they eliminate the need for toxic chemicals and solvents during synthesis; (2) they enable surface modification at well-defined positions with targeting ligands using engineering strategies; (3) they provide the versatility to encapsulate or conjugate diverse biomolecules, including drugs, small interfering RNA (siRNA), antigens, and imaging diagnostic agents; (4) some proteins exhibit natural tumour-binding affinity, and their surface can be further functionalised for enhanced targeting; (5) their metabolic degradation products are amino acids, which are non-toxic; (6) biodegradability and biocompability (7) non-immunogenic; 8) uniform size.[124, 140] There are several types of protein NPs such as albumin, lipoproteins, silk proteins, collagen, viral protein cages, and ferritin that have been explored as DDS in GBM therapy (Figure 1.23).

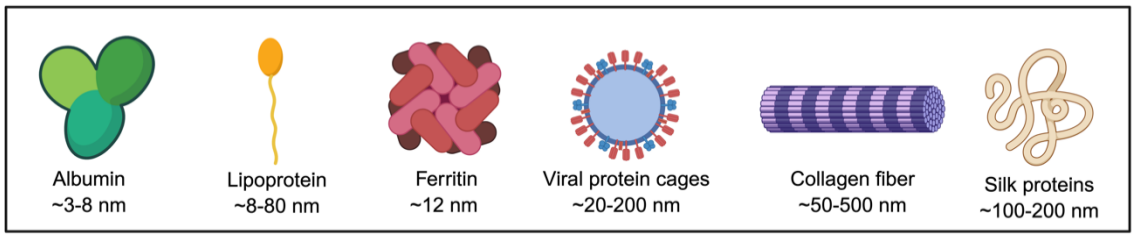

Figure 1.23 Some examples of protein-based nanoparticles (NPs) used in glioblastoma (GBM) treatment. Created with BioRender.

Albumin is one of the most abundant plasma proteins, it exists in various forms such as ovalbumin (OVA), bovine serum albumin (BSA), and human serum albumin (HSA).[124] Albumin exhibits several advantageous properties for a DDS, including prolonged circulation time (up to 19 days), biodegradability, water solubility, and the potential for surface modification.[124] Albumin-based NPs accumulate in solid tumours via the EPR effect, their interactions with glycoprotein 60 (gp60) and secreted protein acidic and rich in cysteine (SPARC) proteins enhances their accumulation within tumours.[141] Albumin combined with PTX (Abraxane®) was the first protein-based nanoformulation approved by the FDA for the treatment of metastatic breast cancer.[142] Zhang *et al*. demonstrated the activity of Abraxane® in GBM treatment, indicating its enhanced brain penetration and tolerability compared to PTX.[143] Furthermore, Qu *et al.* evaluated the effect of Abraxane® and TMZ combination on GBM cells both *in vitro* and *in vivo* (orthotopic xenograft nude mouse model); revealing a synergistic effect on U87MG, LN229 and two primary GBM cell lines (G353 and G393), as well as patient-derived organoids.[144] Helal *et al.* developed HSA NPs loaded with TMZ and evaluated their activity on GL261 GBM cells and BL6 GBM stem cells.[145] The findings demonstrated that HSA NPs enhanced intracellular TMZ retention and exhibited higher toxicity, with cell viability reduced to 61.9 ± 3.0% in GL261 cells and 38.3 ± 4.8% in BL6 cells following treatment with 100 µM TMZ-loaded HSA NPs. Additionally, Kudarha *et al.* developed BSA NPs conjugated with hyaluronic acid for targeted delivery of TMZ via CD44 receptor binding; demonstrating enhanced brain accumulation of TMZ following intravenous (i.v.) route.[146]

Lipoprotein-based NPs are composed of complexes of lipids and proteins and include high-density lipoprotein (HDL), low-density lipoprotein (LDL), very low-density lipoprotein (VLDL).[140] These NPs utilise RMT via apolipoprotein receptors to cross the BBB, facilitating targeted delivery of agents to GBM cells.[140] For instance, Liang *et al.* encapsulated vincristine (VCR) sulfate into naturally available LDL-based NPs modified with a seven peptide (T7) ligand targeting the TfR. T7-LDL-VCR NPs demonstrated anti-glioma effects both *in vitro* (C6 cells) and *in vivo* (in a glioma bearing mouse model).[147]

Silk protein NPs are natural, strong drug delivery carriers that exhibit a high affinity for drugs and enable controlled pH-dependent drug release for cancer therapy.[124] Moreover, collagen, a fibrin type of protein and the main component of ECM, offers the potential of collagen-based NPs for localised, sustained, and targeted drug delivery, and have been investigated in several studies.[148, 149]

Virus-like particles (VLPs), also known as viral protein cages, have a uniform shape, self-assembling capacity, a small size (20-200 nm), the ability to be functionalised, and a hollow structure that allows loading of several types of molecules such as chemotherapeutic drugs, therapeutic genes, and siRNA.[124, 150] While they are virus capsids, they are distinguished from viruses by the absence of infectious genetic material. Therefore, these protein NPs are emerging class of targeted delivery approaches, especially potential to overcome BBB-related challenges in GBM treatment.[151] Commonly used VLPs are derived from animal viruses such as hepatitis B virus (HBV) and human papillomavirus (HPV), bacteriophages like emesvirus zinderi (MS2) and oubevirus durum (Qβ), and plant viruses including cowpea mosaic virus and tobacco mosaic virus (TMV).[151] They have been used as carriers in cancer research due to their water solubility, biocompatibility, and high cellular efficiency.[150] JC polyomavirus (JCPyV), a human virus, has been investigated in GBM gene therapy applications. Due to its natural ability to infect glial cells and cross the BBB, JCPyV-derived VLPs have been engineered to target GBM cells.[150] For example, Chao *et al.* demonstrated that JCPyV-derived VLPs could

deliver suicide genes (e.g. thymidine kinase) into GBM cells via receptor-mediated endocytosis, resulting in tumour growth inhibition in U87 cells.[152]

Ferritin (Ft) is an endogenous protein, found in all living organisms, primarily located in the cytoplasm, although it can be also found in the nucleus and mitochondria, as well as blood plasma.[70, 120] Ft is a spherical protein, consisting of 24 subunits of heavy (H, 21 kDa) and light (L,19 kDa) chains (subunits) in any ratio, and has internal and external diameters of 8 nm and 12 nm, respectively. It is highly thermostable and the cage can withstand temperatures up to 80°C.[140]

Ft together with transferrin (Tf) is responsible for transporting and storing iron (Fe, ≤ 4500 Fe atoms in its cavity), thus regulating the balance of Fe (II) and Fe (III) in the human body.[120] H subunits possess ferroxidase activity, catalysing the oxidation of Fe (II) to Fe (III), whereas L subunits facilitate iron nucleation and mineralisation.[153] In addition to Ft, DNA-binding protein from starved cells (Dps) is an Fe (II) scavenging protein (outer diameter ~9 nm, inner diameter ~4.5 nm) that exhibits ferroxidase activity as a member of the Ft family.[154, 155] Dps (molecular weight ~19 kDa) differs from Ft, Dps consists of 12 subunits with limited iron storage (~500 Fe) capability.[154] In addition, Dps plays a natural role in protecting DNA from oxidative stress and can be used as DDS consequence of its ultra-small structure.[155]

The Ft cage structure (includes 4-fold and 3-fold channels) which facilitate iron transport into the cells (via TfR1) but ferroportin transports iron out of the cells (only known as iron exporter)[153] (Figure 1.24a). Ferroportin downregulation is observed in tumour cells, and it is correlated with poor prognosis. Therefore, delivery of drugs/imaging agents in Ft-based nanocarriers not only leads to GBM cell uptake (via TfR1 upregulation), but also enhances retention through decreased expulsion (ferroportin downregulation). This mechanism facilitates prolonged retention of Ft and its cargo in GBM cells.[156] Ft is widely found in mammalian organs such as liver, spleen, kidney, and bone marrow.[157] Tf, a plasma glycoprotein (80 kDa), plays a vital role in iron metabolism.[158] Under physiological conditions,

Fe (III) binds to Tf, and TfR on the cell surface facilitate iron uptake by cells (Figure 1.24b).[158] In addition, TfR1 also recognises Ft and mediates TfR1-mediated endocytosis via interaction with the H-chain.[159] TfR is highly expressed in red blood cells, endothelial cells in the brain, and cancer cells including GBM.[160]

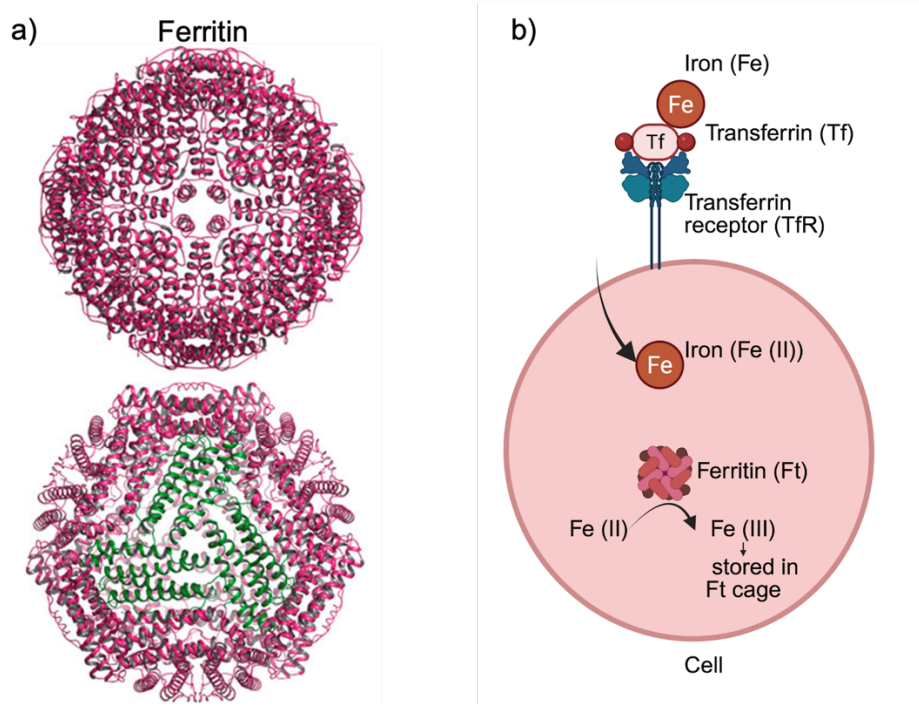

Figure 1.24 Ferritin (Ft) structure and its role in iron (Fe) metabolism illustrated. (**a)** Spherical Ft structure showing its 4-fold channels (top) and 3-fold channels (bottom, green colour).[153] **(b)** Illustration of iron metabolism and the role of Ft. Created with BioRender.

To date, Ft has emerged as a promising DDS in cancer therapy due to its unique biochemical properties, structure and its biocompatibility.[140] In GBM treatment, Ft-based NPs leverage the interaction between Ft and TfR for targeted delivery of drugs/molecules to cross BBB.[21] In addition, the potential of Ft-based DDS in chemotherapy, RT, photodynamic therapy (PDT) and nucleic acid-based therapy have been widely investigated.[157] Notably, Fan *et al.* demonstrated the mechanism of human Ft crossing the BBB via the H-chain of Ft, highlighting why H-Ft has been extensively studied in GBM.[161] For instance, Liu *et al.* reported that PTX-loaded H-Ft accumulated in the brain, resulting in higher median survival time (30 days) compared to naked PTX (14 days) *in vivo*.[162]

Ft cages can be further engineered to enhance their targeting abilities.[163, 164] For instance, Huang *et al.* developed integrin α2β1-targeting modified H-Ft loaded with doxorubicin (DOX) and evaluated its tumour targeting abilities in U87MG cells *in vitro*, and orthotopic U87MG tumour progression.[163] In another study, a STING agonist was encapsulated within RGE fusion H-Ft cages, and these NPs showed enhanced targeting ability in G422 and GL261 glioma cells, three-dimensional (3D) glioma spheroids, and a glioma bearing *in vivo* model.[164] As a result, Ft-based NPs have emerged as a highly promising platform for targeted GBM therapies. Among these, apoferritin (AFt) stands out the most extensively studied protein in Ft-based protein NPs.

1.4.2.4 Apoferritin for development of nanoformulations

Apoferritin (AFt, ~480 kDa) is the hollow Ft protein nanocage, consisting of H and L subunits, formed by the chemical removal of iron atoms from Ft (Figure 1.25). AFt has gained attention as a DDS due to its advantageous properties, including biocompatibility, biodegradability, remarkable protein structure, uniform size, and its intrinsic ability to target TfR1.[122]

AFt can be derived from different species including mice, humans, plants, and horse (Figure 1.25). The H and L chain subunits are expressed in different ratios in different species and tissue types. For instance, L subunits are expressed in the liver and spleen while H subunits have expressed in brain and heart.[154] Among different species, horse spleen and human isoforms have been studied in mammalian drug delivery investigations; L chain shows ~83% sequence homology whereas H chain subunit shows ~55% homology.[165]

AFt has a stable protein structure under physiological pH conditions. However, it disassembles into its subunits under extreme acidic or alkaline conditions (pH ≤ 2.0 or pH ≥ 11.0). When the pH returns to neutral, it can spontaneously reassemble into its spherical structure. This unique self-assembly ability makes AFt a highly attractive candidate for drug encapsulation applications, broadly-speaking for targeted cancer therapies, particularly for GBM.[166]

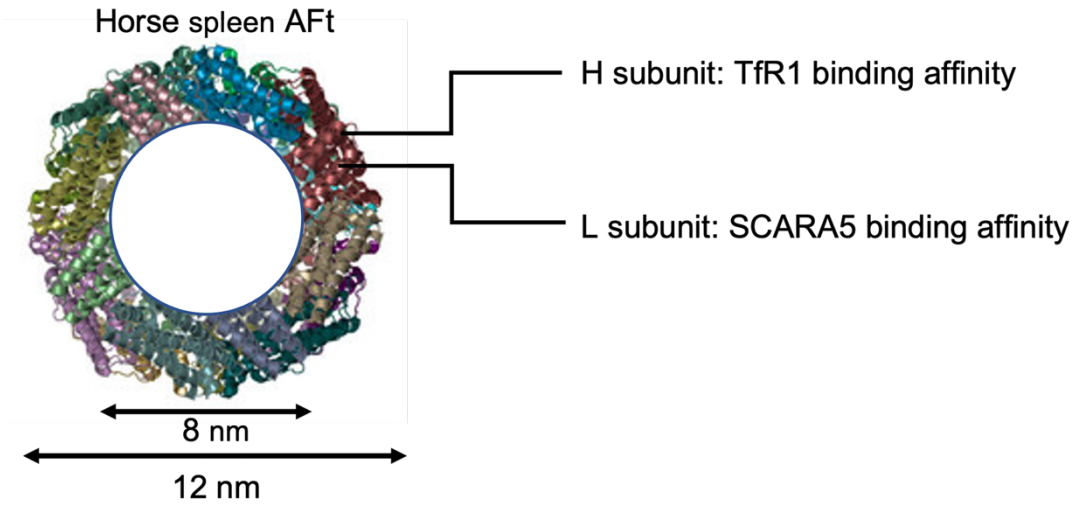

Figure 1.25 Iron-free horse spleen apoferritin (AFt) structure.[167]

AFt nanocages contain 14 channels: 6 hydrophobic (4-fold channels, lined with non-polar amino acids, mainly leucine) and 8 hydrophilic (3-fold channels, lined with polar amino acids), facilitating drug loading into the AFt inner core via the nanoreactor (diffusion) route. In addition, the interior and exterior surface of the AFt cage is negatively charged. Therefore, cations are attracted through the negatively charged 3-fold channels and repelled through the positively charged 4-fold channels. Consequently, both hydrophobic and hydrophilic drugs can be loaded into AFt.[122, 168]

AFt is recognised by several cellular receptors including chemokine (C-X-C motif) receptor 4 (CXCR4), scavenger receptor class A member 5 (SCARA5) and TfR1. However, AFt generally internalises into the cells via TfR1-mediated endocytosis utilising clathrin-coated pits. The H chain of AFt is recognised by, and exhibits strong binding affinity to TfR1, while the L chain tends to bind SCARA5. AFt (and Ft) internalisation is facilitated by the overexpression of TfR1 in cancerous cells, driven by their high iron demand and rapid metabolic turnover.[169, 170] After TfR1-mediated binding of cargo loaded AFt into the cells, the protein cage internalises into a clathrin-coated vesicle. Following vesicle internalisation, it is transported into early endosome (pH 6.5), late endosome (pH 5.5), and then lysosome (pH 4.5) (Figure 1.26). This gradual acidification of the endosome allows for the release of AFt cargo (drug/molecules) due to subunit relaxation and swelling of protein channels.[171]

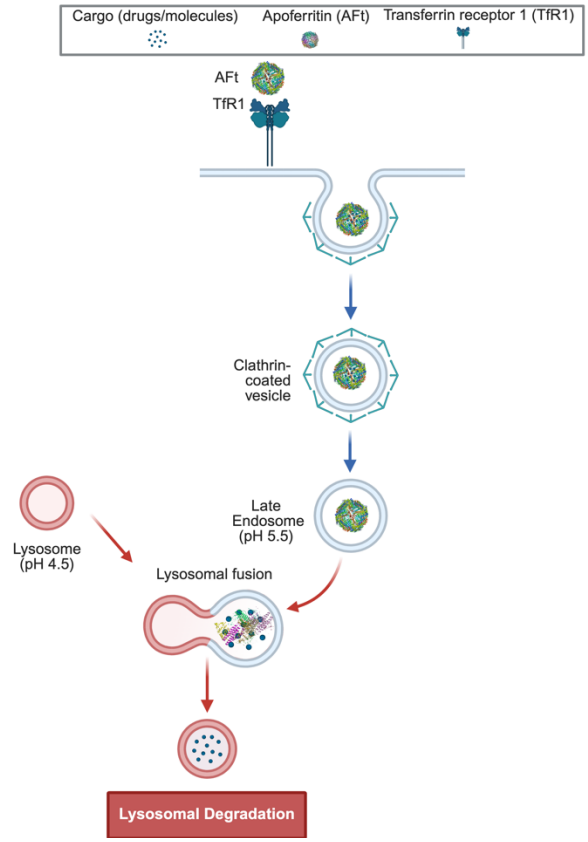

Figure 1.26 Illustration of internalisation of apoferritin (AFt) into the cells via transferrin receptor 1 (TfR1)-mediated endocytosis through clathrin-coated pits. Created with BioRender.

The natural targeting ability of AFt formulations to TfR1 makes them a promising candidate for targeted drug delivery in GBM therapy. In GBM, TfR1 is overexpressed on both tumour cells and BBB endothelial cells[122], facilitating BBB permeation and enhanced uptake of AFt-based NPs. To date, several studies have been carried out to utilise horse spleen AFt as a DDS to improve its bioavailability, cancer selectivity, and enhance the growth inhibitory activity of the encapsulated drugs against GBM. For example, previous studies demonstrated that TMZ, as a small molecule, loaded into horse spleen AFt nanocages via the nanoreactor method, which takes advantage of protein channels for encapsulation, exhibited enhanced activity in U373M and U373V cells, as well as in paediatric glioma cell line models.[83, 172]

In addition to small molecules, larger drug molecules such as DOX can be encapsulated within the AFt cavity using the pH-induced encapsulation method. For instance, Chen *et al.* encapsulated DOX into AFt cages with an encapsulation efficiency of 82%. This AFt

encapsulation enhanced the targeting ability towards GBM cells and tissues in a co-culture model of bEnd.3 mouse brain endothelial cells and C6 rat GBM cells *in vitro* and *in vivo* studies.[173]

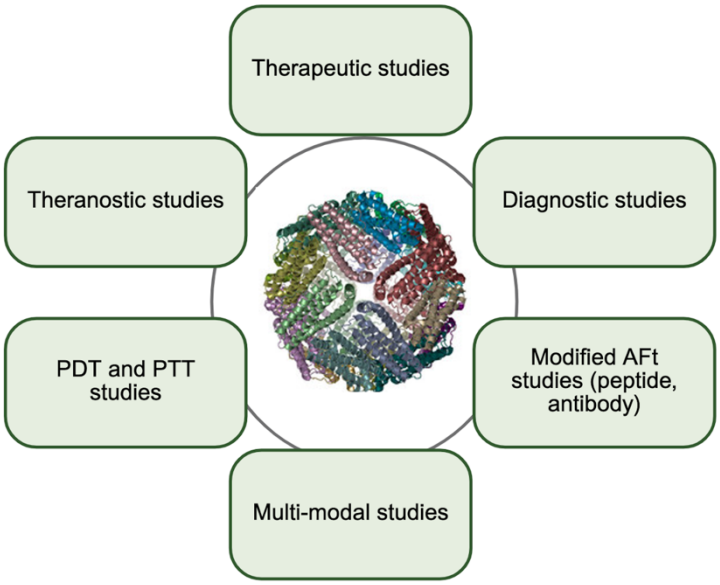

Figure 1.27 The schematic illustration of apoferritin (AFt) applications. Created with BioRender. PDT: photodynamic therapy PTT: photothermal therapy

AFt can be utilised in several applications including diagnostic, therapeutic, theranostic, PDT, and photothermal therapy (PTT) purposes to overcome GBM limitations through targeted therapies (Figure 1.27). To date, the studies have investigated the co-encapsulation of TMZ and copper phenanthroline, as well as the encapsulation of TMZ-DOX conjugates into horse spleen AFt nanocages.[174, 175]

The inner and outer surfaces of AFt nanocages can be modified to enhance targeting abilities and improve drug stability within the cages.[154] For example, Zhai *et al.* modified horse spleen AFt with GKRK-peptide and loaded the cages with VCR, which significantly enhanced anti-tumour effects in both *in vitro* and *in vivo* studies using U87MG cells.[176] Table 1.2 summarises AFt encapsulated agents developed and investigated for GBM. In addition, AFt has been extensively investigated in both unmodified and modified forms as a DDS in other cancer types,

such as breast and colorectal cancer, for single drug encapsulation, combination studies, PTT and PDT applications.[177-179] Altogether, these findings highlight the potential of AFt-based nanocarriers for overcome drug delivery challenges and improve therapeutic outcomes in GBM as well as other cancers.

Table 1.2 A summary of various agents encapsulated or co-encapsulated in unmodified or modified apoferritin (AFt) for effective targeting of glioblastoma (GBM). TMZ: Temozolomide, N3P: N-3-propargyl imidazotetrazonine analog, DOX: Doxorubicin, VCR: Vincristine MTIC: Monomethyl triazene 5-(3-methyltriazen-1-yl)-imidazole-4-carboxamide.

Encapsulation Method	Nanoparticle	Key findings
Nanoreactor	TMZ/ N3P loaded horse spleen AFt[83, 172]	Increased growth inhibitory activity in MGMT-positive (U373M) cells and DIPG glioma spheroids.
Nanoreactor	Cu (phen) and TMZ in horse spleen AFt[174]	Increased TMZ activity in U373M and U373V cells.
Nanoreactor	Copper and TMZ (MTIC) encapsulated in horse spleen AFt[180]	Extended MTIC half-life and enhanced growth inhibitory effect in TMZ-sensitive (U87MG) and TMZ-resistant (T98G) glioma cells.
Nanoreactor	TMZ and DOX conjugate in horse spleen AFt[175]	Encapsulation in presence of copper (II) gluconate (CuGlu) at pH 8.5. Increased the activity in U87MG cells.
pH-induced	DOX loaded horse spleen AFt[173]	Anti-glioma effect in both *in vitro* (bEnd.3 and C6 cells) and *in vivo* (glioma-bearing mice) models.
pH-induced	VCR loaded GKRK peptide modified horse spleen AFt[176]	Higher penetration across *in vitro* co-culture BBB model using bEnd.3 and U87MG cells.

1.4.3 Theranostic approach for glioblastoma

Theranostic devices, which combine various therapeutic (e.g. chemotherapy, PTT) and imaging agents (e.g. MRI, fluorescence) into a single construct, represent strategic tools that allow development of simultaneous cancer diagnosis (imaging) and treatment.[181] Figure 1.28 summarises the theranostic approach, which provides therapy, tumour diagnosis at early stages, therapeutic response-monitoring, and over-dose avoidance; it is highly desirable and plays a crucial role in the management of malignant brain tumours, including GBM.[182]

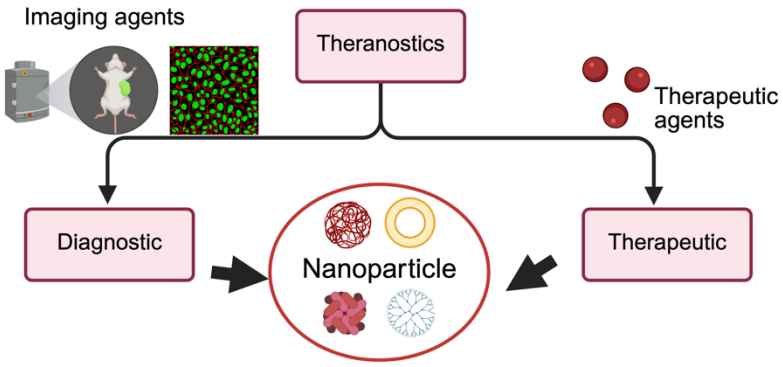

Figure 1.28 A summary of theranostic approach. Created with BioRender.

Multiple fluorescent probes can be used in theranostic systems, which can be broadly categorised as organic, including small-molecule dyes, and inorganic materials such as gold (Au) NPs, Gd-based agents, and inorganic QDs. Organic dyes are commonly encapsulated in nanoparticular systems to enhance their stability, targeting capability, and imaging contrasts for cancer theranostics.[183] However, inorganic probes in the NIR-II region offer advantageous properties such as enhanced imaging resolution, making them promising candidates for theranostics.[99]

In GBM, the deep localisation of tumours and the presence of the BBB limit the theranostic capability; thus, the development of NPs which efficiently across this barrier is critical for theranostic applications. In this context, targeted delivery approaches with functionalisation of NPs or nature`s inherent ability for targeting for theranostic approaches have gained attention.

1.4.4 Recent advances in theranostic nanocarriers

Several types of NPs, including polymeric, lipid-based, and protein-based, are desirable for developing theranostic nanocarriers for cancer, particularly GBM. The combined theranostic approach shows promising results against GBM.[184] Among polymeric and lipid-based NPs,

common theranostic agents include polymeric NPs, magnetic NPs, liposomes, dendrimers, and vesicles.[181]

Multifunctional theranostic platforms integrate active targeting properties with functionalisation of NPs. For GBM theranostics, He *et al.* developed RGD-peptide modified multifunctional dendrimers co-encapsulating DOX and fluorescein isothiocyanate (FI) for targeted theranostics to integrin-overexpressing U87MG cells.[185] In a 2021 study, Polidoro *et al.* utilised peptide (angiopep-2) conjugated hyaluronic acid NPs, integrating targeted delivery and imaging capabilities using Gd-based contrast agent for MRI, to overcome the BBB for GBM therapy (tested on U87 and GS-102 cells).[186] Additionally, Demir *et al.* developed surface-functionalised liposomes using anti-CD44 antibodies co-loaded with curcumin and carbon QDs (particle size: 81.1 ± 16.4 nm), and evaluated their effects in U87MG cells.[187] These results demonstrated enhanced cellular uptake and therapeutic activity, demonstrating the potential of these targeted theranostic liposomes for GBM treatment (Figure 1.29).

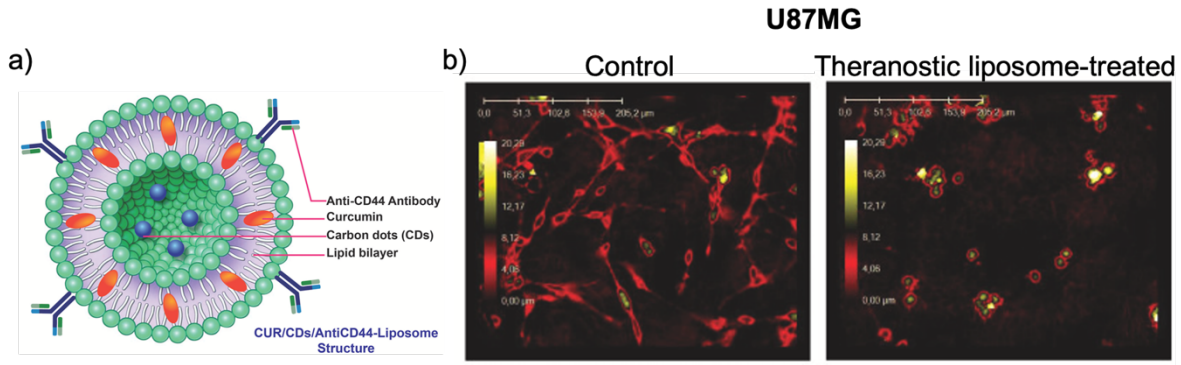

Figure 1.29 Schematic illustration of **(a)** theranostic liposome design co-loaded with curcumin and carbon quantum dots (QDs) for glioblastoma (GBM) treatment. **(b)** Three-dimensional (3D) holographic microscopy results of U87MG cells, comparing control and theranostic formulation treated cells after 24 hours.[187]

In addition to GBM theranostic studies, breast cancer theranostics have been studied; Muthu *et al.* developed a theranostic agent using peptide-modified liposomes co-delivering DOX and CdSe QDs for breast cancer imaging and therapy.[188] However, most cancer theranostic studies published, demonstrate emission within the NIR-I window. Therefore, emerging research in the NIR-II window and multimodal imaging approaches with combination of multiple

treatment methods involve chemotherapy, gene therapy, combined therapies, PDT, and PTT have gained attention in cancer theranostic applications.[189]

NPs can be utilised in cancer theranostics using highly sensitive SWIR probes for improved deep tissue imaging. For example, Song *et al.* employed integrin-specific recognition peptide cyclic RGD-modified PEG-Ag_2S QDs (emission in the NIR-II window, 1100 nm) as both imaging agent and DDS by loading DOX and endothelial inhibitor, an anti-angiogenic agent, (TNP-470). They demonstrated real-time NIR-II fluorescence imaging in U87MG glioma xenografts and achieved enhanced DOX accumulation at tumour tissues due to integrin-targeting ability compared to the untargeted formulation.[190] These findings demonstrate the strong potential of QD-based targeted delivery systems in the NIR-II region for solid tumours, although further studies are required to evaluate their long-term safety and clinical translation.

1.4.5 Protein based nanoparticles in theranostics

Protein based NPs have gained attention in theranostics due to their biocompatibility, biodegradability, and functionalisation. Distinct from other nanocarriers, they can provide benefits such as inherent bioactivity and molecular recognition, biocompatibility, and biodegradation.[191]

Protein NPs can carry both therapeutic drugs and fluorescent agents for *in vivo* tumour imaging applications. For instance, Zayed *et al.* developed a mannose-modified BSA-coated CdSe QD theranostic platform co-encapsulating resveratrol and the hydrophilic cytotoxic agent pemetrexed, demonstrating both fluorescence-based imaging capabilities of breast cancer *in vivo* and tumour reduction.[192] In a GBM theranostic study, angiopep-2 functionalised BSA-coated superparamagnetic iron oxide co-loaded with carmustine and ICG were developed for LDR-mediated targeting of brain tumours.[193] This theranostic platform was evaluated by MRI and *in vivo* fluorescence imaging, demonstrating its potential as a candidate for GBM theranostics.

VLPs have been extensively studied in the theranostics, including PPT and MRI imaging.[194] Qβ-based VLPs were developed the attachment of gold NPs (7 nm) and loading > 500 DOX molecules, demonstrating both cytotoxic macrophages and lung cancer cells *in vitro,* with minimal morphological alterations in the irradiated area.[195] In another study, SPARC-functionalised M13 bacteriophage VLPs were conjugated with DOX and a fluorescent dye to assess their theranostic abilities in prostate cancer cell lines.[196]

The unique structure of Ft NPs can integrate drug delivery, MRI, optical (SWIR) imaging into a single nanoplatform, making it promising candidate for cancer theranostics. For example, Veroniaina *et al.* co-encapsulated within recombinant human H-Ft manganese dioxide (MnO_2) and DOX, demonstrating their MRI signalling ability and growth inhibitory activity in cervical, ovarian, and breast cancer cells.[197] In another study, Nasrollahi *et al.* encapsulated graphene oxide QDs, iron and DOX into Ft protein cages to develop multifunctional platforms for imaging and drug delivery.[198] The natural imaging ability of L-Ft derived from human Ft carrying 1000 Fe atoms was evaluated in breast cancer cells for generation of negative contrast for MRI.[199] Moreover, drug loaded magnetoferritin NPs have been used as theranostic platforms for MRI.[191]

1.4.5.1 Apoferritin as a theranostic tool

The unique hollow structure, self-assembling capability, biocompatibility, and TfR1-mediated targeting properties of AFt nanocages make them attractive candidates for multifunctional medical applications. In addition to their role as drug delivery carriers, AFt nanocages have been further exploited in bioimaging and theranostic applications.[169] Particularly, AFt- based theranostic platforms offer several advantages, including real-time monitoring of pharmacokinetics and biodistribution, visualisation of drug release, tracking of nanoformulations' accumulation at the target site, and assessment of therapeutic efficiency.[200] These properties make AFt a promising candidate for protein-based theranostics, capable of

integrating imaging, targeted delivery, and pH-dependent drug release within a single construct.

Recent studies have explored theranostic strategies using AFt nanocages for the encapsulation of organic dyes, QDs emitting in both NIR-I and NIR-II regions, as well as agents for PDT and PTT.[200-202] For instance, Cutrin *et al.* encapsulated drug molecules and imaging agents together into AFt nanocages for the first-time using curcumin and MRI contrast agent (Gd-HPDO3A) to target hepatocytes via SCARA5.[200]

In another study, folic acid-functionalised AFt nanocages co-encapsulated with PTX and IR1061 (NIR-II organic dye) were employed for PTT in the 4T1 breast cancer model.[201] AFt nanocages co-loaded with DOX and NIR fluorescent dye were evaluated in colorectal cancer cells for PTT.[202] In the study, under acidic conditions, AFt cages disassembled, releasing DOX to kill the cancer cells, while the fluorophore enabled real-time tracking of the NPs. Altogether, these studies demonstrated that combination of drug and imaging agent in AFt nanocages improves therapeutic effects as well as providing monitoring capabilities.

Despite recent developments in theranostic applications of AFt nanocages, most research has focused on organic dyes, or QDs emitting in NIR-I region. However, the limited research that uses NIR-II QDs in AFt-based platforms presents a gap in the field. Therefore, it is necessary to investigate and optimise NIR-II emitting QDs in AFt nanocages to use their beneficial properties for theranostic applications in difficult to treat tumours such as GBM.

1.4.5.2 Future perspectives on protein-based nanoparticles in glioblastoma

According to preclinical data, various NPs including polymeric, lipid-based, and protein-based, have been engineered for GBM therapy, by surface functionalisation. Among them, protein

NPs offer significant advantages in preclinical GBM applications, combining intrinsic biocompatibility with the capability for targeted tumour accumulation and BBB penetration, and theranostic applications. Considering GBM tumour heterogeneity and the challenge associated with crossing the BBB, these advanced NPs play a crucial role in improving therapeutic outcomes for GBM patients. In the future diagnostic, therapeutic, and theranostic approaches, integrating nanocarrier systems with patients' genetic and molecular profiles will enhance personalised medicine.[203]

In the future, next generation protein-based theranostics will combine deep tissue SWIR imaging, FGS, and artificial intelligence (AI) driven image analysis to provide real-time guidance and personalised medicine. Multifunctionality in brain science such as co-delivery of chemotherapeutics, immunotherapeutics, and gene therapy within protein-based NPs such as Ft and VLPs will enable disruption of multiple oncogenic pathways to thwart tumour growth and survival, and overcome resistance mechanisms, enhancing brain tumour management.[192]

Protein-based NPs hold promise for future precision-guided, multimodal GBM therapy. Among protein-based NPs, Ft nanocages have shown potential as a DDS for disease prognosis, prevention, therapy, and vaccine development. However, translating these advanced NPs into the clinic will require batch-to-batch consistency (size, functionality etc.), comprehensive immunogenicity assessments to ensure clearance pathways and minimal off-target effects during sequential dosing.[204]

1.5 Overall hypothesis

We hypothesise that a dual functional theranostic nanoplatform based on AFt nanocages will enable enhanced TMZ delivery, dose reduction, and the potential to overcome TMZ resistance through a natural protein-based delivery system. In addition, it will allow real-time monitoring of GBM by utilising the PL properties of PbS QDs for nanoparticle tracking in 2D, 3D, *ex vivo*, and *in vivo* tumour models. By enabling targeted co-delivery, the AFt based nanoplatform will

improve the therapeutic outcomes in GBM cultures while providing a protective effect for non-cancerous cultures and enabling deep tissue imaging of treatment response via SWIR imaging across *in vitro*, *ex vivo*, and *in vivo* models.

1.6 Project aims and objectives

The overall aim of this PhD project was to develop a novel theranostic formulation for the treatment and monitoring of GBM, one of the most aggressive and lethal brain tumours. This was achieved by integrating diagnostic (imaging) and therapeutic functions into a single protein-based NP system. In this project, horse spleen AFt was employed as a nanocarrier to co-deliver TMZ, a chemotherapeutic drug used for GBM, and PbS QDs, an imaging probe, to GBM cells. This targeted delivery system aimed to reduce off-target effects, overcome potential TMZ resistance mechanisms, and improve GBM management through enhanced therapeutic effect and real-time imaging capability.

To achieve this aim, the project includes the following specific objectives:

- To develop an encapsulation strategy to produce dual-functionalised theranostic nanoplatform by co-encapsulating TMZ and PbS QDs within horse spleen AFt nanocages, utilising the disassembly/reassembly method for PbS QD encapsulation and nanoreactor route for TMZ encapsulation. The results are presented and discussed in Chapter 3.
- To establish the potential of theranostic nanoplatforms by evaluating the cell viability and cancer cell selectivity of AFt formulations in both GBM cell lines and non-cancerous cells. The results are presented and discussed in Chapter 4.
- To evaluate the targeting capability of AFt-based nanoplatforms in different cell lines, depending on the expression profiles of targeting receptor TfR1, and MGMT as a

marker of TMZ resistance, in MGMT-positive GBM cells (U373M cells). The corresponding results are presented and discussed in Chapter 4.

- To investigate the activity of AFt encapsulation compared to naked agents in 3D *in vitro* models (GBM spheroid models) and to probe their long-term (repeated) treatment effects as a mean to facilitate their translation into *in vivo* and preclinical studies. The results are presented and discussed in Chapter 5.
- To assess the imaging performance of PbS QD-containing formulations in depth tumours, such as GBM, by conducting *in vitro* SWIR imaging studies on both two-dimensional (2D) monolayer and 3D spheroid GBM models, as well as on healthy brain tissue samples. The results are presented and discussed in Chapter 6.

Chapter 2 Materials and Methods

2.1 Materials

Materials and equipment used in this work are summarised in the Tables 2.1 – 2.5. All materials were used as received without any further purification. All used equipment was maintained and calibrated as specified by the manufacturer.

Table 2.1 List of equipment and instruments used in the studies.

Materials	Supplier
Brightfield cell counter	DeNovix
C-DiGit blot scanner	LI-Cor Biosciences
Centrifuge 5810 R	Eppendorf
CO_2 incubator	Sayro
Electrophoresis system	Bio-Rad
High resolution transmission electron microscopy (HR-TEM)	JEOL 2100EF
Inverted light microscope	Nikon Eclipse T100 / OLYMPUS CKX53
pH-meter	Mettler Toledo
Plate-reader	Perkin Elmer Envision 2104 Multilabel Reader
Trans-Blot Turbo Transfer System	Bio-Rad
UV-vis spectrophotometer	Agilent Technologies
Zetasizer Nano ZS	Malvern Panalytical
Flow cytometry	Beckman Coulter FC500
SWIR imaging systems	Photon etc.

Consumables used in the research described, together with their suppliers are listed in Table 2.2.

Table 2.2 List of consumables used in the studies.

Materials	Supplier
0.22 µm syringe filter	Sartorius
10-well comb	Novex by life technologies
96-well microplate	Thermo Scientific™
96-Well U-Shaped-Bottom Microplate	Thermo Scientific™
Amersham Protran 0.45 µm nitrocellulose western blotting membrane	GE Healthcare Life Sciences
Amicon ultra- centrifugal filter molecular weight cut-off (MWCO; 30kDa)	Merck Millipore
Folded capillary cell (DTS1070)	Malvern Panalytical
Gel cassette 1.5 mm (NC2015)	Novex by life technologies
Slide-A-Lyzer™ MINI Dialysis Devices, 10K MWCO	Thermo Scientific™
Spectra/Por molecularporous membrane tubing MWCO:12-14 kDa	Spectrum Labs
T25/T75 cm^2 flasks	Corning

Whatman ready to use filter paper	Cytiva

All chemicals, and respective suppliers, used during this research are listed in Table 2.3.

Table 2.3 List of chemicals used in the studies.

Materials	Supplier
1-thioglycerol (TGL)	Sigma-Aldrich
10x trypsin-EDTA solution	Sigma-Aldrich
4% paraformaldehyde solution	Thermo Scientific™
Acrylamide/bis-acrylamide 30% solution	Sigma-Aldrich
Amersham ECL detection reagents	Cytiva
Ammonium persulfate (APS)	Sigma-Aldrich
Astrocyte complete medium	ScienceCell Research Laboratories
Bovine collagen type 1 (C9791)	Sigma-Aldrich
Bradford reagent	Sigma-Aldrich
Bronchial Epithelial Cell Growth Medium (BEGM™) Bulletkit	Lonza
Dithioglycerol (DTG)	Sigma-Aldrich
DMSO	Sigma-Aldrich
Foetal bovine serum (FBS)	Sigma-Aldrich
Fibronectin human plasma (F0895)	Sigma-Aldrich
G418	Corning
Gelcode™ BlueSafe protein stain	Thermo Scientific™
Gentamicin	Sigma-Aldrich
Glycerol	Fisher bioreagents
Glycine	Fisher bioreagents
HEPES	Merck
Horse spleen Ft	Sigma-Aldrich
L-glutamine solution	Sigma-Aldrich
Lead acetate. trihydrate ($Pb(Ac)_2.3H_2O$)	Sigma-Aldrich
MEM Non-essential amino acids (NEAA)	Gibco
Minimum essential medium (MEM)	Sigma-Aldrich
MTT reagent	Merck
N,N,N′,N′-Tetramethyl ethylenediamine (TEMED)	Merck
Non-fat dried milk	Sainsbury
Nonidet P-40 (NP-40)	Sigma-Aldrich
PageRuler™ Plus Prestained Protein Ladder, 10 to 250 kDa	Thermo Scientific™
Penicillin-streptomycin	Sigma-Aldrich
Phosphatase inhibitor cocktail tablets (cOmplete ULTRA Tablets- Mini, EDTA-free, EASYpack)	Roche
Poly-L-lysine	ScienceCell Research Laboratories
PrestoBlue cell viability reagent	Invitrogen
Protease inhibitor cocktail tablets (cOmplete ULTRA Tablets- Mini, EDTA-free, EASYpack)	Roche
Roswell Park Memorial Institute 1640 (RPMI-1640) medium	Sigma-Aldrich
Sodium acetate (NaOAc)	Fisher chemical
Sodium chloride (NaCl)	Fisher chemical
Sodium dodecyl sulfate (SDS)	Thermo Scientific™
Sodium sulfide (Na_2S)	Sigma-Aldrich
Sterile bovine serum albumin (BSA)	Merck
Sterile dimethyl sulfoxide (DMSO)	Honeywell
Sterile filtered HEPES buffer solution	Sigma-Aldrich
TMZ	Sigma-Aldrich
Tris	Thermo Scientific™
β-mercaptoethanol	Sigma

The cell lines used in studies described within this thesis, together with their source are listed in Table 2.4.

Table 2.4 List of the suppliers of used cell lines.

Cells	Supplier
U373M	Gifted by Schering Plough Corporation
U373V	Gifted by Schering Plough Corporation
U87MG	Purchased from American Type Culture Collection (ATCC)
MRC-5	Purchased from ATCC
THLE-2	Purchased from ATCC
Astrocytes	Purchased from ScienCell Research Laboratories

Antibodies used in protein detection, and their suppliers are listed in Table 2.5.

Table 2.5 The list of antibodies used in the studies.

Antibody	Supplier
1° Ab: Anti-human TfR1 monoclonal antibody	ThermoFisher (CAT:136800)
1° Ab: Anti-human MGMT monoclonal antibody	Invitrogen (MA3-16537)
1° Ab: Anti-human GAPDH monoclonal antibody	Sigma-Aldrich (CAT: G8795)
2° Ab: Goat anti-mouse IgG (H+L) superclonal secondary antibody	ThermoFisher (CAT: A28177)
2° Ab: Goat anti-mouse IgG (H+L) cross-adsorbed secondary antibody, Alexa Fluor™ 488	ThermoFisher (CAT: A11001)

2.2 Isolation and preparation of apoferritin from horse spleen ferritin

Horse spleen AFt was generated from horse spleen Ft (Sigma Aldrich, Batch number: SLBZ5776; protein purity ≥ 90%) via reductive demineralisation.[205] First, 0.1 M sodium acetate (NaOAc) buffer (pH 5.5) was used to dilute the Ft concentration to 5.5 mg/mL. The solution was then filled to 30 mL with NaOAc buffer. After that, 0.1 M NaOAc (16.4 g NaOAc dissolved in 2 L) was prepared, and acetic acid (1.5 mL) was added to reduce the pH to 5.5. After being transferred into a dialysis bag, the diluted Ft (dark brown, 5.5 mg/mL) solution was placed in 0.1 M NaOAc buffer (2 L, pH 5.5) at room temperature (RT) with stirring at 300 rpm under a N_2 flow. Thereafter, 3 mL of mercaptoacetic acid was gradually (2 mL of mercaptoacetic acid was added for 2 hours (h) then 1 mL of it for additional 1 h) added to the NaOAc buffer and the sample was dialysed for a 3 h period. These rounds were performed 6 times, each time with freshly made buffer solution and a different dialysis bag rotation. Following the final process,

the protein was dialysed against fresh NaOAc buffer (0.1 M, pH 5.5) without acid for 1 h. The AFt solution was collected from the dialysis bag and filtered using a 0.22 µm syringe filter. Finally, AFt was aliquoted into 1 mL microcentrifuge tubes and stored at -20 °C. The protein concentration of AFt was measured using the Bradford assay (see Section 2.6.1).

2.3 Synthesis of lead sulfide quantum dots and their encapsulation within apoferritin nanocages

PbS QDs were produced using the published method by Hennequin *et al.*[206] Pb^{2+} precursor solution was prepared by dissolving lead acetate in deionised water (0.016 M $Pb(AcO)_2.3H_2O$ solution,30 mL) in a two-necked flask purged with N_2 flow and stirred (Table 2.6). Then, 0.1 mL dithioglycerol (DTG) and 0.26 mL 1-thioglycerol (TGL) were added to the Pb^{2+} solution. DTG and TGL were used as capping agents. The pH of the Pb^{+2} solution was adjusted to 11 by adding triethylamine dropwise. Sodium sulfide (Na_2S) solution (0.1 M, 5 mL) was prepared. Following that, 10.6 mL of Pb^{2+} solution was transferred into a 50 mL flask using a needle, and 0.5 mL of Na_2S solution was added to the Pb^{2+} solution with magnetic stirring at 900 rpm (the molar ratio of Pb:S is 1:0.3). The mixture colour turned dark brown within a few minutes (~2 min) after addition of S^{2-} precursor. The QD solution was stirred under N_2 flow for about 10 min to allow for the growth of QDs, then was transferred into a glass vial washed with N_2. The PbS QDs solutions were stored at 4 °C for further studies.

Table 2.6 Composition of precursor solution.

Volume of initial Pb^{+2} solution	$Pb(Ac)_2.3H_2O$	DTG	TGL
30 mL	0.182 g, 0.00048 mol	0.1 mL, 0.001 mol	0.26 mL, 0.003 mol

A pH-dependent disassembly/reassembly method was used to encapsulate a PbS QD in the AFt nanocage. 1 mL AFt solution was diluted in 0.1 M NaOAc buffer (pH 5.5 adjusted with glacial acetic acid) to a final concentration of 3 mg/mL as determined by Bradford assay. 1mL

of AFt solution was transferred to a dialysis tubing (MWCO:12-14 kDa, Spectrum Labs) and dialysed against 0.1 M NaOAc buffer (pH 5.5) for 1 h before transferring into the NaCl buffer at pH 2 (and stirred for 15 min at 4 °C to facilitate AFt cage disassembly into subunits at the acidic pH.

A vial was purged with N_2 flow, and 1 mL of PbS QDs solution (5 mg/mL) was added using a syringe/needle. Then disassembled AFt solution (AFt to PbS ratio of 1:1 volume/volume (v/v)) was introduced dropwise into the PbS QDs solution under rapid mixing settings and left for 10 min. The solution of PbS QD encapsulated in AFt nanocage was dialysed against 20 mM HEPES buffer (pH 7.4, 2 L) for 2 days at 4 °C and then stored at 4 °C or at -80 °C for future assessment.

2.4 Temozolomide encapsulation within apoferritin nanocages

The nanoreactor method was employed to encapsulate TMZ into AFt since the small size (molecular weight (MW) 194.15 g/mol) of the TMZ molecule is suitable for diffusion across AFt channels (~0.3-0.4 nm in diameter). Firstly, TMZ solution (10 mM, 7.2 µmol) was prepared in DMSO dissolving it on a tube roller; all procedures were carried out in a fume cupboard with appropriate personal protective equipment. The AFt:TMZ molar ratio was set to 1:800, indicating that one mole of AFt nanocages was incubated with 800 moles of TMZ. This molar ratio was chosen based on the previous study with AFt-TMZ[83], which reported efficient TMZ loading into AFt. The AFt solution concentration was determined to be 2 mg/mL by Bradford assay, and 800 µL of AFt was diluted with 0.1 M NaOAc buffer (1.2 mL) to make a total of 2 mL. For encapsulation, 139 µL TMZ was added into the AFt solution (2 mg/mL, 2 mL) under stirring at 4 °C every 30 min to prevent TMZ precipitation (5-times; total 696 µL). Then, to remove unencapsulated TMZ molecules, AFt-TMZ solution was spun using an Amicon centrifugal filter (30 kDa Molecular weight cut-off (MWCO), Merck Millipore, USA) at 4000 *g*, 4

min. Finally, AFt-TMZ was filtered through a 0.22 μm syringe filter and was stored at 4 °C and -80 °C for stability studies.

2.5 Co-encapsulation of lead sulfide quantum dots and temozolomide within apoferritin nanocages

To produce a co-encapsulated formulation, initially PbS QDs were encapsulated inside AFt cages using a pH-dependent disassembly/reassembly method, as described in Chapter 2.2. TMZ (10 mM, 7.2 μmol) was added dropwise in the AFt-PbS solution (2 mL) every 30 min under stirring at 4 °C for encapsulation by diffusion method. The AFt:TMZ molar ratio was chosen at 1:400 as part of the cavity is filled with the QD. To remove unencapsulated TMZ molecules, the resulting solution (AFt-PbS-TMZ) was centrifuged (4000 *g*, 4 min) on an Amicon ultra 4 mL centrifuge filter (30 kDa MWCO), Merck Millipore, USA) and filtered through a 0.22 μm syringe filter. The resulting co-encapsulated formulation, AFt-PbS-TMZ, was stored at 4 °C or at -80 °C for stability studies under N_2 atmosphere.

2.6 Characterisation of formulations

2.6.1 Protein quantification via Bradford assay

The Bradford assay was employed for protein quantification of the samples (AFt formulations and cell lysates).[207] A series of BSA solutions of known concentrations were prepared to generate a standard curve. Initially, 0.01 g BSA was weighed and subsequently dissolved in 1 mL water to prepare a 10 mg/mL BSA solution. Serial dilutions of BSA (1, 2, 4, 6, 8, 10 mg/mL) were prepared in microcentrifuge tubes. From each dilution, 10 μL of sample was extracted and added to 90 μL of distilled water in a 96-well plate; this process diluted the BSA solutions' concentrations by a factor of 10. 10 μL of the 10-times diluted BSA solutions were transferred

into wells (in triplicate), and 140 µL Bradford reagent was subsequently added (final volume of 150 µL per well). The plate was incubated under dark and shaking conditions for 5 min. Then, absorbance was measured at 595 nm using a PerkinElmer Envision plate reader. Subsequently, the mean of each measurement was calculated, and a calibration curve plotted; $R^2 > 0.99$ accuracy was accepted. Unknown protein concentrations were determined using the Equation (2.1):

$$y = mx + c \quad (2.1)$$

In the Equation 2.1, *y* represents the measured absorbance value, while *x* represents the concentration of the unknown sample being determined.

2.6.2 Ultraviolet - visible spectroscopy analysis

Ultraviolet - visible (UV-vis) spectroscopy was utilised to generate a TMZ standard curve for the dependence of absorption intensity on TMZ concentration. TMZ solutions were prepared by diluting 10 mM TMZ in DMSO stock solution with NaOAc buffer (0.1 M, pH 5.5) and DMSO mixture (1:9 v/v) to final concentrations in the range 5-200 µM; TMZ absorption peak is at λ = 330 nm with a molar extinction coefficient of 9800 M^{-1} cm^{-1}. The TMZ solutions were placed into a quartz cuvette and the absorbance was measured on a Varian Cary 50 UV-vis spectrophotometer. The measured absorbance values were used to produce standard curve ($R^2 > 0.99$), which were used and to estimate TMZ concentration in encapsulated formulations (AFt-TMZ and AFt-PbS-TMZ). To assess the amount of TMZ in the AFt-TMZ solution, it was diluted 1:100 with DMSO. However, to determine the quantity of TMZ in AFt-PbS-TMZ solution, the remaining whole solution in the centrifugal filter was used without dilution. The dilution factor was considered during these calculations to ensure the accuracy of the TMZ quantification.

2.6.3 Assessment of drug loading, encapsulation efficiency and protein yield

The percentages of drug loading (DL), encapsulation efficiency (EE), and protein yield (PY) were estimated using the following equations (2.2-2.6), with the UV-vis method employed for their evaluation. In addition, drug:AFt ratio was also determined. Comparison of TMZ encapsulation in AFt and AFt-PbS cages was made. All results are reported as the mean ± standard deviation (SD) (*n* = 6).

$$Drug{:}\,AFt\ = \frac{Final\ moles\ of\ drug\ in\ the\ solution}{Final\ moles\ of\ AFt\ in\ the\ solution} \times 100\% \quad (2.2)$$

$$DL\% = \frac{Number\ of\ encapsulated\ drug\ x\ drug\ MW}{(Number\ of\ encapsulated\ drug\ x\ drug\ MW) + AFt\ MW} \times 100\% \quad (2.3)$$

$$EE\ \% = \frac{Final\ amount\ of\ drug\ (moles)}{Initial\ amount\ of\ drug\ (moles)} \times 100\% \quad (2.4)$$

$$Indirect\ EE\ \% = \frac{Initial\ amount\ of\ drug\ (moles) - Free\ drug\ (moles)}{Initial\ amount\ of\ drug\ (moles)} \times 100\% \quad (2.5)$$

$$PY\% = \frac{Final\ moles\ of\ protein}{Initial\ moles\ of\ protein} \times 100\% \quad (2.6)$$

2.6.4 High resolution transmission electron microscopy analysis for structural visualisation

High resolution transmission electron microscopy (HR-TEM) analysis was utilised to investigate the morphology of PbS QDs (0.5 mg/mL), AFt-PbS, and AFt-PbS-TMZ (protein concentration is 0.5 mg/mL) samples. Uranyl acetate was utilised as a negative stain for AFt samples. PbS QDs were diluted in deionised water, whereas AFt samples were diluted in 0.1

M NaOAc buffer. The AFt samples (3 µL) were deposited on a carbon-coated copper graphene oxide grid and permitted to dry for 3 min. Then, 3 µL of uranyl acetate was added and dried for 3 min and waited for an extra 1 min. The samples were vacuum-dried before being analysed with a JEOL 2100EF TEM microscope at 200 kV. The images obtained were analysed using the ImageJ software to determine the size of nanoparticles.

2.6.5 Protein integrity analysis via non-denaturing polyacrylamide gel electrophoresis

The samples were analysed using non-denaturing polyacrylamide gel electrophoresis (native-PAGE), which does not involve the denaturation of the protein structure. Therefore, sodium dodecyl sulphate (SDS) is not used in this method. Protein integrity had been checked using native-PAGE after the AFt encapsulation process using disassembly/reassembly and/or diffusion techniques. Horse spleen Ft and AFt stocks were used as controls. Table 2.7 demonstrates the required ingredient solutions including Milli Q water, 30% acrylamide, 1.5 M Tris (pH 8.8), and 10% ammonium persulfate (APS), *N,N,N′,N′*-tetramethylethylenediamine (TEMED). Gradient stock solutions (4%, 6%, 8%, 10%, 12%, and 15%) were prepared as 5 mL for each (see Table 2.8). A sample (1.75 mL) of each solution was transferred cassettes, starting with the highest concentration (15%) and decreasing to the lowest concentration (4%) and allowed to dry for 30-45 min. Bis-Tris pre-cast gels (4-16%) were packed with wet tissue prepared at least one day before analysis and kept at 4°C. For each sample, a pre-labelled microcentrifuge tube was prepared containing 15 µL of the sample and 5 µL of native-PAGE loading buffer (4x, Table 2.8). The mixture (18 µL) was transferred into pre-prepared native-PAGE gels and placed in an XCell SureLock Mini-Cell (Invitrogen). Native-PAGE buffer (1x) was used to fill inner chambers of wells and ¼ of the outside chamber. Then, the gel was run at 150 V for 1 h then 250 V for 1 h. After running, it was stained with BlueSafe protein stain (Thermo Scientific) for 1 h and rinsed with deionised water before gel imaging.

Table 2.7 Gradient gel recipes used for Native-PAGE analysis.

	Volumes (mL)				
Gel concentration	**Milli Q water**	**30% Acrylamide**	**1.5 M Tris pH 8.8**	**10% APS**	**TEMED**
4% (5 mL)	3.03	0.666	1.3	0.05	0.005
6% (5 mL)	2.7	1	1.3	0.05	0.005
8% (5 mL)	2.3	1.3	1.3	0.05	0.005
10% (5 mL)	1.9	1.7	1.3	0.05	0.005
12% (5 mL)	1.6	2	1.3	0.05	0.005
15% (5 mL)	1.1	2.5	1.3	0.05	0.005

Table 2.8 Native-PAGE buffer and loading buffer recipes.

4x Native-PAGE loading buffer	**10x Native-PAGE buffer**
500 µL β-mercaptoethanol	150 g glycine
2.4 mL 1 M Tris (pH 6.8)	30 g Tris
3.1 mL dH_2O	1 L dH_2O
4 mg bromophenol blue	
4 mL glycerol	

2.6.6 Size and zeta potential measurements by Dynamic Light Scattering

The average hydrodynamic size, zeta potential, and polydispersity index (PDI) of the particles were determined using the DLS method. The temperature was set at 20 °C for PbS QDs and 25 °C for protein (AFt) samples, respectively. PbS QDs were diluted in deionised water with triethylamine at pH 11 to 0.02 mg/mL, whereas the stock AFt solution (0.05 mg/mL) and AFt samples (0.5 mg/mL) were diluted with 0.1 M NaOAc buffer. After diluting, the samples were filtered using a 0.22 µm syringe filter to eliminate dust and any aggregates. The measurements were performed on a Malvern Zetasizer Nano ZS (scattering angle 173 °C) with three independent repeats and 13 runs per measurement. DTS1070 (Malvern Panalytical) cell was used for zeta potential measurements. Origin and GraphPad Prism software were used to analyse the data.

2.6.7 Stability assessment of formulations using Dynamic Light Scattering

The stability of formulations was assessed by measuring the size and zeta potential of AFt samples (AFt-PbS, AFt-TMZ, and AFt-PbS-TMZ) after one month of storage at T = - 80 °C. Freshly synthesized AFt samples were prepared using their optimised method (Chapters 2.3, 2.4, and 2.5) and stored at T = -80 °C for one month. Following that, the samples were thawed at T = 4 °C. The DLS results obtained (referred to as ‘’1 month’’) were compared to the size and zeta potential measurements of freshly prepared AFt solutions stored at T = 4 °C (referred to as ‘’fresh’’).

2.6.8 Photoluminescence spectroscopy

For photoluminescence spectroscopy, PbS QD-containing samples were dropcast onto glass slide (~ 3 drops) and allowed to dry. The Horyba LabRam system equipped with an InGaAs detector, and a He-Ne laser (λ = 633 nm) was used to record photoluminescence spectra.

PL measurements were also recorded in for serial dilutions (diluted in deionised water with triethylamine at pH 11 to final PbS QD concentrations in the range from 5 mg/mL to 0.25 mg/mL). The solutions were placed into a syringe (1mL, Sartorius) The data were analysed using Origin software.

2.6.9 Short-wave infrared imaging of quantum dots in gel samples

An IR VIVO SynIRgy (Photon etc, Montreal, Canada) imaging system was utilised to assess the imaging capabilities of PbS QDs at National Research Council Canada, Ottawa. SWIR imaging was carried out with a 785 nm laser at 20% power, 850 nm long-pass (LP) emission filter, and a camera exposure time of 3 ms or 1 s. Gel samples containing PbS QDs and AFt-PbS were prepared using a 10% native-PAGE gel. To develop gel samples, sandwich and mix

models were utilised. For the sandwich model, the gel layer (50 µL) was added to a plastic container (diameter ~5 mm), and allowed to dry, followed by a layer of dried PbS QDs (100 µL) before topping with the gel (50 µL). In contrast, mixed samples were prepared without waiting for the bottom gel to dry. The gel samples containing PbS QDs were analysed with SWIR imaging.

2.6.10 *In vitro* drug release studies

In vitro drug release studies on AFt formulations (AFt-TMZ and AFt-PbS-TMZ) were carried out for comparison. Initially, the solutions (n = 4, 400 µL) were placed on a Slide A-Lyzer MINI Dialysis Device (ThermoScientific) and dialyzed at 37 °C under mixing settings at 150 rpm against 0.1 M NaOAc buffer (pH 5.5) or PBS (pH 7.4). UV-vis spectroscopy was used to monitor TMZ leakage and conversion to its degradation product, AIC, in AFt-TMZ and AFt-PbS-TMZ samples after 1 h, 3 h, 5 h, 7 h, 24 h, and 48 h of dialysis (λ = 330 nm for TMZ and λ = 265 nm for AIC). The TMZ release quantity was calculated using the standard curve equation. The percentage of drug release (DR%) was calculated for each time point using Equation 2.7. The cumulative drug release profiles for AFt-TMZ and AFt-PbS-TMZ were plotted using GraphPad Prism.

$$DR\ \% = \frac{Amount\ of\ drug\ release\ (moles)}{Initial\ amount\ of\ drug\ (moles)} \times 100\% \qquad (2.7)$$

2.7 Cell culture studies

2.7.1 Cell stock revival and resuscitation

Frozen cells (stored in liquid nitrogen at -196 °C) were revitalized for cell culture studies. The vial (1 mL) was placed in a pre-heated 37 °C water bath and rotated until cells had thawed

completely. The vial was wiped with 70% IMS and placed within the sterile hood before being transferred to T25 flasks containing pre-heated complete media containing 10% foetal bovine serum (FBS) (6 mL complete medium/ a T25 flask). To allow for cell attachment, the flasks were incubated overnight at 37 °C in a humidified atmosphere containing 5% CO_2. The following day, the cell medium was replaced with fresh complete medium to remove any dead cells and eliminate potential adverse DMSO effects. Cell morphology and attachment to flask surface were checked under an inverted light microscope (Nikon Eclipse T100 / OLYMPUS CKX53). After the cells reached 70-80% confluence, the medium was replaced with fresh complete medium containing 10% FBS.

2.7.2 Cell line cultivation and maintenance

Cell culture studies were conducted using GBM and non-tumourogenic cell lines. In the study, U373M, U373V, U87MG cells were used as GBM cell line models expressing different levels of MGMT while the foetal lung fibroblast line MRC-5, human astrocytes (frontal lobe), and THLE-2 (liver) cells were used as healthy, non-tumourigenic cells. Complete media were prepared for each cell line (summarised in Table 2.9). U373M and U373V cells were cultured in RPMI 1640 medium supplemented with 10% FBS, 1% v/v non-essential amino acids (NEAA), 50 µg/mL gentamicin, and 400 µg/mL G418 (Corning). U87MG cells were cultured in minimum essential media (MEM) supplemented with 10% FBS and 1% L-glutamine, while MRC-5 cells were cultured in MEM with 10% FBS, 1% v/v NEAA, 1% v/v penicillin/streptomycin, 2 mM L-glutamine, 10 mM HEPES buffer. Human astrocytes were cultured in poly-L-lysine-coated (ScienceCell™, 10 mg/mL, CAT: 0413) T75 flasks to promote cell attachment and incubated at 37 °C overnight. The astrocytes were maintained in complete astrocyte medium (ScienceCell ™, CAT: 1801), and passaged using trypsin/EDTA (T/E) solution 0.05% (ScienceCell™, CAT: 0183) and T/E neutralisation solution (TNS, ScienceCell™, CAT:0113) according to manufacturers' recommendations. Human astrocytes

were used up to passage number 10. In addition, THLE-2 cells were used as a hepatocyte cell line and cultured in pre-coated flasks with bovine collagen type 1 (0.03 mg/mL), fibronectin (0.01 mg/mL), 10% BSA solution (0.01 mg/mL) in bronchial epithelial cell growth medium (BEGM, 6 mL). Pre-coated flasks for human astrocytes and THLE-2 cells were incubated in 5% CO_2 at 37 °C for overnight.

Most cell lines were maintained in T25 or T75 flasks according to conventional protocols as follows: before passaging, cells were cultured to a confluency of 70-80%. Then, cells were washed with sterile phosphate buffer saline (PBS) solution; PBS was then aspirated. 500 µL of 1x trypsin was added to flasks, to coat the cells. To activate trypsin (enzyme activity), the flasks were incubated in 5% CO_2 at 37 °C for 3 min. The cells' dissociation was examined under the microscope. Cell medium (4.5 mL) was added to flasks to deactivate the trypsin activity, then cells were resuspended to generate a single cell suspension. The cells were either passaged (1:7) into T25 / T75 flasks to maintain the cell line or seeded into plates for additional experimental analysis. All the cell lines were incubated in 5% CO_2 at 37 °C.

Table 2.9 Supplemented medium details for each cell line.

Cell line	Pre-coated flask	Medium	Supplements
U373M	-	RPMI 1640	10% FBS, 1% NEAA, 50 µg/mL gentamicin, 400 µg/mL G418.
U373V	-	RPMI 1640	10% FBS, 1% NEAA, 50 µg/mL gentamicin, 400 µg/mL G418.
U87MG	-	MEM	10% FBS, 1% L-glutamine
MRC-5	-	MEM	10% FBS, 1% NEAA, 1% v/v penicillin/streptomycin, 2 mM L-glutamine,10 mM HEPES buffer.
Human astrocytes	Poly-L-lysine coated	Astrocyte medium	2% FBS,1% astrocyte growth supplement, 1% penicillin/streptomycin.
THLE-2	Bovine-collagen type 1 (0.03 mg/mL), fibronectin (0.01 mg/mL), 10%BSA (0.01 mg/mL)	BEGM	10% FBS, 1% penicillin/streptomycin.

The astrocyte cell line was maintained using a different protocol from the conventional cell maintenance protocol. T75 pre-coated flasks (2 µg/cm^2) were used. Poly-L-lysine (15 µL; 10 mg/mL) was introduced into a flask that contained 10 mL of sterile water, and the flask was then left overnight in 5% CO_2 at 37 °C to generate poly-L-lysine-coated T75 flasks. Following the overnight period, 15 mL of whole astrocyte medium was introduced to the flask after the flask had been rinsed with sterile water. The cells were subcultured when they achieved 90–95% confluency and seeded into flasks that had been prepared the day before. The cell medium was aspirated and washed with PBS solution before subculturing. To minimise cell damage, a 5 mL PBS and 5 mL 0.05% T/E solution mix was applied to the cells. Cell morphology was observed under a microscope before cells were incubated in 5% CO_2 at 37°C. Following the incubation period, the cells were transferred into a 50 mL tube containing 5 mL of FBS. The flask was incubated for a further minute to gather all the cells. The remaining cells were then collected in flasks and transferred into tubes using 5 mL of TNS solution. After 5 min centrifugation at 1000 rpm, the cells were carefully resuspended with their medium (see Table 2.9).

2.7.3 Cryopreservation for long-term cell storage

The cells were stored in liquid nitrogen (-196 °C) for long-term storage. For cryopreservation, medium was aspirated from the flasks, and the cells were washed with PBS. After aspiration of PBS, 1 mL of trypsin (1x) was added to each flask and flasks returned to the incubator for 3-5 min to allow cell detachment. Then, 1 mL of freezing solution (90% FBS and 10% DMSO) was added to the detached cells. The mix of cells and freezing solution was transferred to a cryovial (1mL for each cryovial). The cryovials were placed into -20 °C as soon as possible to prevent the cells from possible DMSO-adverse effects. Next day, the cryovials were transferred to -80 °C. After 24 h incubation at -80 °C, the vials were transferred to -196 °C liquid nitrogen for long-term storage.

2.8 2D *in vitro* studies

The *in vitro* growth inhibition effects of all formulations in 2D cell culture conditions were examined using both MTT and PB assays. Protein lysates from each 2D cell line were tested with western blot analysis for additional investigation to elucidate the TfR1 expression and AFt formulation response in cancerous and normal cells. MGMT profile of all studied cell lines, and MGMT depletion study with U373M cells (MGMT-positive cell line) after treatment with AFt formulations were investigated by western blot. Following by western blot studies, TfR1 expression from 2D cells was quantified by flow cytometry.

2.8.1 MTT assay

The 3-(4,5-dimethylthiazol-2-yl)-2,5-diphenyltetrazolium bromide (MTT) assay is a widely used, conventional cell viability assay, developed by Mosmann *et al.*[208] that measures the formation of insoluble formazan crystals. After enzymatic reduction by mitochondrial dehydrogenases, the formazan is solubilised, and its optical density is measured at 570 nm.[209] To investigate *in vitro* growth inhibition studies, U373M (MGMT-positive), U373V (MGMT-negative), and U87MG (MGMT-low) GBM cells were seeded in 96 well plates at a density of 650 cells/well in 180 µL medium while MRC-5 foetal fibroblasts and THLE-2 liver cells were seeded the density of 400 cells/well and 5000 cells/well, respectively. After seeding cells and allowing 24 h for cells to attach, cells were treated with 20 µL test compounds (AFt, TMZ, PbS QDs, TMZ + PbS QDs, AFt-PbS, AFt-TMZ, AFt-PbS-TMZ) at 10x final concentrations and incubated for 6 days (Table 2.10). Additionally, a time-zero (T_0) plate was prepared (n = 16 for each cell line) to measure the viable cell numbers` absorbance at the time that cells were treated with test compounds. The perimeter wells of each 96 well plate were filled with 200 µL medium to minimise evaporation. All test compounds' dilutions were prepared in medium supplemented with 10% FBS for each cell line. After incubation for 6 days, the MTT reagent (50 µL, 400 mg/mL) was added into each well, and plates were incubated at 37 °C in a

humidified atmosphere with 5% CO_2 for 2 h to allow formazan production. After incubation with MTT reagent for 2 h, the aqueous well contents were aspirated, and formazan product solubilised in 150 µL/well DMSO. The plates were placed on a shaker for 5 min before the absorbance of each well was read at 570 nm at a plate reader (Perkin Elmer Envision). 50% growth inhibition (GI_{50}) and corresponding half maximal inhibitory concentration (IC_{50}) values were determined for each formulation by MTT assay. Estimated GI_{50} concentrations (µg/mL or µM) were calculated using Equation (2.8):

$$\mathrm{GI}_{50} = \left(\frac{\text{High abs} - \text{GI50 abs}}{High\ abs - low\ abs} \times\ (High\ conc - Low\ conc)\right) + Low\ conc. \qquad (2.8)$$

Table 2.10 Concentration ranges of test agents on the cells adopted in MTT assay.

Test agents	**U373M**	**U373V**	**U87MG**	**MRC-5**
AFt (µM)	0.001-1	0.001-1	0.001-1	0.001-1
DMSO (%)	0.002-2	0.002-2	0.002-2	0.002-2
TMZ (µM)	0.001-1000	0.001-1000	0.001-1000	0.001-1000
PbS QDs (µg/mL)	0.01-100	0.01-100	0.01-100	0.01-100
AFt-PbS (µg/mL)	0.01-100	0.01-100	0.01-100	0.01-100
AFt-TMZ (µM)	0.0001-100	0.0001-100	0.0001-100	0.0001-100
TMZ + PbS QDs (µM)	1-100	1-100	1-100	1-100
AFt-PbS-TMZ (µM)	0.0001-50	0.0001-50	0.0001-50	0.0001-50

Estimated GI_{50} and IC_{50} values were calculated based on PbS QDs concentration (µg/mL) for PbS QDs and AFt-PbS samples and based on TMZ concentration (µM) for TMZ, AFt-TMZ, TMZ + PbS QDs, and AFt-PbS-TMZ formulations. The concentration ranges of all test agents across different cells are summarised in Table 2.10.

2.8.2 PrestoBlue cell viability assay

To validate data obtained from MTT assays, PB cell viability assays, which are resazurin-based, non-toxic, and sensitive,[210] were performed. Figure 2.1 demonstrates the reduction mechanisms of MTT and PB assays.

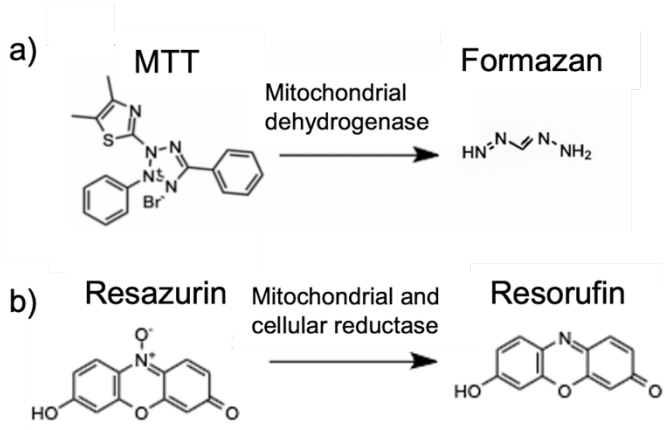

Figure 2.1 Schematic representation of reduction mechanisms underlying the **(a)** MTT and **(b)** PB assays. Created with Chem Draw.

In PB assay experiments, U373M, U373V, U87MG, MRC-5, human astrocytes and THLE-2 cells were used. Identical initial cell numbers and concentration ranges were used per cell line, as those used in MTT assays, to directly compare data from these assays. Therefore, U373M, U373V, U87MG (650 cells/well), MRC-5 (400 cells/well), and additionally human astrocytes and THLE-2 (5000 cells/well) cells were seeded into 96 well plates in 81 µL of cell culture medium and incubated overnight at 37 °C in a humidified atmosphere with 5% CO_2. Table 2.11 summarises seeding densities and assay period used in PB assay. After overnight incubation, cells were treated (9 µL; 10x final concentrations) with AFt, TMZ, PbS QDs, TMZ+ PbS QDs, AFt-PbS, AFt-TMZ, and AFt-PbS-TMZ and incubated for 6 days. To minimise evaporation, 90 µL medium were added to each perimeter well of 96 well plates. PB cell viability reagent (10 µL;10x) was added to the cells in the cell culture medium (final volume 100 µL) according to manufacturer's protocol (CAT: A13262). Final concentration ranges used for astrocyte and THLE-2 cells in PB assays are presented in Table 2.12. The 96 well plates were then wrapped in foil to protect cells from light and incubated at 37 °C in a humidified atmosphere with 5% CO_2 for 3 h. The absorbance of reagent was recorded at 570 and 600 nm (a reference wavelength) on a plate reader (Perkin Elmer Envision) and IC_{50} values were calculated for each test agent. Cell viability% was calculated according to the following equation:

$$Cell\ viability\ \% = \frac{OD\ value\ of\ treated\ cells}{OD\ value\ of\ control\ cells} \times 100\% \quad (2.9)$$

Table 2.11 Summary of the used seeding densities and exposure times.

Cell line	Seeding density (cells/well)	Assay duration (days)
U373M	650	6
U373V	650	6
U87MG	650	6
MRC-5	400	6
Astrocytes	5000	6
THLE-2	5000 cells/well	6

Table 2.12 Concentration ranges of test agents on astrocytes and THLE-2 cells adopted in PB assay.

Test agents	Astrocytes	THLE-2
AFt (μM)	0.001-1	0.001-1
DMSO (%)	0.002-2	0.002-2
TMZ (μM)	0.5-500	0.001-100
PbS QDs (μg/mL)	0.1-100	0.01-100
AFt-PbS (μg/mL)	0.1-100	0.1-100
AFt-TMZ (μM)	1-200	1-200
TMZ + PbS QDs (μM)	0.2-100	0.2-100
AFt-PbS-TMZ (μM)	1-100	1-100

2.8.3 Protein expression analysis via Western blot

Western blot analyses were conducted using protein lysates prepared from cells in 2D culture; protein concentration was determined via Bradford assay. Separation of proteins was conducted via sodium dodecyl sulfate polyacrylamide gel electrophoresis (SDS-PAGE) and proteins were transferred from gel to nitrocellulose membrane prior to incubation with primary and secondary antibodies and protein detection. Firstly, protein lysates from all studied cell lines were extracted from cells cultured in T75 flasks. Protein lysates were prepared using NP-40 lysis buffer (Table 2.13).

For protein lysate preparation, the media from the cells were collected in 15 mL tubes to collect any floating cells within the flask. Subsequently, the T75 flask was washed with PBS (3 mL), and 1.5 mL of trypsin (1x) was added. Following detachment of cells by trypsinisation, trypsin activity was inactivated by adding the cell media, and the mixture was centrifuged at 1200 rpm, 4 °C for 10 min. The cell pellet was washed thrice with ice-cold PBS (10 mL), and the

supernatant was discarded after each centrifugation. After washing, the cell pellet was suspended in NP-40 lysis buffer (300 µL), transferred to a tube, and incubated for 30 min on ice to facilitate lysis and allow proteins to be released from the cells. Following incubation, the samples were centrifuged at 13300 rpm, 4 °C for 10 min. Subsequently, the supernatant was retained, and the protein lysate was stored at -20 °C until use. Protein concentrations were determined by Bradford assay.

Table 2.13 Composition of NP-40 lysis buffer recipe.

Volumes
NP-40 (100 µL)
1 M NaCl (1.5 ml) – 0.58 g in 10 mL
1 M Tris pH 8.0 (500 µL) – 1.21 g in 10 mL
dH_2O (7.9 mL)
1 tablet of protease inhibitors (Roche, PC - 05892791001)
1 tablet of phosphatase inhibitors (Roche (PhosSTOP), PC - 04906845001)

To separate proteins in SDS-PAGE, 10% resolving gel and stacking gel were prepared firstly. The recipes for resolving and stacking gels are detailed in Table 2.14. Following the preparation of resolving gel, 30 min polymerisation period was observed. Subsequently, the stacking gel was prepared, the comb was inserted, and an additional 30 min interval was allowed for polymerisation.

Table 2.14 Recipe of resolving and stacking gels for SDS-PAGE.

Resolving gel (10 mL)	**Stacking gel (5 mL)**
dH_2O (4 mL)	*d*H_2O (3.4 mL)
30% Acrylamide mix solution (3.3 mL)	30% Acrylamide mix solution (830 µL)
1.5 M Tris pH 8.8 (2.5 mL)	1 M Tris pH 6.8 (630 µL)
10% SDS (100 µL)	10% SDS (50 µL)
10% AMPS (100 µL)	10% AMPS (50 µL)
TEMED (4 µL)	TEMED (5 µL)

For SDS-PAGE, equal amounts of protein (50 µg) from samples (18 µL) and protein molecular weight markers (10 µL) were loaded onto gels and electrophoresed at 90 V for 20 min, after which the voltage was increased to 150 V for 1 h. Concurrently, a total of 8 filter papers and a

nitrocellulose membrane were wetted in transfer buffer (1x). After SDS-PAGE completion, proteins were transferred from gels onto the nitrocellulose membrane. This was achieved by placing 4 filter papers and a nitrocellulose membrane first, followed by the gel and 4 filter papers on the Trans-Blot Turbo Transfer System (Bio-Rad). The transfer system was set to 2.5 A, 25 V for 45 min. Air bubbles were eliminated by rolling the top filter papers prior to initiating the transfer. Post-transfer, the membrane was placed in a plastic bag and blocked with 5% milk solution (8 mL in tris-buffered saline and tween 20 (TBST)) for 1 h, incubating at room temperature on an orbital shaker at 100 rpm. Subsequently, the blocking solution was removed, and the membrane was placed in a new plastic bag. Diluted primary antibodies (1° Ab, Table 2.15) in 5% milk solution (8 mL) were added, and the membrane was incubated overnight at 4 °C on an orbital shaker (100 rpm).

Following overnight incubation with 1° Ab, the membrane was washed with TBST solution (3 rounds, 5 min each). Secondary antibody (2° Ab) was applied for 1 h incubation at room temperature. Table 2.15 represents the 1° Abs and 2° Abs used and their respective dilution factors. 2° Ab dilution was optimised based on the protocols for 1° Ab, with 1:2500 dilution applied for TfR1 detection and 1:2000 dilution for MGMT. After incubation, 2° Ab was collected and the membrane was washed with TBST (3 rounds, 5 min each). Lastly, ECL reagent was prepared 1:1 (total 2 mL) by mixing solution A (luminol enhancer solution, 1 mL) with solution B (peroxide solution, 1 mL), and the membrane was incubated with ECL reagent mixture for 5 min in the dark. The protein bands were visualized by C-DiGit blot scanner (LI-Cor Biosciences).

Table 2.15 Primary and secondary antibodies used for western blot.

Antibody	Supplier	Dilution factor
1° Ab: Anti-human TfR1 monoclonal antibody	ThermoFisher (CAT:136800)	1:1000
1° Ab: anti-human MGMT monoclonal antibody	Invitrogen (MA3-16537)	1:500
1° Ab: Anti-human GAPDH monoclonal antibody	Sigma-Aldrich (CAT: G8795)	1:2000
2° Ab: Goat anti-mouse IgG (H+L) superclonal secondary antibody	ThermoFisher (CAT: A28177)	1:2500 /1:2000

TfR1 and MGMT expression profiles of all studied cell lines were assessed by western blot. To examine whether AFt encapsulation of test agents modulates MGMT levels in U373M (MGMT-positive) cells, these cells were plated in T75 flasks and grown to ~80–90% confluency. They were then treated for 6 days with 10 μM TMZ, AFt-TMZ, and AFt-PbS-TMZ (with untreated cells serving as controls; depicted in Figure 2.2). Cellular proteins were collected from each test condition and MGMT expression levels were interrogated by western blot.

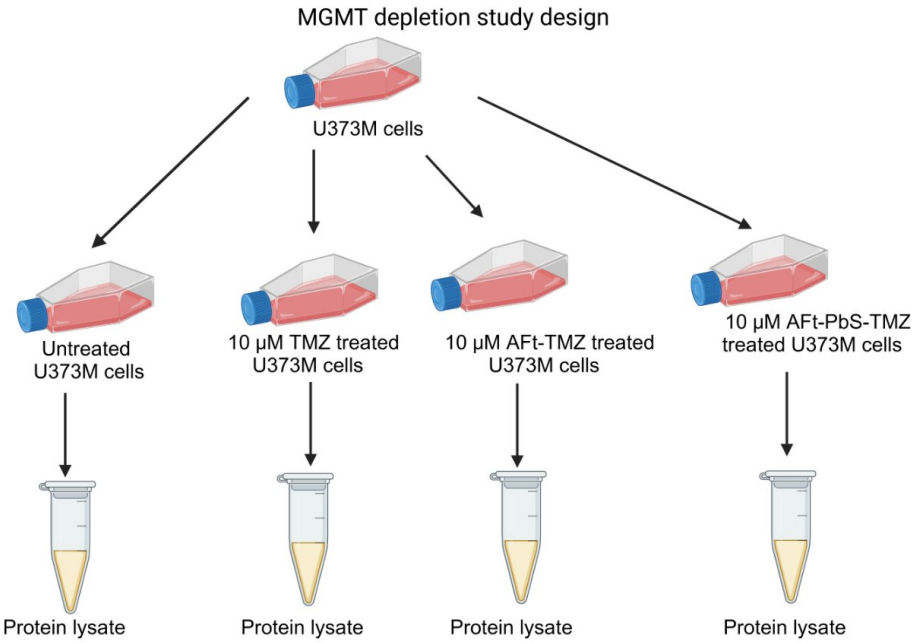

Figure 2.2 Testing the MGMT depletion hypothesis in U373M cells via western blot. Created with BioRender.

2.8.4 Quantification of transferrin receptor 1 expression by flow cytometry

U373M, U373V, U87MG, MRC-5, and astrocyte cells were seeded in T25 flasks and allowed to attach to the surface overnight. The following day, cells were collected by trypsinization (500 µL) and resuspended in PBS (1 mL). The cell suspension was centrifuged at 1,000 rpm for 5 min. The cell pellets were rinsed with ice-cold PBS and centrifuged at 1000 rpm for 5 min. This process was performed three times, each pellet being washed with ice-cold PBS and centrifuged. The pellets were resuspended with 4% paraformaldehyde solution (50 µL) while vortexing before being incubated at room temperature (RT) for 12 min. After incubation, cells were centrifuged and resuspended in PBS (500 µL). At this point, all 2D-cultured cells were fixed and stored at 4 °C until they were stained with antibodies. For flow cytometry studies, the following samples from each cell line were prepared: unstained cells, cells stained with only 2° Ab, and cells stained with 1° Ab and 2° Ab. Unstained cells were ready to use. To prepare stained cells with 2° Ab only, cells were centrifuged, and the pellet rinsed with TBST (3 times). The pellet was then resuspended with 2° Ab (200 µL) and incubated for 1 h at RT.

To prepare cells stained with 1° and 2° Abs, they were centrifuged and resuspended in TBST (500 µL). First, the pellet was resuspended in 100 µL of 1° Ab solution (2 µL TfR1 in 100 µL TBST) and incubated for 1 h at RT on a low-speed rocker. To stain with 2° Ab, cells were centrifuged, and the pellet was rinsed with TBST three times. After centrifugation, the cells were resuspended in 200 µL of 2° Ab (1 µL Ab in 20 mL TBST solution) and incubated at RT for 1 h. After incubation, the cells were pelleted and washed three times with TBST. After staining with both Abs, cells were maintained in 500 µL of PBS at 4 °C overnight. The dilution factors used for both 1° and 2° Abs are detailed in Table 2.16. All samples were analysed using flow cytometry (Beckman Coulter FC500). The single cells were identified, and the shifted signals were compared to signals from unstained cells and cells stained with 2° Ab using Kaluza software.

Table 2.16 Antibodies used for flow cytometry.

Antibody	Supplier	Dilution factor
1° Ab: Anti-human TfR1 monoclonal antibody	ThermoFisher (CAT:136800)	1:50
2° Ab: Goat anti-mouse IgG (H+L) cross-absorbed secondary antibody, Alexa Fluor™	ThermoFisher (CAT: A-11001)	1:20 000

2.9 3D tumour spheroid studies

3D *in vitro* studies represent the tumour *in situ* more precisely than 2D *in vitro* studies.[211] As a result, 2D U87MG cells were utilised to generate 3D spheroid cultures, and their cell viability was examined using the PB assay. Treatment effects were evaluated by measuring spheroid volume. Additionally, 3D U87MG spheroids received subsequent treatments with all formulations to replicate more accurately clinical exposure to drugs. Finally, TfR1 expression in single cells obtained following dissociation of U87MG spheroids were analysed by Kaluza software.

2.9.1 PrestoBlue assay

The PB assay was used to assess cell viability % in U87MG tumour spheroids. U87MG cells (3000 cells/well) were seeded in ultra-low attachment (ULA) plates in 90 µL medium and the plate was parafilmed and centrifuged at 300 *g* for 5 min (Figure 2.3). To prevent evaporation, medium (100 µL) was added to the perimeter wells each plate. The plate was incubated overnight at 37 °C in a humidified atmosphere with 5% CO_2. On day 1, spheroids were treated (10 µL; 10x final concentration) with AFt, TMZ, PbS QDs, TMZ+ PbS QDs, AFt-PbS, AFt-TMZ, and AFt-PbS-TMZ and incubated for 6 days. According to the manufacturer's protocol, after incubation for 6 days, 11 µL of PB reagent was added into each spheroid and plates were wrapped in foil and incubated at 37 °C in a humidified atmosphere with 5% CO_2 for 6 h. The absorbance of PB reagent was recorded at 570 and 600 nm (a reference wavelength) on a

plate reader (Perkin Elmer Envision) and estimated IC_{50} values were calculated for each test agent. Cell viability % was calculated using same equation used in 2D cultures (Equation 2.9).

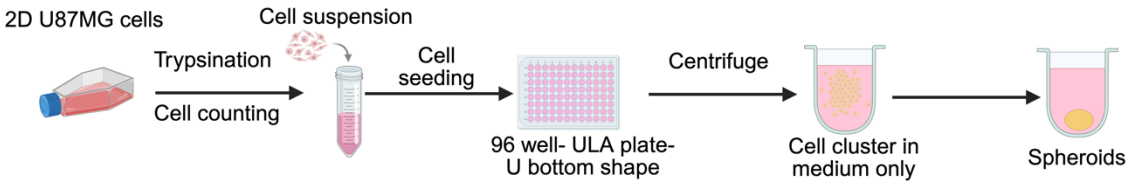

Figure 2.3 Schematic overview of spheroid formation procedure. Created with BioRender.

Estimated IC_{50} values from PB assay in 3D cultures were used to assess the interactions of TMZ and PbS QDs within AFt nanocages through the comparative analysis of AFt-PbS-TMZ formulation with the naked agents TMZ and PbS QDs, using a basic look-see calculation and Chou-Talalay combination index (CI) method. CI was calculated the Equation (2.10), where D_1 and D_2 are the IC_{50} concentrations of TMZ and PbS QDs in AFt-PbS-TMZ, DX_1 and DX_2 are corresponding to the IC_{50} concentration of TMZ and PbS QDs tested alone in 3D U87MG spheroids.

$$Combination\ index\ \ (CI) = \left(\frac{D_1}{DX_1} + \frac{D_2}{DX_2}\right) + \left(\frac{D_1 \times D_2}{DX_1 \times DX_2}\right) \qquad (2.10)$$

2.9.2 Analysis of spheroid volume

Spheroid volumes were evaluated by measuring the horizontal (*d1*) and vertical (*d2*) diameters of each spheroid following treatments, utilising spheroid images captured on specific days (at day 1 and 6) with CellSens Standard software of the microscope (OLYMPUS). Spheroid volume was calculated following Equation (2.11) and the effects of the formulations on spheroid volumes were analysed and compared to cell viability results.

$$Spheroid\ volume = \frac{4\pi}{3} \times \left(\frac{d1}{2}\right)^2 \times \left(\frac{d2}{2}\right) \qquad (2.11)$$

2.9.3 Sequential treatment protocols

To mimic clinical medication use, U87MG spheroids were treated sequentially. The plan required that medium, and treatments be renewed every 6 days with fresh solutions. Spheroids were seeded (3000 cells/well) in ULA plates and incubated overnight at 37 °C, humidified with 5% CO_2. Spheroids were treated with formulations (10 µL; 10x final concentration AFt, TMZ, PbS QDs, TMZ+ PbS QDs, AFt-PbS, AFt-TMZ, and AFt-PbS-TMZ) and incubated for 6 days (1st treatment). On day 7, spheroid images were obtained, and cell viability% was determined using the PB assay.

Following assessment, the medium was replenished for all spheroids and conditions, and test agent treatments (2nd treatment) were added before further incubation for 6 days. On day 14, spheroid photos were acquired, and cell viability was compared to the first treatment results. Spheroids were treated with fresh 10 µL (10x) formulations and incubated for a further 6 days (3rd treatment). On day 21, spheroid images were obtained, and cell viability was compared to the first and second treatment findings. All results and images from days 7, 14, and 21 were examined in comparison analyses. Figure 2.4 illustrates the sequential treatment schedule applied to U87MG spheroids.

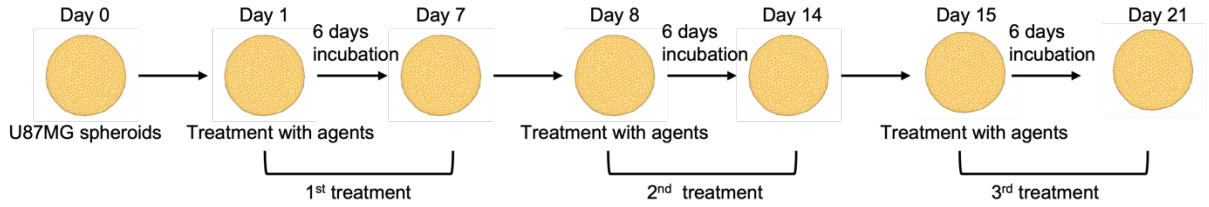

Figure 2.4 Experimental design for sequential treatment of U87MG spheroids with multiple agents over a 21-day period. Created with BioRender.

2.9.4 Quantification of transferrin receptor 1 expression in spheroids by flow cytometry

To analyse spheroid samples using flow cytometry, the spheroids need to be disassociated into single cells. Therefore, on days 1 and 6, U87MG spheroids (*n* = 288, 3000 cells/well) were collected from ULA U-bottom 96 well plates into a 15 mL falcon tube. Spheroids were centrifuged, and the cell pellet was then rinsed with PBS (10 mL) and treated with 1 mL of 5x TE solution. To mechanically separate the spheroids into individual cells, spheroids were incubated for 10 min at 37 °C and gently pipetted up and down every 2-3 min. The cell counter was used to monitor the dissociation success. Cell culture medium (10 mL) was added to neutralise the trypsin after the cells had been separated. After centrifuging the cells, the supernatant was aspirated. The same process was used for 2D cell samples for flow cytometry analysis. TfR1 expression in U87MG spheroids was analysed and compared with TfR1 expression in 2D-cultured U87MG cells.

2.10 Near infrared-II imaging: *in vitro*, *ex vivo* and *in vivo* models

SWIR imaging system (Photon etc, Montreal, Canada, Figure 2.5a) was employed to detect the imaging potential of PbS QDs and PbS QD-containing formulations (AFt-PbS and AFt-PbS-TMZ) in *in vitro* fixed 2D and 3D U87MG GBM models, *ex vivo* brain tissue samples and *in vivo* models were used to evaluate their signal.

2D U87MG cells (1.5 x 10^5 cells per coverslip) were seeded onto sterile coverslips and incubated overnight at 37 °C, humidified with 5% CO_2. The following day, cells were treated for 24 h with 50 µg/mL PbS QDs, AFt-PbS, and AFt-PbS-TMZ. After treatment with test agents, coverslips were washed with 1 mL PBS (3 times) and fixed in 4% paraformaldehyde solution (1 mL) for 12 min at 37 °C. The fixed samples were mounted onto microscope slides using 4

µL of mounting medium. The SWIR imaging was set up at 785 nm laser, 1 W power, 980 nm LP emission filter, or 1250 nm LP emission filter for 0.4 s, 0.5 s, and 0.7 s exposure times.

For 3D *in vitro* studies, U87MG cells were placed at 3000 cells/well in ULA plates using the same methodology as for spheroid generation (see Section 2.9.1). Spheroids were treated on day 1 with 50 µg/mL PbS QDs, AFt-PbS, and AFt-PbS-TMZ for 6 days. The study employed untreated spheroids (6 days) as negative controls. After treatment, spheroids were washed with PBS solution (2 times) and were fixed with 4% paraformaldehyde solution (200 µL, 30 min incubation at 37 °C, humidified with 5% CO_2). The intensity signals being emitted by PbS QDs in three replicates of spheroids were assessed using SWIR imaging.

Thirdly, deep tissue visualisation in brain tissue slices was investigated post-treatment with PbS QDs and AFt-PbS. Based on PbS QD concentration, PbS QDs (4 mg/mL) and AFt-PbS (2.5 mg/mL) were placed in capillary tubes, while brain tissue slices, prepared at thickness of 1 mm, were used for imaging analysis (Figure 2.5b). The imaging capabilities of PbS QDs and their encapsulated form (AFt-PbS) were assessed using the IR VIVO SynIRgy imaging system (Photon etc., Montreal, Canada). SWIR imaging was performed with a 785 nm laser set to 20% power, a 1000 nm LP emission filter, a camera exposure time of 0.1 s, and histogram stretching in the range of 1000-5000.

To examine the real-time imaging capabilities of PbS QDs *in vivo*, nude mice were injected with 200 µL of a PEGylated PbS QD solution (2.4 mg/mL). Assuming an average total blood volume of 2 mL per animal, the final concentration of PbS QDs in the blood was calculated to be 0.24 mg/mL. IR VIVO SynIRgy system (Photon etc., Montreal, Canada) was used to detect fluorescence in a live animal immediately post-injection. At various time points, time-lapse images were captured to assess signal in liver, spleen, and brain. Regions of interest (ROI) corresponding to each organ were manually selected and analysed using PhySpec v2.28.0 software. The normalised intensity versus time profiles for each organ were generated using Origin software. For each organ, two independent datasets were obtained from separate

measurements based on the same *in vivo* images. The average of these datasets was plotted as exponential decay curves, from which time constants (τ, min) were calculated in Origin software. Subsequently, $t_1/_2$ values were then calculated using the Equation (2.12). The selected organs (liver and spleen) were harvested for preliminary step towards full biodistribution studies.

$$t_1/_2 = \tau \times \ln(2) \qquad (2.12)$$

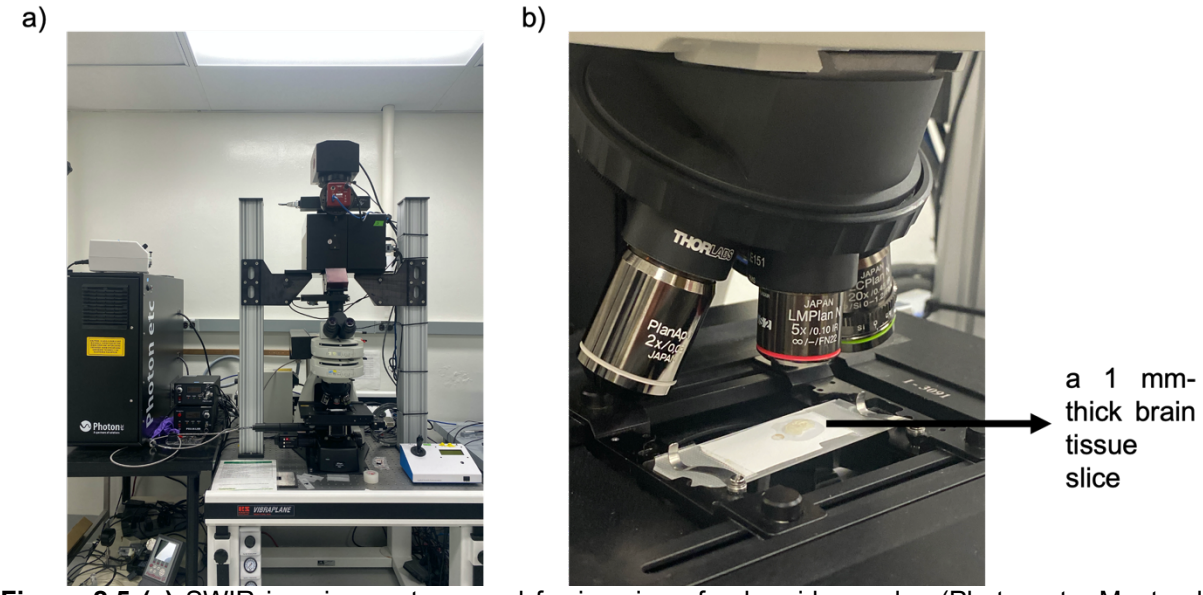

Figure 2.5 (a) SWIR imaging system used for imaging of spheroid samples (Photon etc, Montreal, Canada), **(b)** representative image of a 1 mm-thick brain tissue slice under SWIR imaging system.

2.11 Statistical analysis

Experiments were repeated at least three times (N = 6 internal (technical) replicates), and data are reported as mean ± standard deviation (SD). Statistical differences were analysed using a one-way analysis of variance (ANOVA), followed by the Holm-Sidak method for comparisons involving three or more groups ($n \geq 3$), and t-tests for comparisons between two groups (n = 2). The statistical significance was reported as follows: not significant (ns), (*) $p < 0.05$, (**) $p < 0.01$, (***) $p < 0.001$, and (****) $p < 0.0001$.

Chapter 3 Co-encapsulation and characterisation of lead sulfide quantum dots and temozolomide within apoferritin nanocages

3.1 Background

GBM is one of the most aggressive brain tumours, characterised by rapid progression, high recurrence rates, and poor patient prognosis.[13] Although TMZ is widely used in the clinic with its ability to penetrate BBB, to extend the GBM patient survival, its efficacy in the clinic is limited mostly a consequence of instability at psychological pH, poor tumour selectivity, and resistance mechanisms.[83] Effective diagnosis of GBM presents significant challenges: conventional imaging is hindered by anatomical barriers, and organic dyes suffer from low tissue penetration, and signal interference with low quantum yield (QY) and poor photostability (PS). SWIR imaging (1000-1700 nm) offers deeper tissue penetration, higher resolution, and reduced tissue autofluorescence.[102] PbS QDs exhibit potentially favourable characteristics for SWIR imaging with their intense QY and long-term PS.[105] However, their clinical translation is hindered by potential toxicity and targeting delivery issues. Thus, a nanocarrier system is required that can reduce the problems associated with PbS QDs and TMZ while taking advantage of their beneficial features.

AFt is a versatile nanocarrier due to its unique physicochemical characteristics, which significantly impact the biodistribution and efficacy of NPs.[153] Its natural structure, small size, and TfR1-mediated endocytosis, as TfR1 is overexpressed in GBM and abundant on BBB endothelial cells, facilitate brain drug delivery across the BBB.[122] The hollow protein structure of AFt allows encapsulation of both hydrophilic and hydrophobic agents. Various single agents (e.g. TMZ,[83] DOX,[212] gefitinib,[213], antitumour benzothiazoles[214]) and nanomaterials (e.g. gold NPs (AuNPs)[215], QDs[216]) have been successfully encapsulated into AFt cages. Additionally, AFt's ability to co-loading of multiple diagnostic and therapeutic agents within a single nanoplatform provides targeted delivery to the tumour site, drug release profile visualisation,

pharmacokinetic and biodistribution evaluation, and therapeutic effect assessments, highlighting its potential in cancer theranostics.[200]

This chapter examines the development and characterisation of a theranostic AFt-based nanocarrier system co-loaded with TMZ and PbS QDs (AFt-PbS-TMZ). In the co-encapsulation process, the disassembly/reassembly route was employed to load PbS QD into an AFt cage whereas TMZ, due to its small molecular size, was encapsulated via the diffusion method. The rationale for this combination lies in integrating TMZ's chemotherapeutic activity with the SWIR imaging abilities of PbS QDs, thus enabling a theranostic platform for improved GBM management. This theranostic strategy was designed to enhance targeted delivery to tumour tissues while protecting healthy tissues and reduce TMZ leakage post co-encapsulation. Furthermore, PbS QDs provide NIR-II window imaging capabilities, offering deep tissue visualisation and brain imaging, helping to address the limitations. To support this theranostic strategy, single agent encapsulated AFt formulations (AFt-PbS and AFt-TMZ) were first synthesised. A comprehensive comparative characterisation of these formulations was conducted, with particular emphasis on the theranostic formulation, evaluating parameters such as particle size and zeta potential, protein integrity, PL activity, TMZ release profile, and storage stability over a 1 month period.

Chapter hypothesis: The development of a theranostic AFt nanoplatform co-encapsulating TMZ and PbS QDs will enhance therapeutic activity of TMZ with co-encapsulation, increased TMZ retention within AFt cages, and controlled pH-dependent release compared to single agent encapsulation (AFt-TMZ). In addition, the presence of PbS QDs will enable SWIR imaging for real-time tracking of the delivery system and to contribute to overall therapeutic activity through their potential cytotoxicity toward GBM cells when delivered via TfR1-targeted AFt nanocages, thus providing a multifunctional strategy for targeted GBM theranostics.

Chapter experimental aims: The experimental aims of this chapter include the development of AFt nanocages co-encapsulating chemotherapy drug (TMZ) and imaging agent (PbS QDs),

with high EE, an average diameter of ~ 12 nm, a low PDI, the preservation of the native protein integrity of AFt, and the utilisation of the SWIR imaging capability of PbS QDs. The experiments are designed to evaluate their size and zeta potential stability during storage at 4 °C and after 1 month of storage at -80 °C, and as well as to investigate their controlled release properties under physiological pH conditions, while enabling pH-responsive release of the encapsulated cargo at pH 5.5, corresponding to the endosomal-lysosomal pathway.

3.2 Results and discussion

3.2.1 Morphological and optical properties of lead sulfide quantum dots

PbS QDs, synthesised following a previously published method[206] (see Section 2.3) at a molar ratio of Pb:S = 1:0.3, were characterised in terms of size, morphology, and optical properties using HR-TEM and PL studies. HR-TEM image (Figure 3.1a) analysis revealed that the QDs had a nanocrystalline structure with consistent spherical morphology. Average particle diameter of PbS QDs was determined to be 4.0 ± 0.5 nm in aqueous solution by ImageJ analysis (Figure 3.1a inset). In addition, to investigate PbS QDs' imaging capabilities in the SWIR range, PL emission was recorded using the as-synthesised PbS QDs solution (5 mg/mL). As illustrated in Figure 3.1b, for as-synthesised QDs, PL peaks centered at λem = 1118 nm (1.1 eV) with the full width at half maxima of (FWHM) ~ 155 meV, as expected for this size QDs.[217, 218]

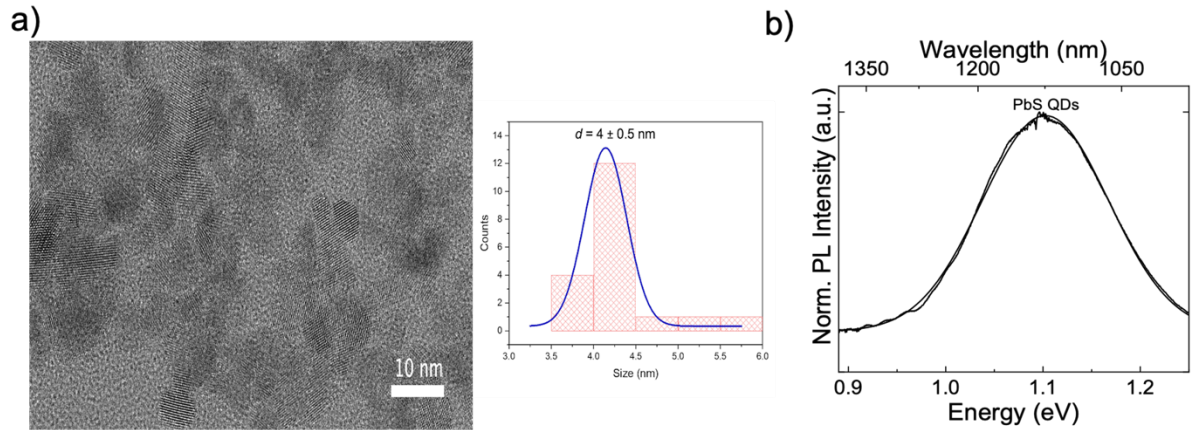

Figure 3.1 (a) Representative HR-TEM image of PbS QDs (inset) size distribution of PbS QDs from HR-TEM analysis. 19 particles were analysed from the HR-TEM image**. (b)** Room temperature photoluminescence (PL) spectra of PbS QDs.

To investigate PbS QDs' imaging capabilities in the SWIR range for over a period of three months, PL emission was recorded using 3 concentrations including the as-synthesised PbS QDs solution (5 mg/mL) and its serial dilutions of 0.5 mg/mL and 0.25 mg/mL. The PL emission was detectable at 5 mg/mL and 0.5 mg/mL concentrations, with PL intensity linearly decreasing with decreasing concentration (Figure 3.2a and inset). Notably, the QD solutions are stable with respect to their optical and morphological properties for a period of at least three months, when stored at 4 °C, under N_2. PbS QDs maintained their PL intensity, with small redshift peak to λem = 1379 nm (0.9 eV) and FWHM ~ 120 eV. This observed redshift is attributed to an Ostwald ripening process observed in all nanoparticle solutions.[219]

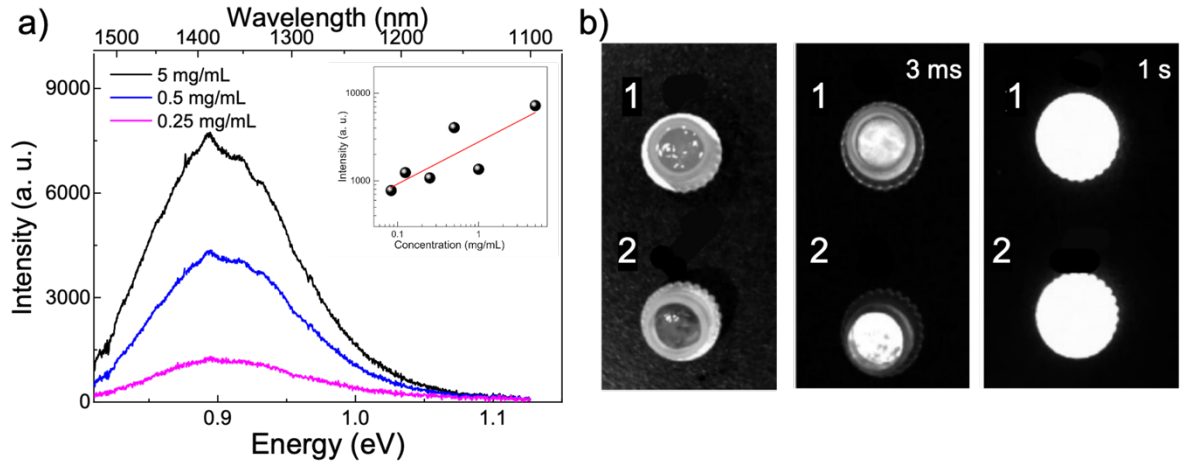

Figure 3.2 (a) Representative room temperature photoluminescence spectra of PbS QD solutions with concentration of 5 mg/mL, 0.5 mg/mL, and 0.25 mg/mL (pH 11, aqueous solution, pH adjusted with triethylamine). **(Inset)** Dependence of PL intensity on the QD concentration. **(b)** Optical (left) of PbS QDs embedded in Native-PAGE gel either in a 'sandwich' sample of a missed sample, and corresponding SWIR images recorded with integration time of 3 ms (middle) and 1 sec (right). The SWIR

PL images were recorded on IR VIVO SynIRgy (785 nm laser at 20% power, emissions long pass filter: 850 nm).

In addition to PL studies, SWIR imaging using a native-PAGE gel (10%) embedded with PbS QDs also confirmed their bright emission signal. The sample was prepared as a 'sandwich' structure with QD layer embedded between the gel and a sample with QDs dispersed in the gel (Figure 3.2b). The mixed sample had brighter luminescence compared to the 'sandwich' sample. The observed difference is due to uniform distribution through the volume and proximity of the QDs to the surface in the mixed sample. Despite a layer of gel with a thickness of 1.5 mm over the QD layer, the QD luminescence was easily detectable, of interest for deep tissue imaging. Overall, the results obtained demonstrated the potential of PbS QDs for imaging in the NIR-II wavelength region for theranostic applications.

3.2.2 Single vs. co-encapsulation of lead sulfide quantum dots and temozolomide within apoferritin nanocages

The protein nanocarrier system (AFt) was selected as the delivery and targeting vehicle for PbS QDs and TMZ. To integrate both imaging and therapeutic agents in a single nanocarrier system, a QD was entrapped in each AFt nanocage by a disassembly-reassembly method, where the AFT cage is disassembled into 24 subunits at pH 2, and the QD are trapped inside the cavity as the cage was reassembled with pH increasing to pH 7. TMZ was then loaded into the formed AFt-PbS nanocages via passive diffusion, using the 'nanoreactor' method, where diffusion of the drug molecule takes place through the 3- and 4-fold channels in the AFt capsule, forming co-encapsulated AFt-PbS-TMZ (Figure 3.3). Calibration curves were utilised to determine protein (Figure 3.4a) and TMZ (Figure 3.4b) concentrations in the formulations by Bradford assay (Figure 3.4c) and UV-vis measurements (Figure 3.4d), respectively.

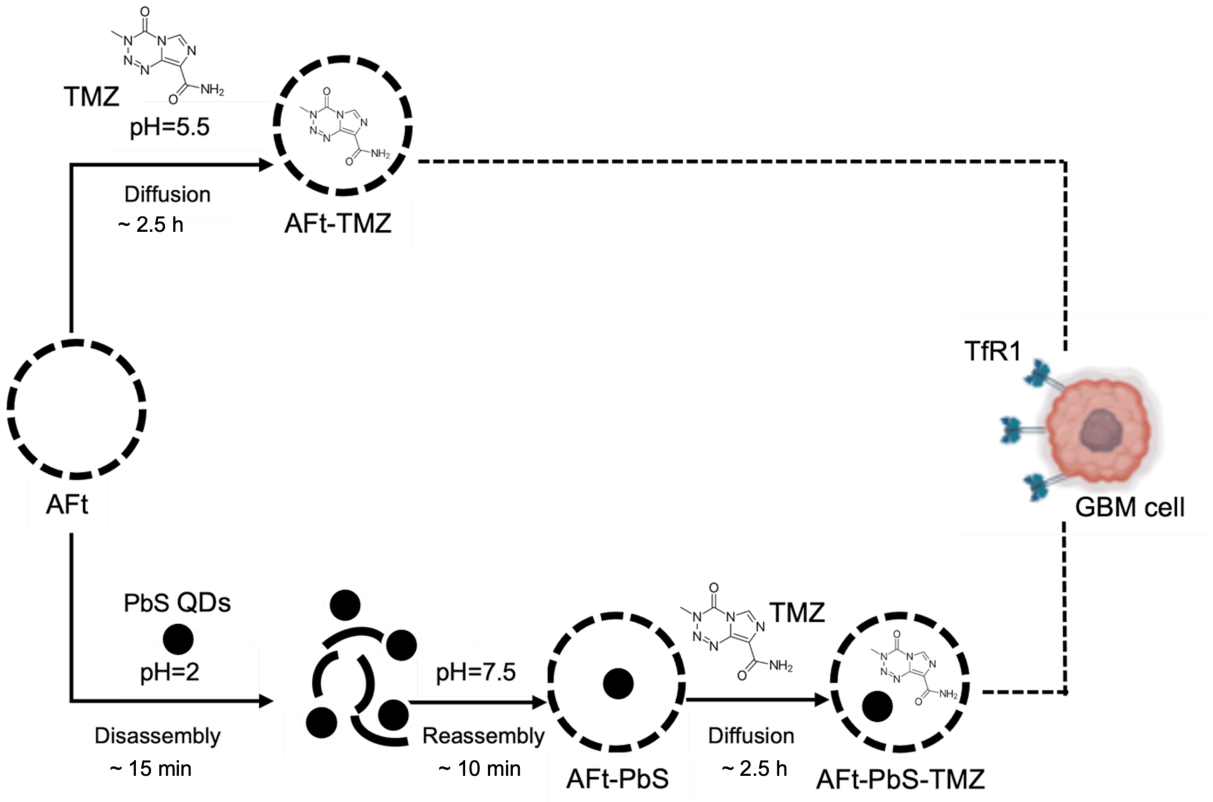

Figure 3.3 Schematic illustration of the single and co-encapsulation processes in the development of the AFt-TMZ (top), AFt-PbS (bottom), and AFt-PbS-TMZ (bottom) for targeting of TfR1 overexpressed in GBM cells.

The encapsulation efficiency (EE) of TMZ in AFt-TMZ and AFt-PbS-TMZ was evaluated using UV-vis spectroscopy by measuring the intensity of the TMZ absorption peak at λ = 330 nm. In the co-encapsulation process, AFt:TMZ molar ratio of 1:400 was used to allow sufficient space in the hollow cage for both agents. The EE of TMZ was determined to be 74.4 ± 11.2%, indicating successful loading of 309 ± 49 TMZ molecules per AFt cage in the final AFt-PbS-TMZ formulation (Table 3.1). The number of TMZ molecules per AFt cage was calculated indirectly based on the original AFt:TMZ molar ratio used in the formulations and EE% determined by UV-vis measurements. Comparable EE%, DL%, and PY% results were observed in single encapsulation formulation (AFt-TMZ), even when a higher AFt:TMZ molar ratio of 1:800 was employed. Additionally, variable AFt:TMZ ratios in both samples (AFt-TMZ and AFt-PbS-TMZ) can be used to explain the variation in the number of encapsulated TMZ molecules per AFt cage. However, high TMZ EE (> 70%) was observed in both formulations. It may be attributed to the small molecular weight of TMZ (194.1 g/mol), which allows it to diffuse through pores between protein subunits. The number of TMZ molecules encapsulated

within AFt cages is consistent with previously reported values.[83, 172] In contrast, the number of encapsulated TMZ molecules within AFt cages exceeds that reported in previous studies with different drugs/molecules. For instance, hydrophobic drugs such as paclitaxel (853.9 g/mol) achieved loading of ~60 molecules per cage using the disassembly/reassembly method,[162] DOX (543.5 g/mol) ~28 molecules per cage via the same method,[220] and Phortress (386.5 g/mol) ~130 molecules per cage using the nanoreactor route.[221] This difference in the number of encapsulated agents might be explained by their larger molecular size compared to TMZ.

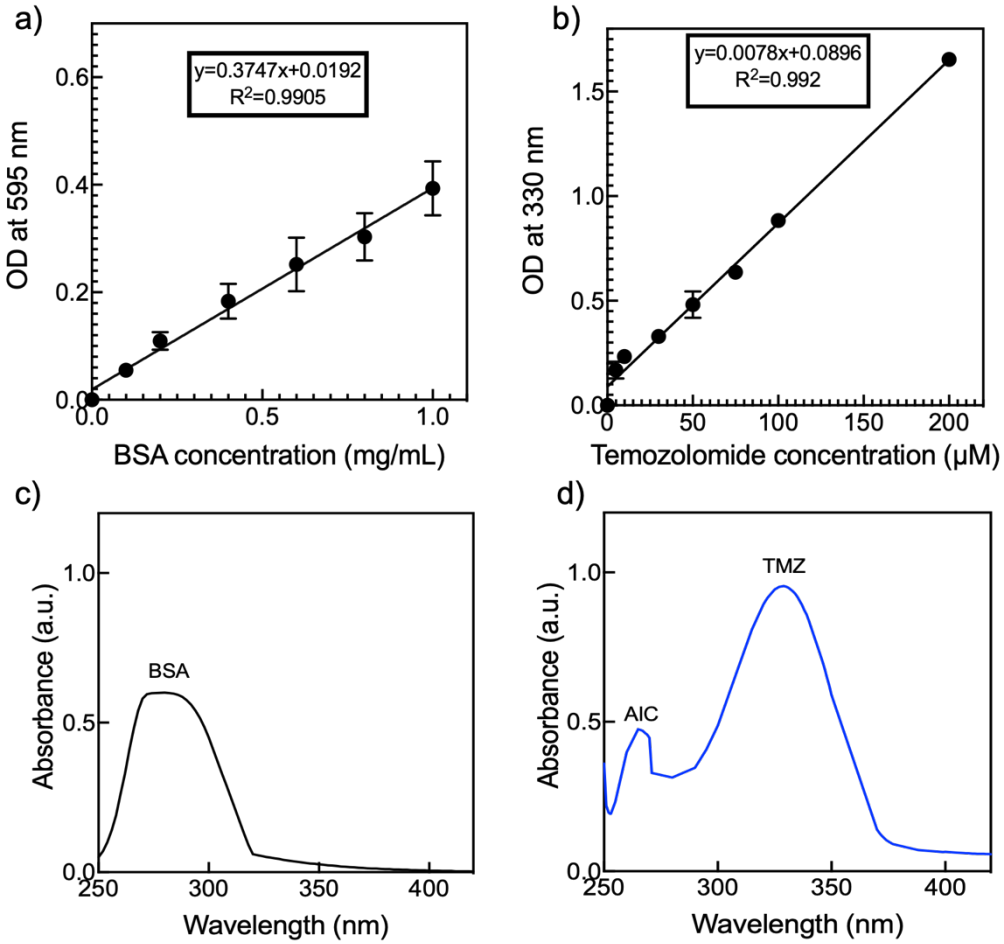

Figure 3.4 Standard curves for **(a)** BSA and **(b)** TMZ, with error bars representing standard deviation (SD, *n* = 3). Representative of UV-vis absorption spectrums of **(c)** BSA at λ = 280 nm and (d) TMZ at λ = 330 nm and AIC at λ = 265 nm.

In the study, TMZ encapsulation within AFt cages was optimised under acidic conditions (at pH 5.5) to enhance TMZ stability. Remarkably, in the co-encapsulation process, the encapsulation environment pH was kept at pH 7.5, to preserve the colloidal stability of PbS

QDs. However, TMZ is known to undergo rapid degradation into its metabolites at physiological pH (TMZ half-life 1.8 h at pH 7.4), and duration of the co-encapsulation process was longer than the TMZ half-life. Therefore, the presence of the TMZ degradation product, metabolite AIC, was also monitored by measuring absorbance at λ = 265 nm. Despite ~ 2.5 h at pH 7.5, only 10% degradation was observed, hence it was concluded that an acceptable co-encapsulation protocol had been optimised. The limited degradation may be attributed to potential interactions between TMZ and PbS QD within AFt cages, or to the formation of metal-protein complexes. Similarly, Li *et al.*[180] reported that TMZ degradation metabolite MTIC can interact with copper ions (Cu^{2+}), thus AFt can act as a copper-bound protein, Cu-MTIC interactions occurred within AFt nanocages, stabilising MTIC and preventing its subsequent hydrolysis. In addition, enhanced TMZ stability has been reported when TMZ bound to different nanocarrier systems.[222, 223] For instance, TMZ binding to HSA was shown to extend TMZ half-life by delaying its hydrolysis.[223] Therefore, the limited degradation observed here, even after ~ 2.5 h at pH 7.5, indicates an additional advantage of co-encapsulation protocol.

Table 3.1 Summary of encapsulation efficiency (EE%), drug loading (DL%), and protein yield (PY%) of AFt nanoparticles (Mean ± SD, *n* = 6).

Nanoformulation	AFt/TMZ molar ratio	EE (%)	DL (%)	PY (%)	Number of molecules per AFt
AFt-TMZ	1:800	73.1 ± 12.1	16.8 ± 0.9	81.6 ± 12.9	516 ± 82
AFt-PbS-TMZ	1:400	74.4 ± 11.2	13.1 ± 3.2	80.1 ± 16.8	309 ± 49

3.2.3 Characterisation of nanoformulations by size, zeta potential, native-PAGE, HR-TEM and photoluminescence

Particle size and zeta potential measurements were performed in 0.1 M NaOAc buffer at pH 5.5 to provide a suitable ionic strength, and TMZ stability of nanoformulations, using DLS. The hydrodynamic size of AFt was first measured as a control to assess potential changes in the protein size before and after encapsulation and was found to be 11.8 ± 1.8 nm. After encapsulation, AFt cages had hydrodynamic sizes of 12.3 ± 0.7 nm, 12.0 ± 0.8 nm, 14.3 ± 0.5

nm for AFt-PbS, AFt-TMZ, and AFt-PbS-TMZ, respectively. Figure 3.5a shows the size distribution profiles of all AFt formulations. Encapsulation of individual agents (PbS QDs and TMZ) resulted in a slight but statistically not significant increase in cage size ($p>0.05$) while co-encapsulation (AFt-PbS-TMZ) demonstrated a significant increase ($p<0.05$). The observed increase in size of AFt-PbS-TMZ may be attributed to cooperative swelling of flexible AFt nanocages, driven by space-filling effects, electrostatic interactions, and slight conformational rearrangements. On the other hand, single agent encapsulation results were consistent with previous studies with AFt-PbS and AFt-TMZ, which found similar size values after encapsulation.[83, 172, 224] In addition to particle size values obtained from DLS measurements, the PDI values of AFt, AFt-PbS, AFt-TMZ, and AFt-PbS-TMZ were found to be 0.27 ± 0.07, 0.27 ± 0.02, 0.25 ± 0.05, 0.26 ± 0.04 for AFt, AFt-PbS, AFt-TMZ, and AFt-PbS-TMZ, respectively. The PDI values represent size distribution of the formulations in the solution and larger PDI values can be related to agglomeration of samples.[225] Therefore, AFt formulations with PDI values below 0.3 indicated a suitable monodisperse particle size distribution.

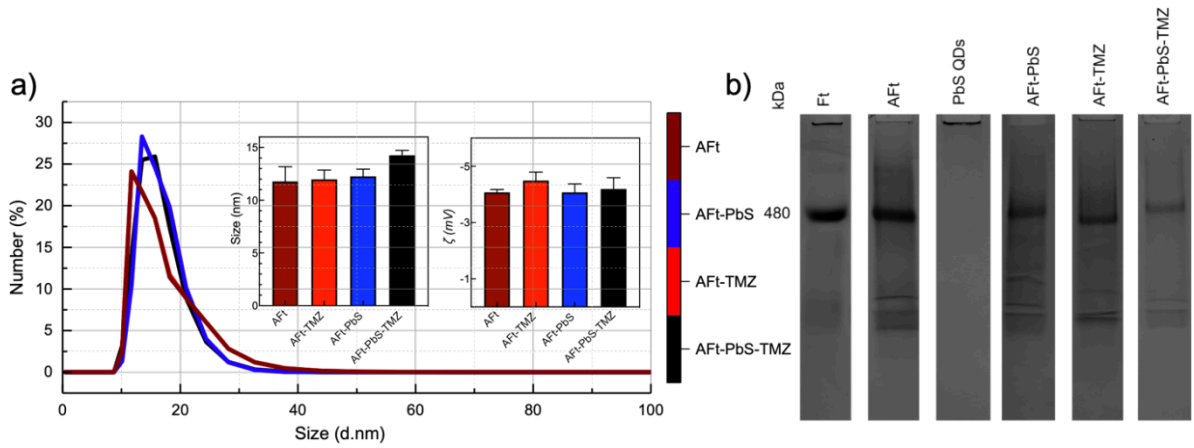

Figure 3.5 Synthesis and characterisation of AFt nanoparticles. **(a)** Size distribution and **(insets)** hydrodynamic size and zeta potential of AFt, AFt-PbS, AFt-TMZ, and AFt- PbS-TMZ measured by dynamic light scattering (DLS. Data are presented as mean ± SD of samples from three independent experiments (n = 3, N = 6). **(b)** Native-PAGE gel results of horse spleen ferritin (Ft), horse spleen AFt, PbS QDs, AFt-PbS, AFt-TMZ and AFt-PbS-TMZ.

To evaluate any effect of encapsulation process in the protein capsule surface, zeta potential values of AFt, AFt-PbS, AFt-TMZ, and AFt-PbS-TMZ were measured and were found to be

-4.1 ± 0.1, -4.1 ± 0.3, -4.5 ± 0.3, -4.2 ± 0.4 mV, respectively. The DLS measurements confirmed that AFt cages had a negative zeta potential value which minimally changed after encapsulation (Figure 3.5a inset). Negatively charged NPs produce fewer immune responses and are repelled by cell membranes reducing non-specific cell uptake which is important for clearance and targeted distribution.[226, 227] Therefore, the negative surface charge of AFt may prolong their circulation time and help to minimise off-target effects.

Protein cage integrity was further confirmed using the native-PAGE method, as described in Section 2.6.5. Following encapsulation, all AFt formulations demonstrated comparable bands at ~480 kDa, showing that the protein cages` structural integrity was maintained. Ft and AFt were used as controls. As expected, PbS QDs did not migrate through the gel. (Figure 3.5b). Altogether, DLS and Native-PAGE results indicated that TMZ and PbS QDs were encapsulated successfully within AFt cavities.

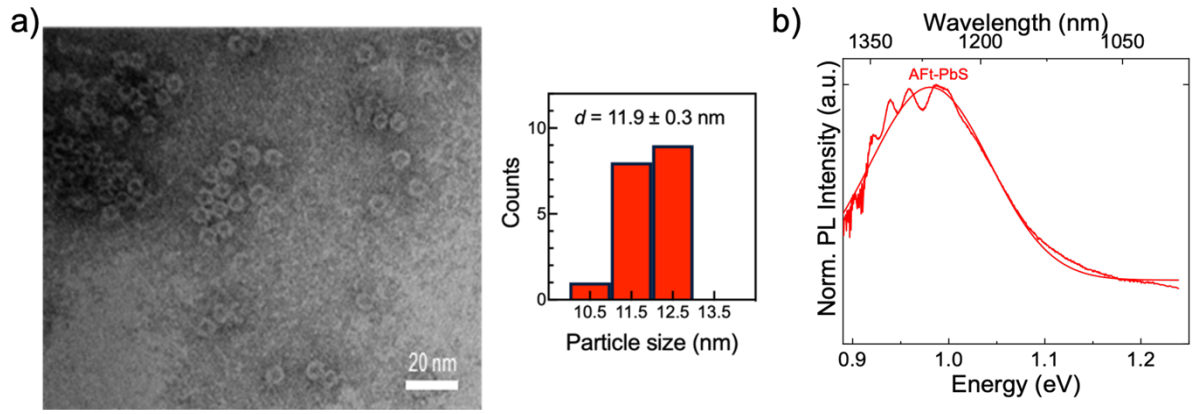

Figure 3.6 (a) Representative HR-TEM image of AFt-PbS, negatively stained with uranyl acetate and a size distribution histogram shown in the insert. 18 particles were analysed from the HR-TEM image. **(b)** Room temperature photoluminescence (PL) spectra of AFt-PbS.

As an initial product of co-encapsulation process, AFt-PbS was characterised by HR-TEM and PL studies (Figure 3.6). As shown in Figure 3.6a, AFt-PbS were negatively stained with uranyl acetate for imaging. Notably, HR-TEM images of AFt-PbS showed the lack of free PbS QDs outside the cages, which suggests successful encapsulation of PbS QDs within the AFt cavity. ImageJ analysis revealed a particle size of 11.9 ± 0.3 nm (Figure 3.6a inset), indicating that the pH-dependent encapsulation process did not significantly alter the size of the AFt nanocages. The PL emission of AFt-PbS was centred at λem = 1265 nm (1 eV) at room

temperature (Figure 3.6b), indicating that encapsulated PbS QDs retained their PL activity within AFt cages. The observed redshift peak may be attributed to Ostwald ripening, as AFt-PbS had been stored at 4 °C, under N_2 for a period of at least one month.[219] A similar shift in PL peak reported in PbS QDs upon aging (see Figure 3.2a). Then, the co-encapsulated formulation (AFt-PbS-TMZ) was evaluated using HR-TEM and PL studies. Figure 3.7a shows the HR-TEM image of AFt-PbS-TMZ. HR-TEM measured diameter (12.1 ± 0.6 nm) was consistent with the DLS-measured hydrodynamic diameter (14.3 ± 0.5 nm), as expected due to the difference between dry-state imaging (HR-TEM) and measurements taken in aqueous solution (DLS). HR-TEM image showed that there was no significant change in the expected size of the AFt cages (~12 nm) after the co-encapsulation process, and each cage successfully entrapped a single PbS QD. Furthermore, the representative AFt-PbS-TMZ structure seen in Figure 3.7a suggests strong interactions between PbS QD and TMZ molecules within AFt nanocages. These interactions may include electrostatic attraction between the functional groups of TMZ and QD surface, as well as hydrogen bonding between the NH_2 groups of TMZ and surface Pb (II) atoms or thiol-based capping agent (1-thioglycerol). In addition, TMZ may interact with the aromatic residues (tryptophan, tyrosine, and phenylalanine) lining in the inner surface of AFt cavity. The interior of AFt nanocages is also rich in hydrogen-bonding carboxylate groups (Aspartate/Glutamate) which have a potential to interact with NH_2 group or five strong hydrogen bond acceptors (N and O) on each TMZ molecule. Therefore, HR-TEM image of co-encapsulated formulation indicate successful co-encapsulation and TMZ-QD interactions in the protein nanocage.

Additionally, the optical properties of PbS QDs were assessed post-encapsulation and compared with PbS QDs alone. The PL emission of PbS QDs alone was centred at λem = 1118 nm (1.1 eV) at room temperature (see Figure 3.1b). After co-encapsulation, their optical characteristics were retained, with only a slight redshift in the emission peak to λem = 1131 nm (1.09 eV**,** Figure 3.7b), likely due to a reduction in quantum confinement strength.[110]

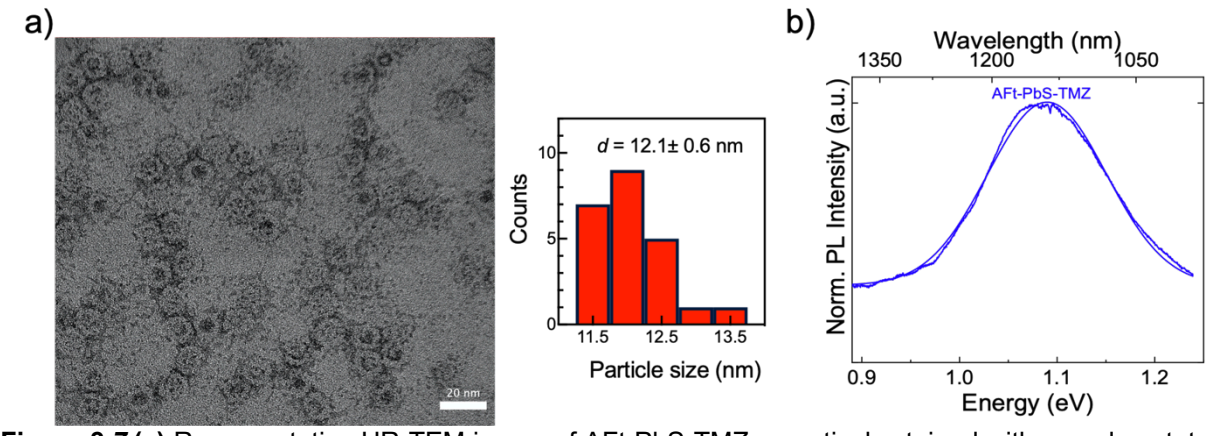

Figure 3.7 (a) Representative HR-TEM image of AFt-PbS-TMZ, negatively stained with uranyl acetate and a size distribution histogram shown in the insert. 23 particles were analysed from the HR-TEM image**. (b)** Room temperature photoluminescence (PL) spectra of AFt-PbS-TMZ.

3.2.4 *In vitro* drug release studies: comparative analysis of AFt-TMZ and AFt-PbS-TMZ

The release profiles of TMZ from both AFt-TMZ and AFt-PbS-TMZ formulations were evaluated *in vitro* under different physiologically-relevant pH conditions over time - at pH 7.4 and pH 5.5, at 37 °C for 72 h, to mimic both healthy and tumour microenvironments and possible release in blood stream (pH 7.4) and intracellular endosome (pH 5.5). However, GBM tumour is more alkaline than surrounding normal brain, facilitating TMZ activation.[228] As shown in Figure 3.8, the cumulative release of TMZ from both formulations was clearly illustrated.

The comparative drug release studies demonstrated rapid release of TMZ from the cages under acidic conditions for both formulations. Notably, TMZ release was ~78% from AFt-TMZ, and ~70% from AFt-PbS-TMZ after 24 h (Figure 3.8a). This slight difference in release percentage values was not statistically significant, suggesting that both AFt formulations exhibited effective drug release in acidic conditions, mimicking the endosomal environment. The results are consistent with pH-triggered drug release in the acidic intracellular endosomal environment following recognition and uptake of AFt nanoformulations by the tumour cells. On the other hand, at pH 7.4, significant difference in release profiles was observed between the

two formulations. For example, after 24 h, 82% TMZ was released from AFt-TMZ, but only 33% TMZ was liberated from AFt-PbS-TMZ. This difference in drug release at physiological pH was highly significant at 24 h ($p < 0.0001$) and remained significant at 48 h ($p < 0.001$). These results demonstrated that the co-encapsulated formulation AFt-PbS-TMZ remained more stable than AFt-TMZ preventing release of TMZ cargo at pH 7.4. This drug release behaviour of AFt-PbS-TMZ might indicate the reduction of premature TMZ release during systemic circulation and only release of drug cargo upon sequestration by tumour cells. This effect may be related to interactions between the PbS QD surface and TMZ. The higher partial charge on TMZ functional groups may interact with surface charge on the PbS QD surface, while at higher pH lead ions may also bind to MTIC, conferring additional stability, as previously reported for CuNPs.[180] Additionally, TMZ may bind to the corona of QDs or π-stack with aromatic residues (tryptophan, tyrosine, phenylalanine) on the AFt (interior) surface and hydrophobic pores. Similarly, enhanced TMZ stability has reported when TMZ binds to carrier systems including protein-based NPs.[223, 229] Overall, the results suggest the advantage of co-encapsulation of PbS QDs and TMZ into AFt nanocages, which may provide additional stabilisation and enable pH-induced control of the rate of TMZ release.

These data support the premise of tumour-targeted delivery and minimisation of off-target toxicity in healthy tissues. In addition, the reduction of TMZ release from AFt-PbS-TMZ under physiological conditions may be attributed to the presence of the PbS QD within the AFt cavity, influencing the release behaviour of TMZ. The presence of a PbS QDs may partially obstruct the AFt channels, thus reducing TMZ leakage resulting in improved retention of TMZ in the AFt-PbS-TMZ formulation. Additionally, the interaction of the PbS QD and TMZ within AFt cages may impact TMZ release. Similarly, Cassioli *et al.* reported comparable results when co-encapsulating copper phenanthroline and TMZ into horse spleen AFt, demonstrating that the co-encapsulated formulation retained 58% TMZ over 24 h (at pH 7.4) in the AFt nanocages, compared with only 18% retention for AFt-TMZ in the absence of copper phenanthroline.[174]

Overall, both AFt formulations (AFt-TMZ and AFt-PbS-TMZ) exhibited a greater stability at pH 7.4 compared to pH 5.5, consistent with previous studies showing pH-dependent drug release from AFt nanocages.[83, 174, 213] This behaviour may be explained by the structural changes in AFt at acidic pH, where protein channels relax and widen, facilitating cargo release. This aligns with the proposed AFt cellular internalisation pathway from vesicle to endosome (early endosome pH 6.5, late endosome pH 5.5) and then lysosomes (pH 4.5). The gradual acidification triggers the release of the agents from AFt cages.[174] Therefore, the observed release profiles in the study support the cancer selective delivery potential of AFt formulations.

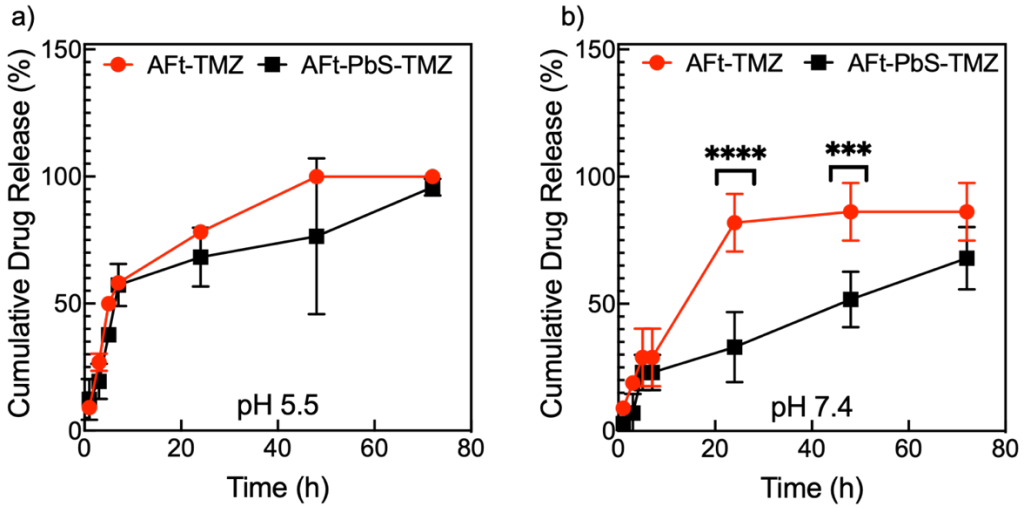

Figure 3.8 Temozolomide (TMZ) release profiles of AFt-TMZ and AFt-PbS-TMZ at **(a)** pH 5.5 and **(b)** pH 7.4 at 37°C.

3.2.5 Assessment of size and zeta potential stability after 1 month storage

To evaluate the stability of nanoformulations, the size and surface charge were measured after one-month storage at -80 °C in 0.1 M NaOAc buffer (pH 5.5). Figure 3.9 demonstrates the comparison of size (Figure 3.9a) and zeta potential (Figure 3.9b) measurements of AFt formulations (AFt-TMZ, AFt-PbS and AFt-PbS-TMZ). The results demonstrated that the hydrodynamic size and zeta potential measurements of AFt samples stored for one month were comparable to those of freshly prepared samples. For example, the average hydrodynamic size of AFt-TMZ was measured at 12.0 ± 0.9 nm for freshly prepared samples

and 11.7 ± 1.7 nm after one month of storage. Similarly, no significant (p > 0.05) changes were observed in the hydrodynamic size of AFt-PbS (fresh: 12.3 ± 0.7 nm; 1 month stored: 13.7 ± 1.7 nm) and AFt-PbS-TMZ (fresh: 14.0 ± 0.5 nm; 1 month stored: 12.6 ± 0.9 nm) formulations.

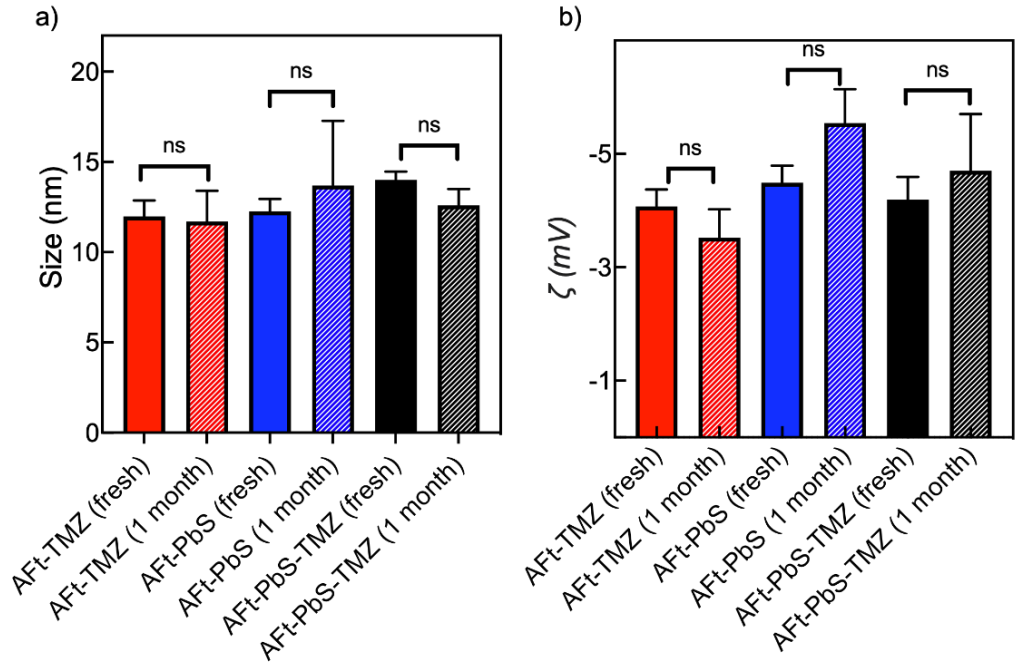

Figure 3.9 Stability study of AFt formulations (AFt-TMZ, AFt-PbS, AFt-PbS-TMZ) monitored by dynamic light scattering (DLS) in terms of **(a)** size and **(b)** zeta potential at storage conditions (T = -80 °C).

In addition, zeta potential measurements using DLS were also employed to evaluate the stability of AFt formulations, providing insight into the presence of agents within the cage. For instance, the average zeta potential was -4.1 ± 0.3 mV for fresh AFt-TMZ and -3.5 ± 0.5 mV for the 1-month-old formulation. After 1 month of storage, the zeta potential values for AFt-PbS and AFt-PbS-TMZ formulations were measured as -5.5 ± 0.6 mV and -4.7 ± 1.0 mV, respectively, with no significant changes observed (p > 0.05). These results suggest that both single and co-encapsulated agents remained within the AFt nanocages over time, exhibiting minimal changes in particle size and zeta potential after 1 month of storage. These results indicate that the AFt formulations maintained their stability and protein integrity following the optimised encapsulation processes. Specifically, AFt-TMZ utilised the nanoreactor encapsulation method, AFt-PbS employed a pH-dependent method and AFt-PbS-TMZ used combination of both techniques. Maintaining the structural integrity of these formulations is

crucial for ensuring the long-term stability of the NPs and supports their potential use in diagnostic, therapeutic, and theranostic applications.

3.3 Conclusion

In conclusion, to combat major limitations associated with conventional imaging and therapy methods for GBM, nanotechnology-based approaches are required. This chapter has demonstrated synthesis and characterisation of PbS QDs and their successful encapsulation in a biocompatible nano-sized delivery vehicle, AFt, to combat their limitations which restrict their clinical use. Additionally, encapsulation of PbS QDs, TMZ, and TMZ+ PbS QDs within AFt cages was successfully optimised and characterised. Distinct encapsulation methods were used as disassembly/reassembly for PbS QDs (entrapped one QD per AFt cage) and passive diffusion for TMZ. Encapsulation resulted in 516 and 309 TMZ molecules per cage for AFt-TMZ and AFt-PbS-TMZ, respectively with >70% EE. High numbers of TMZ molecules per AFt cage were loaded in both formulations, compared to previous reports of encapsulation of other clinical and experimental agents, attributed to the small size and pH-dependent stability of TMZ.

Characterisation studies confirmed that AFt formulations maintained their morphology, size, integrity, as analysed by HR-TEM, DLS, Native-PAGE, and PL measurements. In addition, PbS QDs retained their PL properties post encapsulation, supporting their potential application in NIR-II imaging. Furthermore, *in vitro* release studies demonstrated pH dependent TMZ release, with both formulations releasing >70% TMZ at acidic pH, while showing enhanced stability at pH values associated with the bloodstream. This behaviour makes AFt a promising nanocarrier for targeted delivery applications. Remarkably, the co-encapsulated formulation exhibited better TMZ retention at pH 7.4, making it suitable for *i.v.* delivery and tumour targeted release. Stability evaluations by DLS confirmed that all AFt formulations remained stable in terms of size and zeta potential after one month storage at -80 °C.

Altogether, these results confirmed the suitability of AFt as a multifunctional drug delivery platform for combined diagnostic and therapeutic applications in GBM. However, further investigations are needed to evaluate long-term stability of AFt formulations investigating TMZ stability in AFt cages. In addition, it is necessary to investigate their effect with *in vitro* and *in vivo* studies before clinical translation.

Chapter 4 Comparative analysis of naked and encapsulated formulations in 2D *in vitro* models

4.1 Background

Drug delivery and therapeutic efficacy in the brain are limited by both biophysical and biochemical barriers. One of the obstacles is the BBB, which includes endothelial cells, pericytes, ECM, and astrocytes. These components constitute a selective biophysical barrier that restricts drug passage depending on size, lipophilicity, electric charge, and interactions with BBB proteins. Additionally, the BBB has biochemical barriers, such as drug efflux pumps such as P-gp, which prevent drugs from accumulating in the brain.[38]

Innovative targeted delivery strategies hold promise for GBM therapy, overcoming the challenges posed by the BBB, since they enable selective accumulation of therapeutic agents in tumour tissues while minimising off-target toxicity in healthy tissues. The relationship between iron metabolism and GBM has led to investigation of new approaches focusing on TfR1 expression in GBM therapy, which is overexpressed in GBM cells and abundant in BBB endothelial cells. Additionally, targeting (blocking) ferroportin has become a strategy in GBM research to induce ferroptosis in TMZ-resistant cells, (in combination with TMZ) to reduce resistance.[230] As a result, TfR1-targeted DDS have gained interest for their potential to enhance therapeutic efficacy and overcome resistance mechanisms in GBM management.[31] For this purpose, natural TfR1 binding proteins such as AFt have shown a great potential in the advancement of GBM therapies through development of novel formulations. Previous studies have demonstrated AFt's selective uptake *in vitro* by GBM cells[83, 172, 174] and its ability to accumulate in brain tumours *in vivo*,[173, 176] further supporting its application in advanced GBM strategies such as the use of theranostics. The integration of diagnosis and therapy into AFt presents a promising multifunctional nanoplatform for GBM.

In this chapter, initial evaluation of AFt formulations was performed in 2D monolayer cultures due to their cost-effectiveness and high experimental reproducibility. Comparative *in vitro* growth inhibition of delivery vehicle (AFt), naked (TMZ, PbS QDs) and loaded formulations (AFt-TMZ, AFt-PbS, AFt-PbS-TMZ) was evaluated using MTT and PB methods in both 2D cancerous (GBM) and non-cancerous cell lines. In this chapter and those that follow, ‘’naked’’ refers to free/unencapsulated agents whereas ‘’encapsulated’’ describes agents that have been encapsulated within AFt nanocages. Vehicle refers to AFt (for loaded formulations/AFt-encapsulated agents), or for naked agents, vehicle refers to DMSO/medium/water/TMZ/QD solubilising vehicle. The study used three GBM cell lines, demonstrating different TMZ resistance profiles: U373M (MGMT-transfected), U373V (vector control), and U87MG (MGMT low). In addition, three non-cancerous cell lines were used in the study: human astrocytes, which are required for BBB homeostasis and from which cell type gliomas may derive, MRC-5 foetal lung fibroblasts, and THLE-2, a healthy liver cell line. The selectivity of AFt nanocages toward cancer (GBM) cells was investigated. Moreover, the impact of AFt encapsulation on cellular NP uptake and TMZ resistance mechanisms were investigated by analysing TfR1 and MGMT expression levels respectively in 2D cells. As a result, this chapter provides information pertinent to the diagnostic, therapeutic, and theranostic potential of AFt formulations in comparison to naked agents in 2D *in vitro* models.

Chapter hypothesis: Herein is tested the hypothesis that co**-**encapsulation of TMZ and a PbS QD within AFt nanocages will enhance their *in vitro* growth inhibitory effect in 2D GBM cells compared to their naked agent counterparts and single agent encapsulated formulations. Furthermore, it is examined whether AFt-based TfR1 targeted delivery has potential to minimise potential off-target cytotoxicity by protecting healthy tissues, thus improving therapeutic cancer selectivity and safety.

Chapter experimental aims: The experimental aims of this chapter include the evaluation of whether optimised targeted theranostic AFt formulation enhances the growth inhibitory activity compared to naked agents and single agent encapsulated formulations, and whether it exhibits

cancer selective activity in 2D GBM cultures with different TMZ resistance profiles, using two complementary cytotoxicity assays (MTT and PB), the investigation of off-target cytotoxicity of AFt formulations by assessing their activities in non-cancerous cell lines, evaluating whether targeted delivery mechanism of AFt nanocages is mediated through TfR1 receptor recognition using two complementary approaches: assessment of TfR1 protein levels and single cell receptor expression, and investigation of the mechanisms underlying the enhanced therapeutic activity of AFt encapsulation by examining MGMT protein expression levels, which are associated with TMZ resistance in GBM cells.

4.2 Results and discussion

4.2.1 *In vitro* evaluation of growth inhibition using MTT assay: comparison of naked and encapsulated formulations

The *in vitro* growth inhibitory effects of vehicles (including formulation vehicle AFt), naked agents (TMZ, PbS QDs) and loaded formulations (AFt-PbS, AFt-TMZ, AFt-PbS-TMZ) were initially evaluated by MTT assay in GBM cell lines (U373M, U373V, U87MG) and non-cancerous MRC-5 fibroblasts. In the study, incubation time was selected as 6 days to allow enough time for DNA methylation, MMR activation, and two cell cycle phases progression.

Initially, AFt alone and DMSO (at the vehicular concentrations used) were evaluated using MTT assay and demonstrated insignificant growth inhibitory effects on the studied cell lines. Subsequently, serial dilutions of test agents/formulations were tested, and the adopted concentration ranges are exemplified in Figure 4.2. Then, estimated GI_{50} values were calculated to evaluate the preliminary 2D growth inhibitory effects of naked and loaded formulations in both GBM and non-cancerous cells. The GI_{50} for PbS QDs and AFt-PbS was expressed in μg/mL whereas μM GI_{50} values for TMZ-based treatments (TMZ, AFt-TMZ,

TMZ+PbS QDs, AFt-PbS-TMZ) were reported. The comparative results are summarised in Table 4.1 and illustrated graphically in Figure 4.1.

Comparative analysis of PbS QDs-based formulations revealed that naked PbS QDs exhibited more pronounced growth inhibitory effects, showing low GI_{50} values in both GBM cells as well as in non-cancerous MRC-5 fibroblasts. In contrast, AFt-PbS demonstrated significantly reduced *in vitro* growth inhibition towards MRC-5 lung fibroblasts, with a 19-fold increase in GI_{50} value ($p < 0.0001$), while maintaining its *in vitro* growth effects in all studied GBM cell lines (GI_{50} range: 1.3-2.3 µg/mL, Figure 4.1a). Similar cancer-selective effects of AFt-PbS have been reported, implying protection against cytotoxicity for colorectal[216] and breast[224] cancer cells, previously. These results confirmed that encapsulating PbS QDs in AFt cages provides a protective shield in the non-cancerous MRC-5 fibroblasts.

Table 4.1 Summary of GI_{50} for all formulations following 6 days treatment in the studied cell lines (Mean ± SD, n = 3).

Cell lines	**PbS QDs (µg/mL)**	**AFt-PbS (µg/mL)**	**TMZ (µM)**	**AFt-TMZ (µM)**	**TMZ + PbS QDs (µM)**	**AFt-PbS-TMZ (µM)**
	GI_{50}(PbS QDs)			**GI_{50}(TMZ)**		
U373M	0.3 ± 0.1	1.3 ± 0.8	494.0 ± 21.1	3.7 ± 1.4	0.9 ± 0.1	1.5 ± 0.8
U373V	0.6 ± 0.1	1.6 ± 0.7	24.0 ± 4.9	7.3 ± 2.7	0.9 ± 0.1	3.1 ± 0.6
U87MG	2.7 ± 0.2	2.3 ± 0.1	40.0 ± 3.0	2.5 ± 2.6	1.1 ± 0.1	1.9 ± 0.1
MRC-5	2.6 ± 0.1	47.0 ± 2.5	211.1 ± 43.1	50.0 ± 0.1	2.7 ± 0.1	27.1 ± 1.8

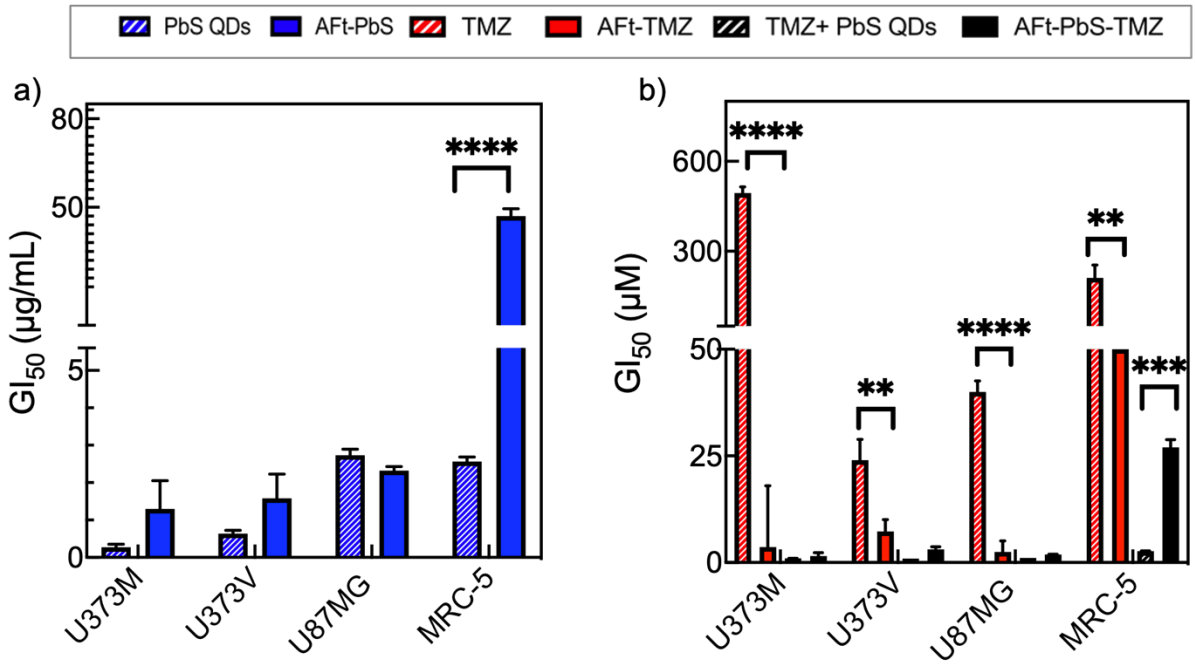

Figure 4.1 GI_{50} values obtained from MTT assay based on **(a)** PbS QDs (µg/mL) and **(b)** TMZ (µM) concentrations on glioblastoma (GBM) and non-cancerous cell lines. Data are presented as mean ± SD of samples from three independent experiments (n = 3, N = 6).

The comparison of cellular growth inhibitory effects of TMZ and AFt-TMZ demonstrated that encapsulation of TMZ in AFt cages significantly reduced GI_{50} values across all studied GBM cell lines (see Table 4.1 and Figure 4.1b). For example, U373M cells (MGMT-positive) exhibited a TMZ GI_{50} of 494.0 ± 21.1 µM, making them 20.6-fold and 12.4-fold less sensitive to naked TMZ than U373V (GI_{50}: 24.0 ± 4.9 µM) and U87MG (GI_{50}: 40.0 ± 3.0 µM) cells, respectively in agreement with previous studies.[83, 174] However, when TMZ is encapsulated within AFt cages, significantly lower TMZ concentrations are required to evoke the same response in all studied GBM cells. AFt-TMZ treatment led to a 134-fold reduction in GI_{50} (p < 0.0001) in U373M (TMZ resistant) cells, while reductions of 3.3-fold (p < 0.01) and 16-fold (p < 0.0001) were observed in U373V (TMZ sensitive) and U87MG (TMZ sensitive) cells, respectively, following 6 days treatment. These results aligned with the findings of Bouzinab *et al*. who found similar GI_{50} values in U373M and U373V cells under same experimental settings.[83] In addition, our findings corroborated those of Shargh *et al.* in paediatric DMG cell lines.[172] However, the activity potentiation conferred by AFt encapsulation in GBM cells was not observed in non-cancerous MRC-5 cells to the same degree. This effect may be attributed to both TfR1 expression levels and pH-dependent stability of TMZ. Although MRC-5 cells are

non-cancerous, they may express basal levels of TfR1 that are enough to permit uptake of AFt nanocages. Additionally, AFt encapsulation may enhance TMZ stability under acidic conditions (pH 5.5), thereby reducing its degradation and increasing intracellular TMZ availability. Additionally, it has been reported that MRC-5 cells express MGMT[231], which is related to TMZ resistance. However, AFt encapsulation may overcome TMZ resistance, thus increase the activity of TMZ in MRC-5 cells.

Furthermore, the naked combination (PbS QDs and TMZ) and co-loaded formulation (AFt-PbS-TMZ) were evaluated for their *in vitro* growth effects. While TMZ + PbS QDs showed lower GI_{50} values in U373M, U373V, and U87MG GBM cells compared to the AFt-PbS-TMZ formulation, the naked combination treatment also inhibited the growth of non-cancerous MRC-5 cells. In contrast, AFt-PbS-TMZ conferred significant ($p < 0.001$, 10-fold) protection for MRC-5 cells, due to its targeted delivery. Moreover, AFt-PbS-TMZ demonstrated enhanced activity in GBM cells relative to AFt-TMZ, highlighting its dual potential for therapeutic and tumour imaging, thus addressing limitations in both conventional treatment and current imaging constraints. Figure 4.2 illustrates percentage (%) cell viability obtained from MTT assays conducted on all studied cell lines, with mean control values defined as 100%.

Overall, preliminary MTT results indicated that AFt-PbS-TMZ demonstrated enhanced cellular growth inhibitory activity in GBM cell lines compared to naked TMZ and AFt-TMZ, while offering protection to healthy cell lines, which was not observed with TMZ + PbS QDs treatment. Considering the targeted delivery capabilities of AFt, and its ability to improve activity in GBM cell lines, AFt-PbS-TMZ may present a promising theranostic nanoplatform for GBM management, combining diagnostic and therapeutic applications in a single platform.

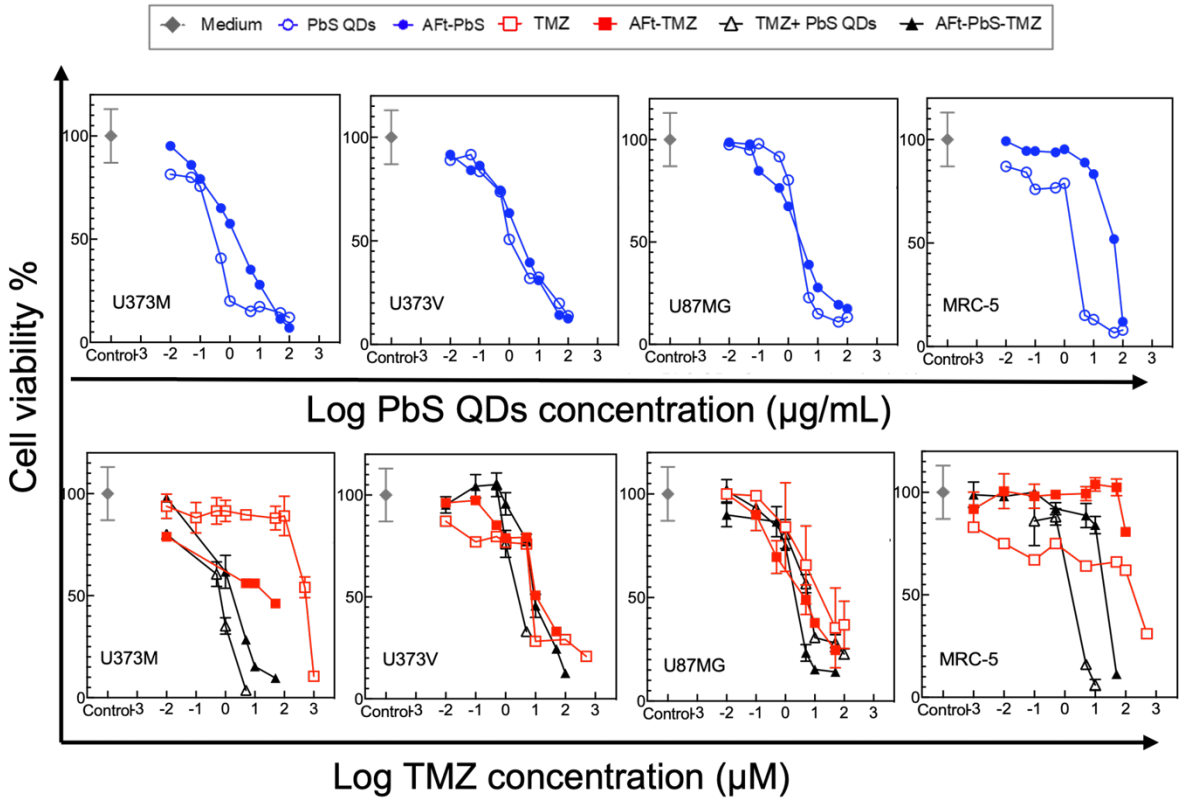

Figure 4.2 Concentration-dependent (lead sulfide quantum dots (PbS QDs) (top) and temozolomide (TMZ) (bottom) growth inhibition profiles of all studied cells determined by MTT assay. U373M, U373V, U87MG were used as glioblastoma (GBM) cells while MRC-5 lung fibroblast served as a non-cancerous cell line. Data are presented as mean ± SD of samples from three independent experiments (n = 3, N = 6).

4.2.2 *In vitro* evaluation of growth inhibition using PrestoBlue Assay: comparison of naked and encapsulated formulations

To validate and support the results from MTT assay, PB assay was performed on the same GBM cell lines and non-cancerous MRC-5 fibroblasts. In addition, human astrocytes and THLE-2 hepatocytes were included as 2D healthy cell line models to assess biocompatibility and off-target toxicity of loaded formulations. Astrocytes play a crucial role in determining and controlling BBB homeostasis[40] whereas THLE-2 hepatocytes serve as healthy liver cells, which are essential for iron homeostasis, drug metabolism and clearance.[232] Several studies reported QDs accumulation in the liver,[233, 234] making it an appropriate 2D cell model for testing potential toxicity of PbS QDs-based formulations. Altogether, AFt-based formulations were evaluated in

various non-cancerous cells, which is crucial for evaluating their potential for clinical translation.

Subsequently, estimated IC_{50} were calculated for each naked/encapsulated formulation and are summarised in Table 4.2. In addition, the comparative IC_{50} values are presented in Figure 4.3. The consistently low IC_{50} values observed for PbS QDs confirmed that their growth inhibitory effect across all studied cell lines. In contrast, AFt-PbS exhibited cancer selectivity via targeting GBM cells yet provided significant protection to non-cancerous MRC-5 fibroblasts ($p < 0.0001$) and astrocytes ($p < 0.001$) (Figure 4.3a). On the other hand, AFt-TMZ resulted in a 3-fold reduction in IC_{50} compared to naked TMZ in U373M cells. In U87MG cells, AFt-TMZ led to a 7-fold decrease in IC_{50}, indicating enhanced activity conferred by AFt encapsulation in GBM cells. However, no significant ($p > 0.05$) change in IC_{50} was observed in U373V cells. Regarding non-cancerous cells, consistent with MTT data, AFt-TMZ caused greater (3.3-fold) growth inhibition than naked TMZ in MRC-5 fibroblasts but showed a 1.3-fold decrease in activity in astrocytes. Finally, when comparing the effects of TMZ + PbS QDs and AFt-PbS-TMZ, naked combination exhibited more potent results in GBM cells, which may be attributed to rapid bioavailability of both agents without requiring release from the nanocarrier. However, this naked combination also showed significant growth inhibition in non-cancerous cells. In contrast, AFt afforded a protective effect in healthy cells and AFt-PbS-TMZ demonstrated a 15-fold reduction in growth inhibition in MRC-5 cells ($p < 0.001$) and a 12-fold reduction in astrocytes ($p < 0.0001$), highlighting its cancer selective targeting potential (Figure 4.3b). Figure 4.4 summarises the comparative cell viability results in each cell line tested for each agent and formulation following 6 days exposure of cells to test agents.

Remarkably, THLE-2 cells exhibited a distinct profile compared to other studied non-cancerous cell lines (MRC-5 and astrocytes). PB assay results showed that there were no significant ($p > 0.05$) differences observed between all naked and loaded formulations (Figure 4.3). This lack of protection towards healthy liver cells may be attributed to the high expression levels of TfR1

in THLE-2 cells (see Section 4.2.4), which plays a central role in iron uptake, and mediates the AFt-based formulation internalisation.

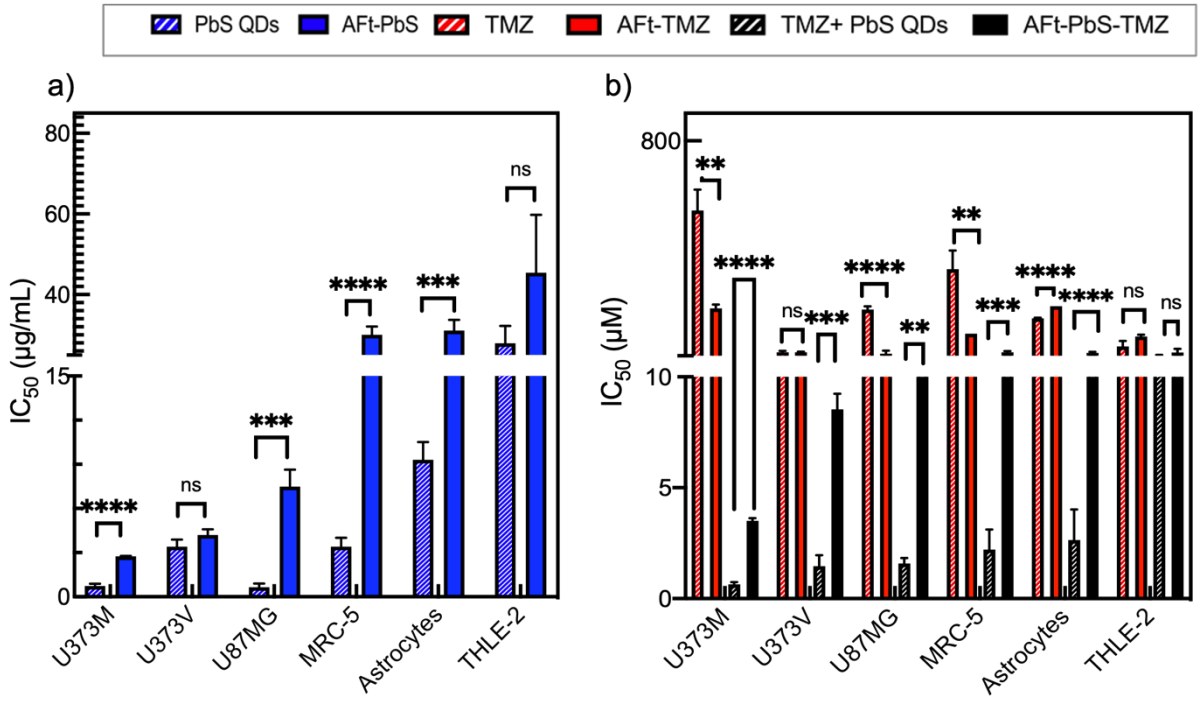

Figure 4.3 (a) Comparison of IC_{50}(PbS QDs) values (μg/mL) for PbS QDs and AFt-PbS in all studied cell lines with PB assay. **(b)** Comparison of IC_{50}(TMZ) values (μM) for TMZ, AFt-TMZ, TMZ+ PbS QDs and AFt-PbS-TMZ in all studied cell lines with PrestoBlue (PB) assay. Data are presented as mean ± SD of samples from three independent experiments (n = 3, N = 6).

Table 4.2 Summary of IC_{50} for all formulations following 6 days treatment in the studied cell lines (Mean ± SD, n = 3).

Cell lines	PbS QDs (μg/mL)	AFt-PbS (μg/mL)	TMZ (μM)	AFt-TMZ (μM)	TMZ + PbS QDs (μM)	AFt-PbS-TMZ (μM)
	IC_{50}(PbS QDs)		IC_{50}(TMZ)			
U373M	0.7 ± 0.2	2.7 ± 0.3	547.0 ± 76.2	192.1 ± 13.8	0.6 ± 0.1	3.5 ± 0.1
U373V	3.4 ± 0.5	4.2 ± 0.4	33.2 ± 4.9	32.9 ± 2.1	1.5 ± 0.5	8.5 ± 0.7
U87MG	0.7 ± 0.3	7.5 ± 1.2	188.0 ± 11.6	27.5 ± 11.2	1.6 ± 0.3	10.9 ± 2.7
MRC-5	3.4 ± 0.6	30.0 ± 2.1	334.3 ± 67.4	>100	2.2 ± 0.9	32.9 ± 4.3
Astrocyte	9.3 ± 1.2	31.1 ± 2.6	156.4 ± 1.9	>200	2.6 ± 1.4	30.5 ± 3.9
THLE-2	27.9 ± 4.3	45.4 ± 14.3	54.5 ± 19.8	89.8 ± 7.2	15.1 ± 8.4	31.9 ± 13.2

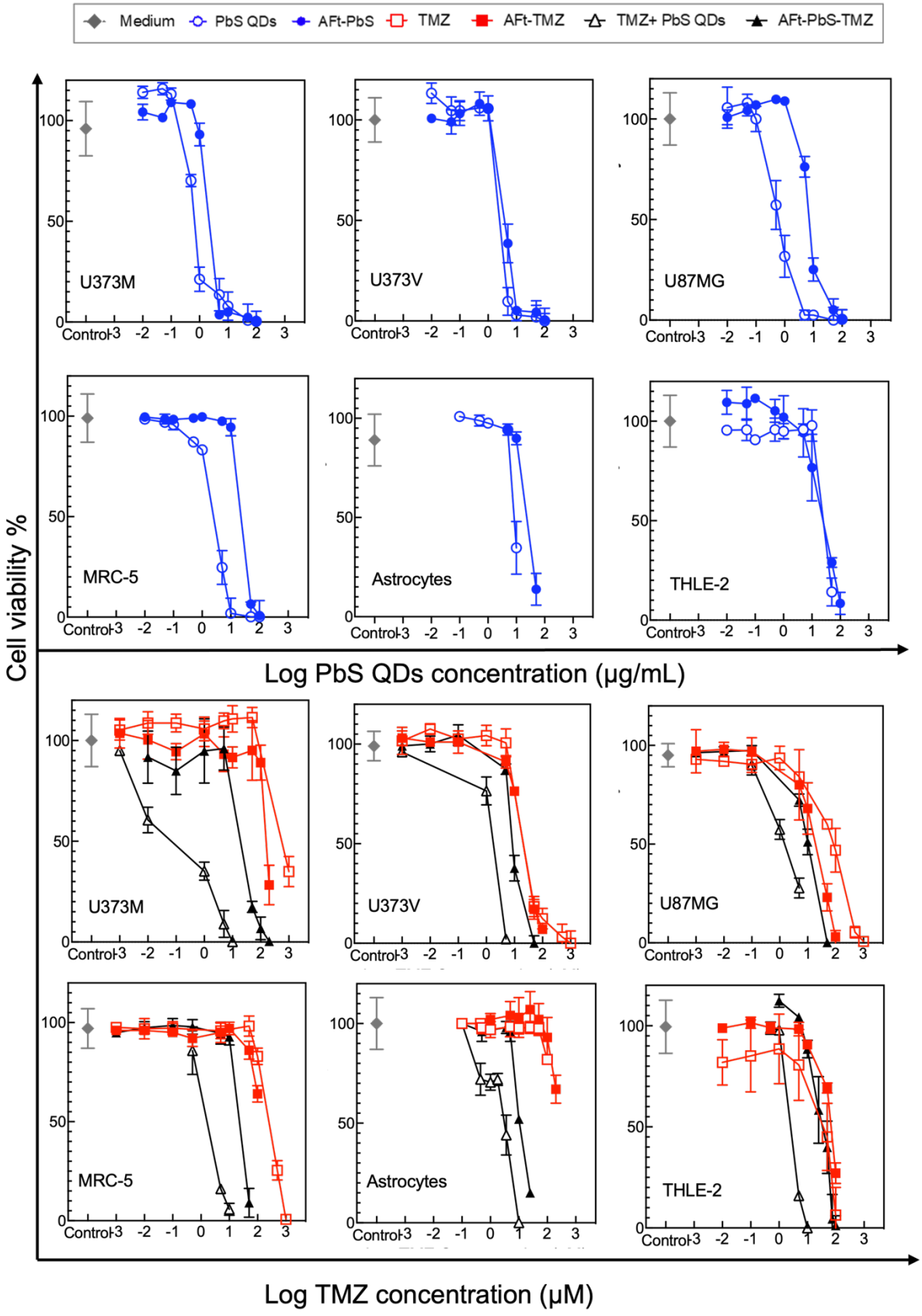

Figure 4.4 Concentration-dependent (lead sulfide quantum dots (PbS QDs, top) and temozolomide (TMZ, bottom) growth inhibition profiles of all studied cell lines obtained from PB assay. U373M, U373V, U87MG were used as glioblastoma (GBM) cells, and MRC-5, astrocytes, and THLE-2 as non-cancerous cell lines in the assay. Data are presented as mean ± SD of samples from three independent experiments (n = 3, N = 6).

4.2.3 Comparative analysis of MTT and PrestoBlue assays for cell viability assessment

The IC_{50} values derived from MTT and PB assays in 2D cell cultures post treatment for 6 days with vehicle control, naked, and loaded formulations were analysed and are presented in Figure 4.5. The administration of AFt alone (vehicle control) yielded similar IC_{50} values in both MTT and PB assays (Figure 4.5a). Although IC_{50} values for AFt alone appeared to fall within the low micromolar range, it is important to note that 1 μM AFt corresponds to 4.6 mg/mL of protein. In the study, the highest initial AFt concentrations tested were 2 mg/mL and 3 mg/mL, which were equivalent to 0.43 μM and 0.65 μM, respectively. Therefore, IC_{50} values could not be experimentally determined, as they exceed the maximum concentration tested. The apparent low micromolar IC_{50} values represent only minimal biological effect, suggesting negligible growth inhibitory effect of AFt on all studied cell lines (Figure 4.5a). On the other hand, the treatment of U87MG and MRC-5 cells with PbS QDs and AFt-PbS for 6 days resulted in observable differences (Figure 4.5b). The observed differences in sensitivity and results may be attributed to the effects of treatments on metabolic activity. In terms of metabolic activity, the MTT assay quantifies the reduction of MTT dye by mitochondrial dehydrogenase enzymes in viable cells, leading to the production of formazan crystals. In contrast, PB assay evaluates the reduction of resazurin to resorufin in viable cells, involving both mitochondrial and cytoplasmic enzymes. Conversion of resazurin to resorufin is associated with cellular redox activity involving NAD(P)H.

To exemplify this point, estimated IC_{50} values calculated for TMZ were as follows 607.0 ± 48.1 μM, 34.1 ± 1.0 μM, 180.1 ± 17.2 μM, and 305.1 ± 39.2 μM in MTT assays and 547.0 ± 76.2 μM, 33.2 ± 4.9 μM, 188.0 ± 11.6 μM, and 334.3 ± 67.4 μM in PB assays for U373M, U373V, U87MG and MRC-5 cells, respectively (Figure 4.5). IC_{50} values obtained for TMZ, TMZ + PbS QDs, and AFt-PbS-TMZ in MTT and PB assays showed non-statistically significant ($p > 0.05$) differences. However, potential variations were observed across different cell lines, which may

be attributed to differences in cellular metabolism, enzyme expression, and redox conditions of each cell line. For example, Lam *et al.*[39] and Soni *et al.*[235] reported IC_{50} values as 105 μM and 300 μM, respectively, for TMZ on U87MG cells following five days treatment. These variations in IC_{50} values, despite using the same cell line (U87MG), may be attributed to differences in experimental conditions (passage number, assay sensitivity etc).

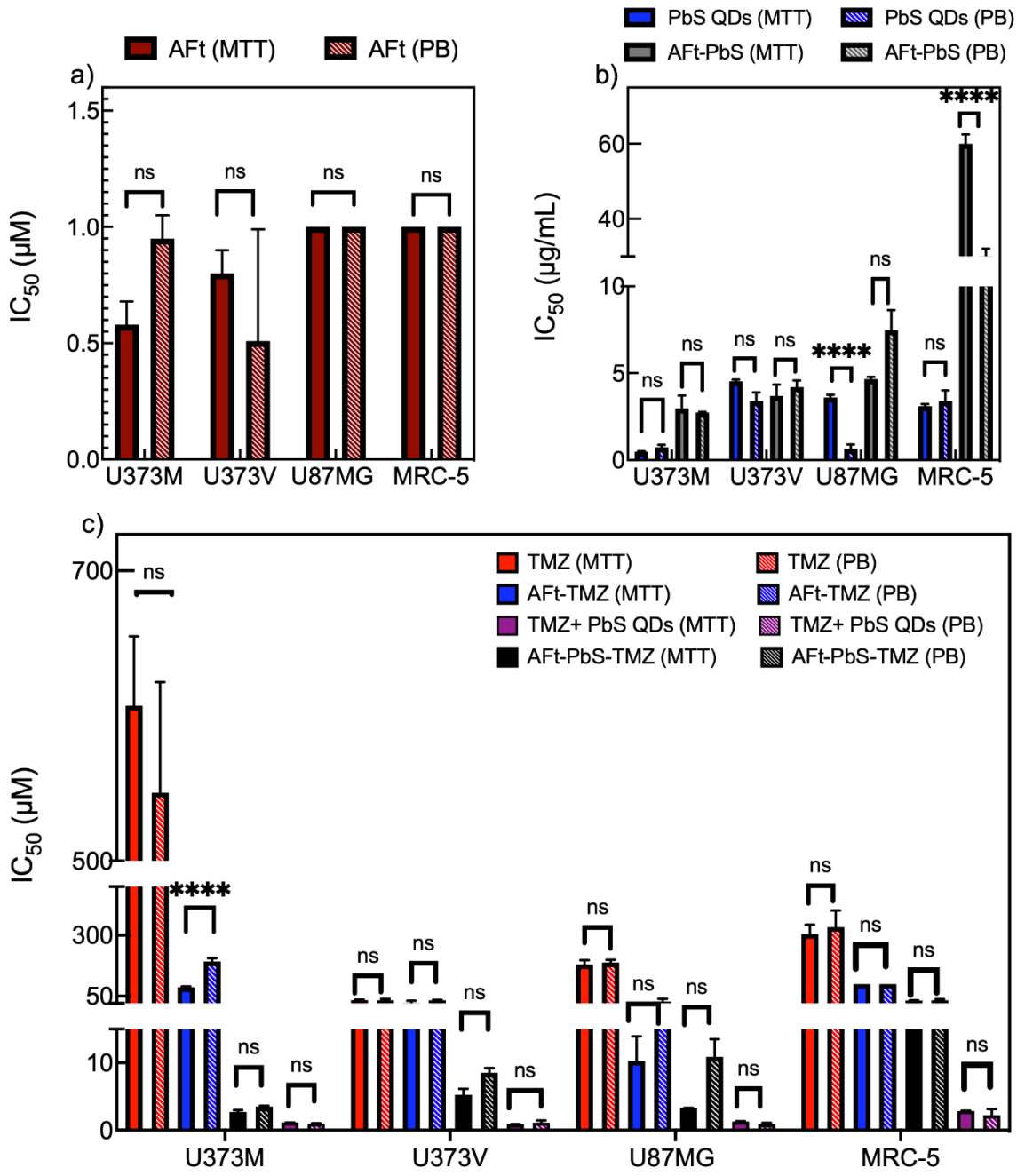

Figure 4.5 Comparison of the effect of naked and loaded formulations on cell proliferation, assessed by MTT and PrestoBlue (PB) assays *in vitro* in GBM cell lines (U373M, U373V, and U87MG) and a healthy cell line (MRC-5). IC_{50} values comparison of **(a)** AFt (vehicle), **(b)** PbS QDs, AFt-PbS, **(c)** TMZ, AFt-TMZ, TMZ+ PbS QDs and AFt-PbS-TMZ on GBM and MRC-5 cell lines. Data are presented as mean ± SD of samples from three independent experiments. (n = 3, N = 6).

On the other hand, AFt-TMZ generated a considerably lower IC_{50} value in U373M cells in the MTT assay than in the PB assay ($p < 0.0005$). This assay-dependent discrepancy between MTT and PB assays is consistent with Bouzinab *et al.* results[83], where MTT and clonogenic assays similarly disagreed when comparing naked TMZ and AFt-TMZ, suggesting that MTT assay appears to give much larger margins in activity differences between TMZ and AFt-TMZ. Consistent with MTT assay results, live cell count assay demonstrated significant ($p < 0.0001$) reduction in U373M cells treated with AFt-TMZ compared to those treated with TMZ.

For the rest of the studied cell lines, however, these two experiments yielded comparable IC_{50} results. The co-encapsulated formulation (AFt-PbS-TMZ) showed no significant differences across examined cell lines, with IC_{50} values as follows: U373M (<4 μM), U373V (<9 μM), U87MG (<12 μM), MRC-5 (<38 μM), and human astrocytes (<35 μM). Overall, MTT and PB results demonstrated a high congruence despite their distinct mechanism of action. Therefore, a comparative analysis between a traditional MTT assay and non-toxic, more widely applicable PB assay provides an approach for assessing cell viability. These data indicate that PB assay is applicable in the subsequent studies including the evaluation of cell viability in 3D tumour spheroids.

4.2.4 Evaluation of expression levels of transferrin receptor 1 and *O*6-methylguanine-DNA methyltransferase

To evaluate the targeting potential of AFt formulations toward GBM cells, the expression of TfR1 was examined across all studied cell lines, including both GBM and non-cancerous cell lines. TfR1 plays a critical role in AFt uptake through its recognition of the H-chain subunit.[159] Therefore, TfR1 expression levels were assessed using two complementary methods: western blotting (to analyse whole-cell lysates) and flow cytometry (to quantify expression at the single-cell level). Western blot analysis results revealed detectable levels of TfR1 in GBM cell lines (U373M, U373V, and U87MG), while expression in non-cancerous cell lines, including MRC-5

fibroblasts and astrocytes, remained below detectable limits (Figure 4.6a). Additionally, TfR1 expression was assessed in THLE-2 liver cells, which demonstrated a high expression profile (Figure 4.6b). The high TfR1 expression in THLE-2 hepatocytes may promote AFt nanocage uptake and may negate any protective effect of AFt encapsulation. Conversely, the low TfR1 levels in MRC-5 fibroblasts and astrocytes may limit AFt internalisation, thus, resulting a protective effect of AFt formulations in these non-cancerous cells. Altogether, TfR1 band intensity profiles of U373M ($p<0.01$), U373V ($p<0.01$), U87MG ($p<0.05$), and THLE-2 ($p<0.05$) cells differed significantly from those of MRC-5 and astrocytes (Figure 4.6b), which were normalised using a housekeeping gene (GAPDH). Similarly, TfR1 expression in GBM cells (U373V, U373M and U87MG) and astrocytes using western blot, confirmed that TfR1 is significantly overexpressed in GBM tissues compared to normal brain tissues.[236] Additionally, Shen *et al.* demonstrated in a number of tissues including brain, ovarian, breast and colorectal greatly enhanced TfR1 expression in malignant versus normal tissues.[30] Hence we conclude that the uptake of AFt is related to TfR1 expression level in the studied cells, consistent with the hypothesis.

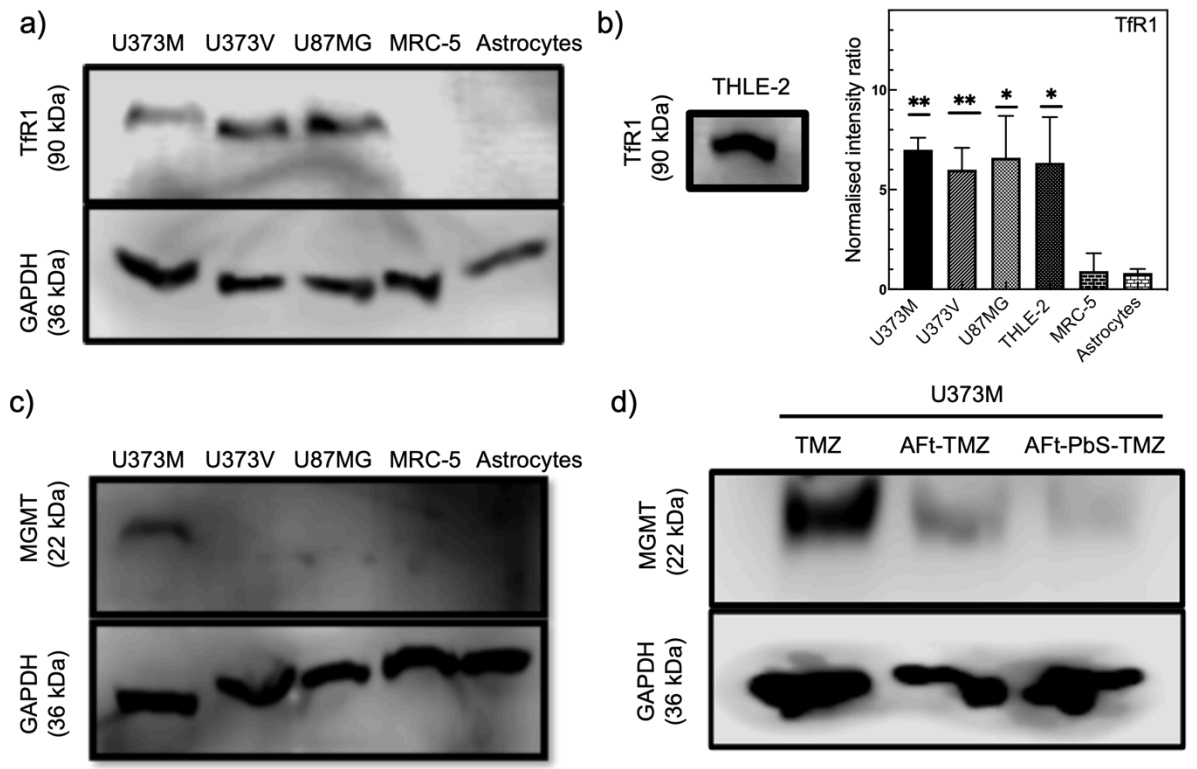

Figure 4.6 (a) Western blot analysis of transferrin receptor 1 (TfR1) and GAPDH (loading control) expressions in all studied cell lines **(b**) western blot analysis of TfR1 expression in THLE-2 liver cells, along with quantification of TfR1 band intensity normalised to GAPDH using LICOR software. **(c)** western blot analysis of MGMT and GAPDH expressions in all studied cell lines. **(d)** MGMT protein expression in U373M cells following 6 days treatment with 10 μM TMZ, AFt-TMZ, and AFt-PbS-TMZ, as determined by western blot.

Western blot was performed to examine the MGMT expression profile of the cells. The hypothesis under investigation was that AFt encapsulation results in enhanced delivery of this chemotherapy agent to cells, overwhelming the MGMT suicide repair protein resulting in its more rapid downregulation. The results confirmed that MGMT expression was detectable in U373M cells, but not in U373V, U87MG, MRC-5 and astrocytes cells (Figure 4.6c). To test the hypothesis proffered (of enhancement of *in vitro* growth inhibitory activity of AFt-encapsulated agent), U373M protein lysates were collected from U373M cells after 6 days treatment with 10 μM TMZ, AFt-TMZ, and AFt-PbS-TMZ, consistent with *in vitro* studies` experimental time. As shown in Figure 4.6d, treatment with both AFt formulations (AFt-TMZ and AFt-PbS-TMZ) led to a notable depletion of MGMT protein levels. Observed MGMT downregulation effect may be attributed to improved TMZ delivery and retention enabled by AFt encapsulation, leading to overwhelming accumulation of DNA damage, depleting MGMT and disabling MGMT- mediated

DNA repair of *O*6MeG, thus sensitizing MGMT-positive GBM cells to TMZ-induced cytotoxicity. MGMT is a suicide protein; once it is depleted, it becomes inactive and unable to repair DNA damage caused by TMZ. Therefore, GBM cells become more sensitive to TMZ-induced cytotoxicity. These results explain the activity of AFt formulations observed in U373M cells, as evidenced by cell viability assays.

In addition to western blot analysis, flow cytometry was utilised to measure the total (both surface and intracellular) expression of TfR1 at the single cell level. Therefore, cells (U373M, U373V, U87MG, and astrocytes) were stained with 1° Ab anti-human TfR1 monoclonal antibody (CAT:136800) and 2° Ab goat anti-mouse IgG (H+L) cross-adsorbed secondary antibody, Alexa Fluor™ 488 (CAT: A11001), respectively. Fluorescence intensities were measured from the single cells and recorded for three conditions: unstained cells, the cells stained with 2° Ab only, and the cells stained with both 1° Ab and 2° Ab. The relative mean fluorescence intensity (MFI) of the cells stained with 2° Ab only was used to correct for non-specific binding. Following that, the fold-change in TfR1 expression was calculated by comparing MFI of the cells stained with both 1° Ab and 2° Ab against MFI of 2° Ab only.

The flow cytometric quantification of TfR1 expression in U373M, U373V, U87MG and astrocytes is summarised in Figure 4.7. The flow cytometry analysis of 2D cells showed that TfR1 expression was significantly higher in U373M ($p < 0.01$), U373V ($p < 0.05$) cells compared to astrocytes, consistent with the western blot data. In contrast, TfR1 expression in U87MG was not significantly different from that in astrocytes based on flow cytometry results, which was lower than the findings from western blot. Differences between western blot and flow cytometry results, despite cell permeabilisation, may be attributed to technical factors. Although both methods detect total protein levels, western blot provides an average protein expression from the whole cell lysate, whereas flow cytometry assesses protein expression at the single cell level. Additionally, differences in antibody binding efficiency and detection sensitivity between the two methods could impact the results. Although the same antibody was used in both methods, its effectiveness in flow cytometry could be different. The

monoclonal antibody used in the study (clone H68.4) recognises an epitope located within residues 3-28 of cytoplasmic tail of TfR, a sequence that is conserved across different human cell lines. However, differences in antibody binding between cell lines are more likely attributable to variations in protein conformations, post-translational modifications, and membrane environment that can affect epitope accessibility rather than epitope sequence.

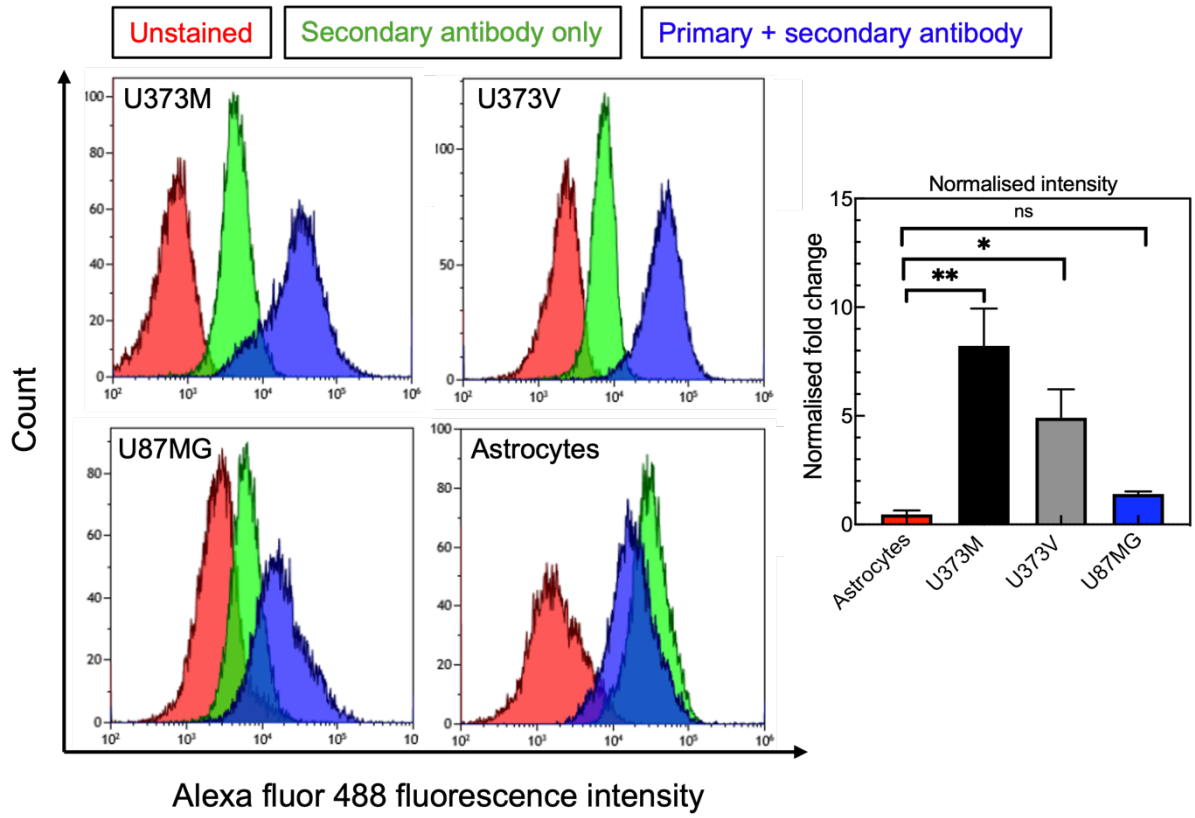

Figure 4.7 Flow cytometric analysis of transferrin receptor 1 (TfR1) expression levels in U373M, U373V, U87MG GBM cell lines and healthy human astrocytes. Representative graphs are shown on the left, with quantification of normalised TfR1 fluorescence intensity presented on the right. Data are presented as mean ± SD of samples from three independent experiments (*n* = 3).

4.3 Conclusion

In summary, the growth inhibitory activity of AFt encapsulation (AFt-PbS, AFt-TMZ, AFt-PbS-TMZ) in comparison to their naked agents (PbS QDs, TMZ, and PbS QDs + TMZ) was successfully demonstrated in 2D monolayer GBM models using both MTT and PB assays. Notably, in both assays, AFt alone was non-toxic whereas co-loaded AFt-PbS-TMZ emerged as the most effective formulation in inhibiting the growth of 2D GBM cell lines, supporting the

initial hypothesis that co-encapsulation of TMZ and PbS QD within AFt nanocages will enhance their *in vitro* growth inhibitory effect in 2D GBM cells compared to their naked agent counterparts and single agent encapsulated formulations. Additionally, it highlighted its promise as a potential non-toxic nanocarrier of therapeutic and imaging agents.

Furthermore, both assays confirmed the cancer selective action of AFt formulations, with lower cytotoxic effect observed in non-cancerous cells. The study also used different GBM cell lines, varying TMZ resistance profiles depending on MGMT expression. The differential expression of TfR1 assessed by western blot and flow cytometry, supported the hypothesis that AFt cage internalises targeted delivery via TfR1, enhancing AFt uptake in TfR1 overexpressing GBM cells while limiting off-target effects in cells with lower TfR1 levels, such as astrocytes and MRC-5 fibroblasts. However, AFt encapsulation did not confer a protective effect in THLE-2 liver cells, which may be attributed to their relatively higher expression of TfR1 levels. Considering TfR1 is a primary pathway of AFt internalisation, the intracellular accumulation of loaded formulations was enhanced, contributing the observed not significant protective effects to hepatocytes.

Importantly, AFt encapsulation (AFt-TMZ and AFt-PbS-TMZ) was able to circumvent TMZ resistance mechanisms conferred by MGMT expression in U373M cells (MGMT-positive), resulting in increased sensitivity to TMZ. These findings not only validate the proposed targeting and therapeutic strategy but also demonstrate the potential of AFt formulations to overcome TMZ resistance in aggressive GBM models.

Overall, 2D *in vitro* studies have demonstrated that AFt functions as a biocompatible nanocarrier for diagnostic, therapeutic, and theranostic applications. Furthermore, PB assays validated the MTT results in 2D cultures, confirming MTT assay as a true representative of activity; and supporting PB assay use in 3D tumour models. Due to the absence of cell-cell interactions and the simplified nature of the tumour microenvironment in 2D monolayers,

further investigation utilising 3D culture models is essential to obtain results that are more relevant and representative of *in vivo* conditions.

Chapter 5 Comparative analysis of naked and encapsulated formulations in 3D *in vitro* models

5.1 Background

The drug development process involves multiple *in vitro* and *in vivo* preclinical tests followed by clinical trials. However, the lack of correlation between *in vitro* and *in vivo* models results in low success rates for drug candidates (> 90% failure rate) in clinical trials, highlighting the need for more predictive pre-clinical models.[237]

In vitro 2D monolayer cultures are the most frequently used models for drug testing in GBM and cancer research. Despite their widespread use, these models present notable limitations, as they do not accurately replicate *in vivo* conditions, there is a lack of cell-cell and cell-ECM interactions, which can result in the loss of phenotypic diversity and cellular polarity. Additionally, in 2D cultures, cells have unlimited access to oxygen and nutrients, which does not represent the metabolic gradients in solid tumours.[238] These factors can alter molecular mechanisms and affect drug response outcomes compared to more complex models.[239] Therefore, selecting more advanced cell culture model is essential for developing novel treatment strategies and obtaining a more comprehensive understanding of the GBM microenvironment.

To enable more predictive translation of 2D culture results into *in vivo* models, advanced *in vitro* models have been developed, including 3D spheroids, organoids, and co-culture systems. These 3D models more accurately mimic the complex tumour microenvironment *in situ* compared to traditional 2D cultures.[237, 240] Cancer cells in 2D culture can generate 3D spheroids and recently, *in vitro* 3D spheroids` generation and cultivation have been successfully optimised (Figure 5.1).

Although the size of Ft/AFt may preclude efficient tumour penetration, their promising targeted

capability due to their natural affinity for TfR1 makes it essential to investigate these protein-based NP systems in complex *in vitro* models. To date, several GBM spheroid studies have been conducted using U251, U87MG, U118MG cells treated with naked TMZ under various conditions.[241-243] Moreover, recent studies have demonstrated the potential of drug encapsulation within Ft/AFt cages within 3D tumour spheroids, including breast cancer (MCF-7, MDA-MB-231) and paediatric diffuse midline glioma (DIPG-IV, -VI, and -XIX) spheroid cultures.[172, 244, 245] The findings revealed that enhanced drug uptake and penetration depth, and effective growth inhibition when compared to naked drugs, highlighting the potential of combining *in vitro* 3D cultures with Ft-based nanocarriers.

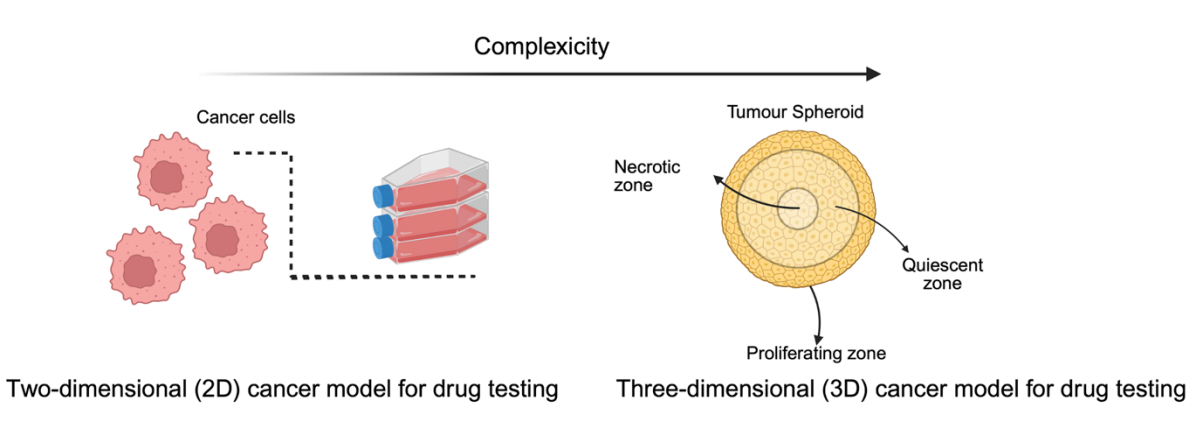

Figure 5.1 Schematic illustration of the comparison between 2D monolayers and 3D spheroid models with complex tumour regions. Created with BioRender.

In this chapter, seeding density and growth conditions were optimised to achieve uniform, consistently growing spheroids. Following that, both naked and loaded AFt formulations were evaluated in 3D U87MG spheroids as a more physiologically relevant GBM model. In addition, a comparative analysis was performed between 2D and 3D spheroid models to assess differences in growth inhibition post-treatment with all formulations and TfR1 expression changes. The study also included sequential treatment conditions in 3D U87MG cultures to mimic clinical drug administration. Considering the role of TfR1 in the uptake of AFt-based formulations and the fact that U87MG cells were found to be MGMT-negative (see Section 4.2.4), TfR1 expression was evaluated to better understand the enhanced antitumour activity of TMZ when entrapped in AFt in 3D cultures.

Chapter hypothesis: Based on the promising results obtained in 2D monolayers**,** it is hypothesised that both naked drugs and encapsulated formulations will exhibit similar effects in 3D GBM spheroid models, which more closely mimic *in vivo* tumour environments due to their complex structure, limitations, and altered expression of receptors such as TfR1. Spheroid cultures will demonstrate greater resistance to TMZ and encapsulated agents because of restricted drug penetration in 3D structure, and intrinsic hypoxic and necrotic features of 3D spheroids.

Chapter experimental aims: The experimental aims of this chapter include the optimisation of cell seeding density to ensure drug penetration in 3D cultures, the investigation of the activity of AFt formulations in 3D spheroid models, the assessment of sequential treatment responses to mimic clinical treatment conditions, and the evaluation of whether TfR1 expression is altered in 3D cultures compared to 2D cultures, and how these differences affect the activity of AFt formulations in 3D spheroid models.

5.2 Results and discussion

5.2.1 Establishing growth of GBM 3D tumour spheroid models

In order to establish the controllable growth of U87MG spheroid, the effect of cell seeding density on the size and morphology of spheroids was monitored. This study aimed to determine the optimal seeding density for generating U87MG spheroids with sizes and densities representative of *in vivo* tumour models. The cells were seeded with densities of 100, 500, 1000, 3000, 5000 cells/well in ULA plates. Culture medium was refreshed every 2-3 days to provide fresh nutrients and remove waste products to encourage the proliferation abilities of U87MG cells. Spheroid morphology was monitored on day 1, day 4, day 5, and day 8.

After seeding and brief centrifugation at 300 *g* for 5 min in ULA plates, U87MG cells formed into spherical spheroid structures at day 1. The diameter of each spheroid was measured horizontally from brightfield microscopy images using ImageJ or CellSens Standard software

associated with microscope. Table 5.1 summarises the evaluation of spheroid diameters (in μm) from day 1 to day 8 across a range of initial seeding densities (100-5000 cells/well). A positive correlation was found between the initial cell number and the average spheroid diameter, with average sizes increasing from 170 ± 25 μm to 700 ± 100 μm and 900 ± 100 μm at day 8 for seeding densities of 100, 3000 and 5000 cells/well, respectively (Table 5.1). Figure 5.2a illustrates these diameter changes in relation to their initial seeding densities. During an 8-day incubation time, spheroid diameters increased by 1.9-fold ($p < 0.05$), 1.5-fold ($p > 0.05$), 1.6-fold ($p > 0.05$, 1.8-fold ($p > 0.05$), 2.1-fold ($p < 0.05$) for initial seeding densities of 100, 500,1000,3000,5000 cells/well, respectively (Figure 5.2a). The overall positive correlation between initial seeding density and spheroid size aligns with previous studies using U87MG cells.[246-248] Additionally, our findings indicate that U87MG cells can form spherical spheroid structures even at lower seeding densities such as 100 and 500 cells/well, consistent with earlier reports demonstrating spheroid formation at seeding densities ranging from 50-200 cells/well[247] and 250-500 cells/well.[248] However, the spheroids generated from 100, 500 and 1000 cells/well demonstrated relatively comparable sizes, suggesting a slower rate of growth associated with higher seeding densities in the study.

To better understand the effect of cell density on spheroid growth, we also assessed spheroid volumes at day 8. Figure 5.2a inset presents the corresponding volume changes relative to initial cell density. On day 8, spheroid volumes were calculated as follows: $(1.8 \pm 0.5) \times 10^6$ μm³ (100 cells/well), $(8.3 \pm 2.7) \times 10^6$ μm³ (500 cells/well), $(1.8 \pm 0.6) \times 10^7$ μm³ (1000 cells/well), $(1.4 \pm 0.4) \times 10^8$ (3000 cells/well), and $(1.9 \pm 0.4) \times 10^8$ (5000 cells/well) (Figure 5.2a inset). Overall, these volume changes corroborate the positive correlation previously observed in diameter measurements. Notably, volume data revealed a dramatic increase between 1000 and 3000 cells/well, which was consistent with diameter measurements. However, spheroid volume is reported to be more sensitive than diameter alone in detecting growth differences for non-uniform morphology of spheroids. While diameter measurements rely on a single

dimension, volume measurements integrate two dimensions, better reflect structural heterogeneity of spheroids.[249]

For seeding densities up to 3000 cells/well, a linear increase of the spheroid size/volume was observed during the time-course. Figure 5.2b demonstrates the growth profile of spheroids seeded at 3000 cells/well and monitored on daily basis (day 1, day 2, day 3, day 4, day 5, and day 7). In this condition, spheroids produced possessed an average diameter of 400 ± 101 µm on day 1 post-seeding, providing a balance between sufficient size and compactness while still allowing penetration of reagents/agents into the hypoxic regions.[250] As shown in Figure 5.2b (seeding density: 3000 cells/well), spheroid diameters increased over the time as follows: 420 ± 18 µm (day 2), 511 ± 36 µm (day 3), 570 ± 60 µm (day 4), 662 ± 47 µm (day 5), and 800 ± 140 µm (day 7). This progressive growth in size is indicative of expected spheroid cell proliferation. At a higher seeding density (5000 cells/well), although a significant increase ($p < 0.05$) was observed in spheroid diameter following 8-day incubation, the increase in size becomes sub-linear, which could be due to nutrient limits and expanding hypoxic cores, as was observed with LN229 and U87MG cells (seeded at 4000-8000 cells/well).[251] In line with these findings, Nakod *et al.* also reported that U87MG spheroids formed with initial seeding densities of 5000, 7500, and 10000 cells/well maintained similar diameters at days 1, 4, and 7, suggesting limited growth, and highlighting the importance of selecting an appropriate initial seeding density.[252]

Table 5.1 The effect of seeding density on U87MG spheroid diameter at day 1 and day 8**.** Data are reported as mean ± SD from two independent experiments ($n = 2$, $N = 6$).

Initial seeding density	Spheroid diameter (day 1)	Spheroid diameter (day 8)
100 cells/well	90 ± 20 µm	170 ± 25 µm
500 cells/well	190 ± 32 µm	280 ± 46 µm
1000 cells/well	190 ± 45 µm	300 ± 39 µm
3000 cells/well	400 ± 101 µm	700 ± 100 µm
5000 cells/well	420 ± 90 µm	900 ± 100 µm

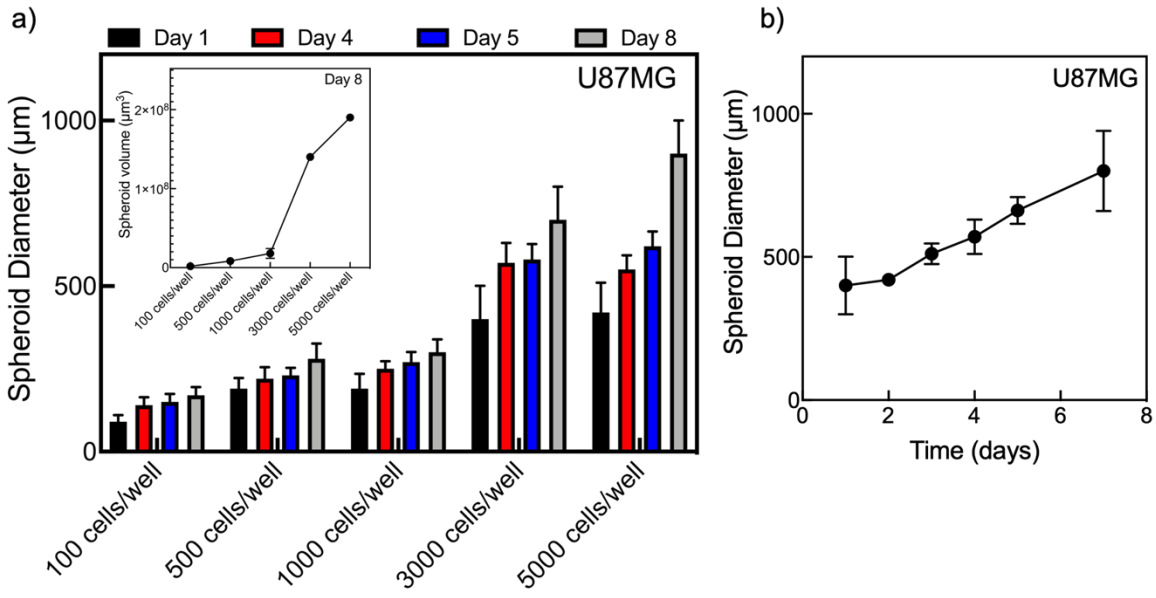

Figure 5.2 (a) The spheroid growth bar graphs for each density at the indicated timepoints (day 1, day 4, day 5, day 8). **(Inset)** spheroid volume at day 8 against the initial seeding densities of cells. (**b)** Change of the average spheroid diameter over 8 day study for spheroids seeded at 3000 cells/well. Values (spheroid diameter) are reported as mean ± SD from two independent experiments (n = 2, N = 6).

Considering these findings and relatively long exposure time with agents in the study (6 days), an optimal seeding density of 3000 cells/well was selected for U87MG cells. Therefore, an optimised seeding density was selected as 3000 cells/well and used for further studies, enabling prediction of naked and encapsulated formulations` treatment outcomes based on spheroid size/volumes.

The growth profile of U87MG spheroids over 21-day period at a seeding density of 3000 cells/well was monitored in terms of morphology, compactness, and size/volume changes. Figure 5.3 presents representative bright field images of U87MG spheroids captured at selected time points (day 1, day 7, day 14, day 21) and their corresponding diameter/volume measurements. On day 1, U87MG spheroids reflected an early-stage of spheroid structure with low compactness and small size/volume (~400 µm in diameter, (3.3 ± 0.3) x 10^7 µm³). On day 7, U87MG spheroids became ~800 µm in diameter and (1.4 ± 0.1) x 10^8 µm³ in volume, and more compact (packed more tightly) with increased darkness, and uniform structure (see Figure 5.3a). Notably, while the diameter increased ~2-fold from day 1 to day 7, the volume exhibited ~4.3-fold increase, indicating that volume measurements provide a more sensitive

assessment of spheroid growth.[249] On day 14, spheroids reached their highest volume (1.8 ± 0.1) x 10^8 µm³ in volume), while their diameter plateaued at ~720 µm, indicating that the proliferation continued, but that overall spheroid growth did not increase further, which might be related to diffusion limits and distance restriction. Between day 14 and day 21, it was observed that overall spheroid growth of U87MG control spheroids did not increase. Following that, on day 21, although compactness of spheroids remained stable, reduction in both diameter (to ~650 µm) and volume (1.4 ± 0.1) x 10^8 µm³) was observed (Figure 5.3b and inset). This decline might be related GBM cell death due to nutrient depletion due to potential increased cell number, and oxygen/nutrient diffusion limitations to dense spheroid cores over the time[253], as the medium was changed weekly to align with the sequential treatment plan. Overall, control U87MG spheroids increased their volumes until day 14 while their diameter plateaued after day 7, as shown in the inset of Figure 5.3b. Consistent with our findings, Vinci *et al.* reported that U87MG spheroid volume reached a plateau at around day 14 within the examined 21-day period.[254] Additionally, it has been reported (by Zhu *et al.*)[253] that when spheroids enlarge, diffusion limitations lead to the formation of hypoxic and nutrient-deprived core regions, thus reducing cell viability.[253] Moreover, nutrient deprivation has been reported to trigger autophagy and mitochondrial stress, which further contribute to cell death.[253] These findings guide the subsequent treatment studies with all formulations by emphasising the importance of initial seeding density, spheroid size/volume, and time-dependent changes in spheroid morphology.

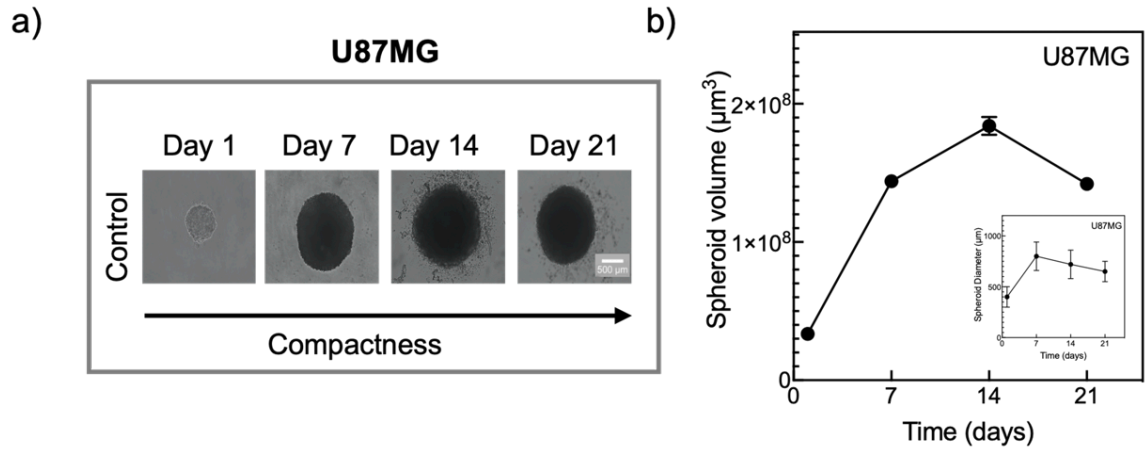

Figure 5.3 (a) Representative bright field microscopic images of untreated (control) U87MG spheroids, and their compactness over 21-day period. **(b)** Spheroid volume and **(inset)** diameter changes of untreated U87MG spheroids at day 1, day 7, day 14, and day 21.

5.2.2 *In vitro* evaluation of growth inhibition using PrestoBlue Assay in 3D tumour spheroids: comparison of naked and encapsulated formulations

To examine consistency with 2D studies, cell growth inhibition in 3D cultures was evaluated using the PB assay. U87MG spheroids were treated with all nanoformulations on day 1, using the same concentrations as those previously used in 2D monolayer cultures, to ensure the effectiveness of the formulations could be compared between 2D and 3D models. In the study, incubation the time was selected as 6 days, consistent with 2D monolayers, to allow enough time for DNA methylation, MMR activation, and two cell cycle phases progression, which are critical for TMZ-induced cytotoxic effects. Figure 5.4 shows the comparative morphological and growth inhibitory effects of vehicle control (AFt), naked, and encapsulated formulations on U87MG spheroids post-treatment on day 7.

To assess the biocompatibility of AFt nanocages as a vehicle control, U87MG spheroids were treated for 6 days with AFt alone (up to 1 μM). Table 5.2 summarises the AFt content in all AFt formulations (AFt-PbS, AFt-TMZ, and AFt-PbS-TMZ) ranging from 0.28 μM to 0.33 μM. Bright field images (Figure 5.4a top panel) showed no significant changes in spheroid structure

across the treatment range (after 0.5 and 1 μM AFt treatments), suggesting no toxicity at the doses used. Figure 5.4b demonstrates the lack of AFt toxicity in U87MG spheroids by PB assays. For instance, AFt-treated spheroid cell viability was found to be 87 ± 23% of control (p > 0.05), after 6 days treatment. Both morphological and viability results infer the biocompatibility of AFt nanocages at tested concentrations, suggesting its suitability as a drug delivery nanocarrier in GBM models.

Table 5.2 The summary of apoferritin (AFt), temozolomide (TMZ) and lead sulfide quantum dots (PbS QDs) concentrations in AFt-PbS, AFt-TMZ, and AFt-PbS-TMZ formulations. Data are presented as mean ± SD samples from 6 independent experiments (n = 6).

	AFt	**TMZ**	**PbS QDs**
AFt-PbS	0.33 μM	-	2500 μg/mL
AFt-TMZ	0.29 μM	2014 ± 160 μM	-
AFt-PbS-TMZ	0.28 μM	2338 ± 451 μM	2100 μg/mL

The summary of the amount of TMZ and PbS QDs in each cage is reported in Table 5.2. Notably, the number of TMZ molecules per cage was estimated to be 516 ± 82 for AFt-TMZ and 309 ± 49 for AFt-PbS-TMZ (see Table 3.1). However, TMZ concentrations measured by UV spectroscopy were higher in AFt-PbS-TMZ (2338 ± 451 μM) than AFt-TMZ (2014 ± 160 μM). This discrepancy may be explained by methodological differences: TMZ concentration in AFt-TMZ was determined by direct measurement after purification of resulting AFt-TMZ solution, whereas TMZ concentration in AFt-PbS-TMZ was calculated from indirect measurements using the remaining whole solution in the centrifugal filter after purification, due to the detection limits of PbS QDs in the UV region. Hence, the use of indirect calculation for AFt-PbS-TMZ may have led to higher values compared with direct quantification of AFt-TMZ. Employing a more specific method such as ultra-performance liquid chromatography-tandem mass spectrometry (UPLC-MS/MS) may provide the accurate determination of TMZ concentrations in both formulations, thus eliminating discrepancies observed between direct and indirect UV-based measurements.

All formulations were compared with their naked counterparts. Figure 5.4a (middle panel) illustrates morphological differences in U87MG spheroids treated with 5 and 50 μg/mL of PbS

QDs and AFt-PbS for 6 days. Notably, the AFt-PbS formulation showed enhanced morphological impact particularly at the lower concentration of 5 µg/mL, suggesting enhanced activity through AFt encapsulation. Figure 5.4c displays the percentage of cell viability across a treatment range of 0.01-100 µg/mL (PbS QDs-based), demonstrating dose-dependent growth inhibition effects for both PbS QDs and AFt-PbS formulations. For instance, 10 µg/mL treatment resulted in 89% cell viability relative to control for PbS QDs, whereas the same concentration of AFt-PbS reduced cell viability to 13% of control, indicating enhanced growth inhibitory activity at lower concentrations after AFt encapsulation. Moreover, IC_{50} values presented in Figure 5.5a revealed that AFt-PbS significantly increased activity ($p < 0.01$ compared to PbS QDs) with spheroid growth inhibition, exhibiting a 3-fold lower IC_{50} value (IC_{50} 7.6 ± 0.9 µg/mL, PbS QDs-based) compared to PbS QDs (IC_{50} 25.8 ± 5.3 µg/mL, PbS QDs-based). Subsequently, Figure 5.4a (bottom panel) displays the morphological changes in spheroids treated with TMZ-based formulations including naked TMZ and AFt-TMZ at 5 and 50 µM for 6 days. Morphological observations revealed that AFt-TMZ treatment induced comparable alterations to those observed with naked TMZ. To further evaluate treatment activity, 3D cell viability was assessed across concentration ranges of 0.01-1000 µM for TMZ, 0.01-200 µM for AFt-TMZ for 6 days, as shown in Figure 5.4d. PB assay results showed that AFt-TMZ treatment at 200 µM reduced cell viability to 26% of the control, whereas treatment with 500 µM of naked TMZ resulted in 34% cell viability after 6 days. Notably, AFt-TMZ exhibited enhanced activity, resulting in a modest but significant 1.5-fold reduction in IC_{50} value compared to naked TMZ (from 258.0 ± 29.8 µM to 177.0 ± 29.6 µM, TMZ-based, $p < 0.01$), as presented in Figure 5.5b. These findings indicate that the encapsulation of TMZ into AFt cages enhanced its activity in GBM spheroids, supporting AFt's potential.

Previous work by Fehlauer *et al.* has demonstrated that following 18 days incubation with a single TMZ dose, U87 and GaMG 3D GBM spheroids exhibited IC_{50} values of 5 µM.[255] In contrast, LN-18 and HF66 spheroids proved more resistant (IC_{50} 900 µM), indicating the relative sensitivity of U87 cells to TMZ.[256] However, U87' sensitivity to TMZ was not replicated

in more complex systems such as patient-derived GBM models and gel-based 3D *in vitro* GBM models; resulting IC_{50} values not being achieved.[257] Therefore, encapsulation of TMZ into AFt cages may overcome TMZ resistance. Consistent with AFt's potential, Shargh *et al.* reported that treatment with 100 μM AFt-TMZ significantly ($p < 0.001$) supressed tumour growth compared to naked TMZ in MGMT-positive and MMR-deficient DMG spheroid cultures.[172] Additionally, increasing AFt-TMZ concentration to 400 μM resulted in marked spheroid shrinkage with apparent surface blebbing, which may be attributable to enhanced apoptosis.[172] To date, researchers have also demonstrated that liposome, protein (AFt), ultra-small large pore silica NP formulations enhance the delivery and activity of drugs including TMZ in GBM spheroid cultures.[172, 258]

Comparable morphological results in spheroids treated with TMZ+PbS and AFt-PbS-TMZ at 5 and 50 μM for 6 days was observed (presented in Figure 5.4a, bottom panel). Particularly at 5 μM, AFt-PbS-TMZ formulation led to spheroid shrinkage and enhanced darker central regions, suggesting improved anti-tumour activity in spheroid cultures through a nanocarrier-based targeted delivery approach. In contrast, naked combination-treated spheroids showed limited morphological disruption compared to AFt-PbS-TMZ. To support these morphological observations, cell viability was evaluated after treatment ranges of 0.01-100 μM for TMZ+ PbS QDs, and 0.01-10 μM for AFt-PbS-TMZ. PB assay results demonstrated that 5 μM treatment with the naked combination did not reduce cell viability (100% of control), while AFt-PbS-TMZ reduced viability to 49%, confirming its improved activity in 3D spheroids. These data are further supported by IC_{50} values: AFt-PbS-TMZ treatment resulted in significant ($p < 0.0001$ compared to TMZ+ PbS QDs) reduction in IC_{50} from 90.0 ± 5.9 to 5.0 ± 0.5 μM (for TMZ+PbS QDs and AFt-PbS-TMZ respectively), representing 18-fold decrease compared to the naked combination of TMZ and PbS QDs (Figure 5.5b). Notably, the naked combination improved TMZ's performance compared TMZ alone, indicating the selective anticancer activity of AFt-PbS[216, 259], and the benefit of combination strategies. In line with these findings, Perini *et al.* also demonstrated that the combination of TMZ and graphene QDs enhanced the therapeutic

activity in 3D U87 GBM spheroids, reducing cell viability to 17% after 14 days of treatment, indicating the potential of QD and anticancer drug combination studies for improving GBM treatment outcomes.[260] Encapsulation of naked combination into AFt nanocages (AFt-PbS-TMZ) exhibited greater therapeutic potential not only in 2D cell culture, but also in 3D tumour spheroids. Previous studies have demonstrated that co-encapsulation into Ft/AFt nanocages enhanced anti-tumour potency and can penetrate in 3D tumour models.[261, 262] For instance, Munir *et al.* reported that co-encapsulation of valproic acid and DOX into Ft cavity enhanced cytotoxicity and disrupted spheroid organisation than naked drugs in 3D MCF-7 (breast), C4-2 (prostate), HT-29 (colon) cancer cell spheroids.[261] NP-based co-delivery of TMZ with other agents is being developed to enhance therapeutic synergy, improve TMZ stability, and increase its accumulation in the brain, thus overcoming the limitations of naked TMZ.[47]

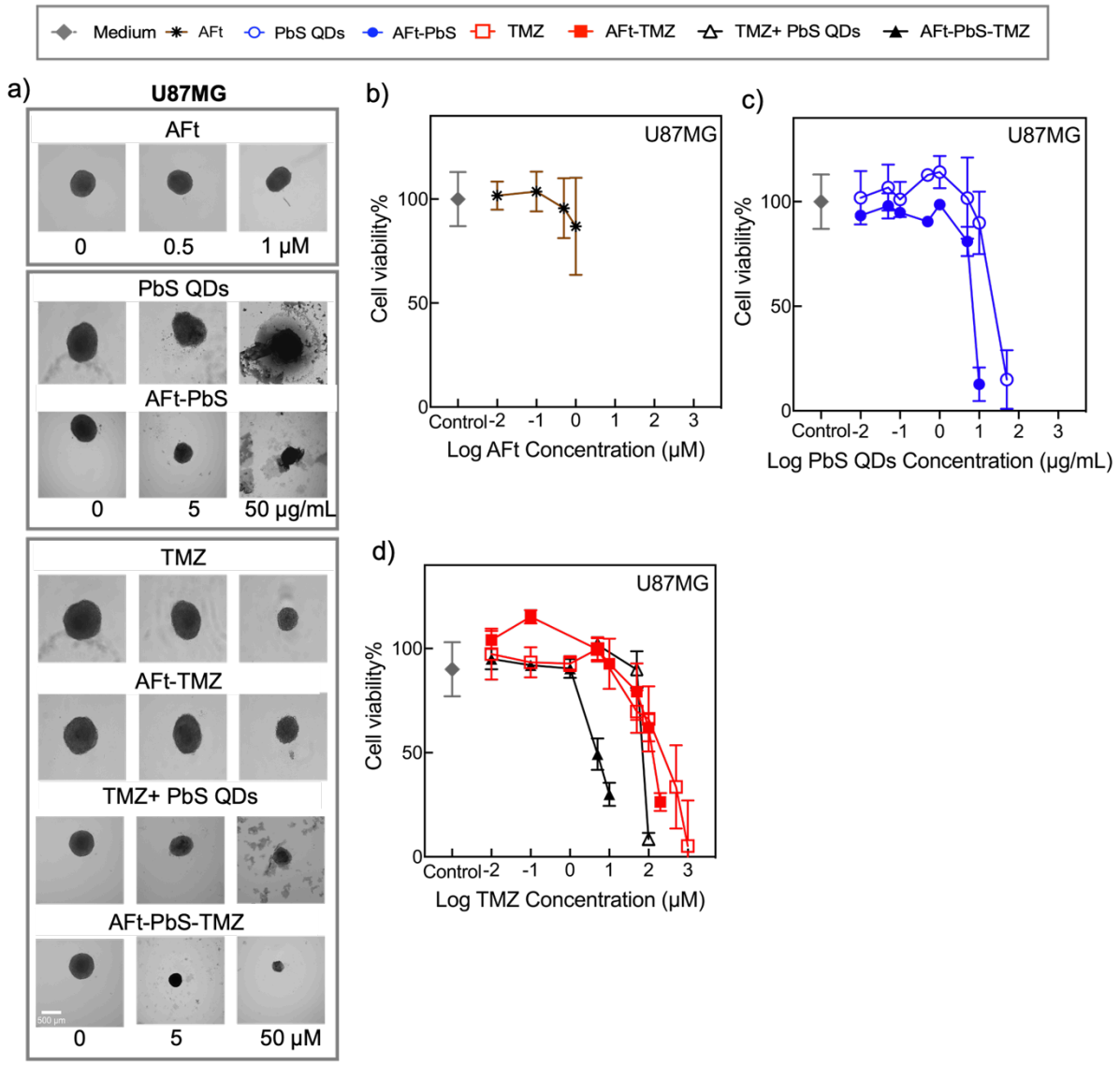

Figure 5.4 (*a*) Representative microscopic images of 3D U87MG spheroids on day 7 including control, 5 (µg/mL or µM) and 50 (µg/mL or µM) treatment (scale bar is 500 µm). **(b)** The effect of AFt (vehicle control), **(c)** PbS QDs and AFt-PbS, (d) TMZ, AFt-TMZ, TMZ+ PbS QDs, AFt-PbS-TMZ on 3D U87MG cell viability with PB assay. Data are presented as mean ± SD of samples from three independent experiments. (n = *3, N* = 6).

Overall, treatment with all AFt-nanoformulations resulted in lower IC_{50} values and enhanced anti-tumour activity compared to naked agents in our 3D spheroid models. These improved therapeutic outcomes of AFt-based delivery systems might be attributed to natural tumour targeting abilities via TfR1, pH-dependent drug release within acidic tumour microenvironment, and co-delivery of the agents (TMZ and PbS QDs) in one structure. Therefore, co-encapsulation into AFt cages offers a promising strategy to reduce the required dose of TMZ, potential overcoming resistance mechanisms to treatments, improve tumour targeting, and efficacy of agents in heterogenic 3D GBM models. These findings are also supported by

previous evaluations in 2D non-cancerous astrocytes and MRC-5 cells, which demonstrated the cancer selectivity of all AFt formulations, including AFt-PbS-TMZ (see Section 4.2.2).

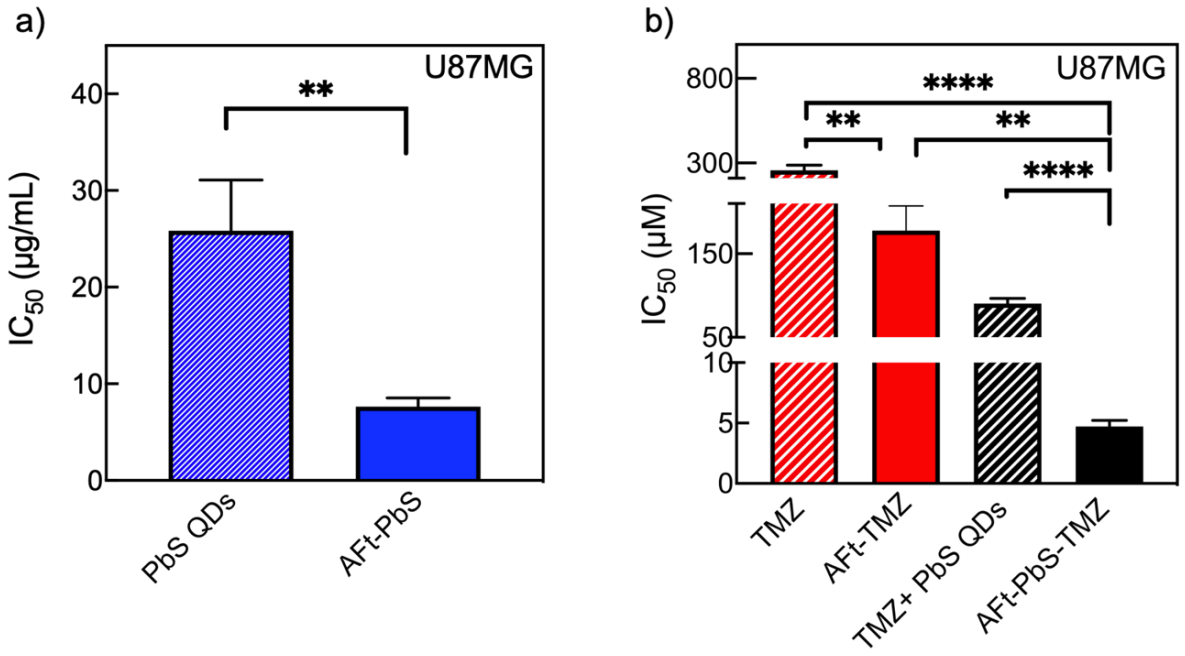

Figure 5.5 Comparison between IC_{50} values of **(a)** PbS QDs and AFt-PbS and **(b)** TMZ, AFt-TMZ, TMZ+ PbS QDs, and AFt-PbS-TMZ on 3D U87MG spheroids. Data are presented as mean ± SD of samples from four independent PrestoBlue (PB) experiments. (n = 4, N = 6).

5.2.3 Quantification of spheroid volume in 3D tumour spheroids after treatment with formulations

To quantitatively evaluate the effects of naked and encapsulated formulations in 3D cultures, spheroid volume changes were measured (see Section 2.9.2). Before and post-treatment, the volumes were tracked and compared across all formulations to evaluate their efficacy in 3D models that more closely mimic *in vivo* conditions. Figure 5.6 summarises the concentration-dependent spheroid volume changes over the 6 day incubation period for control spheroids and for those treated with both naked and encapsulated formulations. The effect of AFt alone (vehicle control) on spheroid volume was assessed over a 0.01-1 µM concentration range (Figure 5.6a). At the highest dose (1 µM; 4.6 mg/mL AFt), spheroid volume decreased from (4.8 ± 1.6) x 10^7 μm^3 (control spheroids) to (3.8 ± 0.6) x 10^7 μm^3, demonstrating a 1.2-fold

reduction (~15% shrinkage). At lower concentration of 0.5 μM AFt (corresponding to 2.3 mg/mL) reduced the volume only to (4.2 ± 1.4) x 10^7 μm^3, indicating a 1.1-fold decrease in spheroid volume (~12.5% reduction, $p > 0.05$). Considering the lower AFt concentrations used in the study (0.28-0.33 μM), the vehicle alone did not produce a significant reduction in 3D spheroid volume. Notably, as seen in Figure 5.6a, measured spheroid volumes in both AFt vehicle and untreated control groups were lower than those observed in the other treatment groups on day 7. The findings suggest that the effect is not attributable to AFt nanocarrier but rather indicates the growth characteristics of the U87MG cells, which may be influenced by passage number or culture conditions.

As shown in Figure 5.6b, the effects of PbS QDs and AFt-PbS were investigated. Following treatment with 5 μg/mL PbS QDs, the volume changed from (1.9 ± 0.2) x 10^8 μm^3 (control spheroids) to (8.6 ± 0.3) x 10^7 μm^3, corresponding to a 2.2-fold decrease (55% reduction relative to the control volume). Additionally, post-treatment with 5 μg/mL AFt-PbS, the volume changed from (1.9 ± 0.2) x 10^8 μm^3 (control spheroids) to (3.9 ± 0.2) x 10^7 μm^3, corresponding to a 4.9-fold reduction in spheroid volume (79.5% reduction relative to the control volume), highlighting the AFt formulation's effectiveness. The results showed that both treatments leading to a concentration-dependent reduction in spheroid volumes. However, AFt-PbS caused a significant ($p < 0.05$) 50% decrease in spheroid volume down to 9.5 x 10^7 μm^3 at lower concentrations (1-5 μg/mL), whereas PbS QDs alone required 10-times higher concentrations (10-50 μg/mL) to achieve a similar effect (Figure 5.5a). These findings indicate an enhanced therapeutic efficacy of the AFt-based formulation in 3D U87MG spheroid cultures.

Figure 5.6c demonstrates the volume differences after treatment with TMZ and AFt-TMZ formulations. For instance, treatment with 5 μM TMZ only reduced the spheroid volume from (1.9 ± 0.4) x 10^8 μm^3 to (1.8 ± 0.3) x 10^8 μm^3, indicating that much higher TMZ concentrations are required to achieve significant volume reduction. AFt-TMZ treatment at 5 μM reduced

spheroid volume to (1.7 ± 0.3) x 10^8 μm^3, which was not significant ($p > 0.05$). Increasing the concentration to 100 μM led to spheroid volume reductions to (4.1 ± 2.9) x 10^7 μm^3 for naked TMZ and (4.4 ± 1.3) x 10^7 μm^3 for AFt-TMZ. The effects of naked TMZ and AFt-TMZ on spheroid volume revealed that AFt encapsulation did not enhance TMZ efficacy in terms of spheroid volume reduction; there was no statistically significant difference ($p > 0.05$) in post-treatment volumes between naked TMZ and AFt-TMZ (Figure 5.6c). This lack of a significant volume reduction following AFt encapsulation may be attributed to three key factors: (1) the AFt nanocage was designed to maintain an internal pH 5.5 to improve the chemical stability of TMZ, and (2) GBM microenvironment itself is mildly acidic (pH 6.2-6.8) due to hypoxia and metabolic activity.[263] These dual acidic conditions may collectively delay the hydrolysis of TMZ, thus altering its activation profile and activity in 3D cultures. In addition, the paradoxical pH conditions in GBM (mildly acidic microenvironment (pH 6.2-6.8) but relatively alkaline intracellular pH 7.1-7.6) may partly explain the similar activity observed for TMZ and AFt-TMZ in 3D cultures. Notably, U87 cells have been shown to regulate and increase their intracellular pH under acidic extracellular conditions through overexpression of Na^+/H^+ exchangers.[228] Consequently, while acidic spheroid microenvironment prolongs the stability of both naked and encapsulated TMZ extracellularly, alkaline intracellular pH favours ring-opening and activation of both formulations when internalised, thus reducing the apparent advantage of AFt encapsulation. (3) Necrotic regions, commonly found in both *in vivo* and 3D spheroid models, may prevent a measurable reduction in spheroid volume, although there is a decrease in cell viability.

The effects of TMZ+ PbS QDs and AFt-PbS-TMZ formulations on spheroid volume were also investigated in comparison as shown in Figure 5.6c. Treatment with 1 μM TMZ+ PbS QDs only modestly reduced spheroid volume from (1.9 ± 0.1) x 10^8 μm^3 (control spheroids) to (1.5 ± 0.1) x 10^8 μm^3, indicating a 1.3-fold decrease. In contrast, 1 μM AFt-PbS-TMZ decreased volumes to (6.6 ± 0.1) x 10^7 μm^3, corresponding to a 2.9-fold reduction. These results demonstrate the potent activity of AFt-PbS-TMZ at such a low concentration of 1 μM. Additionally, spheroids

treated with TMZ + PbS QDs exhibited 50% reduction in spheroid volume of control spheroids reaching 9.5 x 10^7 μm^3 at concentrations between 10 and 50 µM. In contrast, those treated with AFt-PbS-TMZ required at concentrations between 1 and 5 µM. Remarkably, a greater sensitivity (10-times higher) was observed in spheroids exposed to the AFt-PbS-TMZ formulation, that achieved the same level of volume reduction at significantly lower concentrations, between 1 and 5 µM ($p < 0.0001$, Figure 5.6c). These results suggest a strong synergistic effect between TMZ and PbS QDs when co-delivered within AFt nanocages, as supported by both a basic 'look-see calculation' (observed growth inhibition of 51% at 5 µM, (< 2% expected), and the calculated CI = 0.23 < 1 using Chou-Talalay method.[264] These findings highlight the benefits of AFt nanocarrier system for co-delivery in terms of enhancing treatment response compared to naked agents.

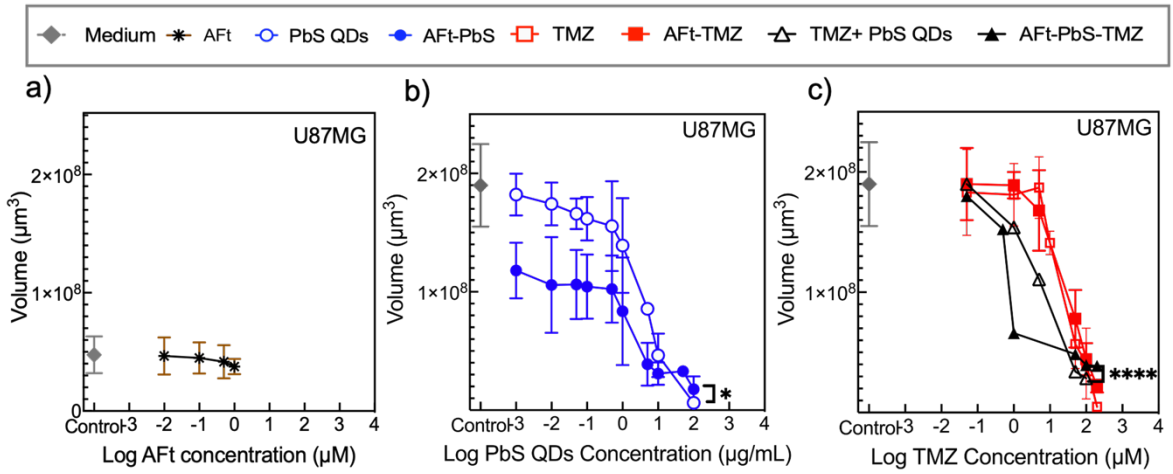

Figure 5.6 Spheroid volume on day 7 treated with **(a)** AFt (vehicle control, 0.01-1 µM), **(b)** PbS QDs (0.001-100 µg/mL) and AFt-PbS (0.001-100 µg/mL), **(c)** TMZ, AFt-TMZ, TMZ+ PbS QDs and AFt-PbS-TMZ. Data are presented as mean ± SD of samples from four independent experiments ($n = 4$, $N = 6$).

Over a 6 day incubation period, untreated spheroids increased their volume, whereas all formulations induced concentration-dependent volume reduction, suggesting that the formulations can penetrate dense spheroid cores and overcome physical and physiological barriers presented in 3D tumour models. Importantly, a combination strategy outperformed naked single agents, and co-encapsulation into AFt cages (AFt-PbS-TMZ) achieved the largest reduction, demonstrating a potential synergistic benefit of co-encapsulation (with enhanced

effect) and targeted delivery (with AFt formulation). More broadly, the findings emphasise the pH-sensitive nature of TMZ, the critical role of nanocarrier design and environment (pH) selection, and the bidirectional influences between the tumour *in situ* (e.g. acidity, hypoxia) and drug formulations (naked and encapsulated). In addition, the formulations impact tumour performance (e.g. tumour growth, therapeutic response) in 3D cultures.

5.2.4 Comparative analysis of cell viability and spheroid volume

Herein, a comparative analysis of both cell viability and spheroid volume across all naked and encapsulated formulations in 3D U87MG models are presented. In addition, to demonstrate the difference between 2D and 3D U87MG models, 3D spheroids` IC_{50} data are compared with the results in 2D monolayers (IC_{50} data from PB assay studies).

AFt-encapsulated formulations (AFt-PbS and AFt-PbS-TMZ) had a significant ($p < 0.01$ for AFt-PbS, $p < 0.0001$ for AFt-PbS-TMZ) impact on viable cancer cell number and corroborative volume reduction of spheroids compared to naked agents. Although AFt-TMZ demonstrated significantly ($p < 0.01$) greater growth inhibition than naked TMZ in cell viability assays, this enhanced activity did not correspond to a significant reduction in spheroid volume over the 6 day treatment period. Table 5.3 represents a summary of the effects of naked versus AFt-encapsulated formulations on GBM spheroids. The most significant ($p < 0.0001$) reductions in both viability and spheroid volume observed in post-treatment with AFt-PbS-TMZ for 6 days.

The IC_{50} values differed for 2D versus 3D U87MG cultures are summarised in Table 5.4. For instance, IC_{50} values (PbS QDs-based) for PbS QDs increased significantly ($p < 0.01$) from 0.7 ± 0.3 µg/mL in 2D monolayers to 26.0 ± 5.3 µg/mL in 3D spheroids, indicating a 37-fold increase in IC_{50} in 3D cultures compared to 2D monolayers. In contrast, AFt-PbS showed similar IC_{50} values (PbS QDs-based) as 7.5 ± 1.2 µg/mL and 8.0 ± 0.9 µg/mL in 2D and 3D cultures, respectively ($p > 0.05$) (Figure 5.7a). Additionally, IC_{50} values increased for TMZ-based treatments, from 188.0 ± 11.6 µM in 2D monolayers to 258.0 ± 29.8 µM in 3D spheroids

for naked TMZ (1.4-fold ($p < 0.05$), and from 28.0 ± 11.2 μM to 177.0 ± 29.6 μM for AFt-TMZ (6.3-fold ($p < 0.01$) (see Table 5.4 and Figure 5.7b). For TMZ + PbS QDs, IC_{50} value (TMZ-based) increased 90.0-fold ($p < 0.0001$). Interestingly, IC_{50} value (TMZ-based) for AFt-PbS-TMZ dropped from 11.0 ± 2.7 μM in 2D monolayers to to 5.0 ± 0.5 μM in 3D cultures, representing a 2.2-fold reduction ($p < 0.05$). Overall, 3D spheroid cultures required higher IC_{50} values than 2D monolayers to achieve the same inhibitory effect. Abbas *et al.* also reported significant ($p < 0.01$) differences in drug responsiveness between 2D and 3D colorectal cancer models. For example, in CaCo-2 cells the IC_{50} value for cisplatin increased from 107.0 μg/mL in 2D monolayers to 315.9 μg/mL in 3D spheroids.[237]

However, the AFt-PbS-TMZ formulation was found to be more effective in 3D cultures than 2D monolayers (Figure 5.6b). Juarez-Moreno *et al.* similarly observed that folic acid-functionalised silver and upconverting NPs exhibited greater (20%) uptake in 3D melanoma cultures compared to 2D cultures.[265] This enhanced activity of AFt-PbS-TMZ in 3D cultures might be explained by a combination of several factors including acidic and hypoxic spheroid microenvironment, the presence of PbS QDs and their associated activities (e.g. ROS production, cellular stress, and altered drug release) in 3D cultures, as well as the upregulation of TfR1 expression in these cultures (see Section 5.2.6). Additionally, TMZ may exhibit greater stability within the AFt nanocarrier and in the relatively more acidic microenvironment of 3D cultures compared to 2D monolayers, thus enhancing its therapeutic effect in 3D cultures. In the short term, this stability maintains TMZ in its inactive prodrug form; however, prolonged stability increases drug availability, thus facilitating uptake and subsequent activation, which can enhance its therapeutic activity in 3D cultures. In line with this, Tafech *et al.* compared intracellular pH regulation in U87 and F98 brain tumour cells grown as 2D monolayers and 3D spheroids to evaluate its impact on TMZ activity. The researchers showed that U87 cells in 3D spheroids tend to have lower intracellular pH compared to their 2D models. The researchers further reported that U87 cells regulate intracellular acidity through Na^+/H^+ exchange, consuming intracellular ATP. Hence, sustained exchanger activity may deplete ATP reserves,

compromise mitochondrial function, and contribute to higher mortality in U87 cells compared to F98 cells. Consequently, the increased acidic environment in 3D spheroids not only enhances TMZ`s stability and uptake, but may also exacerbate metabolic stress, and this combination may significantly increase its therapeutic activity in 3D cultures compared to 2D monolayers in the long term.[228]

In summary, growth inhibition and volume reduction data showed that AFt encapsulated formulations enhanced the activity of their naked counterparts in 3D spheroids. The activity differences between 2D and 3D cultures indicate the importance of using advanced 3D spheroids to predict *in vivo* results more accurately. Moreover, to evaluate formulations` activity more comprehensively, spheroid studies were expanded to include sequential treatments with each formulation, mimicking more closely a clinically-relevant dosing schedule.

Table 5.3 A summary of the effects naked and apoferritin (AFt)-encapsulated formulations on glioblastoma (GBM) spheroids. The statistical significance was reported as follows: not significant (ns), (*) $p < 0.05$, (**) $p < 0.01$, (***) $p < 0.001$, and (****) $p < 0.0001$.

Comparison	3D cell viability significance	3D volume significance
PbS QDs vs AFt-PbS	**	*
TMZ vs AFt-TMZ	**	ns
TMZ+ PbS QDs vs AFt-PbS-TMZ	****	****

Table 5.4 The comparative summary of IC_{50} obtained from PrestoBlue (PB) assay performed in 2D and 3D U87MG cultures.

Growth condition	PbS QDs (µg/mL)	AFt-PbS (µg/mL)	TMZ (µM)	AFt-TMZ (µM)	TMZ + PbS QDs (µM)	AFt-PbS-TMZ (µM)
	IC_{50}(PbS QDs)			IC_{50}(TMZ)		
2D	0.7 ± 0.3	7.5 ± 1.2	188.0 ± 11.6	28.0 ± 11.2	1.0 ± 0.2	11.0 ± 2.7
3D	26.0 ± 5.3	8.0 ± 0.9	258.0 ± 29.8	177.0 ± 29.6	90.0 ± 5.9	5.0 ± 0.5

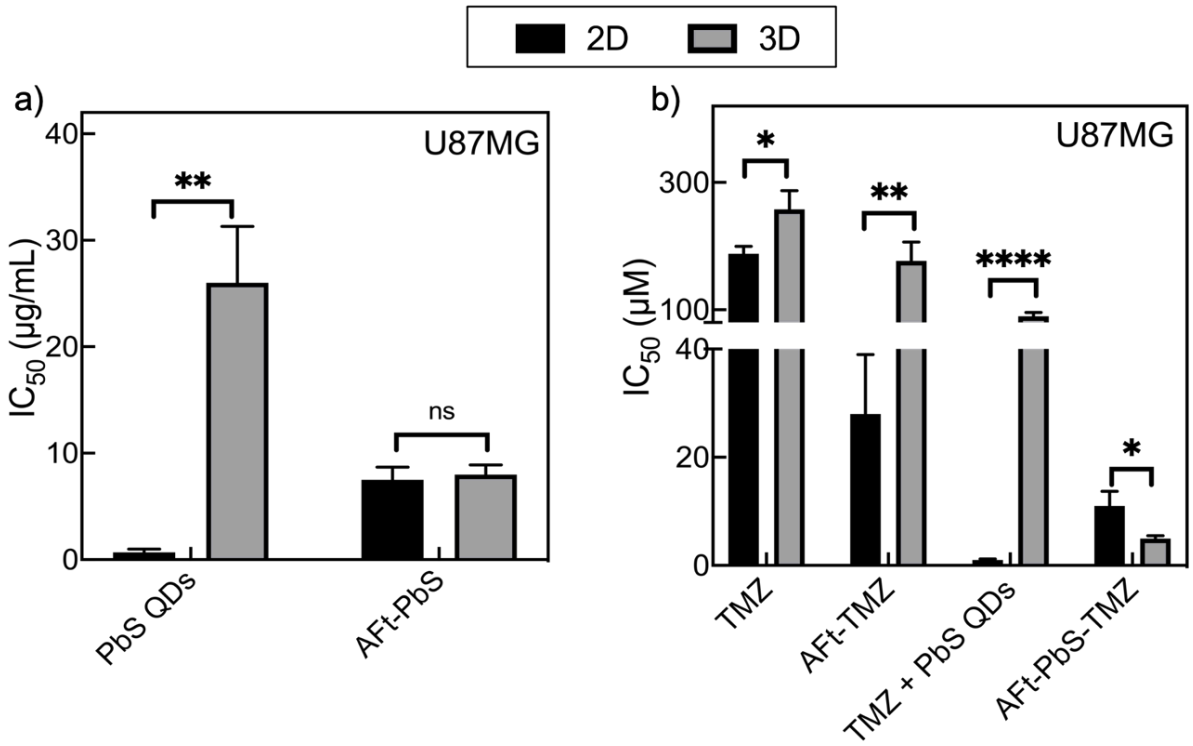

Figure 5.7 IC_{50} comparisons of **(a)** PbS QDs and AFt-PbS and **(b)** TMZ, AFt-TMZ, TMZ+ PbS QDs, AFt-PbS-TMZ in 2D and 3D U87MG cultures. Data are presented as mean ± SD of samples from at least three independent experiments (*n* = 3*, N* = 6*).*

5.2.5 Sequential treatment of 3D tumour spheroids with all formulations

To replicate clinical administration, where patients receive repeated treatment cycles rather than single dose, an *in vitro* sequential treatment strategy was developed. The experimental design consisted of a three-phase treatment plan at identical doses over 21 days (every 6 days). To understand the effects of all formulations within the sequential treatment plan, GBM spheroid morphology including volume and compactness, as well as cell viability assessed by PB assay, were compared across all naked and encapsulated treatment groups.

The effects of AFt (vehicle control) were investigated with sequential treatments to test drug delivery vehicle biocompatibility over the time in U87MG spheroids. Figure 5.8 summarises the morphological and volumetric effects of repeated AFt exposure (0.5 µM and 1 µM) over 21-days. Following treatment with AFt at 0.5 and 1 µM concentrations, spheroid structures remained similar to untreated control spheroids, exhibiting indistinguishable growth and morphology (Figure 5.8a). PB assays results also demonstrated that no IC_{50} values were

determined for AFt over the time and reported as ≥ 1 μM. Considering the lower AFt concentrations used the study for AFt formulations (0.28-0.33 μM), the nanocarrier exhibited no toxicity over 21 days. The volume measurements corroborated these findings: following AFt treatment across the 0.01-1 μM range, only minimal changes in spheroid volume were observed. For instance, on day 7, at the highest dose (1 μM; 4.6 mg/mL AFt), spheroid volume decreased from (4.8 ± 1.6) x 10^7 μm^3 (control spheroids) to (3.8 ± 0.6) x $10^7 \mu m^3$, representing 85% of control. After the 2nd 1 μM AFt treatment on day 14, the volumes were identical as (1.8 ± 0.2) x 10^8 μm^3 for both control and treated spheroids ($p > 0.05$, 100% of control). Following the 3rd treatment at 1 μM AFt (on day 21), control spheroids measured as (1.2 ± 0.1) x 10^8 μm^3 whereas those treated reported as (1.1 ± 0.1) x 10^8 μm^3 ($p > 0.05$, 88% of control). Notably, the changes in untreated spheroid volumes occurred between day 7 and day 14, whereas a decreasing trend (in spheroid volumes) was observed over later days (between day 14 and day 21). These results strongly support AFt's non-toxicity over 21 days and its safety profile, suitability as a drug delivery vehicle for subsequent studies (Appendix I).

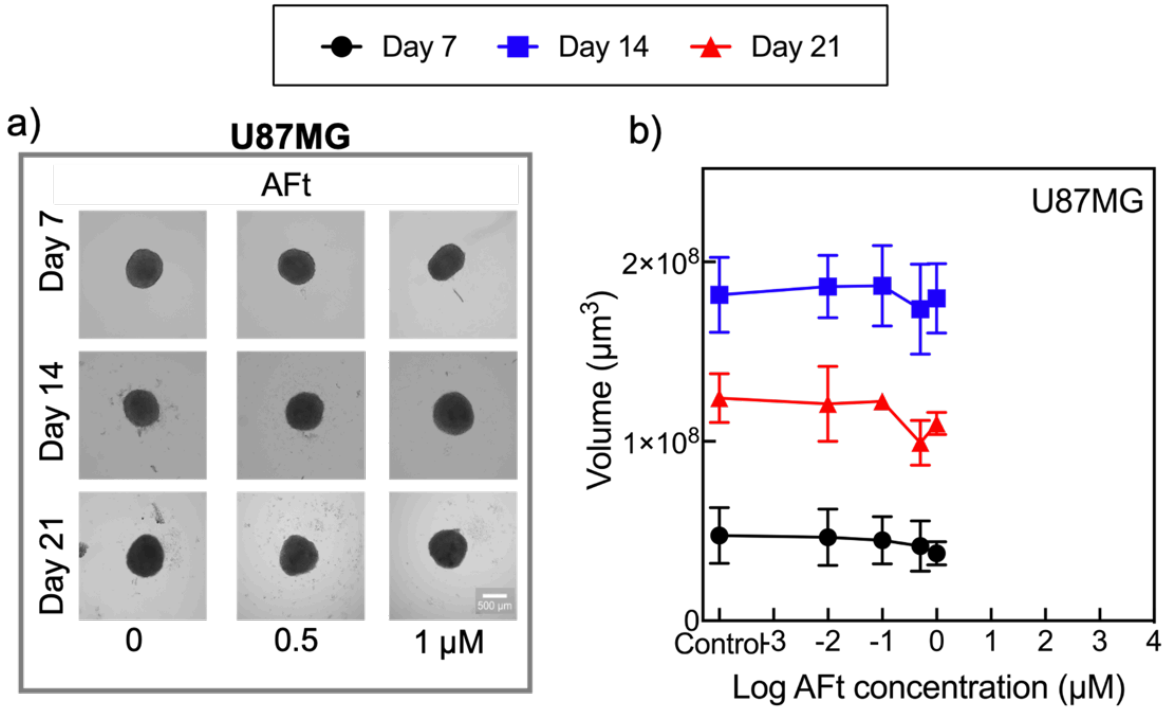

Figure 5.8 (a) Representative bright field microscopic images of 3D U87MG spheroids on day 7, day 14, and day 21 after treatment with AFt (vehicle control) at 0 μM (control), 0.5 μM, and 1 μM (scale bar is 500 μm). **(b)** The spheroid volume changes on day 7, day 14, and day 21 following sequential exposure to AFt. Data are presented as mean ± SD of samples from three independent experiments (*n = 3, N = 6*).

The effects of repeated PbS QDs vs AFt-PbS treatments were investigated to evaluate their performance on spheroid growth and morphology, viability, and volume over 21 days (Figure 5.9). Figure 5.9a (top panel) and (bottom panel) shows the morphological changes observed during sequential treatment with naked PbS QDs and AFt-PbS, respectively. Morphological assessments showed that repeated treatments (PbS QDs and AFt-PbS) disrupted spheroid integrity, indicating weakness in the ECM, and reduced cell-cell interactions over 21 days. Moreover, consistent data were obtained from spheroid volume measurements; sequential PbS QDs` treatment reduced the spheroid volume steadily, with the smallest volume observed at day 21 (Figure 5.9b). For instance, on day 7, following treatment with 25 µg/mL PbS QDs, the volumes fell from (1.2 ± 0.1) x 10^8 µm³ in controls to (2.3 ± 0.1) x 10^7 µm³ in treated spheroids (5.2-fold decrease; 80 % reduction of the control volume). On day 14, after the 2nd treatment, control spheroids grew to (1.6 ± 0.5) x 10^8 µm³ whereas treated spheroids' volume reduced to (1.0 ± 0.1) x 10^7 µm³ (16-fold decrease; 94% reduction of the control volume). On day 21, following 3rd treatment with 25 µg/mL PbS QDs, controls reached to (2.2 ± 0.73) x 10^8 µm³ (12-fold decrease; 92% reduction of the control volume) (Figure 5.9b).

A reduction in volume was also observed for sequential AFt-PbS treatments in 3D U87MG spheroids, demonstrating the shrinkage differed from that seen with naked PbS QDs (Figure 5.9c). For example, on day 7, following treatment with 25 µg/mL AFt-PbS, spheroid volume decreased from (1.3 ± 0.1) x 10^8 µm³ in controls to (3.1 ± 0.9) x 10^7 µm³ in treated spheroids (4.3-fold decrease; 77% reduction relative to control). On day 14, control spheroid volume increased to (1.9 ± 0.3) x 10^8 µm³, whereas treated spheroids shrank to (9.2 ± 1.1) x 10^7 µm³ (2.0-fold decrease; 50% reduction relative to control). On day 21, control spheroid volume was (1.7 ± 0.1) x 10^8 µm³, whereas treated spheroids measured (7.4 ± 1.3) x 10^7 µm³ (2.4-fold decrease ;58% reduction relative to control).

Furthermore, repeated PbS QDs exposure sensitised U87MG spheroids to treatments yielding lower IC_{50} values (Figure 5.9d). For example, the IC_{50} value (PbS QDs-based) significantly ($p < 0.05$) dropped from 37.0 ± 12.0 µg/mL to 15.9 ± 6.8 µg/mL (2.3-fold reduction) from day 7 to

day 14 with further decrease to 13.6 ± 5.6 µg/mL by day 21 (2.7-fold reduction overall; $p < 0.05$). There was no significant ($p > 0.05$) change (from 15.9 ± 6.8 µg/mL to 13.6 ± 5.6 µg/mL) observed between day 14 and day 21. These data suggest that the greater effect of PbS QDs occurred between 1st and 2nd treatment. These results may be explained by the development of larger hypoxic and necrotic regions within spheroid core over the time, as well as putative upregulation of stress-related pathways when cells exposed to repeated dosing of PbS QDs.[216]

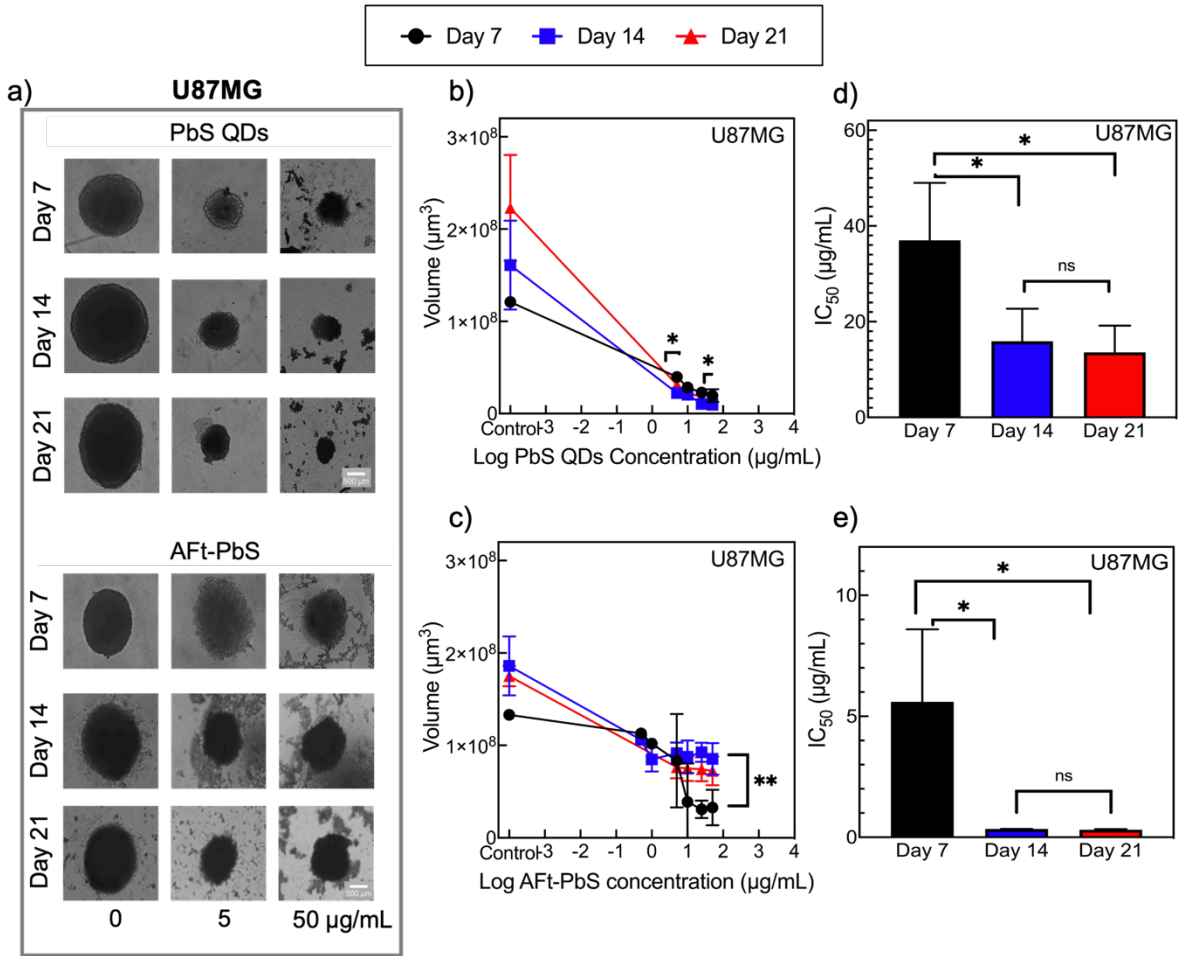

Figure 5.9 (a) Representative bright field microscopic images of 3D U87MG spheroids on day 7, day 14, and day 21 after treatment with either PbS QDs (top panel) or AFt-PbS (bottom panel) at 0 µg/mL (control), 5 µg/mL, and 50 µg/mL (scale bar is 500 µm). **(b)** The spheroid volume changes on day 7, day 14, and day 21 following sequential exposure to PbS QDs and **(c)** AFt-PbS, **(d)** IC_{50} (µg/mL) values obtained with PB assay after three-phase treatment (day 7, day 14, and day 21) with PbS QDs and **(e)** AFt-PbS on 3D U87MG cell viability. Data are presented as mean ± SD of samples from three independent experiments. ($n = 3$, $N = 6$).

A comparable trend was observed when sequential AFt-PbS treatments were administered to 3D U87MG spheroids. The IC_{50} value (PbS QDs-based) for AFt-PbS fell from 5.6 ± 3.0 µg/mL on day 7 to 0.3 ± 0.1 µg/mL on day 14, and then to 0.3 ± 0.3 µg/mL on day 21 (Figure 5.9e),

demonstrating the significant 16.5-fold reduction ($p < 0.05$) between the 1st and 2nd treatments. Compared to naked PbS QDs, AFt-PbS was significantly more potent in reducing cell viability of 3D U87MG spheroids, with lower IC_{50} values recorded at each time point (day 7, 14, and 21). Compared to naked PbS QDs, AFt-PbS exerted its effect by directly reducing cell viability before any measurable decrease in spheroid volume. This effect might be explained by targeted delivery capability of AFt, which showed the antitumour effect in U87MG spheroids.

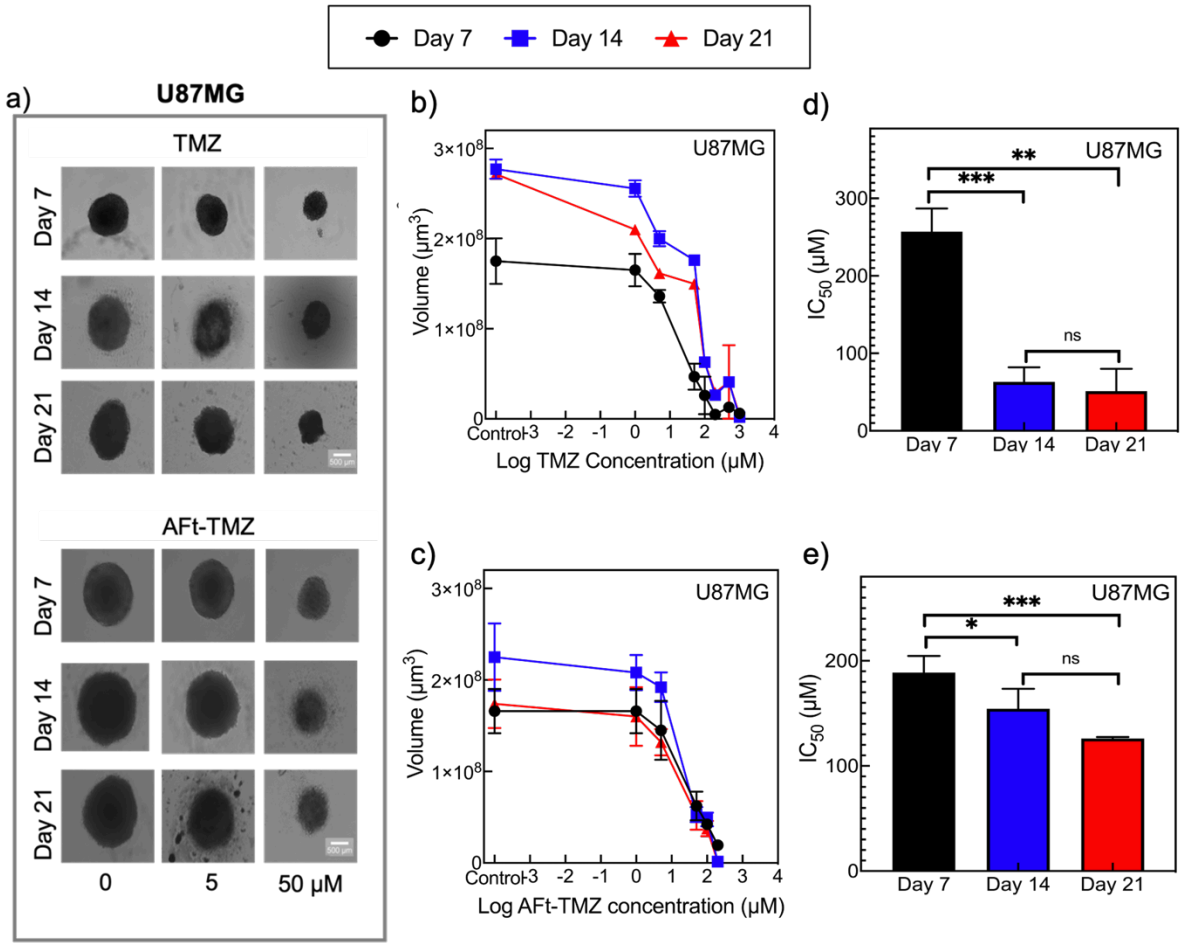

Figure 5.10 (a) Representative microscopic images of 3D U87MG spheroids on day 7, day 14, and day 21 after treatment with either TMZ (top panel) or AFt-TMZ (bottom panel) at 0 µg/mL (control), 5 µM, and 50 µM (scale bar is 500 µm). **(b)** The spheroid volume changes on day 7, day 14, and day 21 following sequential exposure to TMZ and **(c)** AFt-TMZ, **(d)** IC_{50} (µM) values obtained with PB assay after three-phase treatment (day 7, day 14, day 21) with TMZ and **(e)** AFt-TMZ on 3D U87MG cell viability. Data are presented as mean ± SD of samples from three independent experiments. (n = 3, N = 6).

The sequential dose response of naked TMZ and AFt-TMZ was investigated in U87MG spheroids and presented in Figure 5.10. Figure 5.10a (top panel) and (bottom panel) shows the morphological changes observed during sequential treatment with naked TMZ and AFt-TMZ, respectively. Repeated treatments with both agents (TMZ and AFt-TMZ) disrupted

spheroid architecture by day 21. However, frayed and cavernous spheroids were observed after sequential TMZ treatment. In contrast, AFt-TMZ produced a slower and more gradual response. Figure 5.10b represents the spheroid volume changes after repeated dosing of TMZ (1-1000 μM) over 21 days. For instance, on day 7, post-treatment with 200 μM TMZ, the volume fell from (1.7 ± 0.2) x 10^8 μm³ to (4.8 ± 0.1) x 10^6 μm³ (35-fold decrease; 97% reduction of the control volume). After the 2nd treatment with same dosage (200 μM) TMZ, the control spheroids grew to (2.7 ± 0.1) x 10^8 μm³ while treated volumes were (2.6 ± 0.4) x 10^7 (10.4-fold decrease; 90% reduction of the control volume). On day 21, the control volume remained stable at (2.7 ± 0.9) x 10^8 μm³ whereas TMZ treated spheroid volume changed to (2.9 ± 0.3) x 10^7 μm³ (9.3-fold reduction, 89% reduction of the control volume). The dose-dependent volume reduction by naked TMZ indicated that TMZ was able to exert its effect principally after the 1st treatment (on day 7). Latterly (days 14 and day 21), spheroids appeared to become less responsive to naked TMZ. Consistent with these observations, Günther *et al.* reported that GaMG GBM spheroids exhibited resistance to TMZ after 2nd treatment (on day 13).[53] Recently, Yamashiro *et al.* compared U87MG cells continuously exposed to TMZ for 4 and 6 months and found that continuous exposure (over 6 months) to TMZ could induce the development of highly resistant U87MG cells via MMR dysfunction (decreased expression of MSH2 and MSH6 proteins).[266]

The repeated dosing of AFt-TMZ (1-200 μM) also induced spheroid volume reduction, as shown in Figure 5.10c. For example, on day 7, post-treatment with the 1st dose of 200 μM AFt-TMZ, the volume changed from (1.7 ± 0.3) x 10^8 μm³ to (1.9 ± 0.2) x 10^7 μm³ (9-fold reduction, 89% decrease relative to control volume). After the 2nd treatment with 200 μM AFt-TMZ, the control spheroids grew to (2.2 ± 0.4) x 10^8 μm³ whereas treated spheroid volumes reduced to (1.5 ± 1.5) x 10^6 μm³ (147-fold reduction; 99.3% decrease relative to control volume). On day 21, following the 3rd treatment with 200 μM AFt-TMZ, control spheroid volume started to decrease to (1.7 ± 0.3) x 10^8 μm³ while treated spheroid volume fell to (1.5 ± 5.5) x 10^6 μm³ (113-fold reduction; 99.1% decrease relative to the control volume). In contrast to naked TMZ,

AFt-TMZ shows a modest initial effect, then it increases its activity following the 2nd and 3rd treatment doses. This observation may be related to the beneficial effect of AFt encapsulation, possible early penetration via higher TfR1 expression, and prevention of premature ring-opening of TMZ to its triazene-– courtesy of AFt`s acidic buffer environment (pH 5.5).

IC_{50} values (TMZ-based) for TMZ and AFt-TMZ were obtained on day 7, day 14, day 21. The results showed that naked TMZ proved more potent, producing a 4.1-fold fall in IC_{50} value (from 258.0 ± 29.8 μM to 62.9 ± 18.8 μM) between day 7 and day 14 ($p < 0.001$), the interval in which most of its 21-day activity was realised. The 3rd treatment yielded only a further 1.2-fold decline in IC_{50} value (from 62.9 ± 18.8 μM to 51.2 ± 28.9 μM) from day 14 to day 21 ($p > 0.05$). However, sequential TMZ treatments yielded an overall 5.1-fold reduction in IC_{50} (from 257.0 ± 30.0 μM to 51.2 ± 28.9 μM, $p < 0.01$) (Figure 5.10d). In contrast, repeated AFt-TMZ treatment decreased IC_{50} gradually from 177.0 ± 29.6 μM to 154.3 ± 19.1 μM between day 7 and day 14, and then to 126.1 ± 1.4 μM on day 21 (1.2-fold after each treatment), for a cumulative 1.5-fold reduction over 21 days ($p < 0.001$) (Figure 5.10e). Although AFt-TMZ appeared to exert a greater effect on day 7 with lower IC_{50} values compared to naked TMZ, this initial effect was not sustained over 21-day period. By days 14 and 21, TMZ exhibited significantly (at least $p < 0.05$) enhanced growth inhibitory effects compared to AFt-TMZ. These findings might be explained by three different factors including down-regulation of TfR1 due to repeated dosing which limited AFt uptake, increased spheroid compactness over time which limits NP penetration (AFt-TMZ) rather than naked drug (TMZ), and acidic pH (5.5) used to load TMZ into AFt nanocages stabilised TMZ, however, this prolonged stability may persist in hypoxic cores in spheroids, developing a slow-release profile. Therefore, while AFt encapsulation protected TMZ during formulation, it may also delay its intracellular activation, may explain the long-term effect of AFt-TMZ under the same dose schedule.

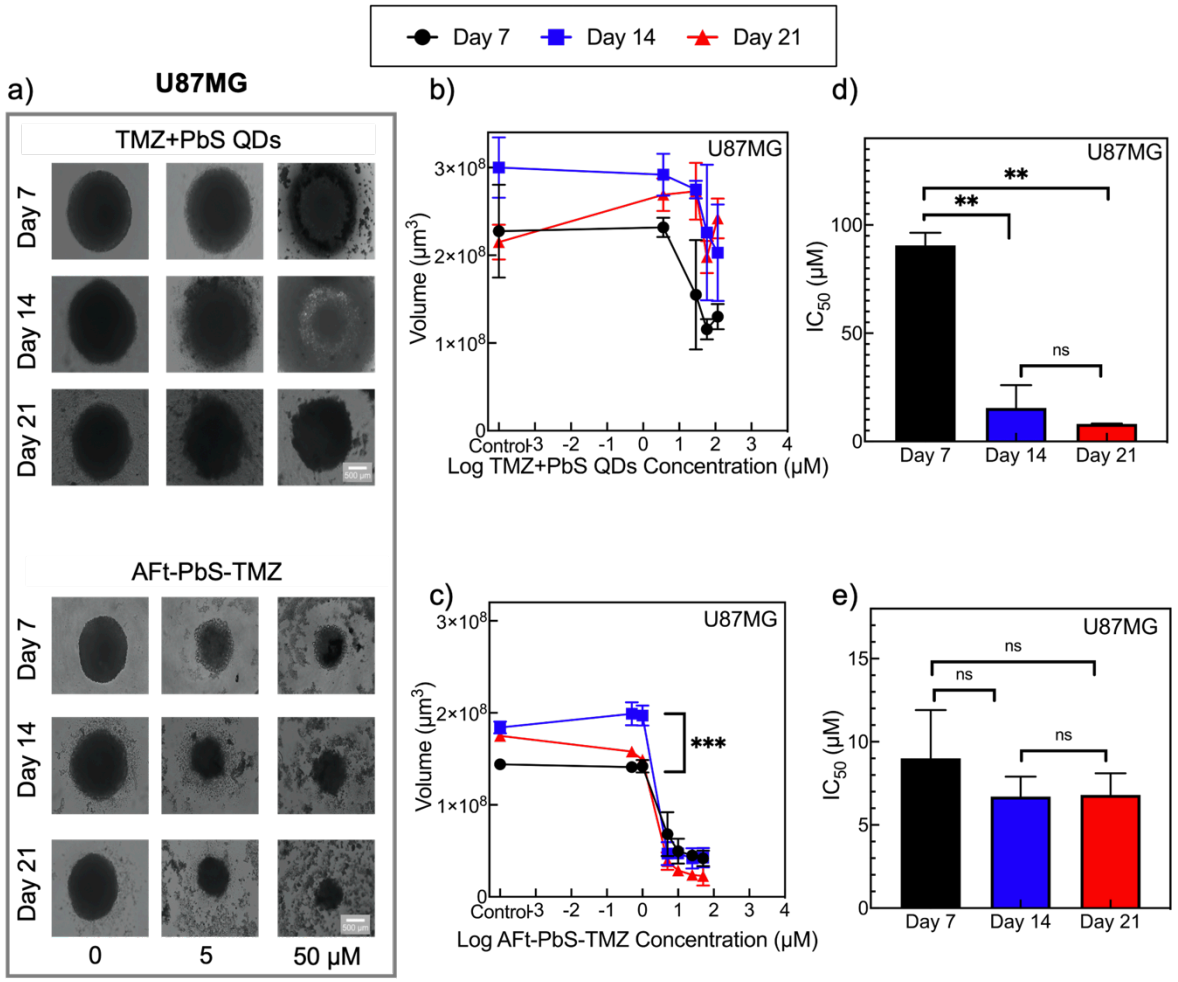

Figure 5.11 (a) Representative microscopic images of 3D U87MG spheroids on day 7, day 14, and day 21 after treatment with either TMZ+PbS QDs (top panel) or AFt-PbS-TMZ (bottom panel) at 0 μg/mL (control), 5 μM, and 50 μM (scale bar is 500 μm). **(b)** The spheroid volume changes on day 7, day 14, and day 21 following sequential exposure to TMZ+PbS QDs and **(c)** AFt-PbS-TMZ, **(d)** IC_{50} (μM) values obtained with PB assay after three-phase treatment (day 7, day 14, and day 21) with TMZ+PbS QDs and **(e)** AFt-PbS-TMZ on 3D U87MG cell viability. Data are presented as mean ± SD of samples from three independent experiments. (n = 3, N = 6).

The sequential treatment effects of TMZ+PbS QDs versus AFt-PbS-TMZ are compared in U87MG spheroids in Figure 5.11. Morphological changes observed during sequential treatment with naked TMZ+PbS QDs and AFt-PbS-TMZ are presented in Figure 5.11a (top panel) and (bottom panel), respectively. Post-treatment with naked combination, U87MG spheroids remained largely intact and spherical over 21 days. In contrast, AFt-PbS-TMZ induced spheroid disruption even at day 7. At both concentrations (5 and 50 μM), the AFt-PbS-TMZ formulation produced more disintegration than the naked combination. These data show that repeated dosing of the naked combination presented resistance to full collapse

whereas AFt-PbS-TMZ produced rapid spheroid disruption after the 1st treatment. Additionally, tracked volumes post-treatments are presented in Figure 5.11b (for TMZ+ PbS QDs) and Figure 5.11c (for AFt-PbS-TMZ). For instance, post-treatment with the 50 μM naked combination, spheroid volume began to reduce from (2.3 ± 0.5) x 10^8 μm³ (control spheroids) to (1.2 ± 0.1) x 10^8 μm³ after 1st treatment (1.9-fold reduction; 48% decrease relative to control). On day 14, control spheroids continued to grow to (3.0 ± 0.3) x 10^8 μm³ whereas 2nd treated with 50 μM TMZ+ PbS QDs spheroid volume was (2.3 ± 0.8) x 10^8 μm³ (1.3-fold reduction; 23% decrease relative to control). On day 21, the control spheroids had begun to shrink slightly (down to (2.1 ± 0.2) x 10^8 μm³), whereas treated spheroids increased their volume to (2.4 ± 0.3) x 10^8 μm³ after 3rd treatment (1.2-fold increase; 14% increase in volume relative to control spheroids) (Figure 5.11b). These results suggest that the spheroids may develop resistance to TMZ+ PbS QDs treatment, as evidenced by their regrowth. In contrast, a single dose of AFt-PbS-TMZ produced a sharp fall in volume even at lower concentration of 5 μM. For example, on day 7, following 1st treatment with 5 μM AFt-PbS-TMZ, the volume fell from (1.41 ± 0.3) x 10^8 μm³ (control spheroids) to (6.8 ± 2.4) x 10^7 μm³ (2.1-fold reduction; 52% decrease relative to the control volume). On day 14, control spheroids grew to (1.8 ± 0.6) x 10^8 μm³ whereas treated spheroids reduced their volume to (4.7 ± 0.1) x 10^7 μm³ following 2nd treatment with same dose of AFt-PbS-TMZ (3.8-fold reduction; 74% reduction relative to the control volume). On day 21, the untreated spheroid volume declined to (1.4 ± 0.4) x 10^8 μm³ while following the 3rd 5 μM AFt-PbS-TMZ dose treated spheroids measured (3.9 ± 0.9) x 10^7 μm³ (3.6-fold decrease; 72% reduction) (Figure 5.11c). These results indicate that AFt-PbS-TMZ produced a stronger initial effect at only 5 μM (10-times lower dose from the naked combination), and sustained spheroid volume inhibition through days 14 and 21 without regrowth.

The IC_{50} values for TMZ+ PbS QDs (Figure 5.11d) and AFt-PbS-TMZ (Figure 5.11e) were obtained on day 7, day 14, day 21. Post-treatment with naked combination, the IC_{50} value dropped from 90.0 ± 5.9 μM to 15.5 ± 10.5 μM between the 1st and 2nd treatments (5.8-fold, $p < 0.01$). However, the IC_{50} value only declined further to 8.2 ± 0.1 μM on day 21, representing

only 1.9-fold decrease between the 2nd and 3rd treatments ($p > 0.05$), resulting in an overall 11.1-fold reduction in IC_{50} values between days 7 and 21 ($p < 0.01$). These results indicate that the greatest effect arose between the first two exposures to the naked combination. On the other hand, AFt-PbS-TMZ demonstrated the most potent activity after the 1st treatment (IC_{50} 9.0 ± 4.0 μM). Subsequent doses conferred additional statistically insignificant reductions in IC_{50} values to 6.7 ± 1.2 μM on day 14 and 6.8 ± 1.3 μM on day 21) (overall 1.32-fold reduction from day 7 to day 21). This rapid effect might be explained by early penetration of AFt-encapsulated TMZ+ PbS QDs, due to higher TfR1 expression profile in spheroids, leading to increased growth inhibition effect via greater uptake after only one exposure with AFt-PbS-TMZ. Altogether, at least two sequential naked combination treatments were required to reach AFt-PbS-TMZ potency after its 1st treatment cycle. Therefore, AFt-PbS-TMZ showed greater anti-tumour activity in spheroids, consistent with TfR1 targeted delivery of more agents to the tumour cells, reducing the need for sequential treatments. Recently, Shaikh *et al.* demonstrated that a single administration of exosome co-loaded with gold NPs and TMZ inhibited tumour growth in *in vitro* (U87 and U251 cells) and *in vivo* (U87 cells-bearing xenograft mice) GBM models.[267]

Overall, AFt-PbS-TMZ presented the most effective strategy in sequential treatments as well as a single dose treatment with its AFt-mediated targeted delivery, and dual agent advantage of TMZ and PbS QDs combined. Among PbS QDs-based treatments, the AFt-PbS formulation (IC_{50} 5.6 ± 1.0 μg/mL) outperformed naked PbS QDs (IC_{50} 37.0 ± 8.0 μg/mL) on day 7 ($p < 0.001$), maintained its activity on day 14 (0.3 ± 0.1 μg/mL versus 15.9 ± 6.8 μg/mL, $p < 0.05$), and day 21 (0.3 ± 0.1 μg/mL versus 13.6 ± 5.9 μg/mL, $p < 0.05$), confirming AFt encapsulation advantageous in spheroid cultures (Figure 5.12a). At day 21, within the TMZ-based treatments, naked TMZ, AFt-TMZ, TMZ+ PbS QDs, and AFt-PbS-TMZ, efficacy ranked as follows: AFt-PbS-TMZ (IC_{50} 6.8 ± 1.3 μM) > TMZ+ PbS QDs (IC_{50} 8.2 ± 0.1 μM) > TMZ (IC_{50} 51.2 ± 28.9 μM) > AFt-TMZ (IC_{50} 126.1 ± 1.4 μM) (Figure 5.12b).

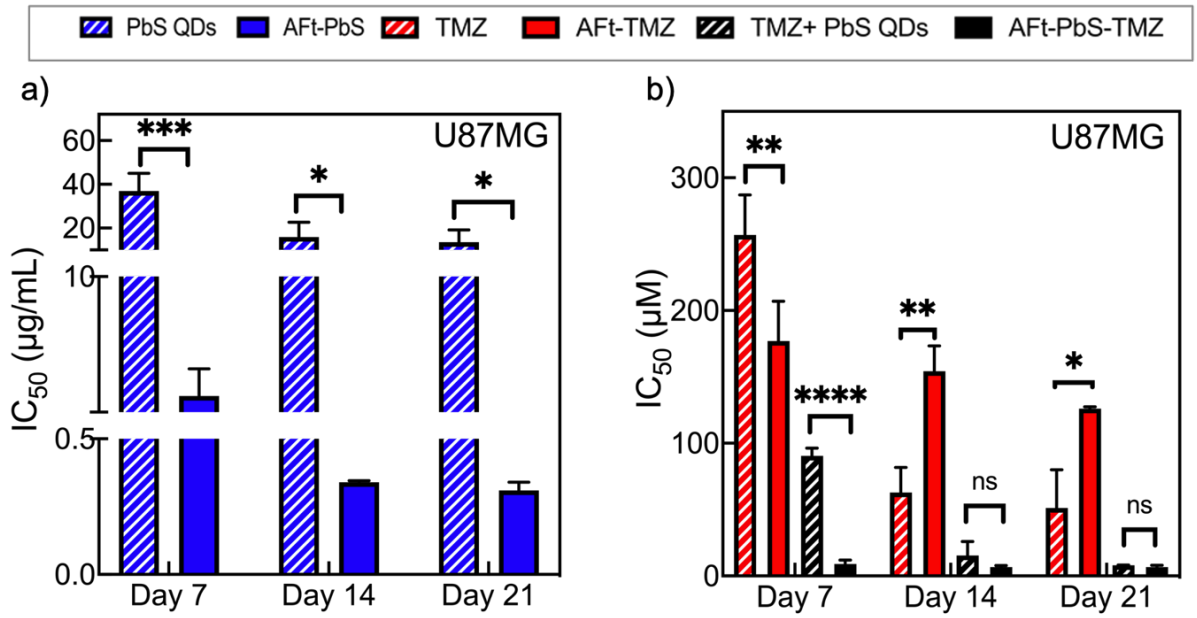

Figure 5.12 IC_{50} comparisons in 3D U87MG spheroids following three-phase treatment cycles over 21-day period. **(a**) Comparison between PbS QDs and AFt-PbS and **(b)** comparison between TMZ, AFt-TMZ, TMZ+ PbS QDs, AFt-PbS-TMZ. Data are presented as mean ± SD of samples from three independent experiments (n = 3, N = 6).

AFt formulations (AFt-PbS and AFt-PbS-TMZ) had greater effect in sequential treatments whereas only TMZ alone produced more potent growth inhibition than AFt-TMZ. However, AFt-PbS-TMZ remained superior to all other formulations, rapidly achieving a low IC_{50} value after the 1st treatment. Taken together, all formulations demonstrated that sequential treatments improved the single dose therapy response via reducing cell viability, and spheroid size/volume over time (21 days). This improved effect with sequential treatment might be explained by heterogenous penetration, overcoming resistance mechanisms, spheroid structure weakness (weak ECM, and cell-cell interactions) with repeated dosing. In addition, all formulations` effects on later days (between day 14 and day 21) were not statistically significant. As shown in Figure 5.3, even untreated (control) U87MG spheroids had ceased growing by day 14 and retained their volume to day 21. The obtained results suggest that increased spheroid density over time may have hindered drug penetration, specifically, spheroids may have developed necrotic and hypoxic core regions[253], thus reducing overall treatment efficacy. However, sequential treatment may allow therapies to reach deeper spheroid layers once the outer layers had been disrupted with earlier treatment. Therefore, broadly-speaking, sequential treatment

data may guide future *in vivo* studies. To better predict therapeutic outcomes prior to *in vivo* studies, future investigations may involve (1) the examination of cumulative drug penetration in 3D spheroids using Orbitrap secondary ion mass spectrometry (Orbi-SIMS), (2) the exploration of potential TMZ resistance mechanisms that can be raised between treatment cycles by the expression of MGMT and MMR proteins via western blot, (3) the evaluation of TfR1 expression affecting delivery efficiency using western blot or flow cytometry, and (4) the assessment of MGMT expression and *O*6MeG lesions in spheroids following exposure to naked and AFt encapsulated formulations using western blot.

5.2.6 Flow cytometry analysis of TfR1 expression of 3D tumour spheroids

To characterise TfR1 expression in 3D U87MG cultures to test the hypothesis that AFt formulations exert a selective effect on U87MG spheroids, total (both surface and intracellular) TfR1 expression was measured in 3D cultures. Spheroids were harvested at two time points: day 1 (early-stage spheroids) and day 6 (mature spheroids) dissociated enzymatically into single cells and cells analysed by flow cytometry (see Section 2.9.4) In addition, 2D U87MG monolayers were also examined for comparison to reveal whether (or how) 3D culture and its maturation alters TfR1 expression. A comparative evaluation of TfR1 expression provides the uptake behaviour of AFt formulations in 2D and 3D GBM cultures.

Notably, at day 1 post-seeding, single cells derived from 3D early-stage spheroids exhibited a 2.4-fold ($p < 0.05$) higher median fluorescence intensity for TfR1 compared to 2D monolayers, indicating rapid TfR1 upregulation in spheroid formation. The difference in 2D and 3D cultures might be explained by the possibility that cells in 3D culture may experience limited access to nutrients and iron compared to 2D monolayers. In addition, at day 1, the histogram in Figure 5.13 demonstrated a broad peak, suggesting cell to cell variability in TfR1 levels in early-stage spheroid cultures. Similarly, Barroso *et al.* reported heterogeneity of TfR1 expression in breast cancer spheroids (MDA-MB-231).[268] The heterogenous TfR1 profile within spheroids might be associated with various iron demand among proliferating versus quiescent cells.[30] Additionally,

it may reflect limited access to nutrients, therefore, to sequester iron that is needed to support growth, cells must adapt and upregulate TfR1 expression.[269] In contrast, at day 6, median TfR1 intensity in 3D cultures remained similar to cells in 2D culture, however, the fold-increase had fallen to 1.62-fold, which was not significant ($p > 0.05$) (see Figure 5.13). Sarisozen *et al.* found the similar reduction profile of TfR1 in ovarian spheroids at different days (3,5,8 days) by flow cytometry analysis.[270] The decrease in receptor expression might be related to oxygen levels, medium composition, serum factors, diffusion barriers in mature spheroids at day 6.[211] Considering these factors, although nutrient depletion might be expected to trigger TfR1 upregulation to meet higher iron demand over 6 days, prolonged hypoxia and metabolic stress in mature spheroids (day 6) may instead induce TfR1 downregulation, due to reduced proliferation rates and increased cell death within the spheroid core.

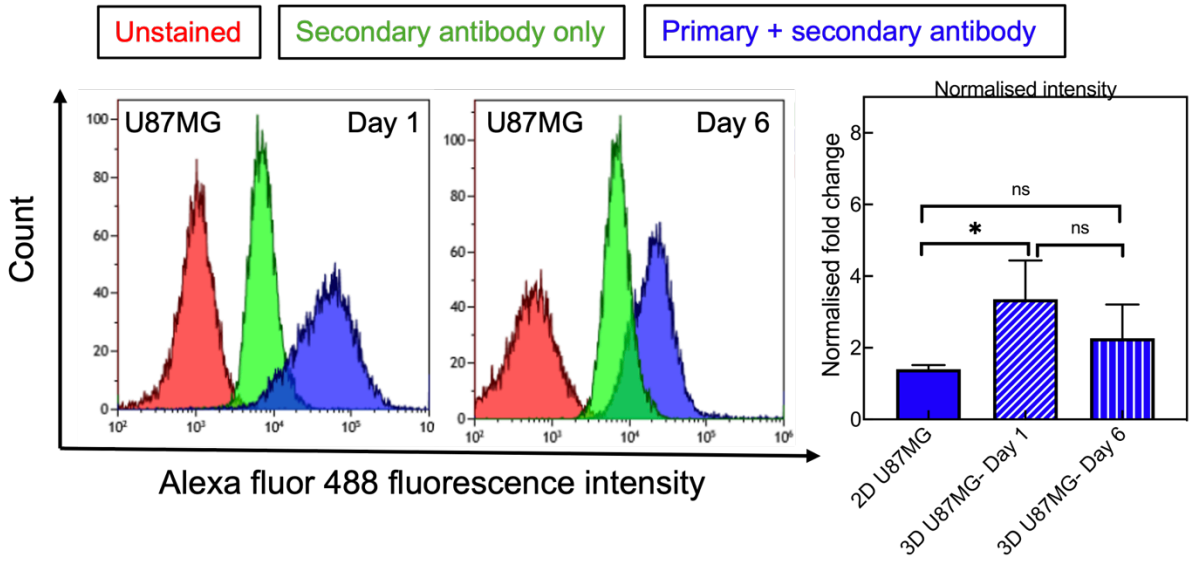

Figure 5.13 Flow cytometric analysis of TfR1 expression levels in U87MG spheroids collected on day 1 and day 6. Representative flow cytometry histograms are shown on the left, while the corresponding quantification of normalised TfR1 fluorescence intensity is presented on the right. The analysis includes a comparison between 3D U87MG spheroids (day 1 and day 6) and 2D U87MG monolayers. Data are presented as mean ± SD of samples from three independent experiments ($n = 3$).

Altogether, considering AFt nanocarrier`s exploitation of TfR1 for cellular entry, the upregulation of TfR1 at day 1 provides an explanation for enhanced effects of AFt formulations on day 7 in 3D cultures. In this context, all treatments administered at day 1 yielded greater anti-proliferative results for AFt encapsulated agents when compared to their naked counterparts. However, changes (down regulation) of TfR1 levels on cells of day 6 spheroids

might explain the sequential treatments data obtained latterly (day 14 and day 21). Flow cytometry data highlight the heterogeneity in receptor expression within 3D tumour models, importance of administration time, and more broadly, spheroid (tumour) stage for receptor-targeted therapies' outcomes.

5.3 Conclusion

In conclusion, all AFt formulations and their corresponding naked agents were comprehensively investigated in a clinically relevant 3D GBM model (U87MG spheroids). The study integrated several points including spheroid morphology, cell viability via PB assay, spheroid volume tracking, a 21-day sequential treatment schedule, and TfR1 expression profiling by flow cytometry following spheroid dissociation into single cells.

Remarkably, AFt alone (vehicle control) exhibited no toxicity at vehicular concentrations used in 3D cultures, confirming its biocompatibility for further studies. The formulations were analysed in comparison with their naked counterparts in spheroid cultures designed to mimic 2D experimental settings (with a consistent 6-day incubation). Under single dose treatment conditions, on day 7, the effectiveness of formulations ranked as follows: AFt-PbS > PbS QDs, AFt-TMZ > TMZ, AFt-PbS-TMZ > TMZ+ PbS QDs, demonstrating that AFt encapsulation significantly enhanced the activity of naked agents in 3D cultures, consistent with 2D results. It supports the initial hypothesis that both naked drugs and encapsulated formulations exhibit similar effects in 3D GBM spheroid models. However, 3D cultures were generally more resistant to treatments compared to 2D cultures.

Among all tested formulations, dual agent AFt-PbS-TMZ demonstrated the most significant growth inhibitory activity and spheroid volume reduction, corroborated by morphological optical imaging in a more relevant tumour *in situ* model. The sequential treatment protocol (6 day treatments repeated weekly over three weeks) demonstrated cumulative drug accumulation, potential resistance to repeated dosing, and growth inhibition effects that more closely resemble clinical dosing schedules than a single dose test. Sequential treatment results

showed that repeated dosing improved the activity of all formulations. By day 21, the relative effectiveness of formulations as followed: AFt-PbS > PbS QDs, TMZ > AFt-TMZ, AFt-PbS-TMZ > TMZ+ PbS QDs. Unlike in a single dose result obtained on day 7, AFt-TMZ lost its effectiveness over time, whereas the other AFt formulations remained active in sequential treatments. This difference may be attributed to delayed TMZ release from AFt cages, and down regulation of cellular TfR1 expression over time within spheroid cultures. Remarkably, none of the formulations produced a further statistically significant advantage between day 14 and day 21, suggesting that two doses may be sufficient to achieve therapeutic benefit under these experimental conditions.

Overall, AFt encapsulation enhanced the activity of naked agents by exploiting targeted delivery via TfR1 expression in tumour spheroids. However, TfR1 expression levels changed over time; early-stage spheroids showed increased TfR1 expression, whereas mature spheroids reverted to 2D baseline level. Despite TfR1 expression changes, AFt-PbS-TMZ as a promising candidate for further *in vivo* studies, demonstrating the advantage of co-delivery agents within a single nanocarrier system via delivering more agents, overcoming resistance mechanisms into 3D tumour model that better predicts clinical results. In addition, AFt-PbS-TMZ, as a theranostic formulation, holds potential to monitor treatment response which is important for effective GBM management. However, further investigations are needed to evaluate safety profile, *in vivo* therapeutic efficacy, biodistribution, and imaging capabilities.

Chapter 6 Imaging performance of naked and encapsulated formulations in *in vitro*, *ex vivo* and *in vivo* models

6.1 Background

Imaging plays a crucial role in GBM diagnosis (particularly in tumour characterisation and localisation), as well as monitoring treatment response and guiding further clinical decisions.[87] Imaging techniques including MRI, CT and PET are widely used in clinical applications for GBM.[89] Although these imaging methods provide valuable diagnostic and post-treatment information, they suffer from some limitations: (1) low sensitivity in distinguishing tumour tissue from non-cancerous brain tissue, which leads to false positives, (2) limited signal penetration and resolution due to physical barriers such as the skull, and (3) the lack of a real-time guide in surgery or drug delivery.[271]

Recent advances in imaging systems enable improved sensitivity, resolution, and deep tissue penetration as well as providing real-time guides to disease progression or treatment response. Among these developments, fluorescence imaging has gained wide attention due to its high sensitivity, harmless radiation, low cost, and its potential for real-time monitoring, particularly in the near-infrared wavelength region, NIR-I, 650-900 nm. However, tissue scattering and autofluorescence restrict deep tissue imaging in the NIR-I region. SWIR imaging also referred as NIR-II (1000-1700 nm), offers deep tissue penetration, minimal background autofluorescence, giving it a high potential for clinical translation.[102] SWIR imaging could offer significant benefits for brain tumour imaging applications. In this context, QDs, particularly PbS QDs, have been explored as imaging probes in the SWIR window due to their tuneable emission, high PL, quantum yield, and PL stability, making them potentially suitability for deep tissue imaging.[272] However, to date, the deployment of NIR-II probes is limited by the availability and sensitivity of bioimaging systems with detection in this wavelength range.

Biocompatibility is an important factor for developing NP-based SWIR emitting platforms and its clinical translation. Delivering PbS QDs into brain tumours poses certain challenges including crossing the BBB, avoiding potential toxicity, and immune clearance.[273] Therefore, to combat these challenges, PbS QDs have been capped with different ligands and/or encapsulated within biocompatible nanocarrier devices. In this study, an AFt nanocarrier system has been explored to significantly enhance the clinical potential of PbS QDs as SWIR probes. To date, Ft/AFt have been investigated as a theranostic platform for brain tumour applications particularly for drug delivery and MRI-guided imaging[198, 200], yet there remains limited work on integrating NIR-II imaging labels. The combination of SWIR imaging with targeted drug delivery holds potential for improved diagnostic sensitivity in GBM.

In this chapter, the SWIR imaging abilities of PbS QD-containing formulations (PbS QDs alone, AFt-PbS, and AFt-PbS-TMZ) were investigated using both 2D monolayers and 3D spheroid models of U87MG GBM cells. To further evaluate the formulations' deep tissue imaging abilities, *ex vivo* brain slices were utilised post-treatment with PbS QDs and AFt-PbS formulations for comparison. In addition to AFt encapsulation, PEGylated PbS QDs were evaluated initially in *in vivo* and then *ex vivo* models to test their biocompatibility, imaging performance, and preliminary biodistribution in more advanced biological systems. These assessments aimed to provide guidance for AFt-based formulations that will be tested in future studies.

Chapter hypothesis: Herein is tested the hypothesis that PbS QD-containing formulations (PbS QDs, AFt-PbS and AFt-PbS-TMZ) will enable SWIR imaging of GBM cells in *in vitro* 2D and 3D cultures, as well as in *ex vivo* models, due to the deep tissue imaging abilities of PbS QDs. Additionally, AFt encapsulation is hypothesised to enhance the SWIR signal clarity in the deep tissue regions by facilitating selective accumulation of cargo in GBM tumours via TfR1-targeted delivery, while minimising off-target signals from non-cancerous tissue, thus improving imaging specificity, contrast, and real-time monitoring potential.

Chapter experimental aims: The experimental aims of this chapter include evaluating the SWIR imaging abilities of PbS QDs following their encapsulation and co-encapsulation within AFt nanocages, assessing whether AFt encapsulated formulations enable real-time monitoring potential in 2D and 3D GBM cultures as well as in *ex vivo* brain tissues, and investigating how PEGylation influences the *in vivo* activity and organ distribution, with particular focus on brain accumulation, of PbS QDs.

6.2 Results and discussion

6.2.1 Evaluation of imaging performance in *in vitro* 2D models

Imaging potential of PbS QD-containing formulations was evaluated using SWIR imaging systems (Photon etc, Montreal, National Research Council Canada). This study aimed to determine SWIR signal and retention of PL activity from PbS QDs *in vitro* in U87MG monolayers, thereby enabling the monitoring of treatment response following exposure to the formulations.

In 2D monolayer studies, the incubation time with agents was set to 24 h to allow time for cellular uptake. The selected 24 h incubation time also helps to minimise any potential cytotoxic effects of PbS QDs in GBM cells, which could hinder the detection of the SWIR signal. All PbS QD-containing formulations were applied a concentration of 50 µg/mL. This concentration was chosen based on *in vitro* studies (25 µg/mL and 50 µg/mL) conducted in 3D cultures, where the IC_{50} value for PbS QDs was found to be 25 µg/mL following 6 days treatment (see Section 5.2.2), hence 50 µg/mL representing 2 x IC_{50} values was used. To ensure consistency throughout 2D and 3D imaging tests, a concentration of 50 µg/mL was chosen in 2D imaging studies.

Following QD treatment, to avoid the influence of any surface accumulated/attached agents, U87MG cells were washed with PBS before fixation (see Section 2.10). Bright field images of fixed U87MG cells before (Figure 6.1a) and after treatment with 50 µg/mL of PbS QDs (Figure

6.1b), AFt-PbS (Figure 6.1c), and AFt-PbS-TMZ (Figure 6.1d) for 24 h, revealed the presence of cells at different stages of cell cycle, and with no morphological changes indicative of cellular toxicity.

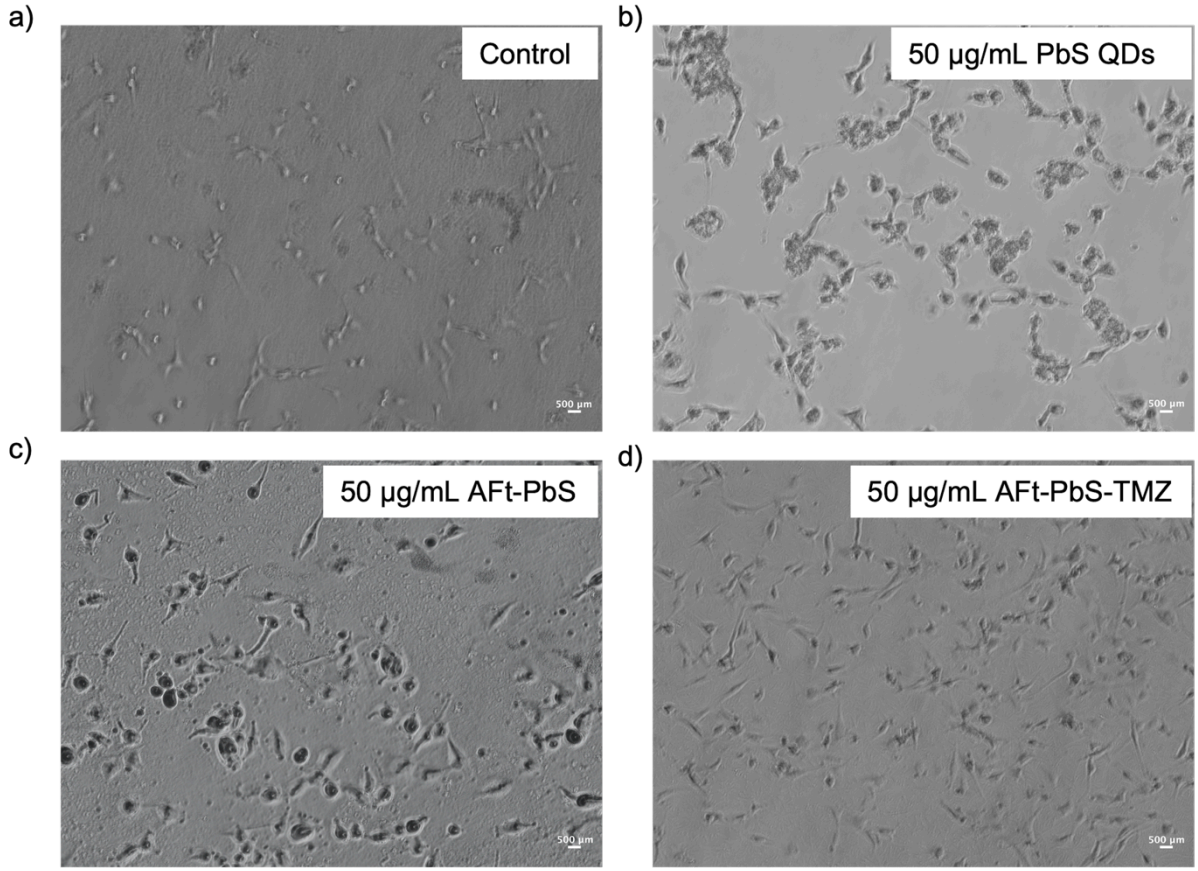

Figure 6.1 Bright field images of fixed U87MG monolayers **(a)** untreated control, treated with 50 µg/mL **(b)** PbS QDs, **(c)** AFt-PbS, **(d)** AFt-PbS-TMZ for 24 h, acquired using a 10x objective. Scale bar is 500 µm.

In fixed U87MG monolayers, SWIR signal detectability was evaluated following 24 h treatment with AFt-PbS. Figure 6.2 demonstrates bright field and corresponding SWIR images of fixed U87MG cells after treatment with 50 µg/mL AFt-PbS formulation. The images showed that SWIR signals were detectable in 2D monolayers, demonstrating successful AFt-PbS uptake by the cells. Additionally, the PL obtained in the NIR-II region indicated that AFt encapsulated PbS QDs retained their PL activity in the cells. The comparison of bright field image acquired at 5x objective (Figure 6.2a) with SWIR images captured under the same objective with 0.5 s exposure time (Figure 6.2b) revealed detectable SWIR signals intracellularly following AFt-

PbS treatment. To obtain more defined signals from the cells, a higher magnification objective (20x) was used. Images of 2D U87MG cells treated with 50 µg/mL AFt-PbS, acquired using a long pass LP-980 nm filter and 0.4 s exposure time (Figure 6.3c). With the LP-1250 nm and exposure time of 0.7 s (Figure 6.2d), enhanced depth of SWIR signal detection was achieved as well as minimised background noise, in agreement with prior findings in the NIR-II imaging (>1000 nm), where reduced tissue scattering and autofluorescence lead to improved depth and signal-to-noise ratio.[274] Both images (Figure 6.2c and Figure 6.2d) demonstrate the clear PL signals from AFt-PbS within the GBM cells with clarity and brightness. These findings illustrate the potential of AFt encapsulation to retain PbS QDs' PL activity and enable selective imaging of cancer cells via a targeted delivery approach. Similarly*, in vitro* in 2D SK-BR-3 cells, Sun *et al.* demonstrated PbS QDs/anti-HER-2 conjugate imaging capabilities.[275] Additionally, recombinant protein-coated PbS QDs (1150 nm emission peak) for *in vitro* fluorescence imaging have been demonstrated in breast tumour cells (KPL-4).[276] Other encapsulation approached have been reported before, with Cao *et al.* demonstrating that oil soluble PbS QDs encapsulated in biodegradable micelles retained their PL activity.[277] These QDs were internalised by *in vitro* tumour cells before being used for *in vivo* imaging, where they were successfully visualised, with experimental support provided by Miss Dongling Zhang and Dr. Maria Moreno of the National Research Council Canada, our collaborators in Ottawa.

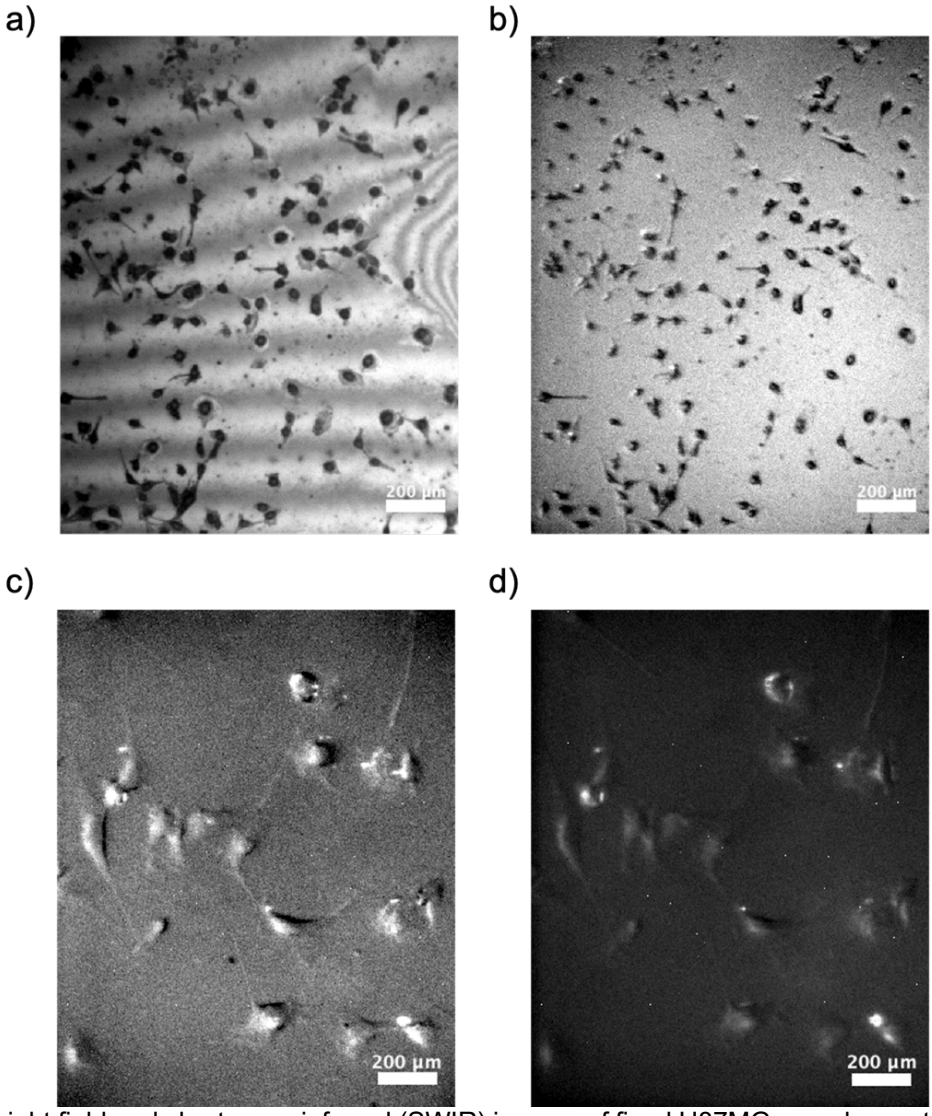

Figure 6.2 Bright field and short wave infrared (SWIR) images of fixed U87MG monolayers treated with 50 µg/mL AFt-PbS for 24 h. **(a)** Bright-field image acquired at 5x objective, **(b)** SWIR image obtained using a 980 nm long-pass (LP) filter, 0.5 s exposure, 5x objective, **(c)** SWIR image obtained using 980 nm LP filter, 0.4 s exposure, 20x objective, **(d)** SWIR image obtained using 1250 nm LP filter, 0.7 s exposure, 20x objective. All SWIR images were acquired using a 785 nm laser at 10% power. Scale bar is 200 µm. All images were acquired with assistance from Miss Dongling Zhang (National Research Council Canada).

6.2.2 Evaluation of imaging performance in *in vitro* 3D and *ex vivo* models

Evaluation of imaging capabilities in *in vitro* 3D and *ex vivo* models is essential to guide translation from 2D monolayers to *in vivo* biological systems. However, QD-based imaging investigations in spheroid models, particularly in NIR-II region, remain limited. To bridge this gap, this study aimed to evaluate the potential of PbS QD-containing formulations for deep

tissue penetration and NIR-II signal detection in more clinically-relevant models. Their performance was initially tested in *in vitro* 3D GBM spheroids to validate the initial hypothesis that PbS QD-containing formulations, particularly AFt formulations, offer enhanced depth tissue imaging performance for GBM management.

In the study, the 2 x IC_{50} treatment concentration of 50 µg/mL was used, for all formulations including PbS QDs, AFt-PbS and AFt-PbS-TMZ. In addition, the incubation time was selected as 6 days to allow enough time for NP uptake, and accumulation in the compact spheroid cultures, consistent with the previous 2D and 3D cell viability studies. The SWIR images obtained of untreated (control) and treated U87MG spheroids are presented in Figure 6.3, demonstrating depth imaging capabilities of these formulations in dense spheroids, and the accumulation potential of each formulation within 3D GBM models. As shown in Figure 6.3a, SWIR signals were detected from fixed U87MG spheroids post treatment for 6 days with all tested formulations using a 785 nm laser, LP-980 nm filter, 1.5 W power, 5x IR objective, and 0.03 s exposure time. Notably, SWIR signals were not detected in control (untreated) spheroids, confirming the specificity of the signals to PbS QD-containing formulations. However, the PL emission in PbS QD-treated spheroids (~ 500 µm in diameter, on day 7) was observed mostly at the periphery, as evidenced by strong NIR-II signals observed within outer spheroid regions. This accumulation may be either due to stronger PL intensity of QDs closer to surface, limiting sub-surface detection or due to limited diffusion into dense spheroid cores (on day 7). It may also reflect the viability of core cells within the spheroids since limited nutrient and oxygen diffusion can compromise the survival of the cells in the spheroid core. This could be further investigated using live/dead cross-sectional staining in future experiments. Signals from AFt-PbS and AFt-PbS-TMZ-treated spheroids may be indicative of enhanced uptake and SWIR emission compared to PbS QDs alone-treated spheroids, therefore suggesting that AFt encapsulation could enhance cellular uptake via targeted delivery facilitated by the AFt nanocarrier. These results confirmed PL stability in complex biological systems (3D spheroids),

deep tissue penetration, and retention of PL emission properties of all formulations within 3D tumour models.

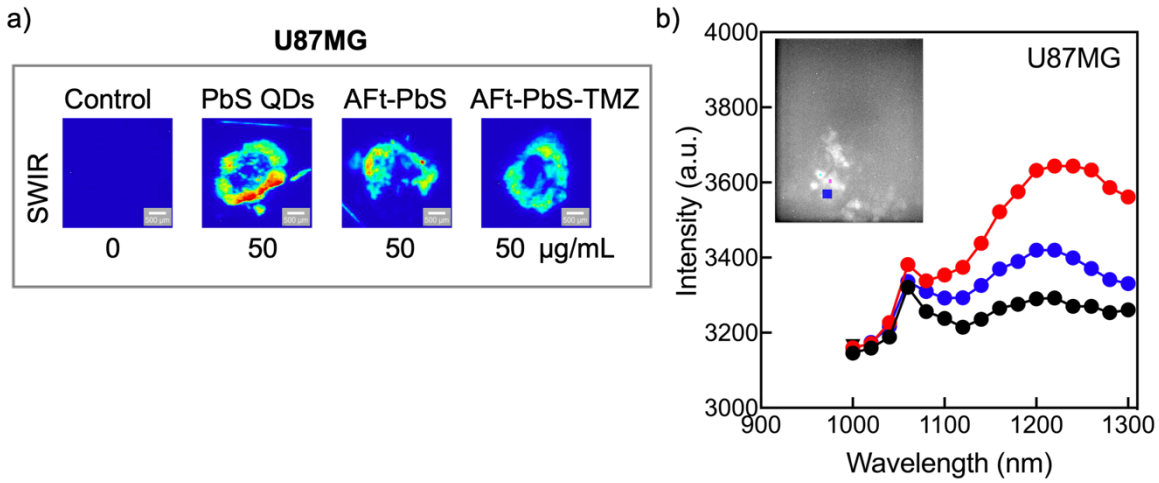

Figure 6.3 (a) Short wave infrared (SWIR) images of fixed U87MG spheroids untreated (control) and treated with 50 µg/mL PbS QDs, AFt-PbS, and AFt-PbS-TMZ for 6 days. Images were obtained using 785 nm laser, 1.5 W, 5x IR objective, 0.03 s exposure, 980 nm LP filter, and histogram stretching 20-5000. Scale bar is 500 µm **(b)** Representative intensity profiles of AFt-PbS accumulation in selected spheroid regions (inset) illustrating selected emission regions in AFt-PbS treated U87MG spheroids.

Recent studies have reported similar results of QDs' emission in NIR region and penetration to spheroid interiors by virtue of their signal that can be detected within 3D structures.[278-280] For instance, Yakavets *et al.* demonstrated NIR imaging capabilities of copper indium selenide/zinc sulfide based QDs (PL peak centred at 750 nm, NIR-I) in head and neck 3D spheroids. However, these QDs showed limited penetration, reaching only ~ 56 µm from the spheroid edges. The core of the spheroids (~ 400 µm) did not accumulate enough QDs, which researchers attributed to limited diffusion into the 3D spheroids.[279] In a study by Jarockyte *et al.*, CdSe/ZnS QDs (PL peak centred at 625 nm, NIR-I) were applied to breast cancer spheroids, they were localised mostly at the periphery. However, MCF-7, MDA-MB-231, and NIH3T3 spheroids allowed limited penetration of QDs, reaching up to 25 µm into cellular spheroids after 24 h incubation.[280] These findings highlight the current limitations of QDs penetration in the NIR-I window in 3D spheroid models due to scattering, consistent with a previous study reporting penetration depths up to 100 µm.[281] Therefore, there is a need for NIR-II imaging to enable deeper tissue visualisation.

To determine whether the obtained SWIR signals originate from the PbS QD-containing formulations in 3D cultures, the cores of spheroids treated with 50 µg/mL of AFt-PbS were selected randomly for analysis, and the corresponding areas are shown in the inset of Figure 6.3b. The intensity profiles across selected emission regions in AFt-PbS treated spheroids were analysed; the hyperspectral analysis is presented in Figure 6.3b. These analyses also aimed to demonstrate whether AFt formulations were capable of diffusing beyond the periphery of the spheroids and penetrate deeper into the cores. The findings indicated that all selected core regions of the spheroids exhibited peak emissions centred within the comparable NIR-II wavelengths, particularly at 1050 nm and 1200 nm. We note that the used imaging system enables only macroscopic imaging and does not allow to determine lateral distribution of the PL signal. Based on the previously characterised PL properties of AFt-PbS (see Section 3.2.3), these dual peaks may be attributed to several factors including sample age, size heterogeneity (protein aggregation), and biological autofluorescence. Additionally, the observed peak in the spheroid cores demonstrate the internalisation of AFt-PbS into inner layers of spheroids, which is challenging in dense 3D spheroids. These results indicate the potential of PbS QDs, AFt-PbS, and AFt-PbS-TMZ formulations as SWIR emitters for monitoring treatment response in 3D tumour models, supporting the initial hypothesis that PbS QD-containing formulations will enable SWIR imaging of GBM cells in *in vitro* 3D cultures. AFt encapsulated formulations' retained SWIR signal stability originated from PbS QDs, penetrate depth tissues make them suitable candidates for imaging applications. Particularly, the AFt-PbS-TMZ formulation presents an advanced potential as a multifunctional platform for future theranostic applications.

To corroborate the capabilities of PbS QD-containing formulations to emit strong NIR-II signals through brain tissues, imaging studies were performed with QD-based formulations placed under brain tissue slices. Figure 6.4a demonstrates the findings under a 1 mm thick brain tissue slice overlaying capillary tubes with PbS QDs (4 mg/mL) and AFt-PbS (2.5 mg/mL). At the identical depth of 1 mm, the NIR emission through the brain tissue was detected for both

formulations (PbS QDs and AFt-PbS), with PL intensity scaling linearly with QD concentration (Figure 6.4a). Their corresponding concentration-dependent intensity profiles were presented in Figure 6.4b. The higher PL intensity observed for PbS QDs (4 mg/mL, PL intensity:3500 a.u.) compared to AFt-PbS (2.5 mg/mL, PL intensity: 2700 a.u.), which may explain by their concentrations. Importantly, at 2.5 mg/mL, AFt-PbS reached a PL intensity of 2700, whereas PbS QDs alone yielded only 2188 at the same concentration. In healthy brain tissue slices, AFt encapsulation may contribute to enhance signal intensity by improving the stability of PbS QDs within the tissue.[206] These findings suggest that PbS QDs-containing AFt formulations can facilitate NIR-II imaging through brain tissue with reduced scattering and deeper tissue penetration. In addition, image intensity and clarity might be influenced by depth and concentration.[97]

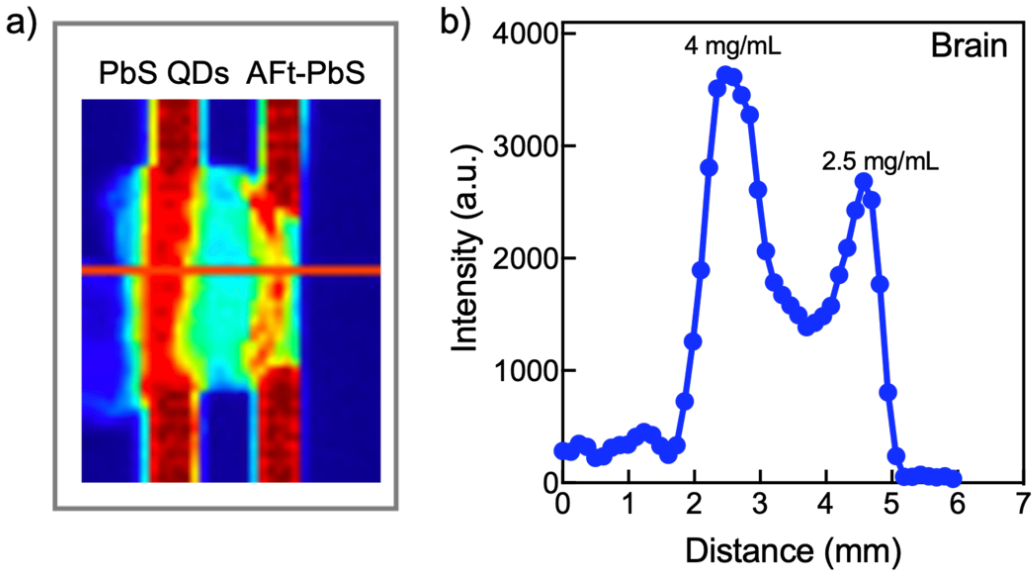

Figure 6.4 (a) Capillary tubes loaded with PbS QDs (4 mg/mL) and AFt-PbS (2.5 mg/mL) overlaid with brain tissue slices and their corresponding **(b)** concentration-dependent intensity profile (785 nm laser at 20% power, 1000 nm LP, exposure time:0.1 s, histogram stretching: 1000-5000).

In vitro 3D spheroids and imaging of the QDs under tissue slices demonstrated that PbS QD-containing AFt formulations may be used as NIR-II probes while AFt encapsulation offers biocompatibility and potential for selective cancer imaging. Therefore, these results support further development of AFt-PbS-TMZ as a potential NIR-II imaging probe for GBM theranostics.

6.2.3 Evaluation of imaging performance in *in vivo* and *ex vivo* models

Although this PhD project mainly investigated the imaging performance of PbS QDs, AFt-PbS, and AFt-PbS-TMZ formulations, extensive *in vivo* studies were not possible. Only one type of PbS QD could be selected for the *in vivo* exploratory study – PbS/PEG. PEGylation represents an alternative promising strategy to AFt encapsulation: PEGylation is known to enhance biocompatibility, *in vivo* stability and pharmacokinetic properties of NPs.[113] Therefore, the imaging abilities of PEGylated PbS QDs were evaluated in *in vivo* and *ex vivo* models within the SWIR window. Accordingly, PEGylated PbS QDs might be a reference for future *in vivo* studies with PbS QD-containing formulations including PbS QDs, AFt-PbS, and AFt-PbS-TMZ.

To examine the real-time *in vivo* imaging capabilities of PEGylated PbS QDs, mice were injected via the tail vein with a PbS QD solution in water (200 µL; 2.4 mg/mL), resulting in a final concentration of 0.24 mg/mL (QDs synthesised by Miss Ellie B. Ward, see Section 2.10). These PbS/PEG QDs have PL emission centred at 968 nm. Time-lapse SWIR images were captured over 2 h, and representative live mice images at 0, 12, 60,106 min post-injection are presented in Figure 6.5a. A clearly measurable NIR-II fluorescence signal was observed immediately after injection, spreading through the veins, followed by stronger PL emission observed in the specific organs including liver and spleen, indicating the preliminary biodistribution profiles of the PbS QDs, consistent with previous reports demonstrating predominant clearance through the liver, spleen then kidneys and urinary tract.[113, 282] During the study (~2 h), a gradual decrease in the SWIR signal intensity was observed, as expected for PEGylated NPs. In agreement with our findings, Tang *et al.* reported PEGylated Ag_2Se QDs rapidly (24 min) cleared from the blood and accumulated mainly in the liver and spleen.[283] In addition to the accumulation in the major organs, bright emission was detected in a triangular-shaped fat pad in mice's necks at the beginning of the experiments, consistent with a previously published report.[284]

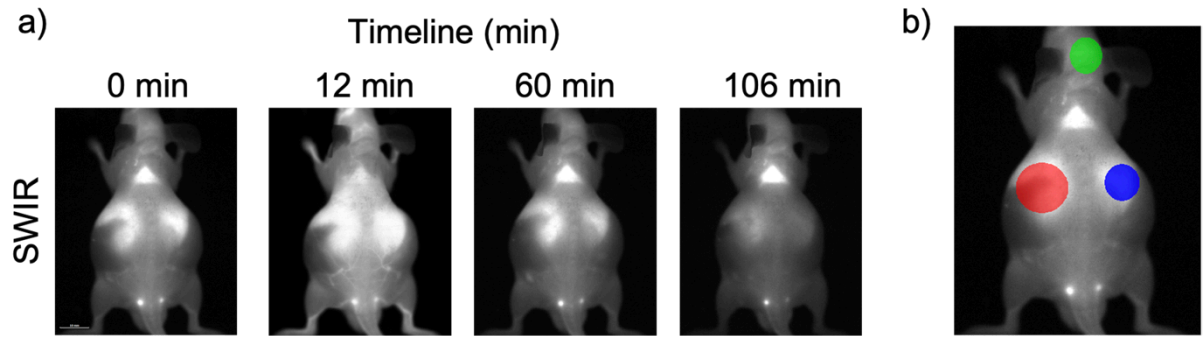

Figure 6.5 *In vivo* SWIR imaging of PEGylated PbS QDs using IR VIVO SynIRgy system. **(a)** Time-lapse short-wave infrared (SWIR) images of live nude mice captured at various time points (0,12, 60, and 106 min) post-injection of PEGylated PbS QDs. Images were acquired using a 785 nm laser, 1000 nm LP filter, 0.05 s exposure time. **(b)** The regions of interest (ROI) selection for brain (green), liver (red), and spleen (blue) for quantitative signal analysis.

To quantify the NIR-II signal intensity within the specified organs (liver, spleen, brain), regions of interest (ROIs) were selected in the *in vivo* images for the liver (red), spleen (blue), and brain (green), as shown in Figure 6.5b. The SWIR intensity changes in the selected organs over the time were determined with quantitative intensity analysis from the *in vivo* images and presented in Figure 6.6a; data represent the average of two datasets. Additionally, their corresponding time-constants (τ) were determined from the average of two datasets as 36.0 ± 4.0 min for the liver, 24.0 ± 2.0 min for spleen, 17.0 ± 1.0 min for brain. These findings suggest that the PEGylated PbS QDs were cleared most rapidly from the brain, followed by the spleen, while longest retention remained in the liver, indicating organ-specific biodistribution. These preliminary biodistribution studies, demonstrating particularly liver and spleen accumulation, are consistent with previous preclinical *in vivo* studies.[113, 285] In addition, the intensities in the organs were analysed by two independent measurements and selection criteria; the comparative results are illustrated in Figure 6.6b-d for the liver, spleen, and brain, respectively. These two independent analyses found that the liver exhibited the highest signal (2895.5 ± 206.9 arb.un.) with a slower rate of decay (Figure 6.6b) whereas brain demonstrated the lowest signal (2165.5 ± 36.1 arb.un.) with the most rapid decay (Figure 6.6d). On the other hand, the spleen illustrated a moderate signal (2811 ± 6.2 arb.un.) with relative to faster clearance observed in the liver (Figure 6.6c). Taken together, PEGylated PbS QDs showed significant and prolonged accumulation in the liver ($t_1/_2$ = 25.0 ± 3.0 min), intermediate retention in the

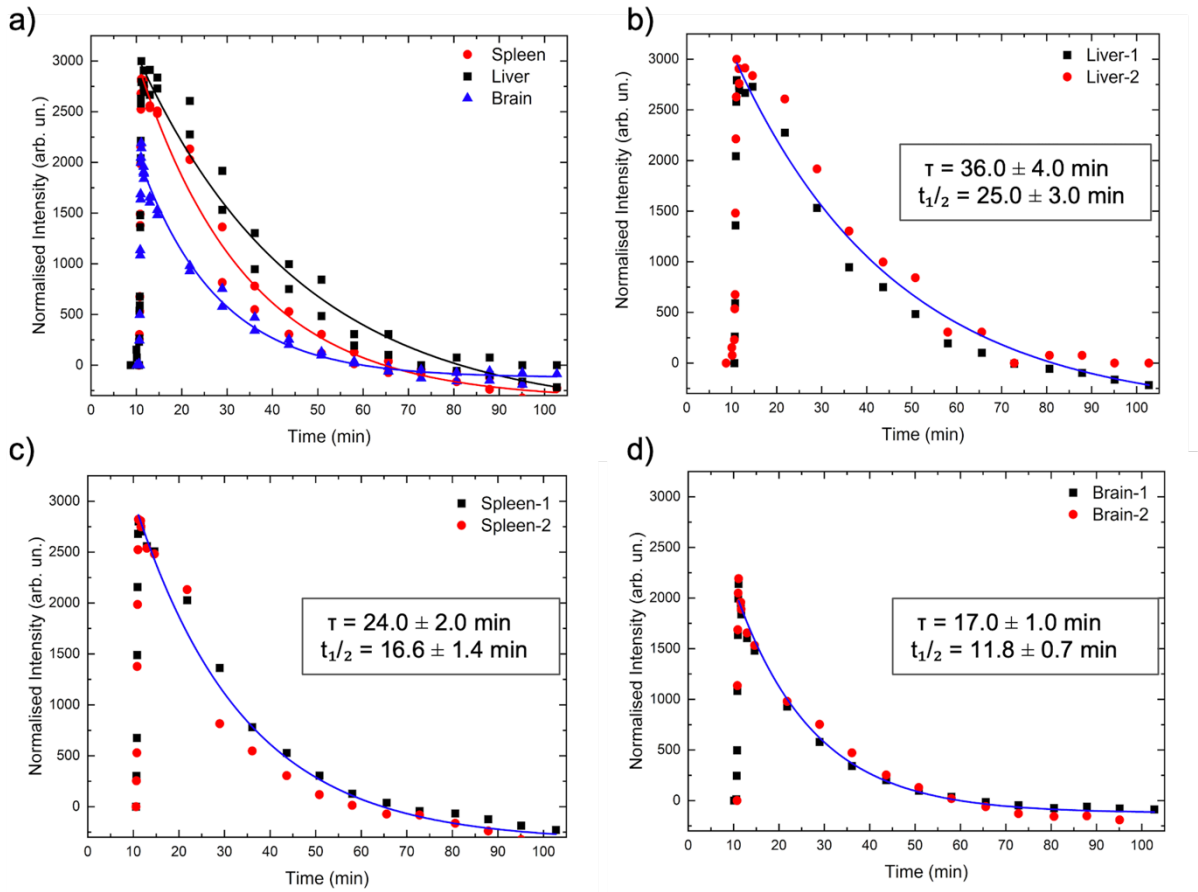

Figure 6.6 (a) The normalised intensity profiles of the selected major organs (liver, spleen, brain) over time, based on short wave infrared (SWIR) signal obtained from the *in vivo* images. Individual normalised intensity decay curve profiles from two independent measurements (1 and 2 represent the first and second independent measurements, respectively) for **(b)** liver, **(c)** spleen, and **(d)** brain. Time constants (τ, min) and half-life ($t_1/_2$, min) calculated from exponential decay fitting of SWIR intensity in liver, spleen, and brain following PEGylated PbS QDs treatment.

spleen ($t_1/_2$ = 16.6 ± 1.4 min), and limited uptake was observed in the brain ($t_1/_2$ = 11.8 ± 0.7 min). This limited uptake from brain may be improved by AFt encapsulation due to high TfR1 expression of BBB endothelia.[286, 287] Previously, Zamberlan *et al.* employed LNH_2-capped PbS QDs (with a PL peak centred at 1220 nm) for NIR-II imaging and detected *in vivo* signals only in liver and spleen, but not in the brain, indicating that these QDs did not cross the BBB.[113] In contrast, in our study, SWIR signals were detected in the brain after treatment with PEGylated PbS QDs, suggesting a potential to cross the BBB, possibly facilitated by PEGylation. Similarly, AFt encapsulated formulations (AFt-PbS and AFt-PbS-TMZ) may facilitate BBB crossing through TfR1-mediated transcytosis related to upregulated TfR1 expressions in both BBB endothelial and GBM cells.[30, 287] Supporting this hypothesis, Bradshaw *et al.* demonstrated that

AFt-PbS was well-tolerated over a period of 15 days in acute toxicity evaluations carried out in both female mice without tumour and mice with HCT-116 colorectal tumours.[216]

To evaluate the presence of QDs in the organs after 2 h *in vivo* imaging, the SWIR images of the organs were recorded *ex vivo*. Figure 6.6a shows the *ex vivo* SWIR images of these organs obtained post-experiment; and their corresponding signal intensities were quantified to assess the organ specific retention of PEGylated PbS QDs, as shown in Figure 6.7b. *Ex vivo* images demonstrated that the fluorescence signal in the liver was notably stronger than in the spleen after ~2 h post-injection. These results were also supported by quantitative analysis, which showed that *ex vivo*, liver exhibited a significantly ($p < 0.01$) higher signal intensity (3618 ± 103 arb.un.) compared to the spleen (1446 ± 5 arb.un.), indicating ~2.5-fold higher accumulation in the liver (Figure 6.7b).

The QD PL intensities recorded in the liver and spleen were comparable when measured *in vivo* and their corresponding signals *ex vivo*. The results showed that the emission intensity in the area of liver recorded *in vivo* (2895 ± 146 arb.un.) was slightly lower than *ex vivo* (3618 ± 103 arb.un.). In contrast, the QD emission intensity recorded in the area of the spleen *in vivo* (2811 ± 14 arb.un.) was higher than *ex vivo* (1446 ± 5 arb.un.). These results can be explained by deeper location of liver compared to spleen *in vivo*, which may have an impact on reduced *in vivo* signal in the liver due to increased depth in mice. Similarly, Tang *et al.* demonstrated masked liver fluorescence *in vivo* following AG_2Se QDs treatment, whereas spleen exhibited a clearer signal.[283] According to Zamberlan *et al.*, increased *ex vivo* liver tissue thickness (0-4 mm) resulted in decreased intensity as might be expected.[113] In addition, the lower *ex vivo* signal observed in the spleen might be attributed to faster clearance of QDs from the spleen compared to the liver, resulting in a shorter accumulation time.[288] Lin *et al.* reported that their cadmium-free indium phosphide/ zinc sulfide QDs with different surface functional groups accumulated in major organs of mice within 2 h post-administration with the highest concentrations observed in the kidney, heart, spleen, liver and brain. However, after 24 h,

concentrations in kidney, heart, spleen, and brain decreased while the accumulation in the liver increased over the time.[288]

Demonstrated in this work is the capability to detect emission of the PbS QDs in the SWIR wavelength range from such depths is promising for bioimaging, particularly considering the deeper anatomical location of liver (several millimetres below the surface and rib cage). Taken together, these findings indicate that SWIR signal intensity is strongly depth-dependent, and PbS QDs as SWIR emitters are potential candidates for deep tissue imaging applications. Therefore, AFt-PbS and AFt-PbS-TMZ formulations may enhance PbS QDs capability with targeted delivery, improved tissue accumulation, signal retention in depth, hence offering promising platforms for GBM theranostic applications.

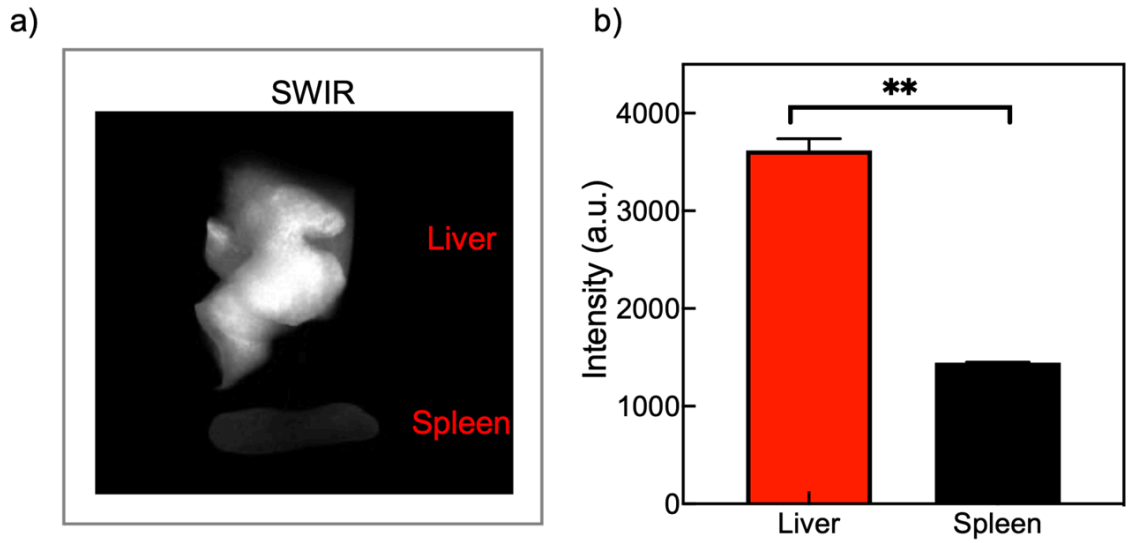

Figure 6.7 *Ex vivo* short-wave infrared (SWIR) imaging of harvested organs using IR VIVO SynIRgy system. **(a)** SWIR images of the liver and spleen at the end of the experiment (2 h). Images were obtained under 785 nm, 1000 nm LP, 50 ms exposure time. **(b)** The comparison analysis of intensities of the liver and spleen *ex vivo*. Data presented as average of two data sets.

6.3 Conclusion

In conclusion, the SWIR imaging capabilities of PbS QD-containing formulations (PbS QDs, AFt-PbS and AFt-PbS-TMZ) were comprehensively examined in biological systems including 2D and 3D U87MG GBM cell cultures and *ex vivo* brain tissues. Additionally, PEGylated PbS QDs were evaluated in both *in vivo* and *ex vivo* models, functioning as a reference for future

in vivo studies involving PbS QD-containing formulations. These assessments provide a comprehensive understanding of the potential of PbS QDs, AFt-PbS, and AFt-PbS-TMZ in the SWIR window, particularly for deep tissue GBM imaging applications.

PbS QD-containing formulations were found to be suitable for imaging 2D GBM monolayers, as supported by the detection of a NIR-II signal following AFt-PbS treatment in 2D U87MG cells. Additionally, consistent with the 2D imaging results, SWIR signals were also detected in 3D U87MG spheroids post-treatment with all tested formulations, demonstrating the deep tissue imaging capabilities of PbS QD-containing formulations in complex and dense spheroid models. *Ex vivo* brain tissue imaging corroborated the obtained 2D and 3D imaging findings, revealing penetration of signal through the brain tissue, with detectable SWIR signal post-treatment with both PbS QDs and AFt-PbS formulations. Importantly, AFt-based formulations demonstrated signal retention, enhanced clarity, reaching deeper regions within the biological systems via a (TfR1-) targeted delivery approach. Among all tested formulations, AFt-PbS-TMZ displayed dual functionality combining enhanced therapeutic potential and cancer-selective imaging with targeted delivery, enabling real-time imaging for GBM. In addition to AFt-based formulations, the imaging performance of PEGylated PbS QDs was evaluated both *in vivo* and *ex vivo*. PEGylated PbS QDs were biocompatible, well tolerated by mice, and demonstrated a strong SWIR signal via accumulated in the specific organs (liver, spleen, and brain). These findings validate PbS QD' imaging capabilities and provide valuable preliminary data prior to comprehensive biodistribution studies. Broadly-speaking, these outcomes support further pre-clinical and clinical translation potential of PbS QD-containing formulations for biomedical applications, particularly for high-resolution imaging in deep tissues.

The assessments of PbS QDs' imaging capabilities indicate that they exhibit strong fluorescence intensity, enabling deep tissue imaging, as well as enhanced stability using protein encapsulation or PEGylation, making them suitable candidates for SWIR imaging applications. Although NIR-II emission is ideal for penetrating deeper *in vivo*, the limited capacity of NIR-II probes for crossing the BBB, along with the lack of availability of NIR-II

imaging systems, significantly hampers GBM detection. Therefore, targeted delivery systems can improve the accumulation of PbS QDs within GBM tumours. Consistent with the chapter hypothesis, both single PbS QDs' encapsulation and co-encapsulation of TMZ and PbS QD within AFt nanocages potentially enable real-time monitoring, improve tumour-specific accumulation in GBM, reduce off-target signal in non-cancerous tissues in the SWIR window. Thus, an AFt-PbS-TMZ formulation may be a candidate for improved imaging specificity, contrast and real-time theranostic capabilities in the NIR-II window. However, the development of appropriate imaging systems and further investigations are needed to facilitate to clinical translation, including *ex vivo* and *in vivo* biodistribution, tolerability and therapy-monitoring studies to evaluate their long-term safety and efficacy.

Chapter 7 Final discussion

Despite the current standard of care with TMZ, GBM prognosis remains poor due to disease heterogeneity, the invasive and aggressive nature of GBM, limited TMZ delivery, systemic toxicity, and TMZ resistance.[83] To overcome these limitations, targeted therapies aim to exploit genetic alterations in tumours while sparing healthy tissues.[54] In our study, we developed a multifunctional theranostic platform combining both NIR-II imaging agents, PbS QDs, and therapeutic delivery of TMZ within AFt nanocages, with innate TfR1-mediated targeting ability to GBM cells.[83, 173] This theranostic protein-based NP addresses two key limitations of current GBM management: (1) limited deep tissue imaging and (2) inadequate tumour specific TMZ delivery.[289]

AFt encapsulation has been reported to enhance growth inhibition and tumour specific targeted delivery in multiple cancer cell lines, including GBM[83, 173, 174], colorectal[216], and breast cancer[224, 290], mostly in 2D monolayers. However, despite 2D monolayers' widespread use, these models present notable limitations to represent *in vivo* tumour.[238] Our findings in 3D GBM cultures corroborated 2D findings that AFt encapsulation enhanced TMZ activity in line with the statement of AFt formulations selectively target GBM cells via H-subunit's natural binding to TfR1, which is overexpressed in highly proliferative cancer (GBM) cells with high iron demands.[161] In addition to targeting, AFt offers several advantageous properties including a small nanoscale size (~12 nm), negative surface charge, biocompatibility, and the ability to encapsulate a broad range of drugs and imaging agents.[212] These properties contribute to AFt's potential as a promising targeted delivery nanocarrier for diagnostic, therapeutic, and theranostic applications with reduced immune clearance and non-specific cellular uptake.[212]

However, clinical translation of GBM therapeutics is often hindered by the permeability of the BBB.[41] Although convection-enhanced delivery (CED) enables direct infusion of NPs into brain tissue, its clinical application is limited by invasiveness and variable drug distribution that highlight the need for BBB-penetrating delivery systems.[121, 291] Strategies to overcome this

restrictive barrier, include overexpressed TfR1 receptor targeting to facilitate receptor-mediated endocytosis.[41] Previously, drugs such as TMZ[128], paclitaxel[292], DOX[293] encapsulated NPs have been conjugated to transferrin to enhance the drug delivery to the brain by receptor mediated endocytosis. In addition to BBB limitations, tolerance to TMZ-induced *O*6-MeG lesions through MMR loss, intrinsic and acquired resistance mechanisms, involving the DNA repair enzyme MGMT and ABC proteins such as P-gp, further compromise the therapeutic activity of TMZ in GBM.[85] In line with previous studies' hypothesis[83, 172], our western blot analysis demonstrated rapid MGMT depletion following treatment with AFt formulations, indicating the potential of AFt encapsulation to sensitize GBM cells to TMZ treatments. Moreover, AFt encapsulation may further overcome efflux transporters, such as ABC proteins (e.g P-gp), further investigation is required to confirm this mechanism. These findings hold significant promise for overcoming delivery barriers and TMZ chemoresistance mechanisms to improve clinical GBM outcomes.

High failure rates in the development of novel drugs can be partially attributable to reliance on 2D models.[238] Therefore, we extended our research to include GBM tumour spheroid models to more accurately mimic tumour heterogeneity with gradients of oxygen, nutrients, proliferation rates, and altered gene expression profiles.[294] Our findings suggested that among all tested formulations, the co-encapsulation of TMZ and PbS QDs within AFt nanocages (AFt-PbS-TMZ) indicated the most growth inhibition in both 2D GBM monolayers and U87MG spheroids. The co-encapsulated formulation significantly reduced spheroid volume, cell viability, demonstrating the benefit of AFt mediated co-delivery.[244] 3D GBM spheroids are less sensitive to treatments, with higher IC_{50} values compared to 2D cultures.[237, 265] However, the co-encapsulated formulation enhanced its activity in 3D cultures compared to 2D monolayers, consistent with a previous report demonstrating folic-acid functionalised silver and upconverting NPs, where 20% higher uptake in 3D cultures was reported.[265] The differences observed between 2D and 3D cultures may be attributed to variations in pH conditions (more acidic pH levels (reaching pH ~6.4) observed in the central core of the U87 spheroids after 72h

of spheroid formation[295]), altered cellular signalling, enhanced cell-cell interactions, and the presence of heterogenous cell populations in 3D cultures.[211]

In the clinic, TMZ is administered concomitantly with radiotherapy for 6 weeks, followed by 6 28-day cycles of TMZ on five consecutive days within the interval of four weeks.[53, 54] In our sequential treatment experiments, a three-phase treatment plan with naked or AFt encapsulated formulations led to U87MG spheroid destruction, and improved the single dose therapy outcomes. Remarkably, spheroids exposed to naked TMZ or the naked combination (mix of TMZ and PbS QDs) acquired resistance[53, 266], whereas those receiving AFt formulations did not, corroborating earlier findings that AFt carriers can circumvent TMZ resistance.[83, 172] Additionally, a single low dose (5 μM, TMZ-based) of AFt-PbS-TMZ was sufficient to inhibit GBM growth in our spheroid models to levels comparable with those reported by Shaikh *et al.* using exosome carriers co-loaded gold NPs and TMZ.[267]

PbS QDs offer promising cancer imaging capabilities in the SWIR, a consequence of their high PL, photostability, and narrow emission spectra.[272] However, conventional NIR-I probes are restricted by their limited tissue penetration and poor resolution.[102, 279, 281] Herein, we demonstrate that PbS QDs, when (co)-encapsulated in AFt nanocages, enable imaging in the SWIR window in 2D GBM cultures, 3D GBM spheroids, and brain tissue slices, overcoming scattering and depth barriers in GBM.[296] While AFt nanocages have been explored previously as theranostic platforms[198, 200], most studies lacked NIR-II imaging and in-depth evaluation in GBM tissues. Notably, we achieved up to 1000 μm imaging depth through brain slices in the NIR-II window, which is 10-fold deeper than previously reported for NIR-I probes.[281] The novelty of our co-encapsulation strategy lies in the integration of a NIR-II imaging probe and a therapeutic agent within a targeted nanosized carrier, representing several key advancements, including combination therapy, enhanced therapeutic activity, the ability to overcome TMZ resistance through a targeted protein-based nanoplatform, and high-quality deep tissue imaging performance. Overall, our findings highlight the potential of AFt as diagnostic,

therapeutic, and theranostic protein NPs for real-time GBM monitoring and management, with broader applications for cancer theranostics.

However, it is important to acknowledge the limitations of horse spleen AFt and its particle production methods when considering the potential clinical applications. In the study, AFt was derived from horse spleen Ft, which is commonly employed as protein based nanocarrier system due to its availability and well-known protein structure. However, for clinical translation, regulatory requirements would necessitate the use of human Ft isoforms to minimise immunogenicity and compliance with biopharmaceutical safety standards.[297] In terms of NP production, microfluidic systems offer advantages in scalability, reproducibility, process control, which are critical for regulatory approval, large-scale manufacturing, and speed up the production of NPs.[298] Therefore, future optimisation of the current encapsulation and co-encapsulation protocols may involve the implementation of microfluidic-based synthesis platforms, which would provide improved control over particle size distribution, monodispersity, and encapsulation efficiency during large-scale production.

Chapter 8 Conclusions and future work

8.1 Conclusions

GBM remains a major clinical challenge due to its resistance to conventional treatments and the presence of restrictive barriers such as BBB. Due to these barriers and the deep anatomical location of brain tumours hinder both therapeutic delivery and imaging. Therefore, new strategies that enable targeted delivery and facilitate deep tissue imaging are critical for improved GBM treatment and monitoring approaches.

This study developed a multifunctional platform for treatment, monitoring, and therapy of GBM tumours, by integrating nanotechnology, cancer biology, and imaging strategies. AFt as a drug delivery vehicle provides a promising platform for theranostics, enabling co-encapsulation of chemotherapeutic drug TMZ and imaging agent PbS QDs. TMZ is clinically used for GBM treatment, but drug resistance often thwarts successful outcomes, whereas PbS QDs offer deep tissue imaging in the NIR-II, making them suitable for visualising depth tumours such as GBM. This AFt-based platform is being developed to deliver drugs/ imaging agents directly to GBM tumours, enabling treatment, deep tissue imaging and therapy monitoring.

In summary, PbS QDs were successfully synthesised to exploit their promising PL activity in the SWIR region. However, their potential cytotoxicity necessitates use of a biocompatible nanocarrier. Similarly, TMZ requires a DDS to enable targeted delivery and overcome drug resistance in GBM. To combat these limitations, encapsulation methods were optimised for naked PbS QDs (disassembly/reassembly), naked TMZ (nanoreactor), and their combination (TMZ+PbS QDs) within AFt nanocages. The developed co-encapsulated formulation (AFt-PbS-TMZ) was produced using disassembly/reassembly for PbS QD (entrapped one QD per AFt cage) and nanoreactor routes for TMZ.

Single encapsulations yielded one QD entrapped per AFt cage for AFt-PbS and ~516 TMZ molecules per cage for AFt-TMZ. Particularly, AFt-PbS-TMZ resulted in ~309 TMZ molecules with >70% EE. All formulations were comprehensively characterised by DLS for NP size and zeta potential, native-PAGE for protein integrity, HR-TEM for morphology, *in vitro* release profiling, and storage stability. In addition, PL activity of PbS QD-containing formulations (PbS QDs, AFt-PbS, and AFt-PbS-TMZ) were evaluated. The results showed that AFt formulations retained their size, charge, protein integrity, morphology, and PL activity following encapsulation process.

The biological activity of formulations was evaluated against 2D GBM cells, including TMZ-resistant (MGMT-positive) and TMZ-sensitive (MGMT-negative), as well as non-cancerous cells. By exploiting upregulated TfR1 expression in 2D GBM cells, AFt formulations exhibited cancer selectivity and enhanced cytotoxicity to GBM cells compared to their naked counterparts while reducing the activity of formulations in non-cancerous cells (MRC-5 and astrocytes). Western blot and flow cytometry results supported TfR1-dependent AFt-uptake. Notably, AFt-TMZ and AFt-PbS-TMZ enhanced the activity of TMZ resulting in potentiated cytotoxicity in MGMT-positive and MGMT-negative GBM cells. Particularly in MGMT-positive (U373M) cells, both AFt formulations (AFt-TMZ and AFt-PbS-TMZ) indicated a reduction in MGMT expression, thus overcoming TMZ resistance and driving their enhanced *in vitro* growth inhibitory effects. Among all tested formulations, AFt-PbS-TMZ exhibited enhanced therapeutic effect with a potential for SWIR imaging. Notably, AFt alone (vehicle control) proved to be non-toxic in 2D cultures.

The formulations were investigated in comparison with their naked counterparts in TMZ-sensitive U87MG spheroids, representing 3D GBM tumour models. These GBM models are important for evaluating treatment success by allowing drug/imaging agent penetration into deeper tumour regions. Consistent with 2D results, AFt encapsulation enhanced the activity of naked agents in 3D GBM cultures, depending on the upregulated TfR1 expression in the spheroid cultures (Figure 5.13). Among all tested formulations, AFt-PbS-TMZ demonstrated

the most enhanced GBM spheroid growth, viability, and volume reduction, demonstrating AFt's co-delivery advantages. However, 3D GBM cultures in our study were generally more resistant to treatments compared to 2D monolayers, demonstrating the importance of testing formulations in more clinically-relevant 3D models for their successful pre-clinical and clinical translation. Remarkably, AFt alone (vehicle control) exhibited no toxicity in 3D cultures, further validating its biocompatibility as a delivery vehicle. Therefore, the developed AFt-based co-delivery platform offers a promising strategy for therapeutic, diagnostic, and theranostic applications in GBM.

We also investigated the imaging capabilities of PbS QD-containing formulations in the SWIR range post-encapsulation within AFt nanocages, with a particular focus on the potential of the co-encapsulated platform as a theranostic agent. Imaging performances of the formulations were tested in different biological models: (1) 2D monolayers representing simplified *in vitro* systems, (2) 3D spheroids representing depth GBM tumours, and (3) *ex vivo* brain tissue slices (1 mm thickness). Among all tested models, PbS QD-containing formulations retained their SWIR signal intensity following encapsulation into AFt nanocages, confirming stability, and imaging ability of PbS QDs in AFt nanocages. Remarkably, in 3D spheroids and brain tissue models, AFt formulations enabled SWIR imaging within deep tissue, potentially resulting in treatment response monitoring.

In conclusion, TMZ encapsulation in AFt potentiates therapeutic activity in malignant GBM 2D and 3D cultures. TfR1 upregulation is associated with AFt formulations' uptake and its cancer selective activity in GBM cultures. AFt alone demonstrated non-toxicity (2D and 3D), confirming all activity originated from the encapsulated agents. Co-encapsulation offers the potential to direct theranostic molecules to the tumour site, image deep tumour tissue, enhance activity of the therapeutic moiety and protect normal tissues from toxic effects of both imaging and therapeutic agents. In addition, this cross-disciplinary platform is worthy of further preclinical evaluation *in vivo* and potential clinic translation, leading to better outcomes for GBM

patients. Additionally, AFt offers a biocompatible and versatile platform that can be adaptable to other difficult to treat solid tumours in the future. However, further investigations are required.

8.2 Future work

Future studies may include advanced experimental settings to enable a deeper understanding of AFt-based formulations' behaviour, including possible resistance mechanisms, tumour targeting ability, and long-term safety. These investigations will guide AFt nanocarriers' application for effective GBM treatment. Therefore, future work may focus on following directions to better predict the therapeutic, diagnostic, and theranostic potential of AFt-based formulations:

- *In vitro* stability studies of AFt formulations focusing on TMZ stability within AFt and AFt-PbS nanocages using high-performance liquid chromatography (HPLC) and/or liquid chromatography-mass spectrometry (LC-MS) methods to quantify TMZ amount at different time points and conditions (pH, temperature, etc.), which is critical for predicting the shelf-life, storage conditions of AFt formulations for future studies.
- The assessment of environmental pH in spheroid cultures to investigate how the tumour microenvironment may affect TMZ release from AFt nanocages, considering pH-dependent stability of TMZ and using acidic pH (5.5) condition to increase TMZ stability in AFt nanocages. This will provide a better understanding of the performance of AFt-TMZ formulation observed in 3D GBM cultures.
- The examination of cumulative drug penetration and evaluation of intracellular drug levels in 3D GBM spheroids following exposure to naked and AFt encapsulated formulations using Orbi-SIMS and HPLC, respectively to assess the distribution profile of encapsulated formulations within different spheroid regions such as core, providing a more predictive model for *in vivo* efficacy.
- The assessment of potential TMZ resistance mechanisms that may emerge between treatment cycles with TMZ-containing formulations (AFt-TMZ and AFt-PbS-TMZ) by

analysing MGMT and MMR proteins, such as MSH2 and MLH1, via western blot in 3D spheroids and GBM tissue samples. This may guide optimisation of treatment schedules and strategies in the clinic.

- The evaluation of TfR1 expression in 3D spheroids and GBM tissues at different time points using western blot and flow cytometry after treatment with formulations to determine whether TfR1 expression is altered upon treatment, affecting the targeted delivery mechanism of AFt and it's *in vivo* efficacy. This may help to guide re-treatment intervals depending on the TfR1 expressions.
- The assessment of *O*6-MeG lesions in cells of spheroids treated with TMZ, AFt-TMZ, and AFt-PbS-TMZ formulations to evaluate the DNA alkylation effect induced by TMZ following treatments using western blot and/or ELISA assays. This investigation may support the findings from *in vitro* growth inhibition assays by demonstrating that AFt encapsulation enhances TMZ delivery to GBM cells.[83]
- Transcriptomic and/or proteomic analysis using RNA-Seq and/or mass spectrometry of GBM spheroids following treatment with naked and AFt encapsulated formulations, to investigate how AFt encapsulation induces MGMT depletion and elucidate underlying molecular pathways.
- The assessment of BBB penetration of AFt formulations compared to naked agents using *in vitro* transwell assay with brain endothelial cells and advanced organ-on-a-chip models, in order to evaluate their ability to cross BBB via TfR1-mediated targeted delivery.
- The evaluation of cellular uptake of PbS QD-containing formulations at 5 min, 30 min, 1 h, and 6 h post-treatment to determine the minimal exposure time needed for the TfR1-mediated internalisation while minimising PbS QDs-associated potential toxicity.
- The assessment spheroid core viability using live/dead cross-sectional staining to compare core versus peripheral cell viability to understand accumulation of formulations in 3D spheroids. This study will help to clarify how AFt-based formulations

penetrate and kill cells through the dense spheroids, complementing PB cell viability results in 3D cultures.

- To better represent *in vivo* tumour microenvironment and assess the impact of ECM components on AFt delivery, future studies may involve evaluating AFt formulations in 3D co-culture spheroid models using astrocytes and fibroblast embedded in ECM-mimicking hydrogels, patient-derived GBM cells/tissues, and organoid models. These advanced models will enable the investigation of how ECM affects drug penetration and provide formulation activity, and cancer selectivity.
- *In vivo* and *ex vivo* comprehensive biodistribution studies (preliminary AFt biodistribution studies have been performed in collaboration with colleagues in Canada and are reported in Appendix 1) to further evaluate the long-term safety, *in vivo* stability, clearance profile from the body, and organ accumulation of naked and AFt formulations. These studies may complement by pharmacokinetic (PK) and pharmacodynamic (PD) studies to investigate circulation time of formulations and their efficacy *in vivo*.
- To demonstrate *in vivo* efficacy studies of all formulations and *in vivo* real-time imaging potential of PbS QD-containing formulations (PbS QDs, AFt-PbS, AFt-PbS-TMZ), *in vivo* GBM tumour models (such as orthotopic GBM mouse model) can be used to evaluate their efficacy and track tumours through intact skull using SWIR advantages.

9.References

1. M. Pichaivel, G. Anbumani, P. Theivendren and M. Gopal, *An overview of brain tumor*, IntechOpen, 2022, **1**, 1-10.
2. D. Hanahan and R. A. Weinberg, *Cell*, 2000, **100**, 57-70.
3. H. P. Bhambhvani, M. Granucci, A. Rodrigues, B. W. Kakusa and M. H. Gephart, *J Clin Neurosci*, 2020, **80**, 121-124.
4. X. Li, Y. Ma, Z. Fan and R. Khandia, *Brain Tumors: Advancements in Diagnostics and Innovative Therapies*, *CRC Press*, 2024, **1**, 1-126.
5. Q. T. Ostrom, S. S. Francis and J. S. Barnholtz-Sloan, *Curr Neurol Neurosci Rep*, 2021, **21**, 1-12.
6. S. H. Torp, O. Solheim and A. J. Skjulsvik, *Acta Neurochir (Wien)*, 2022, **164**, 2453-2464.
7. J. Zhou, L. Gu, F. Du, C. Li, F. Zhang, X. Zhang, J. Pang, B. Xie, X. Wang and J. Peng, *Sci Rep*, 2025, **15**, 19228.
8. P. Rezanejad-Asl, P. Parhizkar Roudsari, N. Rezaei, M. Sharafkhah, G. Roshandel, H. Poustchi, S. Sepanlou and R. Malekzadeh, *BMC Cancer*, 2025, **25**, 210.
9. A. M. Filho, A. Znaor, C. Sunguc, M. Zahwe, R. Marcos-Gragera, J. D. Figueroa and F. Bray, *J Neurooncol*, 2025, **172**, 567-578.
10. D. Sipos, B. L. Raposa, O. Freihat, M. Simon, N. Mekis, P. Cornacchione and Á. Kovács, *Cancers*, 2025, **17**, 146.
11. S. Rathi, J. I. Griffith, W. Zhang, W. Zhang, J. H. Oh, S. Talele, J. N. Sarkaria and W. F. Elmquist, *J Intern Med*, 2022, **292**, 3-30.
12. D. N. Louis, A. Perry, P. Wesseling, D. J. Brat, I. A. Cree, D. Figarella-Branger, C. Hawkins, H. Ng, S. M. Pfister and G. Reifenberger, *Neuro Oncol*, 2021, **23**, 1231-1251.
13. W. Wu, J. L. Klockow, M. Zhang, F. Lafortune, E. Chang, L. Jin, Y. Wu and H. E. Daldrup-Link, *Pharmacol Res*, 2021, **171**, 105780.
14. M. Nakada, D. Kita, T. Watanabe, Y. Hayashi, L. Teng, I. V. Pyko and J.-I. Hamada, *Cancers*, 2011, **3**, 3242-3278.
15. J. J. Valenzuela-Fuenzalida, L. Moyano-Valarezo, V. Silva-Bravo, D. Milos-Brandenberg, M. Orellana-Donoso, P. Nova-Baeza, A. Suazo-Santibáñez, M. Rodríguez-Luengo, G. Oyanedel-Amaro and J. Sanchis-Gimeno, *J Clin Med*, 2024, **13**, 3460.
16. A. Dhiman, Y. Shah, D. Rana and K. Garkhal, *RSC Pharm*, 2025, **2**, 207-234.
17. N. Singh, A. Miner, L. Hennis and S. Mittal, *Cancer Drug Resist (Alhambra, Calif.)*, 2021, **4**, 17.
18. A. C. Tan, D. M. Ashley, G. Y. López, M. Malinzak, H. S. Friedman and M. Khasraw, *CA Cancer J Clin*, 2020, **70**, 299-312.
19. T. Kanderi, S. Munakomi and V. Gupta, in *StatPearls [Internet]*, StatPearls Publishing, 2024, **1**, 1-22.
20. N. A. O. Bush, S. M. Chang and M. S. Berger, *Neurosurg Rev*, 2017, **40**, 1-14.
21. J. Li, Z. Zhang, B. Zhang, X. Yan and K. Fan, *Biomater Sci*, 2023,**11**, 3394-3413.
22. M. D. Kelly, M. R. Pawlak, K. H. Zhan, G. A. Shamsan, W. R. Gordon and D. J. Odde, *APL Bioeng*, 2024, **8(3)**, 036102.
23. A. O. Sasmita, Y. P. Wong and A. P. K. Ling, *Asia Pac J Clin Oncol*, 2018, **14**, 40-51.
24. S. M. B. Rodriguez, A. Kamel, G. V. Ciubotaru, G. Onose, A.-S. Sevastre, V. Sfredel, S. Danoiu, A. Dricu and L. G. Tataranu, *Int J Mol Sci*, 2023, **24**, 11110.
25. X.-P. Li, Z.-Q. Guo, B.-F. Wang and M. Zhao, *Front Oncol*, 2023, **13**, 1236246.
26. S. Park, M. V. Maus and B. D. Choi, *NPJ Precis Oncol*, 2024, **8**, 279.
27. X. Bu and L. Wang, *Int J Mol Med*, 2024, **55**, 39.
28. D. F. Leitner and J. R. Connor, *Biochim Biophy Acta Gen Subj*, 2012, **1820**, 393-402.
29. M. J. Ramalho, J. A. Loureiro, M. A. Coelho and M. C. Pereira, *Pharmaceutics*, 2022, **14**, 279.

30. Y. Shen, X. Li, D. Dong, B. Zhang, Y. Xue and P. Shang, *Am J Cancer Res*, 2018, **8**, 916.
31. M. D. Caverzan and L. E. Ibarra, *Int J Biol Macromol*, 2024, 134777.
32. Q. Wang, B. Hu, X. Hu, H. Kim, M. Squatrito, L. Scarpace, A. C. DeCarvalho, S. Lyu, P. Li and Y. Li, *Cancer Cell*, 2017, **32**, 42-56.
33. H. S. Phillips, S. Kharbanda, R. Chen, W. F. Forrest, R. H. Soriano, T. D. Wu, A. Misra, J. M. Nigro, H. Colman and L. Soroceanu, *Cancer Cell*, 2006, **9**, 157-173.
34. R. G. Verhaak, K. A. Hoadley, E. Purdom, V. Wang, Y. Qi, M. D. Wilkerson, C. R. Miller, L. Ding, T. Golub and J. P. Mesirov, *Cancer Cell*, 2010, **17**, 98-110.
35. C. Xu, P. Hou, X. Li, M. Xiao, Z. Zhang, Z. Li, J. Xu, G. Liu, Y. Tan and C. Fang, *Cancer Biol Med*, 2024, **21**, 363-381.
36. K. Wadhwa, P. Chauhan, S. Kumar, R. Pahwa, R. Verma, R. Goyal, G. Singh, A. Sharma, N. Rao and D. Kaushik, *Oncol Res*, 2024, **32**, 877.
37. Q. Tang, T. Ren, P. Bai, X. Wang, L. Zhao, R. Zhong and G. Sun, *Biochem Pharmacol*, 2024, **230**, 116588.
38. M. Ahmed, M. Canney, A. Carpentier and A. Idbaih, *Rev Neurol (Paris)*, 2023, **179**, 430-436.
39. M. S. Lam, J. J. Aw, D. Tan, R. Vijayakumar, H. Y. G. Lim, S. Yada, Q. Y. Pang, N. Barker, C. Tang and B. T. Ang, *Small*, 2023, 2302280.
40. G. Schiera, C. M. Di Liegro, G. Schirò, G. Sorbello and I. Di Liegro, *Cells*, 2024, **13**, 150.
41. M. Duan, R. Cao, Y. Yang, X. Chen, L. Liu, B. Ren, L. Wang and B.-C. Goh, *Cancers*, 2024, **16**, 3300.
42. D. Petrenko, V. Chubarev, N. Syzrantsev, N. Ismail, V. Merkulov, S. Sologova, E. Grigorevskikh, E. Smolyarchuk and R. Alyautdin, *Molecules*, 2022, **27**, 3507.
43. C. Fernandes, A. Costa, L. Osório, R. C. Lago, P. Linhares, B. Carvalho and C. Caeiro, *Exon Publications*, 2017, 197-241.
44. J. I. Traylor, M. N. Pernik, A. C. Sternisha, S. K. McBrayer and K. G. Abdullah, *Cancers*, 2021, **13**, 580.
45. V. Di Nunno, L. Gatto, A. Tosoni, S. Bartolini and E. Franceschi, *Front Oncol*, 2023, **12**, 1067252.
46. E. D. Kirson, Z. Gurvich, R. Schneiderman, E. Dekel, A. Itzhaki, Y. Wasserman, R. Schatzberger and Y. Palti, *Cancer Res*, 2004, **64**, 3288-3295.
47. N. Iturrioz-Rodríguez, N. Sampron and A. Matheu, *Theranostics,* 2023, **13 (9)**, 2734-2756.
48. S. Khagi, R. Kotecha, N. T. N. Gatson, S. Jeyapalan, H. I. Abdullah, N. G. Avgeropoulos, E. T. Batzianouli, M. Giladi, L. Lustgarten and S. A. Goldlust, *Oncologist*, 2025, **30**, oyae227.
49. O. Rominiyi, A. Vanderlinden, S. J. Clenton, C. Bridgewater, Y. Al-Tamimi and S. J. Collis, *Br J Cancer*, 2021, **124**, 697-709.
50. M. Cuperlovic-Culf, M. Touaibia, P.-D. St-Coeur, J. Poitras, P. J. Morin and A. S. Culf, *Metabolites*, 2014, **4**, 807-830.
51. R. Stupp, W. P. Mason, M. J. Van Den Bent, M. Weller, B. Fisher, M. J. Taphoorn, K. Belanger, A. A. Brandes, C. Marosi and U. Bogdahn, *N Engl J Med*, 2005, **352**, 987-996.
52. H. Wu, W. Gao, P. Chen, Y. Wei, H. Zhao and F. Wang, *Heliyon*, 2024, **10**.
53. W. Günther, E. Pawlak, R. Damasceno, H. Arnold and A. Terzis, *Br J Cancer*, 2003, **88**, 463-469.
54. G. Thomas and R. Rahman, *Curr Oncol Rep*, 2025, 1-24.
55. J. Zhang, M. FG Stevens and T. D Bradshaw, *Curr Mol Pharmacol*, 2012, **5**, 102-114.
56. A. Stéphanou and A. Ballesta, *Pharmacol Res Perspect*, 2019, **7**, e00454.
57. M. Fresnais, S. Turcan, D. Theile, J. Ungermann, Y. Abou Zeed, J. R. Lindner, M. Breitkopf, J. Burhenne, W. E. Haefeli and R. Longuespée, *Biomedicines*, 2021, **10**, 1.
58. K. Hwang, J.-H. Lee, S. H. Kim, K.-O. Go, S. Y. Ji, J. H. Han and C.-Y. Kim, *In vivo*, 2021, **35**, 2015-2023.

59. L. Gatto, E. Franceschi, A. Tosoni, V. D. Nunno, S. Bartolini and A. A. Brandes, *Immunotherapy*, 2022, **14**(10), 799-813.
60. R. Ortiz, G. Perazzoli, L. Cabeza, C. Jiménez-Luna, R. Luque, J. Prados and C. Melguizo, *Curr Neuropharmacol*, 2021, **19**, 513-537.
61. H. Li, Y. Wu, Y. Chen, J. Lv, C. Qu, T. Mei, Y. Zheng, C. Ye, F. Li and S. Ge, *Acta Neuropathol Commun*, 2025, **13**, 126.
62. M. Belanich, T. Randall, M. A. Pastor, J. T. Kibitel, L. G. Alas, M. E. Dolan, S. C. Schold Jr, M. Gander, F. J. Lejeune and B. F. Li, *Cancer Chemother Pharmacol*, 1996, **37**, 547-555.
63. S. Smalley, A. J. Chalmers and S. J. Morley, *Mol Cancer*, 2014, **13**, 144.
64. M. Butler, L. Pongor, Y.-T. Su, L. Xi, M. Raffeld, M. Quezado, J. Trepel, K. Aldape, Y. Pommier and J. Wu, *Trends Cancer*, 2020, **6**, 380-391.
65. S. Spiegl-Kreinecker, C. Pirker, M. Filipits, D. Lötsch, J. Buchroithner, J. Pichler, R. Silye, S. Weis, M. Micksche and J. Fischer, *Neuro Oncol*, 2010, **12**, 28-36.
66. A.-M. Barciszewska, D. Gurda, P. Głodowicz, S. Nowak and M. Z. Naskręt-Barciszewska, *PLoS One*, 2015, **10**, e0136669.
67. A. B. Jones, K. Tuy, C. C. Hawkins, C. H. Quinn, J. Saad, S. E. Gary, E. A. Beierle, L. Ding, K. M. Rochlin and L. S. Lamb, *Cancers*, 2024, **16**, 2852.
68. Y. Tian, Y. Lei, Y. Wang, J. Lai, J. Wang and F. Xia, *Int J Oncol*, 2023, **63**, 119.
69. J. L. Munoz, N. D. Walker, K. W. Scotto and P. Rameshwar, *Cancer Lett*, 2015, **367**, 69-75.
70. J. M. Bradley, Z. Bugg, J. Pullin, G. R. Moore, D. A. Svistunenko and N. E. Le Brun, *Nat Commun*, 2025, **16**, 4695.
71. A. Gont, J. E. Hanson, S. J. Lavictoire, D. A. Parolin, M. Daneshmand, I. J. Restall, M. Soucie, G. Nicholas, J. Woulfe and A. Kassam, *Oncotarget*, 2013, **4**, 1266.
72. J. R. Pearson and T. Regad, *Signal Transduct Target Ther*, 2017, **2**, 1-11.
73. T. Guha and D. Malkin, *Cold Spring Harb Perspect Med*, 2017, **7**, a026187.
74. M. J. Lee, H. S. Choi, E. J. Min, S. B. Jo, J.-S. Park and Y. A. Joe, *Biomol Ther (Seoul)*, 2025, **33**, 606.
75. A. Zanotto-Filho, E. Braganhol, K. Klafke, F. Figueiró, S. R. Terra, F. J. Paludo, M. Morrone, I. J. Bristot, A. M. Battastini and C. M. Forcelini, *Cancer Lett*, 2015, **358**, 220-231.
76. C.-J. Lin, C.-C. Lee, Y.-L. Shih, T.-Y. Lin, S.-H. Wang, Y.-F. Lin and C.-M. Shih, *Free Radic Biol Med*, 2012, **52**, 377-391.
77. D. Hanahan and R. A. Weinberg, *Cell*, 2011, **144**, 646-674.
78. A. I. Cortes Ballen, M. Amosu, S. Ravinder, J. Chan, E. Derin, H. Slika and B. Tyler, *Cells*, 2024, **13**, 1574.
79. C. Rapôso, J. L. V. Araújo and N. B. dos Santos, *Exon Publications*, 2021, 171-185.
80. S. Han, Y. Liu, S. J. Cai, M. Qian, J. Ding, M. Larion, M. R. Gilbert and C. Yang, *Br J Cancer*, 2020, **122**, 1580-1589.
81. I. De Souza, L. Monteiro, C. Guedes, M. Silva, M. Andrade-Tomaz, B. Contieri, M. Latancia, D. Mendes, B. Porchia and M. Lazarini, *Cell Death Dis*, 2022, **13**, 591.
82. F. Fontana, E. Carollo, G. E. Melling and D. R. Carter, *Cancers*, 2021, **13**, 749.
83. K. Bouzinab, H. S. Summers, M. F. Stevens, C. J. Moody, N. R. Thomas, P. Gershkovich, N. Weston, M. B. Ashford, T. D. Bradshaw and L. Turyanska, *ACS Appl Mater Interfaces*, 2020, **12**, 12609-12617.
84. J. A. Dutra, M. T. Luiz, A. G. Tavares Junior, L. D. Di Filippo, S. G. Carvalho and M. Chorilli, *Curr Pharm Des*, 2022, **28**, 2073-2088.
85. C. P. Heming, W. Muriithi, L. W. Macharia, P. Niemeyer Filho, V. Moura-Neto and V. Aran, *Heliyon*, 2022, **8**(10), e11171.
86. M. E. Hegi, A.-C. Diserens, T. Gorlia, M.-F. Hamou, N. De Tribolet, M. Weller, J. M. Kros, J. A. Hainfellner, W. Mason and L. Mariani, *N Engl J Med*, 2005, **352**, 997-1003.
87. T. C. Ryken, N. Aygun, J. Morris, M. Schweizer, R. Nair, C. Spracklen, S. N. Kalkanis and J. J. Olson, *J Neurooncol*, 2014, **118**, 435-460.

88. H. M. Mansour, S. Shah, T. M. Aguilar, M. Abdul-Muqsith, G. S. Gonzales-Portillo and A. I. Mehta, *Cancers*, 2024, **16**, 3984.
89. D. Henssen, F. Meijer, F. A. Verburg and M. Smits, *Br J Radiol*, 2023, **96**, 20211232.
90. M. Dumba, A. Fry, J. Shelton, T. C. Booth, B. Jones, H. Shuaib and M. Williams, *Neurooncol Pract*, 2022, **9**, 487-495.
91. G. Shukla, G. S. Alexander, S. Bakas, R. Nikam, K. Talekar, J. D. Palmer and W. Shi, *Chin Clin Oncol*, 2017, **6**, 40.
92. Z. Wu, L. Dai, K. Tang, Y. Ma, B. Song, Y. Zhang, J. Li, S. Lui, Q. Gong and M. Wu, *Regen Biomater*, 2021, **8**, rbab062.
93. D. Li, C. B. Patel, G. Xu, A. Iagaru, Z. Zhu, L. Zhang and Z. Cheng, *Front Immunol*, 2020, **11**, 592389.
94. B. Y. Cheong, J. M. Wilson, O. A. Preventza and R. Muthupillai, *Tex Heart Inst J*, 2022, **49**, e217680.
95. A. Verger and K.-J. Langen, *Exon Publications*, 2017, 155-174.
96. W. Liang, S. He and S. Wu, *Adv NanoBiomed Res*, 2022, **2**, 2200087.
97. F. Wang, Y. Zhong, O. Bruns, Y. Liang and H. Dai, *Nat Photonics*, 2024, **18**, 535-547.
98. N. W. Nkune, K. Moloudi, B. P. George and H. Abrahamse, *RSC Adv*, 2025, **15**, 22267-22284.
99. H. M. Gil, T. W. Price, K. Chelani, J.-S. G. Bouillard, S. D. Calaminus and G. J. Stasiuk, *Iscience*, 2021, **24**.
100. S. Li, D. Cheng, L. He and L. Yuan, *Front Bioeng Biotechnol*, 2021, **9**, 768698.
101. J. Wang, Y. Liu, C. Qi, Z. Luo, J. Wei, G. Wang, M. Ismail, Y. Zhong and B. Shi, *Coord Chem Rev*, 2025, **534**, 216591.
102. M. J. Moreno, B. Ling and D. B. Stanimirovic, *Expert Opin Drug Discov*, 2020, **15**, 903-915.
103. F. P. García de Arquer, D. V. Talapin, V. I. Klimov, Y. Arakawa, M. Bayer and E. H. Sargent, *Science*, 2021, **373**, eaaz8541.
104. P. Chakraborty, S. S. Das, A. Dey, A. Chakraborty, C. Bhattacharyya, R. Kandimalla, B. Mukherjee, A. V. Gopalakrishnan, S. K. Singh and S. Kant, *J Control Release*, 2022, **350**, 698-715.
105. L. Dirheimer, T. Pons, F. Marchal and L. Bezdetnaya, *Pharmaceutics*, 2022, **14**, 2136.
106. H. Yukawa, K. Sato and Y. Baba, *Adv Drug Deliv Rev*, 2023, **200**, 114863.
107. B. Gidwani, V. Sahu, S. S. Shukla, R. Pandey, V. Joshi, V. K. Jain and A. Vyas, *J Drug Deliv Sci Technol*, 2021, **61**, 102308.
108. A. Hamidu, W. G. Pitt and G. A. Husseini, *Nanomaterials*, 2023, **13**, 2566.
109. A. Loskutova, A. Seitkali, D. Aliyev and R. Bukasov, *Int J Mol Sci*, 2025, **26**, 6674.
110. T. T. Ngo, S. Masi, P. F. Mendez, M. Kazes, D. Oron and I. M. Seró, *Nanoscale Adv*, 2019, **1**, 4109-4118.
111. F. Wang, F. Ren, Z. Ma, L. Qu, R. Gourgues, C. Xu, A. Baghdasaryan, J. Li, I. E. Zadeh and J. W. Los, *Nat Nanotechnol*, 2022, **17**, 653-660.
112. M. Jiao, A. S. Portniagin, X. Luo, L. Jing, B. Han and A. L. Rogach, *Adv Optl Materials*, 2022, 2200226.
113. F. Zamberlan, L. Turyanska, A. Patane, Z. Liu, H. Williams, M. Fay, P. Clarke, Y. Imamura, T. Jin and T. Bradshaw, *J Mater Chem B*, 2018, **6**, 550-555.
114. X. Shi, S. Chen, M.-Y. Luo, B. Huang, G. Zhang, R. Cui and M. Zhang, *Nano Res*, 2020, **13**, 2239-2245.
115. J. Qu, I. Golovynska, J. Liu, J. Qu and S. Golovynskyi, *J Biophotonics*, 2024, **17**, e202400171.
116. W. Tang, W. Fan, J. Lau, L. Deng, Z. Shen and X. Chen, *Chem Soc Rev*, 2019, **48**, 2967-3014.
117. S. Tran, P.-J. DeGiovanni, B. Piel and P. Rai, *Clin Transl Med*, 2017, **6**, 44.
118. Y. Nakamura, A. Mochida, P. L. Choyke and H. Kobayashi, *Bioconjug Chem*, 2016, **27**, 2225-2238.
119. H.-J. Liu and P. Xu, *Adv Drug Deliv Rev*, 2022, **191**, 114619.

120. G. Lai, H. Wu, K. Yang, K. Hu, Y. Zhou, X. Chen, F. Fu, J. Li, G. Xie and H.-F. Wang, *Front Bioeng Biotechnol*, 2024, **12**, 1403511.
121. J. Xie, Z. Shen, Y. Anraku, K. Kataoka and X. Chen, *Biomaterials*, 2019, **224**, 119491.
122. X. Sun, Y. Hong, Y. Gong, S. Zheng and D. Xie, *Int J Mol Sci*, 2021, **22**, 7023.
123. N. Šamec, A. Zottel, A. Videtič Paska and I. Jovčevska, *Molecules*, 2020, **25**, 490.
124. Y. Miao, T. Yang, S. Yang, M. Yang and C. Mao, *Nano Converg*, 2022, **9**, 2.
125. A. Zielińska, F. Carreiró, A. M. Oliveira, A. Neves, B. Pires, D. N. Venkatesh, A. Durazzo, M. Lucarini, P. Eder and A. M. Silva, *Molecules*, 2020, **25**, 3731.
126. D. S. Jain, R. B. Athawale, A. N. Bajaj, S. S. Shrikhande, P. N. Goel, Y. Nikam and R. P. Gude, *DARU J Pharm Sci*, 2014, **22**, 18.
127. M. J. Ramalho, E. Sevin, F. Gosselet, J. Lima, M. Coelho, J. A. Loureiro and M. Pereira, *Int J Pharm*, 2018, **545**, 84-92.
128. M. J. Ramalho, I. D. Torres, J. A. Loureiro, J. Lima and M. C. Pereira, *ACS Appl Nano Mater*, 2023, **6**, 14191-14203.
129. A. Banstola, R. Duwa, F. Emami, J.-H. Jeong and S. Yook, *Mol Pharm*, 2020, **17**, 4386-4400.
130. P. Sun, Y. Xiao, Q. Di, W. Ma, X. Ma, Q. Wang and W. Chen, *Int J Nanomedicine*, 2020, 6673-6688.
131. J. Yu and Y. Xue, *PeerJ*, 2024, **12**, e17979.
132. L. Eltaib, *Polymers,* 2025, **17**(7), 833.
133. T. G. Floyd, P. Gurnani and J. Y. Rho, *Nanoscale*, 2025, **17**, 7738-7752.
134. N. Iturrioz-Rodríguez, R. Bertorelli and G. Ciofani, *Adv NanoBiomed Res*, 2021, **1**, 2000054.
135. J. Gao, Z. Wang, H. Liu, L. Wang and G. Huang, *Drug Discov Ther*, 2015, **9**, 205-212.
136. F. C. Lam, S. W. Morton, J. Wyckoff, T.-L. Vu Han, M. K. Hwang, A. Maffa, E. Balkanska-Sinclair, M. B. Yaffe, S. R. Floyd and P. T. Hammond, *Nat Commun*, 2018, **9**, 1-11.
137. J. Zhang, X. Xiao, J. Zhu, Z. Gao, X. Lai, X. Zhu and G. Mao, *Int J Nanomed*, 2018, 3039-3051.
138. G. Ak, A. Ünal, T. Karakayalı, B. Özel, N. S. Günel and Ş. H. Şanlıer, *Colloids Surf B Biointerfaces*, 2021, **206**, 111946.
139. A. L. Martínez-López, C. Pangua, C. Reboredo, R. Campión, J. Morales-Gracia and J. M. Irache, *Int J Pharm*, 2020, **581**, 119289.
140. A. Mohanty and I.-K. Park, *Chonnam Med J*, 2023, **59**, 1.
141. C.-E. Tincu, C. V. Andrițoiu, M. Popa and L. Ochiuz, *Polymers*, 2023, **15**, 3969.
142. M. J. Hawkins, P. Soon-Shiong and N. Desai, *Adv Drug Deliv Rev*, 2008, **60**, 876-885.
143. D. Y. Zhang, C. Dmello, L. Chen, V. A. Arrieta, E. Gonzalez-Buendia, J. R. Kane, L. P. Magnusson, A. Baran, C. D. James and C. Horbinski, *Clin Cancer Res*, 2020, **26**, 477-486.
144. S. Qu, S. Qi, H. Zhang, Z. Li, K. Wang, T. Zhu, R. Ye, W. Zhang, G. Huang and G.-z. Yi, *J Exp Clin Cancer Res*, 2023, **42**, 285.
145. D. O. Helal, M. M. Abdel-Mottaleb, A. O. Kamel, N. Rouatbi, S. Han, A.-S. Geneidi, K. T. Al-Jamal and G. A. Awad, *J Pharm Pharmacol*, 2023, **75**, 921-930.
146. R. R. Kudarha and K. K. Sawant, *J Drug Delivery Sci Technol*, 2021, **61**, 102129.
147. M. Liang, C. Gao, Y. Wang, W. Gong, S. Fu, L. Cui, Z. Zhou, X. Chu, Y. Zhang and Q. Liu, *Drug Deliv*, 2018, **25**, 1652-1663.
148. A.-A. Idu, M. G. Albu Kaya, I. Rău, N. Radu, C.-E. Dinu-Pîrvu and M. V. Ghica, *Materials*, 2024, **17**, 3510.
149. B. Guzdek, K. Fołta, N. Staniek, M. Stolarczyk and K. Krukiewicz, *Int J Mol Sci*, 2025, **26**, 6513.
150. K. R. Kim, A. S. Lee, S. M. Kim, H. R. Heo and C. S. Kim, *Front Bioeng Biotechnol*, 2023, **10**, 1106767.
151. M. J. Rohovie, M. Nagasawa and J. R. Swartz, *Bioeng Transl Med*, 2017, **2**, 43-57.
152. C.-N. Chao, Y.-H. Yang, M.-S. Wu, M.-C. Chou, C.-Y. Fang, M.-C. Lin, C.-K. Tai, C.-H. Shen, P.-L. Chen and D. Chang, *Sci Rep*, 2018, **8**, 2213.

153. A. Mohanty, A. Parida, R. K. Raut and R. K. Behera, *ACS Bio Med Chem Au*, 2022, **2**, 258-281.
154. A. I. Kuruppu, L. Turyanska, T. D. Bradshaw, S. Manickam, B. P. Galhena, P. Paranagama and R. De Silva, *Biochim Biophys Acta Gen Subj*, 2022, **1866**, 130067.
155. A. W. Al-Ani, L. Zhang, L. Ferreira, L. Turyanska, T. D. Bradshaw and N. R. Thomas, *Nanomedicine*, 2019, **20**, 102005.
156. K. M. Troike, S. Z. Wang, D. J. Silver, J. Lee, E. E. Mulkearns-Hubert, N. Hajdari, P. K. Ghosh, K. E. Kay, J. L. Beilis and S. E. Mitchell, *Neurooncol Adv*, 2024, **6**, vdad154.
157. Z. Tu, P. Timashev, J. Chen and X. J. Liang, *BMEMat*, 2023, **1**, e12022.
158. M. Zakaria, T. Hassan and M. Blumenberg, *Iron Metabolism: A Double-Edged Sword*, *Biochemistry*, 2022,1-162.
159. L. Li, C. J. Fang, J. C. Ryan, E. C. Niemi, J. A. Lebrón, P. J. Björkman, H. Arase, F. M. Torti, S. V. Torti and M. C. Nakamura, *Proc Natl Acad Sci*, 2010, **107**, 3505-3510.
160. T. Koneru, E. McCord, S. Pawar, K. Tatiparti, S. Sau and A. K. Iyer, *ACS Omega*, 2021, **6**, 8727-8733.
161. K. Fan, X. Jia, M. Zhou, K. Wang, J. Conde, J. He, J. Tian and X. Yan, *ACS Nano*, 2018, **12**, 4105-4115.
162. W. Liu, Q. Lin, Y. Fu, S. Huang, C. Guo, L. Li, L. Wang, Z. Zhang and L. Zhang, *J Control Release*, 2020, **323**, 191-202.
163. C.-W. Huang, C.-P. Chuang, Y.-J. Chen, H.-Y. Wang, J.-J. Lin, C.-Y. Huang, K.-C. Wei and F.-T. Huang, *J Nanobiotechnol*, 2021, **19**, 1-17.
164. B. Wang, M. Tang, Z. Yuan, Z. Li, B. Hu, X. Bai, J. Chu, X. Xu and X.-Q. Zhang, *Bioact Mater*, 2022, **16**, 232-248.
165. Z. Wang, C. Li, M. Ellenburg, E. Soistman, J. Ruble, B. Wright, J. X. Ho and D. C. Carter, *Acta Cryst Biol Crystallogr*, 2006, **62**, 800-806.
166. C. Zhang, X. Zhang and G. Zhao, *Nanomaterials*, 2020, **10**, 1894.
167. C. J. Russo and L. A. Passmore, *Science*, 2014, **346**, 1377-1380.
168. D. Belletti, F. Pederzoli, F. Forni, M. A. Vandelli, G. Tosi and B. Ruozi, *Exp Opin Drug Deliv*, 2017, **14**, 825-840.
169. H. Veroniaina, X. Pan, Z. Wu and X. Qi, *Expert Rev Anticancer Ther*, 2021, **21**, 901-913.
170. P. V. Candelaria, L. S. Leoh, M. L. Penichet and T. R. Daniels-Wells, *Front Immunol*, 2021, **12**, 583.
171. Q. Guo, C. Qian, X. Wang and Z.-M. Qian, *Exp Mol Med*, 2025, 1-9.
172. V. H. Shargh, J. Luckett, K. Bouzinab, S. Paisey, L. Turyanska, W. G. B. Singleton, S. Lowis, P. Gershkovich, T. D. Bradshaw, M. F. G. Stevens, A. Bienemann and B. Coyle, *ACS Appl Mater Interfaces*, 2021, **13**, 35266-35280.
173. Z. Chen, M. Zhai, X. Xie, Y. Zhang, S. Ma, Z. Li, F. Yu, B. Zhao, M. Zhang and Y. Yang, *Mol Pharm*, 2017, **14**, 3087-3097.
174. M. L. Cassioli, M. Fay, L. Turyanska, T. D. Bradshaw, N. R. Thomas and A. Pordea, *RSC Adv*, 2024, **14**, 14008-14016.
175. K. Du, Q. Xia, H. Heng and F. Feng, *ACS Appl Mater Interfaces*, 2020, **12**, 34599-34609.
176. M. Zhai, Y. Wang, L. Zhang, M. Liang, S. Fu, L. Cui, M. Yang, W. Gong, Z. Li and L. Yu, *Drug Deliv*, 2018, **25**, 1013-1024.
177. F. Varmaghani, R. Rafipour, S. Kashanian, H. Zhaleh and S. Hashemi, *ChemSelect*, 2025, **10**, e202404507.
178. K. Xiong, X. Lin, J. Kou, F. Wei, J. Shen, Y. Chen, L. Ji and H. Chao, *Adv Healthc Mater*, 2024, **13**, 2302564.
179. S. Zhao, P. Liu and Y. Li, *Sci Rep*, 2024, **14**, 29402.
180. X. Li, F. Shao, J. Sun, K. Du, Y. Sun and F. Feng, *ACS Appl Mater Interfaces*, 2019, **11**, 41935-41945.
181. M. d'Angelo, V. Castelli, E. Benedetti, A. Antonosante, M. Catanesi, R. Dominguez-Benot, G. Pitari, R. Ippoliti and A. Cimini, *Front Bioeng Biotechnol*, 2019, **7**, 325.
182. S. Jeyamogan, N. A. Khan and R. Siddiqui, *Arch Med Res*, 2021, **52**, 131-142.

183. M. Qindeel, M. Irfan, S. Ullah, S. Fathi-karkan, Z. Kharaba, A. Rahdar, M. Aliahmad and M. A. Aboudzadeh, *J Drug Deliv Sci Technol*, 2024, **102**, 106322.
184. B. A. Lakshmi and Y.-J. Kim, *Int J Mol Sci*, 2022, **23**, 1641.
185. X. He, C. S. Alves, N. Oliveira, J. Rodrigues, J. Zhu, I. Banyai, H. Tomas and X. Shi, *Colloids Surf B Biointerfaces*, 2015, **125**, 82-89.
186. M. S. Muthu, S.A. Kulkarni, A. Raju and S.S. Feng, *Biomaterials*, 2012, **33**, 3494-3501.
187. B. Demir, H. Moulahoum, F. Ghorbanizamani, F. B. Barlas, O. Yesiltepe, Z. P. Gumus, K. Meral, D. O. Demirkol and S. Timur, *J Drug Deliv Sci Technol*, 2021, **62**, 102363.
188. M. S. Muthu, S. A. Kulkarni, A. Raju and S.S. Feng, *Biomaterials*, 2012, **33**, 3494-3501.
189. N. Kaur, P. Gautam, D. Nanda, A. S. Meena, A. Shanavas and R. Prasad, *Bioconjug Chem,* 2024, **35**, 1283-1299.
190. C. Song, Y. Zhang, C. Li, G. Chen, X. Kang and Q. Wang, *Adv Funct Mater*, 2016, **26**, 4192-4200.
191. Y. Hua, Z. Qin, L. Gao, M. Zhou, Y. Xue, Y. Li and J. Xie, *J Control Release*, 2024, **371**, 429-444.
192. D. G. Zayed, S. M. Ebrahim, M. W. Helmy, S. N. Khattab, M. Bahey-El-Din, J.-Y. Fang, K. A. Elkhodairy and A. O. Elzoghby, *J Nanobiotechnol*, 2019, **17**, 7.
193. L.-H. Liu, Y.-F. Liu, H.-B. Zhang, X.-L. Liu, H.-W. Zhang, B. Huang, F. Lin and W.-H. Li, *Technol Cancer Res Treat*, 2024, **23**, 15330338241281321.
194. Y. H. Chung, H. Cai and N. F. Steinmetz, *Adv Drug Deliv Rev*, 2020, **156**, 214-235.
195. C. E. Benjamin, Z. Chen, P. Kang, B. A. Wilson, N. Li, S. O. Nielsen, Z. Qin and J. J. Gassensmith, *J Am Chem Soc*, 2018, **140**, 17226-17233.
196. D. Ghosh, A. G. Kohli, F. Moser, D. Endy and A. M. Belcher, *ACS Synth Biol*, 2012, **1**, 576-582.
197. H. Veroniaina, Z. Wu and X. Qi, *J Adv Res*, 2021, **33**, 201-213.
198. F. Nasrollahi, B. Sana, D. Paramelle, S. Ahadian, A. Khademhosseini and S. Lim, *Adv Ther*, 2020, **3**, 1900183.
199. V. Bitonto, D. Alberti, R. Ruiu, S. Aime, S. G. Crich and J. C. Cutrin, *J Control Release*, 2020, **319**, 300-310.
200. J. C. Cutrin, S. G. Crich, D. Burghelea, W. Dastru and S. Aime, *Mol Pharm*, 2013, **10**, 2079-2085.
201. L. He, F. Qing, M. Li and D. Lan, *Int J Nanomed*, 2020, 2337-2349.
202. C.-Y. Lin and M.-J. Shieh, *Bioconjug Chem*, 2018, **29**, 1384-1398.
203. M. Mendes, J. J. Sousa, A. Pais and C. Vitorino, *Pharmaceutics*, 2018, **10**, 181.
204. V. Deivayanai, P. Thamarai, S. Karishma, A. Saravanan, P. Yaashikaa, A. Vickram, R. Hemavathy, R. Rohith Kumar, S. Rishikeshavan and S. Shruthi, *Cancer Pathog Ther*, 2024, **2**, E01-E16.
205. K. K. Wong, H. Cölfen, N. T. Whilton, T. Douglas and S. Mann, *J Inorg Biochem*, 1999, **76**, 187-195.
206. B. Hennequin, L. Turyanska, T. Ben, A. M. Beltran, S. I. Molina, M. Li, S. Mann, A. Patane and N. R. Thomas, *Adv Mater*, 2008, **20**, 3592-3596.
207. M. M. Bradford, *Anal Biochem*, 1976, **72**, 248-254.
208. T. Mosmann, *J Immunol Methods*, 1983, **65**, 55-63.
209. M. Ghasemi, T. Turnbull, S. Sebastian and I. Kempson, *Int J Mol Sci*, 2021, **22**, 12827.
210. B. Luzak, P. Siarkiewicz and M. Boncler, *Toxicol In Vitro*, 2022, **83**, 105407.
211. B. Pinto, A. C. Henriques, P. M. Silva and H. Bousbaa, *Pharmaceutics*, 2020, **12**, 1186.
212. S. Dostalova, K. Vasickova, D. Hynek, S. Krizkova, L. Richtera, M. Vaculovicova, T. Eckschlager, M. Stiborova, Z. Heger and V. Adam, *Int J Nanomed*, 2017, 2265-2278.
213. A. I. Kuruppu, L. Zhang, H. Collins, L. Turyanska, N. R. Thomas and T. D. Bradshaw, *Adv Healthc Mater*, 2015, **4**, 2816-2821.
214. A. F. Breen, G. Wells, L. Turyanska and T. D. Bradshaw, *Cancer Rep*, 2019, **2**, e1155.
215. T. N. Aslan, E. Aşık, N. T. Güray and M. Volkan, *J Biol Inorg Chem*, 2020, **25**, 1139-1152.
216. T. D. Bradshaw, M. Junor, A. Patane, P. Clarke, N. R. Thomas, M. Li, S. Mann and L. Turyanska, *J Mater Chem B*, 2013, **1**, 6254-6260.

217. I. Grevtseva, K. Chirkov, O. Ovchinnikov, M. Smirnov and A. Perepelitsa, *J Lumin*, 2024, **267**, 120348.
218. A. P. Litvin, A. A. Babaev, P. S. Parfenov, E. V. Ushakova, M. A. Baranov, O. V. Andreeva, K. Berwick, A. V. Fedorov and A. V. Baranov, *J Phys Chem C*, 2017, **121**, 8645-8652.
219. S. Egelhaaf, U. Olsson, P. Schurtenberger, J. Morris and H. Wennerström, *Physl Rev E*, 1999, **60**, 5681.
220. M. Bellini, S. Mazzucchelli, E. Galbiati, S. Sommaruga, L. Fiandra, M. Truffi, M. A. Rizzuto, M. Colombo, P. Tortora and F. Corsi, *J Control Release*, 2014, **196**, 184-196.
221. A. F. Breen, D. Scurr, M. L. Cassioli, G. Wells, N. R. Thomas, J. Zhang, L. Turyanska and T. D. Bradshaw, *Int J Nanomed*, 2019, 9525-9534.
222. A. Di Martino, P. Kucharczyk, Z. Capakova, P. Humpolicek and V. Sedlarik, *J Nanopart Res*, 2017, **19**, 71.
223. M. Rubio-Camacho, J. A. Encinar, M. J. Martínez-Tomé, R. Esquembre and C. R. Mateo, *Biomolecules*, 2020, **10**, 1015.
224. L. Turyanska, T. D. Bradshaw, J. Sharpe, M. Li, S. Mann, N. R. Thomas and A. Patanè, *Small*, 2009, **5**, 1738-1741.
225. K. N. Clayton, J. W. Salameh, S. T. Wereley and T. L. Kinzer-Ursem, *Biomicrofluidics*, 2016, **10**, 054107.
226. X. Zhang, G. Ma and W. Wei, *NPG Asia Mater*, 2021, **13**, 52.
227. S. Hosseini, J. Mohammadnejad, S. Salamat, Z. B. Zadeh, M. Tanhaei and S. Ramakrishna, *Mater Today Chem*, 2023, **29**, 101400.
228. A. Tafech, P. Jacquet, C. Beaujean, A. Fertin, Y. Usson and A. Stéphanou, *Biology*, 2023, **12**, 1221.
229. A. Di Martino, P. Kucharczyk, Z. Capakova, P. Humpolicek and V. Sedlarik, *J Nanopart Res*, 2017, **19**, 1-16.
230. H. Sun, J. Zhang, H. Qi, D. Jiang, C. Hu, C. Mao, W. Liu, H. Qi and J. Zong, *Cell Death Discov*, 2025, **11**, 407.
231. H. Xie, R. Tubbs and B. Yang, *Int J Clin Exp Pathol*, 2015, **8**, 1790.
232. H. Gao, Z. Jin, G. Bandyopadhyay, G. Wang, D. Zhang, K. C. e Rocha, X. Liu, H. Zhao, T. Kisseleva and D. A. Brenner, *Cell Metab*, 2022, **34**, 1201-1213. e1205.
233. S. Harris and K. Kim, *Nanomaterials*, 2024, **14**, 1086.
234. A. Kermanizadeh, L. G. Powell and V. Stone, *J Toxicol Environ Health B*, 2020, **23**, 137-176.
235. V. Soni, M. Adhikari, H. Simonyan, L. Lin, J. H. Sherman, C. N. Young and M. Keidar, *Cancers*, 2021, **13**, 4485.
236. X.-R. Ni, Y.-Y. Zhao, H.-P. Cai, Z.-H. Yu, J. Wang, F.-R. Chen, Y.-J. Yu, G.-K. Feng and Z.-P. Chen, *J Neurooncol*, 2020, **148**, 245-258.
237. Z. N. Abbas, A. Z. Al-Saffar, S. M. Jasim and G. M. Sulaiman, *Sci Rep*, 2023, **13**, 18380.
238. Y. S. Cha, A. Michaels, J. Z. Wang, Y. Niu, Y. Lin, L. Zhu, X. Zhu, K. Wang, M. Murray and F. Zhou, *J Pharm Investig*, 2025, **11**(7), 1-17.
239. N. Yadav and B. W. Purow, *J Neurooncol*, 2024, **166**, 213-229.
240. A. Carlos, M. Mendes, M. T. Cruz, A. Pais and C. Vitorino, *Cancer Lett*, 2024, 217392.
241. P. Shaw, N. Kumar, A. Privat-Maldonado, E. Smits and A. Bogaerts, *Cancers*, 2021, **13**, 1780.
242. M. Davy, L. Genest, C. Legrand, O. Pelouin, G. Froget, V. Castagné and T. Rupp, *Cancers*, 2023, **15**, 4478.
243. M.-E. Oraiopoulou, E. Tzamali, S. E. Psycharakis, G. Tzedakis, T. Makatounakis, K. Manolitsi, E. Drakos, A. F. Vakis, G. Zacharakis and J. Papamatheakis, *Sci Rep*, 2024, **14**, 3759.
244. Z. Wang, Y. Zhao, S. Zhang, X. Chen, G. Sun, B. Zhang, B. Jiang, Y. Yang, X. Yan and K. Fan, *Theranostics*, 2022, **12**, 1800.
245. Y. Dong, Y. Ma, X. Li, F. Wang and Y. Zhang, *Mol Pharm*, 2021, **18**, 3365-3377.
246. S. R. Alves, I. R. Calori, H. Bi and A. C. Tedesco, *OpenNano*, 2023, **9**, 100116.

247. S. Kessel, S. Cribbes, O. Déry, D. Kuksin, E. Sincoff, J. Qiu and L. L.-Y. Chan, *SLAS Technol*, 2017, **22**, 454-465.
248. C. Bach, A. Glasow, R. Baran-Schmidt, H. Oppermann, C. Bach, J. Meixensberger, E. Güresir and F. Gaunitz, *Front Bioeng Biotechnol*, 2024, **12**, 1471012.
249. F. Piccinini, A. Tesei, M. Zanoni and A. Bevilacqua, *Biotechniques*, 2017, **63**, 227-229.
250. S. J. Han, S. Kwon and K. S. Kim, *Cancer Cell Int*, 2021, **21**, 1-19.
251. S. K. Singh, S. Abbas, A. K. Saxena, S. Tiwari, L. K. Sharma and M. Tiwari, *Biotechniques*, 2020, **69**, 333-338.
252. P. S. Nakod, Y. Kim and S. S. Rao, *Cell Mol Bioeng*, 2021, **14**, 639-651.
253. S. Zhu, J. Yin, X. Lu, D. Jiang, R. Chen, K. Cui, W. He, N. Huang and G. Xu, *Sci Rep*, 2025, **15**, 9751.
254. M. Vinci, S. Gowan, F. Boxall, L. Patterson, M. Zimmermann, W. Court, C. Lomas, M. Mendiola, D. Hardisson and S. A. Eccles, *BMC Biol*, 2012, **10**, 1-21.
255. F. Fehlauer, M. Muench, E. Richter and D. Rades, *Oncol Rep*, 2007, **17**, 941-945.
256. N. Yang, T. Yan, H. Zhu, X. Liang, L. Leiss, P. Ø. Sakariassen, K. O. Skaftnesmo, B. Huang, D. E. Costea and P. Ø. Enger, *J Transl Med,* 2014, **12**, 278.
257. M. Vaezzadeh, E. Kachooei, S. Krishnamurthy, P. Manandhar, A. Nadort, G. J. Guillemin, A. Di Ieva, M. Santiago, B. Heng and A. Guller, *Adv Ther*, 2023, **6**, 2300197.
258. T. I. Janjua, Y. Cao, A. Ahmed-Cox, A. Raza, M. Moniruzzaman, D. T. Akhter, N. L. Fletcher, M. Kavallaris, K. J. Thurecht and A. Popat, *J Control Release*, 2023, **357**, 161-174.
259. L. Turyanska, T. D. Bradshaw, M. Li, P. Bardelang, W. C. Drewe, M. W. Fay, S. Mann, A. Patanè and N. R. Thomas, *J Mater Chem*, 2012, **22**, 660-665.
260. G. Perini, V. Palmieri, G. Friggeri, A. Augello, M. De Spirito and M. Papi, *Cancer Nanotechnol*, 2023, **14**, 13.
261. I. Munir, F. Nazir and G. Yesiloz, *ACS Appl Mater Interfaces*, 2024, **16**, 70187-70204.
262. C. Ning, Y. Dong, K. Yang, X. Li, F. Wang and Y. Zhang, *ACS Biomater Sci Eng*, 2023, **9**, 2572-2583.
263. J. J. Walsh, M. Parent, A. Akif, L. C. Adam, S. Maritim, S. K. Mishra, M. H. Khan, D. Coman and F. Hyder, *Front Oncol*, 2021, **11**, 692650.
264. T.-C. Chou, *Cancer Res*, 2010, **70**, 440-446.
265. K. Juarez-Moreno, D. Chávez-García, G. Hirata and R. Vazquez-Duhalt, *Toxicol In Vitro*, 2022, **85**, 105461.
266. K. Yamashiro, K. Nakao, S. Ohba and Y. Hirose, *Anticancer Res*, 2020, **40**, 1315-1323.
267. S. Shaikh, M. Younis, K. A. Shahzad, G. Renjie, Z. Na, Q. Bingyao and L. Yuan, *ACS Appl Nano Mater*, 2025, **8**, 11192-11200.
268. M. M. Barroso, J. Ward, L. Wang, K. Tubbesing, A. Rudkouskaya, D. Kingsley and D. Corr, *FASEB J*, 2019, **33**, 496.498-496.498.
269. X. Huang, J. Zhuang, S. W. Chung, B. Huang, G. Halpert, K. Negron, X. Sun, J. Yang, Y. Oh and P. M. Hwang, *ACS Nano*, 2018, **13**, 236-247.
270. C. Sarisozen, A. H. Abouzeid and V. P. Torchilin, *Eur J Pharm Biopharm*, 2014, **88**, 539-550.
271. Y. Li, Y. Ma, Z. Wu, R. Xie, F. Zeng, H. Cai, S. Lui, B. Song, L. Chen and M. Wu, *Front Immunol*, 2021, **12**.
272. X. Zhang, S. Li, H. Ma, H. Wang, R. Zhang and X.-D. Zhang, *Theranostics*, 2022, **12**, 3345.
273. M. Zhang, B. P. Bishop, N. L. Thompson, K. Hildahl, B. Dang, O. Mironchuk, N. Chen, R. Aoki, V. C. Holmberg and E. Nance, *Nanoscale Adv*, 2019, **1**, 3424-3442.
274. Y. Sun, X. Zhong and A. M. Dennis, *J Biomed Opt*, 2023, **28**, 094805-094805.
275. J. Sun, M.-Q. Zhu, K. Fu, N. Lewinski and R. A. Drezek, *Int J Nanomed*, 2007, **2**, 235-240.
276. A. Sasaki, Y. Tsukasaki, A. Komatsuzaki, T. Sakata, H. Yasuda and T. Jin, *Nanoscale*, 2015, **7**, 5115-5119.
277. J. Cao, H. Zhu, D. Deng, B. Xue, L. Tang, D. Mahounga, Z. Qian and Y. Gu, *J Biomed Mater Res Part A*, 2012, **100**, 958-968.

278. Y. Han, H. Liu, M. Fan, S. Gao, D. Fan, Z. Wang, J. Chang, J. Zhang and K. Ge, *J Colloid Interface Sci*, 2022, **616**, 595-604.
279. I. Yakavets, A. Francois, M. Guiot, N. Lequeux, A. Fragola, T. Pons, L. Bezdetnaya and F. Marchal, *Cancers*, 2020, **12**, 3727.
280. G. Jarockyte, D. Dapkute, V. Karabanovas, J. V. Daugmaudis, F. Ivanauskas and R. Rotomskis, *Biochim Biophys Acta Gen Subj*, 2018, **1862**, 914-923.
281. T. Mangeolle, I. Yakavets, N. Lequeux, T. Pons, L. Bezdetnaya and F. Marchal, *Photodiagnosis Photodyn Ther*, 2019, **26**, 150-156.
282. S. Li, J. Wei, Q. Yao, X. Song, J. Xie and H. Yang, *Chem Soc Rev*, 2023, **52**, 1672-1696.
283. H. Tang, S.-T. Yang, D.-M. Ke, Y.-F. Yang, J.-H. Liu, X. Chen, H. Wang and Y. Liu, *Toxicol Res*, 2017, **6**, 693-704.
284. B. A. Arus, J. Yiu, J. G. Lingg, A. Hofmann, A. R. Fumo, H. Ji, C. Jethwa, R. K. Park, J. Henderson and K. Mishra, *BioRxiv*, 2024, 2024.2006. 2010.597863.
285. M. L. Schipper, Z. Cheng, S.-W. Lee, L. A. Bentolila, G. Iyer, J. Rao, X. Chen, A. M. Wu, S. Weiss and S. S. Gambhir, *J Nuclear Med*, 2007, **48**, 1511-1518.
286. W. A. Jefferies, M. R. Brandon, S. V. Hunt, A. F. Williams, K. C. Gatter and D. Y. Mason, *Nature*, 1984, **312**, 162-163.
287. K. B. Johnsen, A. Burkhart, F. Melander, P. J. Kempen, J. B. Vejlebo, P. Siupka, M. S. Nielsen, T. L. Andresen and T. Moos, *Sci Rep*, 2017, **7**, 1-13.
288. G. Lin, T. Chen, Y. Pan, Z. Yang, L. Li, K.-t. Yong, X. Wang, J. Wang, Y. Chen and W. Jiang, *Nanotheranostics*, 2020, **4**, 173.
289. R. Sangubotla, K. S. Gubbiyappa, R. Devarapogu and J. Kim, *Biochim Biophys Acta Mol Basis Dis*, 2025, 167653.
290. H. Abuzaid, S. Abdelrazig, L. Ferreira, H. M. Collins, D.-H. Kim, K.-H. Lim, T.-S. Kam, L. Turyanska and T. D. Bradshaw, *ACS Omega*, 2022, **7**, 21473-21482.
291. Y.-E. Seo, T. Bu and W. M. Saltzman, *Current Opin Biomed Eng*, 2017, **4**, 1-12.
292. L. Shan, X. Shan, T. Zhang, K. Zhai, G. Gao, X. Chen and Y. Gu, *RSC Adv*, 2016, **6**, 77987-77998.
293. Y. Cui, Q. Xu, P. K.-H. Chow, D. Wang and C.-H. Wang, *Biomaterials*, 2013, **34**, 8511-8520.
294. P. Nayak, V. Bentivoglio, M. Varani and A. Signore, *Cancers*, 2023, **15**, 4846.
295. C. H. Williams, L. R. Neitzel, J. Cornell, S. Rea, I. Mills, M. S. Silver, J. D. Ahmad, K. G. Birukov, A. Birukova and H. Brem, *Exp Hematol Oncol*, 2024, **13**, 13.
296. H. Zhao, C. Li, X. Shi, J. Zhang, X. Jia, Z. Hu, Y. Gao and J. Tian, *EBioMedicine*, 2024, **106,** 105243.
297. S. Yin, K. Davey, S. Dai, Y. Liu and J. Bi, *Particuology*, 2022, **64**, 65-84.
298. M. H. Mansor, Z. Gao, F. Howard, J. MacInnes, X. Zhao and M. Muthana, *Pharmaceutics*, 2025, **17**, 95.

10. Appendices

10.1 Appendix I

To assess the biocompatibility and biodistribution of horse spleen AFt as a delivery vehicle, *in vivo* imaging was performed using CF770-labeled horse spleen AFt in mice (10 mg/kg). All images were acquired by Dr. Umar Iqbal (National Research Council Canada). Figure 10.1 presents dorsal and ventral time-lapse fluorescence imaging of mice captured at various time points (pre-scan, 10 min, 30 min, 1 h, 3 h, 6 h, 24 h, and 48 h) following tail vein injection. The fluorescence intensity peaked between 1-3 h post-injection and decreased over 48 h.

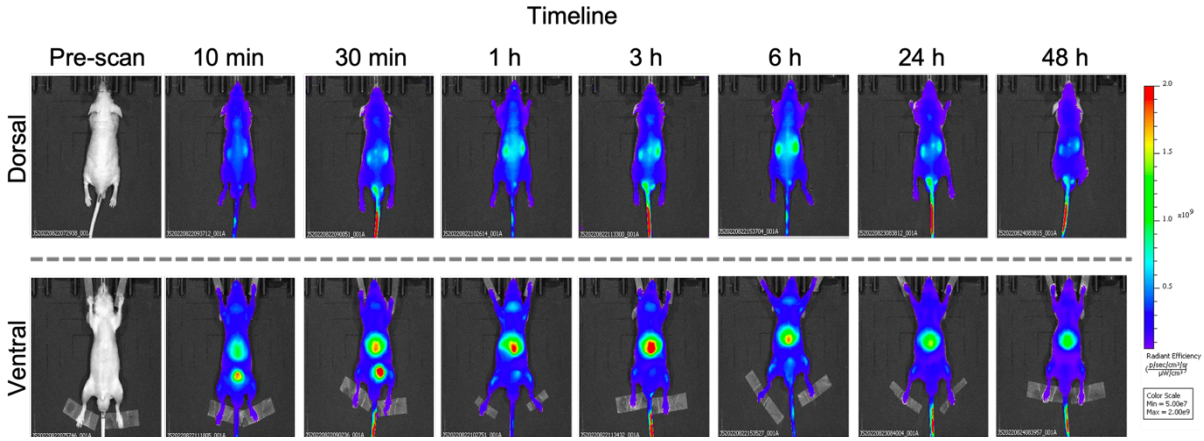

Figure 10.1 *In vivo* dorsal and ventral time-lapse fluorescence imaging of mice (10 mg/kg) following intravenous (tail vein) injection of CF770-labeled horse spleen AFt. Images were acquired at baseline (pre-scan), and at 10 min, 30 min, 1 h, 3 h, 6 h, 24 h, and 48 h post-injection.

At the 48 h time point, the major organs including heart, brain, liver, spleen, lungs, and kidneys were harvested for *ex vivo* imaging. Figure 10.2a shows the fluorescence accumulation in the liver, spleen, and kidneys. Quantitative analysis of total radiant efficiency from these organs (Figure 10.2b) corroborated the imaging results, and demonstrating the highest signals in the kidneys, liver and spleen, and minimal accumulation in the heart and brain, suggesting the clearance of AFt from the body.

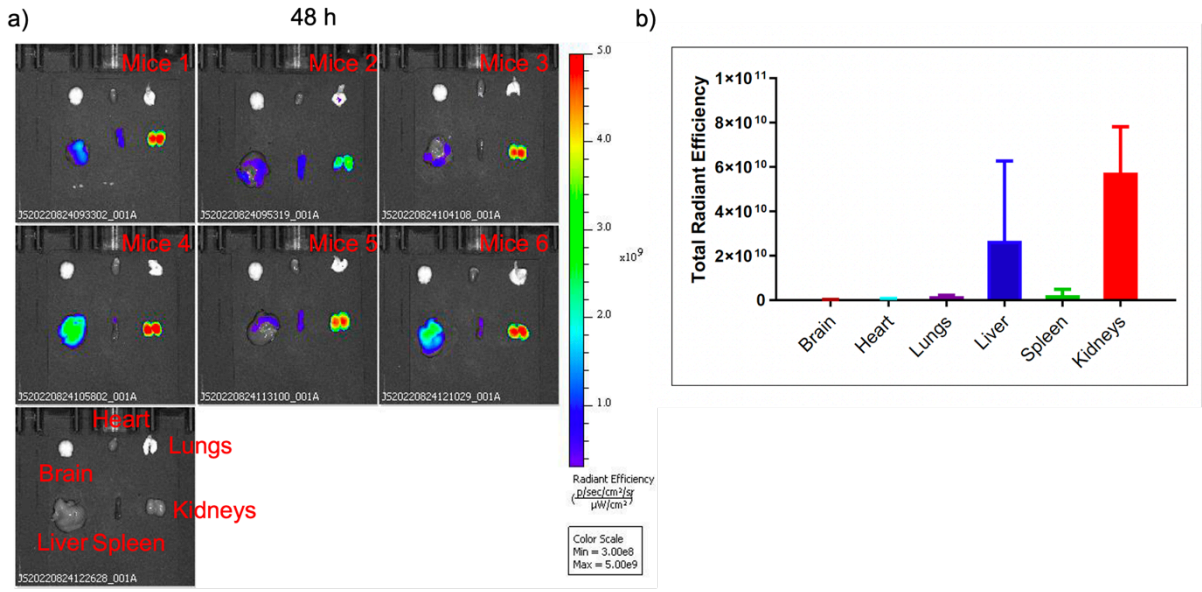

Figure 10.2 (a) *Ex vivo* fluorescence imaging of organs after 48 h following intravenous (tail vein) injection of CF770-labeled horse spleen AFt. **(b)** Quantification of *ex vivo* imaging of horse spleen AFt-CF770 total radiant efficiency (n = 6, mean ± SD).